Durham E-Theses

A study of extensive air showers at sea level

Fatemi, S. J.

How to cite:

Use policy

A Study of Extensive Air Showers

at Sea Level

by

S.J.Fatemi, B.Sc.

A thesis submitted to the University of Durham

for the Degree of Doctor of Philosophy

APRIL 1981

Thesis
1981/FAT

CONTENTS

ABSTRACT

The lateral distribution of muons of energy
$E_\mu > 500$ MeV in E.A.S. of median size 3.10^5 particles at
sea level and their correlation to the electron structure
function (shower age parameter) has been investigated using
a large flash tube chamber operated in conjunction with the
Durham E.A.S. array. The lateral distribution seems to be
not dependent on shower size, but for the more inclined and
older showers it tends to be flatter. Old showers of a given
size are found to contain a greater total number of muons than
young showers of the same size.

A measurement of the size spectrum has been performed
in which the size and collecting area take into account the
age parameter of a single shower. Except at very small and
large shower sizes, the spectrum shows a close agreement with
the spectrum obtained assuming all showers obey the Greisen
average lateral structure function.

A search for charged e/3 particles (quarks) close to
the core of E.A.S. has been carried out using the flash tube
chamber. In 511.2 hours running time, 2 low efficiency tracks
have been observed but none fulfil all the criteria as a
genuine quark candidate. A search for any preferred arrival
direction of showers in galactic coordinates has been carried
out. The results show an overall isotropic primary flux but
in the galactic chart two anomalous regions (regions with an
excess of events) are observed. Correlation of the regions
with the known cosmic ray sources (supernova remnants, pulsars,
quasars, X and γ -ray sources) have been studied.

PREFACE

This thesis describes the work performed by the author in the Physics Department of the University of Durham while he was a research student under the supervision of Dr. F. Ashton.

The Durham E.A.S. array, in conjunction with a large flash tube chamber, has been used to study the different components of E.A.S.

The author has shared with his colleagues the collection of the data obtained by the flash tube chamber and has been responsible for the calculations and data interpretation described in the thesis. Air shower information was supplied by Dr. M. G. Thompson, Mr. A.C. Smith, Mr. T. R. Stewart and Mr. M. Treasure.

Some preliminary results, described in this thesis, on electron density fluctuation, muons and the size spectrum, have been reported by Ashton et al (1977).

iii

ACKNOWLEDGEMENTS

CHAPTER 1

INTRODUCTION

1.1   HISTORICAL REVIEW

In the year 1900, when Elster and Geitel used electro-
scope techniques to study the electrical conductivity of air,
they noticed the existence of a radiation which continuously
ionized the air in the electroscope.   In the same year,
independently, Wilson studied this ionizing radiation using
an ionization chamber, where he noticed the penetrability of
this radiation, which could pass through a thick layer of earth.
Although they did not think it was due to x-rays or radio-
active radiation against which the devices were shielded, it
was thought that it could be due to some radioactive substances
still unknown in the earth's crust.   If this was the case
as we go high in the altitude, there should be less ionization
in the apparatus.   According to this expectation, Gockel
(1910,1911) performed a balloon experiment at various heights
above sea level and their experiment showed the expected effect
weakly in their limited range of height of observation.

The continuation of this work was by Hess (1912) who
extended the height of observation.   He first observed a
slight decrease and later a rapid increase up to an altitude
of 5 km.   The result made it evident that the unknown radiation
came from high altitudes.   Kolhorstr (1914) performed a balloon
experiment and confirmed the Hess result when ionization
increased up to an altitude of 9 km.   It was argued that it
could be due to radioactive gases high in the atmosphere or
might be due to thunderstorms.   The radiation discovered by

Hess was later investigated in more detail in a series of experiments by Millikan (1923-1926). As an example, he performed the experiments some metres under the surface of two lakes which were thought to be free from radioactive contamination. The result showed in both places a decrease with depth indicating a radiation travelling downwards in the air. He also performed experiments at much higher altitudes, up to 15 km, and his overall result showed that the discovered radiation came from above the atmospheric surface of the earth and was given the name 'cosmic rays'. Since then, they have been the subject of intensive study. At the time, γ radiation was the only known penetrating radiation, so the cosmic rays were assumed to be photons. The next investigations used detectors like the cloud chamber and Geiger-Muller counter to identify and study the charged particles. A great number of different particles were found to be involved in cosmic rays. Positrons were discovered in electron-photon cascades by Blacket and Occhialini in 1932. Muons were discovered by Anderson and Neddermeyer in 1937, and the mass of the muon was found to be about 200 electron masses, it being unstable and decaying into an electron and two neutrinos with a decay constant of 2 μs. Muons are secondary particles produced by π-μ decay, the pions being produced when primary cosmic rays (which are mainly protons) interact in the atmosphere. At sea level there is a considerable flux of muons and they form the major component of radiation able to penetrate 10cm of lead.

1.2   THE NATURE AND ENERGY SPECTRUM OF THE PRIMARY COSMIC
       RAYS

The problem in investigating the nature of primary

cosmic ray particles are their low intensity at high energies
($\gtrsim 10^{14}$ eV), and especially their decreasing intensity as
the primary energy increases. Primary particles with energy
up to 10^{20} ev have been detected and so far no cut-off has
been observed.

At low energies ($\lesssim 10^{13}$ ev) direct measurements are
possible by sending balloon and satellites to high altitudes.
In the energy region $10^{10} - 10^{13}$ eV, the composition of the
primary flux is given by Juliussen (1975), and is shown in
Table 1.1. A comparison between this composition and that
of the universe shows that there is a considerable excess of
light nuclei (about 10^6 times more) in the primary radiation.
This can be explained by the fragmentation of heavier nuclei
in penetrating the amount of matter in space (~ 1 H atom cm^{-3})
on their way to the earth. Another point from the table is
an increase in the relative abundance of heavy nuclei with
increasing primary energy. This is seen especially for iron
where at 10^{13} eV, it is as abundant as hydrogen nuclei in
primary cosmic rays. Balasubrahmanyan and Ormes (1973)
suggest that at high energies ($\gtrsim 10^{14}$ eV), the composition
of primary particles are dominated by iron nuclei. A consider-
able work of interest concerning this matter is given by
Ulejniczak and Wolfendale (1977). They assumed a linear
extrapolation to the higher energy region which was based
on the measured low energy spectra of various components of
the primary cosmic rays. They obtained the relative flux of
iron nuclei to be only 25% for 10^{14} eV and 31% for 10^{15} eV,
which does not show firm evidence for much of a change in

Z Elements	Kinetic energy per nucleus (eV)			
	10^{10}	10^{11}	10^{12}	10^{13}
1 Hydrogen	58± 5	47± 4	42± 6	24± 6
2 Helium	28± 3	25± 3	20± 3	15± 5
3-5 Light nuclei	1.2±0.1	1.1±0.1	0.6±0.2	-
6-8 Medium nuclei	7.1±0.4	12.2±0.8	14± 2	-
10-14 Heavy nuclei	2.8±0.2	6.7±0.5	10± 1	-
16-24 Very heavy nuclei	1.2±0.2	3.6±0.4	4± 1	-
26-28 Iron group nuclei	1.2±0.2	4.5±0.5	10± 2	24± 7
$\geqslant$ 30 very,very heavy nuclei		0.007 ± 0.004		

TABLE 1.1 : Composition of cosmic rays at high energies
(after Julliussen et al, 1975).

composition. Information on the energy spectrum of primary particles in this energy has been summarized by Kempa et al (1974) and the result is shown in Figure 1.1. The most important aspect of the spectrum is the evidence of a "bump" in the region of $10^{14} - 10^{15}$ eV. The existence of the bump may be due to the contribution of pulsars to the cosmic ray flux (Karakula et al, 1974).

1.3   ORIGIN OF COSMIC RAYS

        Since the discovery of the cosmic radiation, the problem of the origin and the acceleration mechanism of these very high energy particles has been studied. The primary particles can in principle have three origins.

        (a) Solar origin.

        (b) Galactic origin.

        (c) Universal or extra-galactic origin.

(a) Solar origin : At first it was believed that the sun is the only producer of observed cosmic rays. The idea started after the observed increase of cosmic ray intensity at the time of solar activity was observed. It indicated that there is an acceleration mechanism available on the sun which can produce particles with energies up to 10 GeV. Later, it was suggested by some workers that particles of higher energies also originate from the sun where their energies are acquired from the interplanetary magnetic field (H) in storage time of $10^3 - 10^8$ years before reaching to the earth.

        The objection to this idea could be seen from a calculation (Galbraith, 1958). The comparatively weak interplanetary magnetic fields ($\sim 10^{-5}$ gauss) are not able to confine a proton of 10^{14} ev to the solar system. This
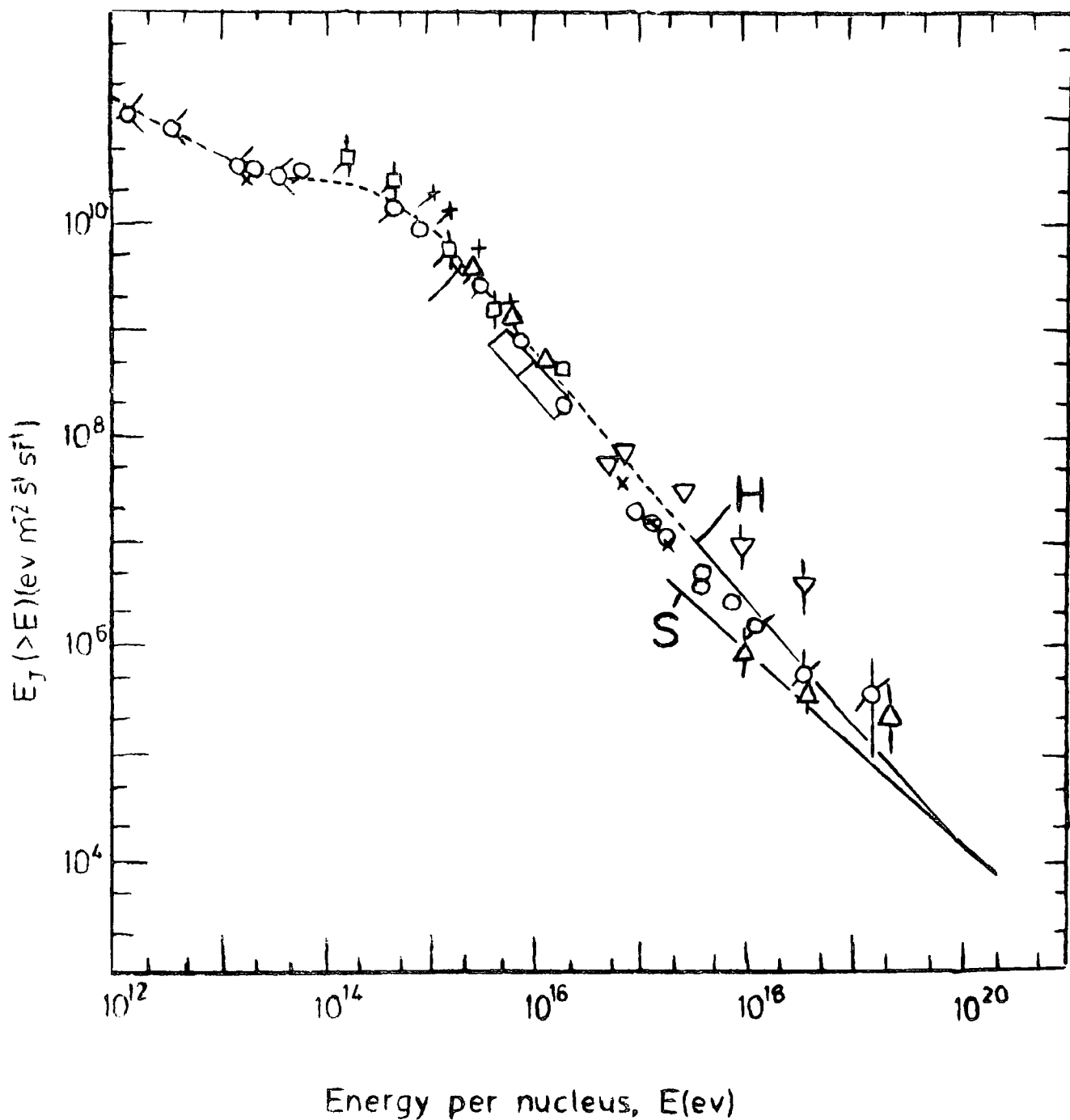
Figure 1.1 : The integral primary cosmic ray spectrum.
Combination of data from Figure 2 and Figure 4
of Kempa et al (1974).

would result in an anisotropy of the radiation and it is

not observed.   Therefore, the sun cannot be the only

cosmic ray source.   The necessity of other cosmic ray

sources and a more powerful mechanism of particle accelera-

tion is required.

(b) Galactic origin : The assumption is that other stars like

the sun in the galaxy (containing 10^{11} stars) generate cosmic

rays.   The required total observed flux would not be possible

to produce.   Therefore we have to look for additional sources

in other types of star.   Several suggestions have been made,

for example, stars such as magnetic variable stars as well

as novae and supernovae are considered.   However, the energies

obtained by particlesaccelerated at their region of origin

are not likely to be as great as those observed for the

highest energy particles.   Therefore an additional accelera-

tion process is necessary, which is possibly the collision

of cosmic ray particles with magnetised gas clouds as they

stream through the arms of the galaxy.

(c) Extra-Galactic origin :   There is a suggestion that very

high energy cosmic ray particles producing E.A.S. of great

size have extra-galactic origin because their energies are

too high to be confined within the galaxy by the galactic

magnetic field.   Therefore they leak out from one galaxy into

space and then enter other galaxies to contribute an extra-

galactic component to the cosmic ray flux.

1.4   SECONDARY PARTICLES IN THE ATMOSPHERE

On entering the earth's atmosphere, the primary

particles which are now known mainly to be protons and

α-particles, interact strongly with the nuclei of the air

molecules. In these interactions a variety of secondary particles are produced. They are mainly of π-mesons (pions) and are partly kaons, hyperons and nucleons. The secondary pions have three charge modes (π^+, π^- and π^0) which are produced in equal numbers.

The neutral pions decay with life time of 10^{-16} sec into two photons and further the two photons produce an electron-photon cascade in the atmosphere. The enormous number of electrons and photons forming the electromagnetic cascade of E.A.S. originate from these neutral mesons.

Cosmic ray muons are the result of charged meson decays and because of their relatively long life time (2.10^{-6} sec) a considerable flux of them is observed at sea level. In E.A.S. they form the muon component where the properties of these muons reflect the characteristics of the nuclear interactions from which their parent mesons originate.

At sea level most of the particles in a shower are electons and muons, and the propagation of these and other secondary particles through the atmosphere is shown in Figure 1.2 where a proton primary particle is assumed.

1.5   THE QUARK SEARCH

Since the introduction of quark theory, many experiments have been performed to search for these fractionally charged particles. Naturally the search was first carried out at accelerators where carefully controlled experiments could be done. The negative results of accelerators indicate that the quark mass may be greater than the maximum kinematically possible for production at present accelerator energies. This was the reason that attention was

Primary proton
$(E \geqslant 10^{13} ev)$

air nucleus

π^+, π^- π^+ π^- π^0 π^0 π^0

μ^+

n,p

e^+ e^- γ e^-

μ^-

$\mu^\pm$

nucleon
cascade

e-γ
cascade

e^+

e^-
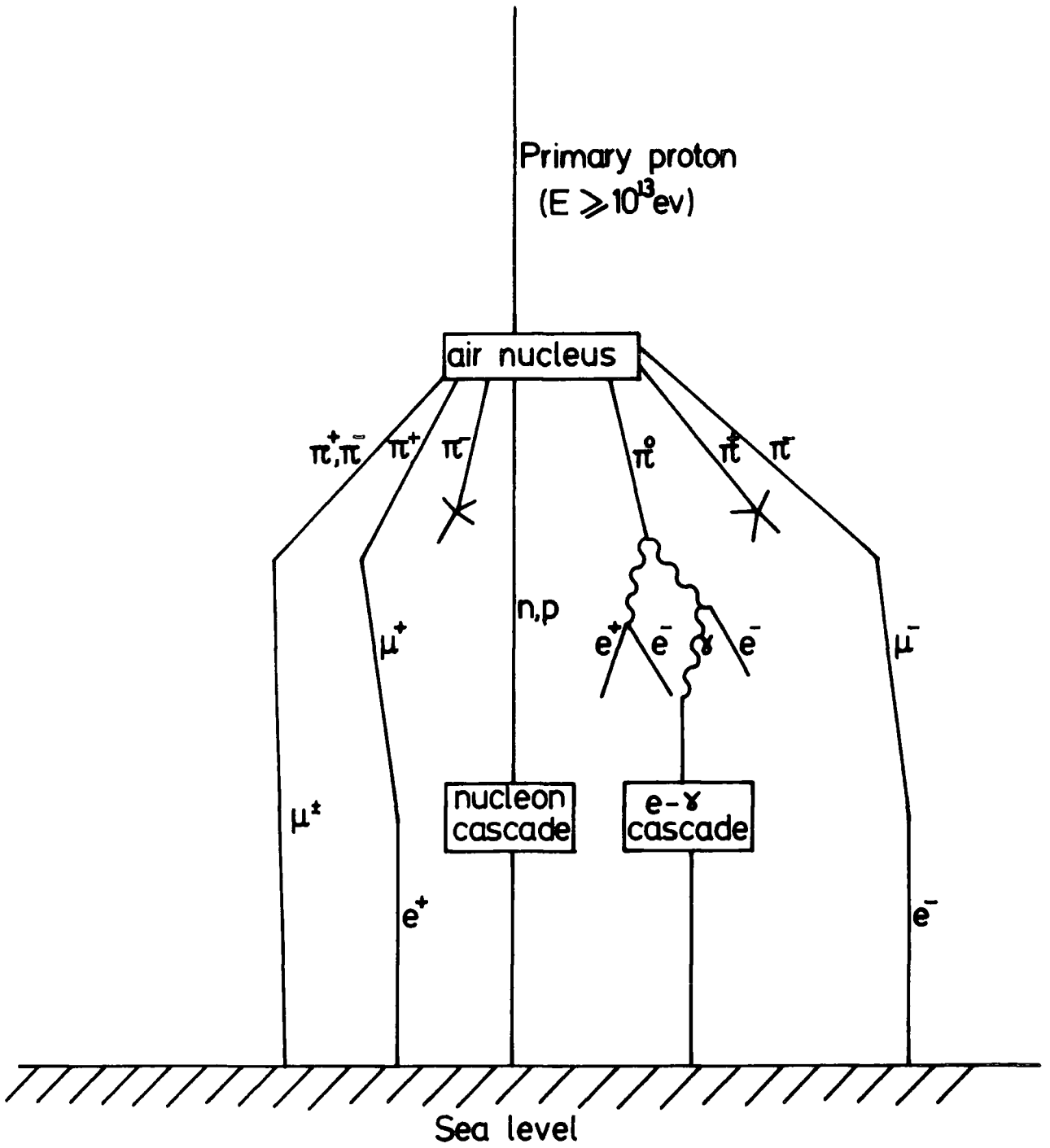
Sea level

Figure 1.2 :   Diagram showing the major processes taking

place in the atmosphere when an extensive

air shower is observed at sea level.

focused on searches in cosmic rays which are sources of much
higher energies. The unique importance of cosmic rays comes
from the fact that it is the only beam of particles with
energy greater than 10^{12} eV that exists in the nature.
The present search for quarks is described in Chapter 7, where
an investigation close to the core of E.A.S. with medium size
3.10^5 particles is described.

1.6   THE SIGNIFICANCE OF COSMIC RAY STUDIES

It is the broad cosmic ray energy range from about
10^8 eV to an unknown upper limit (recorded up to 10^{20} eV)
which makes it of interest in two different fields of study.
These are studies aimed at obtaining new information in the
fields of elementary particle physics (e.g. quarks) and
astrophysics (sources, acceleration mechanisms, composition
etc).   It was cosmic ray studies that led to the discovery
of many fundamental phenomena such as the observation of
very high transverse momentum of secondary particles in some
collisions and the change of their multiplicity with energy
etc. which is of importance in the investigation of high
energy collisions.

Over the years, most of the elementary particles such
as muons, mesons and kaons, have also been discovered in
cosmic rays where their properties were qualitatively known
before using accelerators to study them.   Accelerators which
produce artificial particle beams can be used up to energies
of about 10^{12} eV. To increase the beam energy of accelerators
up to 10^{15} eV will take some time and even then this energy
is in the relatively low cosmic ray energy range. In spite
of this problem, accelerators are still of great importance

since they give good information concerning low energy

nuclear interactions which is compared and extended in

cosmic ray experiments.

The cosmic rays have also been the source of search

for particles theoretically predicted such as quarks, tachyons

and magnetic monopoles.

Cosmic rays are also a powerful source of astrophysical

information where high energy X and γ rays are the examples

of reliable sources of interest.

Also, very high energy cosmic ray particles in the

E.A.S. region with Ep $\gtrsim$ 10^{15} eV are of interest because of

the reason that they may not be affected greatly by existing

magnetic fields on their way to earth and hence show the

direction of the source. They are also a probe to investigate

the condition of the galaxy and beyond it which is of astron-

omical interest.

Chapter 8 gives the arrival direction analysis of

E.A.S. in galactic coordinates where any preferred arrival

direction (e.g. a point source) has been investigated in some

detail.

CHAPTER 2

THE DURHAM E.A.S. ARRAY AND THE FLASH TUBE CHAMBER

2.1   INTRODUCTION

The flash tube chamber is a large visual detector and has been used in conjunction with the Durham E.A.S. array to study the characteristics of E.A.S. at sea level. It was originally built to search for quarks and later was modified to look at strongly interacting particles (hadrons), through their burst production in the chamber.

The major aim of the present experiment was to investigate the muon component of E.A.S, but because of the observation of some low efficiency tracks throughout the experimental runs, an effort was also made to identify whether any low ionizing tracks could have been produced by fractionally charged particles (quarks). The array information apart from using it to measure the major shower parameters (i.e. core position and shower size), was also used to study the electron structure function of E.A.S. which is characterised by the age parameter of the shower. Also, from the density information of the array, the fluctuations of the electron density were also studied in some detail.

2.2   THE FLASH TUBE CHAMBER

2.2.1 Construction of the Chamber

The scale diagram of the neon flash tube chamber is shown in Figure 2.1 . The chamber has been constructed of about 11000 flash tubes. The tubes are cylindrical and 2 metres in length with mean external diameter 1.78 cm and an internal diameter of 1.58 cm. They are made of soda glass

LMS.

LEAD

8 layers — F1a

IRON

A

6 layers — F1b

46 layers — F2a

48 layers — F2b

8 layers — F3a

B

8 layers — F3b
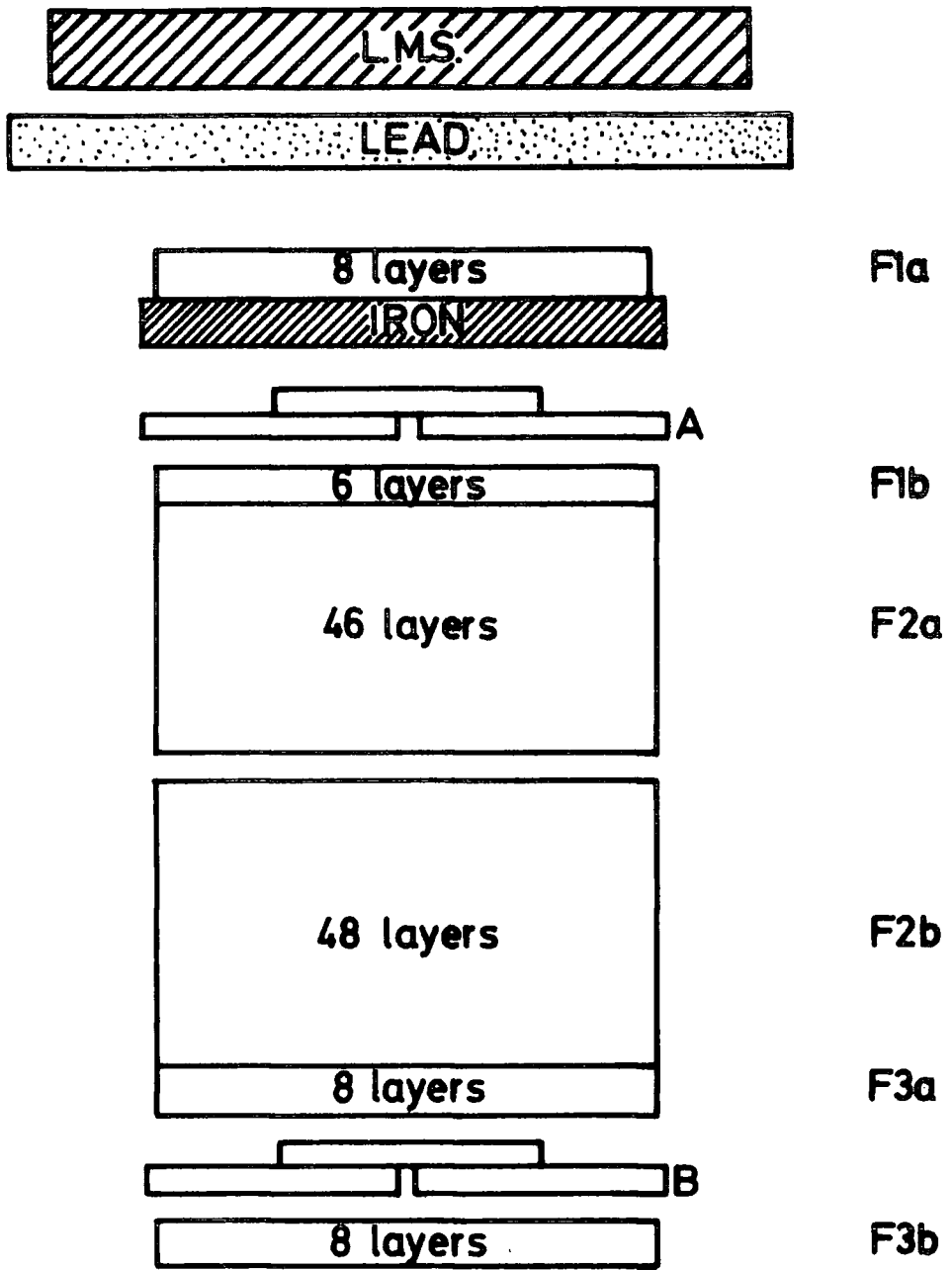
FRONT VIEW

scale: 0 20cm

Figure 2.1 (a) : Front view of the chamber.

N M S

LEAD

8 layers   F1a

IRON

A

6 layers   F1b

46 layers   F2a

48 layers   F2b

8 layers   F3a

B

8 layers   F3b
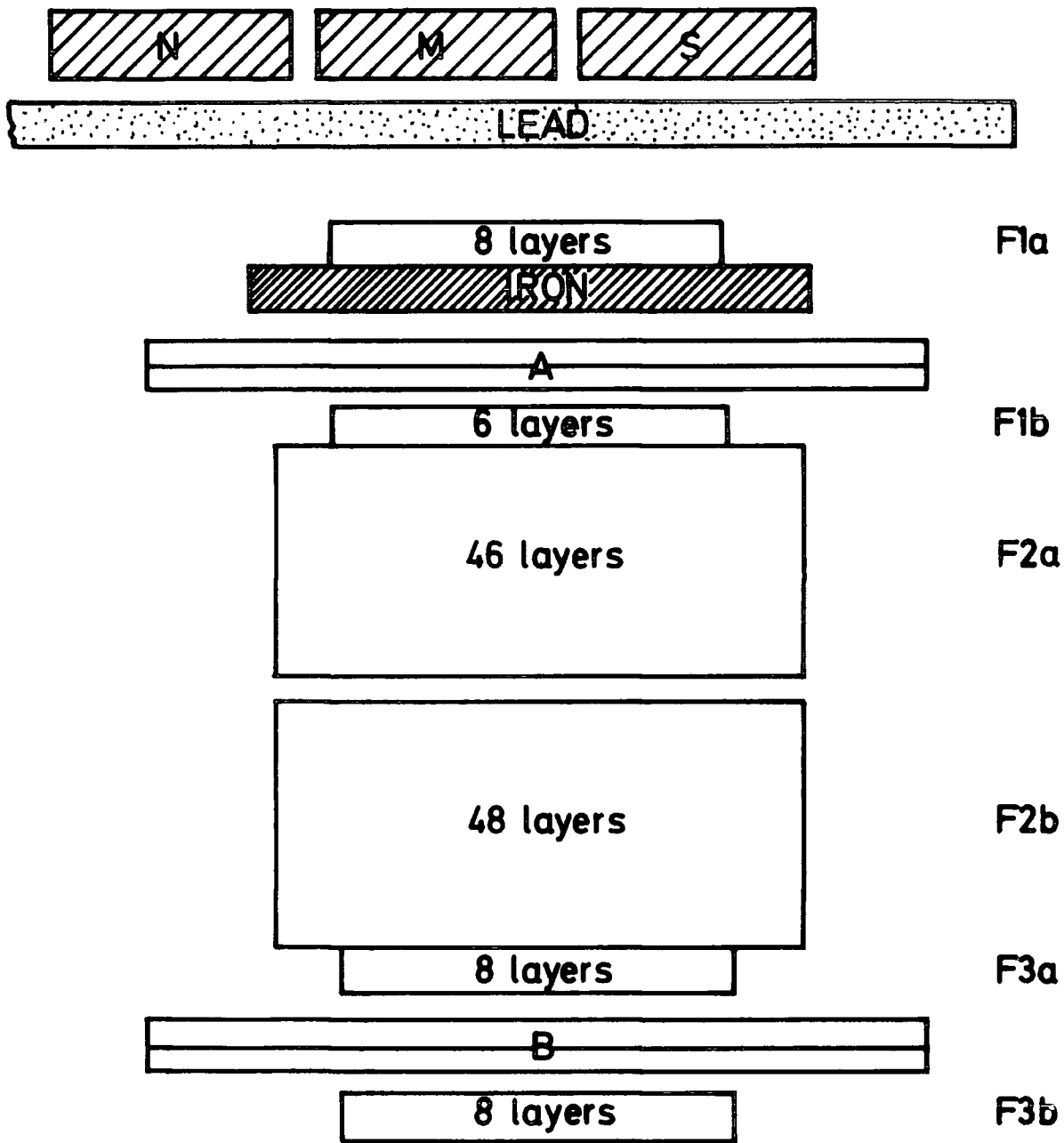
SIDE VIEW

scale:
0   20cm

Figure 2.1 (b) :   Side view of the Chamber.

filled with neon gas (98%) and helium gas (2%) to a pressure 60 cm of mercury.

The tubes are covered with polythene sleeving to prevent light passing through the neighbouring tubes. The tubes are distributed in 124 layers of 84 or 85 tubes per layer and between every two layers of tubes is an aluminium electrode, 0.122 cms thick and with an area of 2.94 m^2. The arrangement of different sections of the chamber is shown in Figure 2.1 . From the top to the bottom, it consisted of a layer of 15 cm of lead, 8 layers of flash tubes (F1a), a layer of 15 cm of iron, three plastic scintillators, each 1.05 m^2 area designated A plus a further 4 blocks of flash tubes, F1b (6 layers), F2a (46 layers), F2b (48 layers) and F3a (8 layers), three plastic scintillators each of 1.05 m^2 area (B) and the final part is 8 layers of flash tubes (F3b). The scintillators (A and B) were not used in the present work. The shielding materials of the chamber are the 15 cm of lead absorber on the top and at the sides 30 cm barytes concrete walls designed around the chamber to cut out the soft component (electrons and photons) of E.A.S, while allowing penetrating particles (muons) to pass through the chamber. During the time that the experiment is running, the chamber remained in the dark and the photographs are taken by a camera without a shutter. This means that the camera is continuously sensitive to an event and it winds on automatically by one frame after each event.

2.2.2 The High Voltage Pulsing System

A high voltage pulse is applied to the electrodes of the chamber to operate the flash tubes which are affected by

the passage of the particles. It is supplied by a high
voltage pulsing system which consists of a thyristor pulsing
unit and an air spark gap shown in Figure 2.2. The high
voltage pulse is produced after the triggering requirement of
the array is established. It is produced by a 5 volt trigger
pulse which is used to trigger a thyristor, producing an output
pulse of 300 volts. This voltage pulse is applied to the
primary of a high voltage transformer and produces an output
as the trigger pulse for the spark gap. A voltage of 16Kv is
applied across the main spark gap, which causes the gap to
break down when the trigger spark is produced. The pulse
applied to the electrodes of the chamber has a shape which is
approximately rectangular with a height of 8 KV and a length
of 10 μs.

2.2.3 Properties of Flash Tubes

When a charged particle passes through a flash tube
it ionizes the gas and leaves a trail of positive ions,
electrons and excited atoms along its track. After a time
delay between the passage of the ionizing particle the high
voltage pulse is applied to the electrodes. This causes a
breakdown of the neon gas in the tube and a visible discharge
results in the tube. The problem of ionization and what
causes the discharge has been discussed in detail by Lloyd
(1960). The conclusion is that only the electrons which are
produced initially are responsible for the discharge. He
concluded that positive ions, metastable neon atoms and
produced photons do not contribute to the probability of
discharge and can have little or no effect.

Lloyd set up diffusion equations for electrons
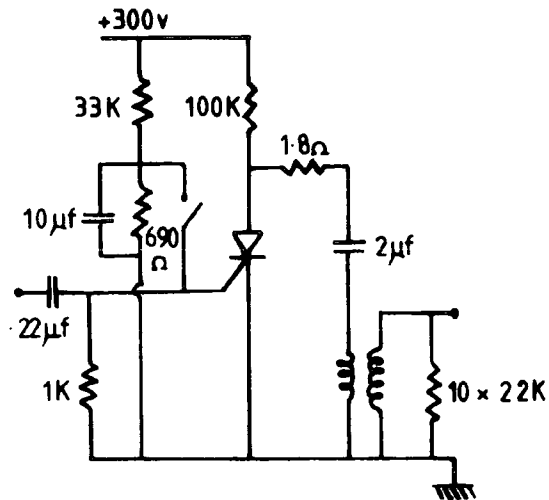
Figure 2.2 (a) : High voltage pulsing unit.
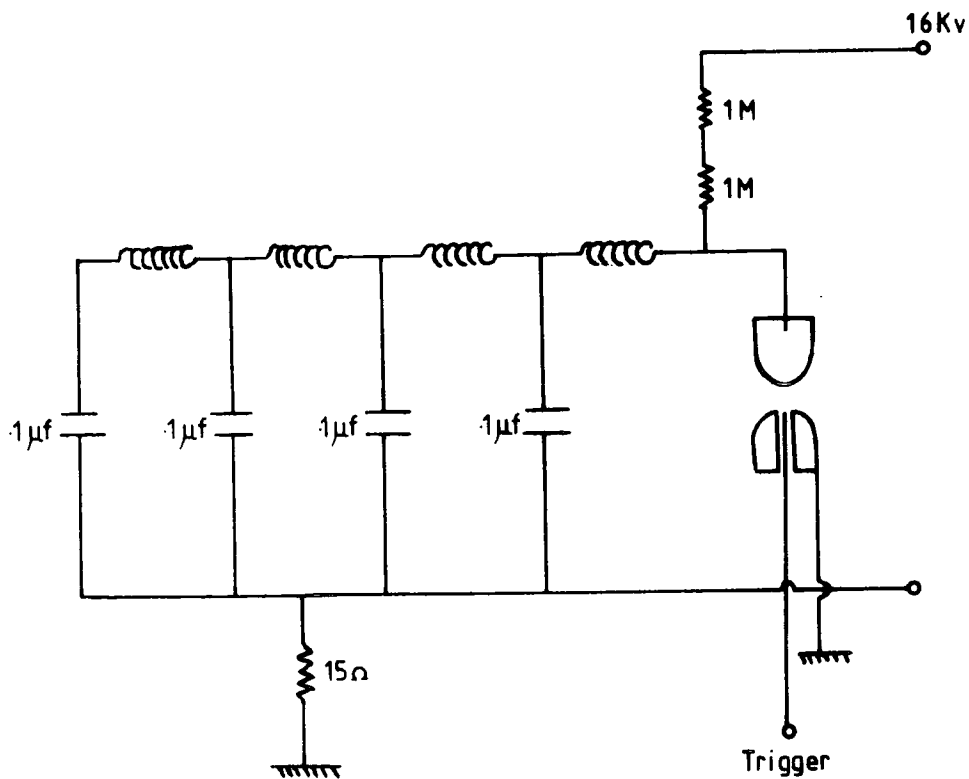
Figure 2.2(b) : Spark gap and delay line.

produced in the tube and solved them. The solution gave the

probability of a discharge occurring, when a high voltage

pulse is applied to the tube in a time T_D after passage of

a charged particle. This probability is known as the internal

efficiency, and he expressed it as a function of $\dfrac{D \cdot T_D}{a^2}$ and in

terms of a parameter $af_1 Q_1$, where D is the diffusion coefficient

of thermal electrons, a is the internal radius of the tube,

f_1 is the probability that a single electron is capable of

producing a flash when a high voltage pulse is applied, and

Q_1 is the number of initial electrons produced per unit length

in the neon gas. The only parameter dependent on the charge of

the particle is Q_1 and is related to the ionization loss of

the particle in the gas which is a function of the square of

the electric charge. This forms the basis of the use of the

flash tube chamber in the search for quarks, since the term

$af_1 Q_1$ is 1/9 for a particle of $e/3$ compared to that of charge e.

Using the Lloyd theory, the internal efficiency of the tube

as a function of time delay for different values of the $af_1 Q_1$

parameter has been calculated and are shown in Figure 2.3.

It is seen from this figure that the efficiency of the tube

falls off as the time delay increases. This is due to the

fact that the initial number of electrons in the gas will

decrease due to diffusion to the glass tube walls where they

stick.   The longer the time delay the greater is the prob-

ability that no electrons remain in the gas.

2.3   THE E.A.S. ARRAY EXPERIMENT

2.3.1 Introduction

The Durham E.A.S. array consists of 14 plastic

scintillation counters which are located around the neon
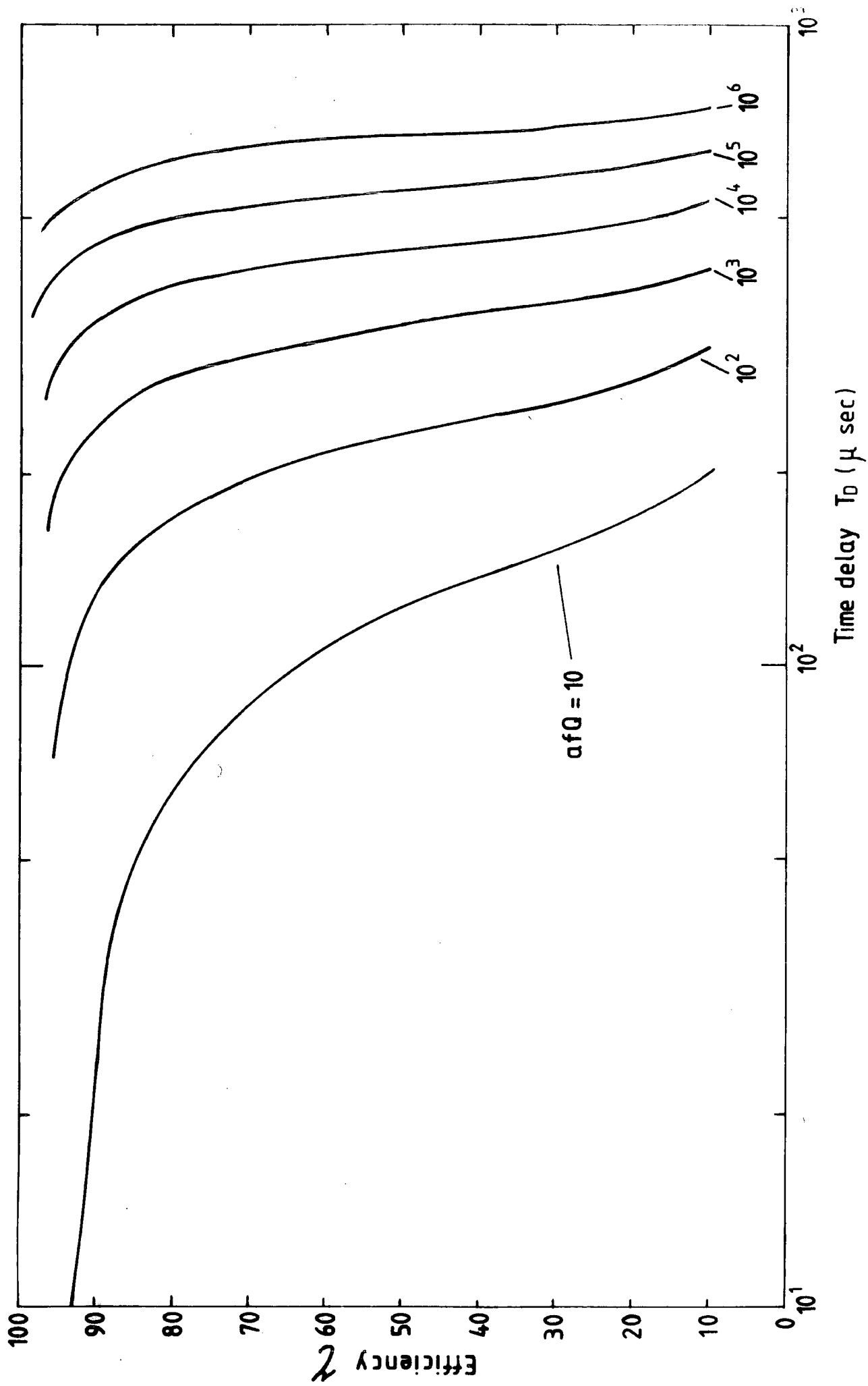
Figure 2.3 : Predicted variation between the internal efficiency of the flash tubes and the high voltage pulse time delay for different values of the parameter afQ. afQ = 10 gives a good fit to the measured efficiency versus time delay curve for relativistic muons traversing the chamber.

flash tube chamber inside a cirlce of radius of $\simeq 60$ m. The detectors have areas varying from $2m^2$ to 0.75 m^2. The location of these detectors are shown in Figure 2.4, which are essentially arranged in a triangular symmetry. All of the detectors are used to obtain the density measurements and seven of them also give the fast timing information. The density and fast timing detectors are the central detector, C, 0.75 m^2 and six 2 m^2 detectors, which are also shown in Figure 2.4. These detectors give time markers when the shower front passes through them, which are relayed to the laboratory, where they are converted into time differences relative to the time the shower front passes through the central detector C and stored to determine the arrival direction (θ and ϕ) of the shower. The operation mechanism of the array will be given later, when the various kinds of detectors are described in the next section.

2.3.2 The Detecting Elements and Fast Timing Technique of the Array

The main detecting elements of the array are plastic scintillation counters. These are the 2 m^2 detectors, 11,13,31,33,51,53, the central 0.75 m^2 detector C, the 1 m^2 detectors 41,52,32 and the 1.6 m^2 detectors 42,12,62,61. The first two sets of detectors are used to select E.A.S. events as well as for density and fast timing measurements, and the rest are used only for particle density measurements. The detectors consist of one or more slabs of plastic scint- illator viewed by four photomultiplier tubes to measure the particle densities in a shower. The fast timing detectors have an extra one or two fast timing tubes (Philips 56 AVP), to
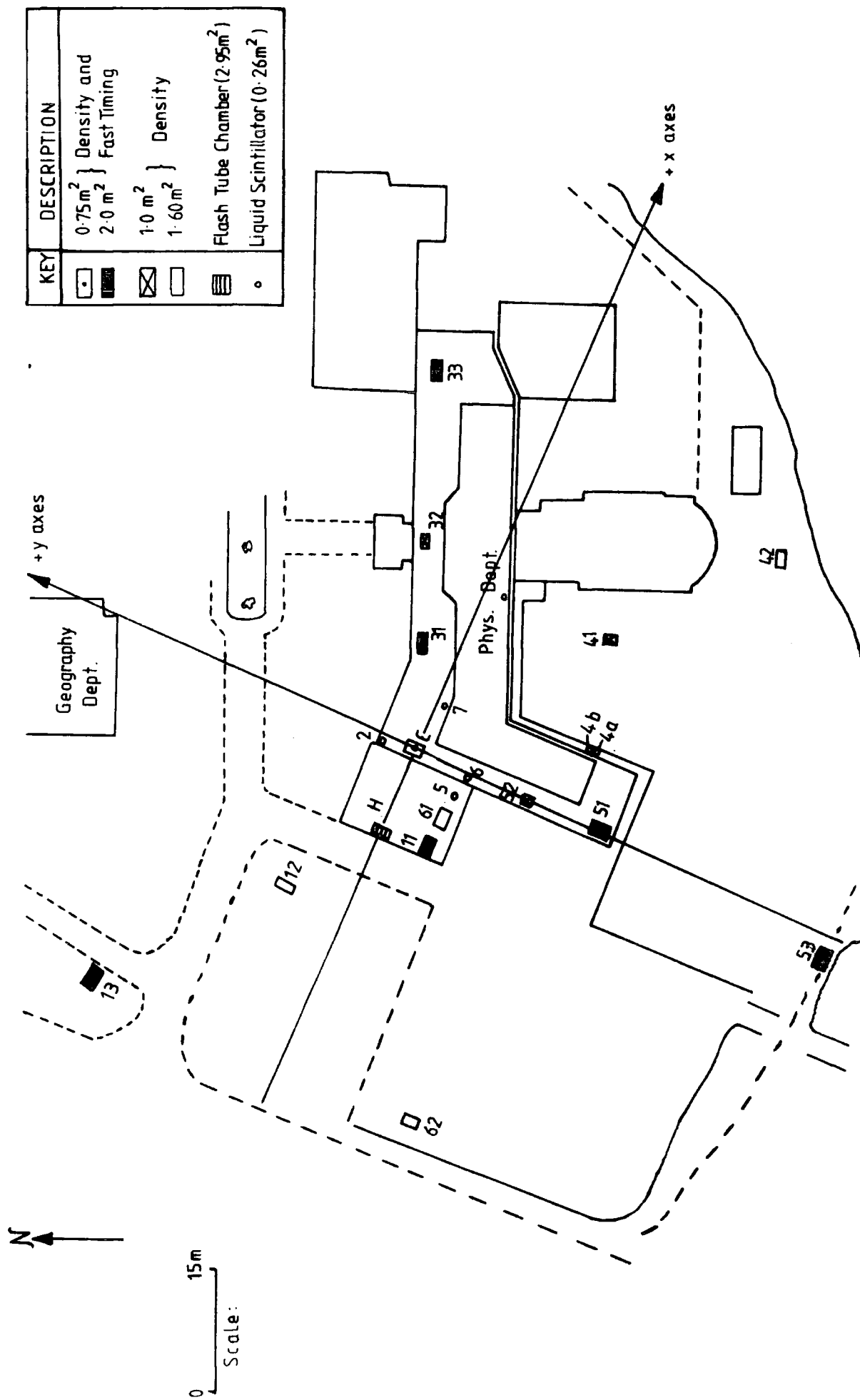
Figure 2.4 : Scale diagram of the Durham Extensive Air Shower Array.

generate the fast timing pules.

It is the relationship of the time delays between pulses which is of interest and gives information on the arrival time of the shower front for the determination of the shower axis spatial direction. To do this, 6 time to amplitude converters (T.A.C's) were used, and the procedure was to take a pulse from the central detector C to start each of the six T.A.C's and stop them by the pulses from the relevant detectors. These pulses are already artificially delayed by various timing cables such that the central detector pulse (common pulse) always arrives in the laboratory before any other pulse. Therefore, the produced outputs of the T.A.C's are proportional to the time difference of the central detector pulse and one of the other detector pulses which are required to calculate the arrival direction of the shower (θ and ϕ) where the various delays in the cables are known.

Each detector also contains a head amplifier and E.H.T. distribution unit which are attached to the wall of the detector box. The box of the scintillator is made of wood and is weather-proofed with bitumen paint and aluminium foil, covered and protected also by a weather-proofed hut.

2.3.3 The E.H.T. Distribution units and the Head Amplifiers

The E.H.T. distribution units are used to supply the high voltage needed for the two types of photomultiplier tubes in the array. Each type of tube needs a working voltage which, in the present case, are set to be 2.4 KV and 2.7 KV for the density and fast timing tubes respectively. The high voltage supply to each detector is connected to a resistor chain

through a coaxial cable. Since the voltage of the similar
tubes in a detector (i.e. slow tubes) are not exactly the
same, the resistor chain is used to adjust and distribute
each tube voltage independent of the others. A resistor
chain is shown in Figure 2.5 which represents the sections
of the E.H.T. distributions at each detector. In each
detector there is also a mixer amplifier which is used to
add and amplify the output pulses of the four density photo-
multiplier tubes of each detector, as is shown in Figure 2.6.
A +24 volt power supply unit in the laboratory is used to
operate all the amplifiers in the array.

2.3.4 The Linearity of Response of Photomultiplier Tubes

In the array there are three types of photomultiplier
tubes, (P.M.T), their purpose being to convert the light output
of the scintillators into electrical pulses which in turn is
a measure of particle number. One of the necessary
characteristic of the tubes which should be known is their
response to various light input intensities. To examine this,
light emitting devices could be used (i.e. light emitting
diodes) to give similar light pulses to those obtained from
the scintillator. As the intensity of light falling on the
tubes could be varied, it was possible to examine the linearity
of response of the P.M.T. as a function of light input. The
investigation was made for all three different tubes. It
was found that the tubes were linear over the range of applied
voltages in the present experiment.
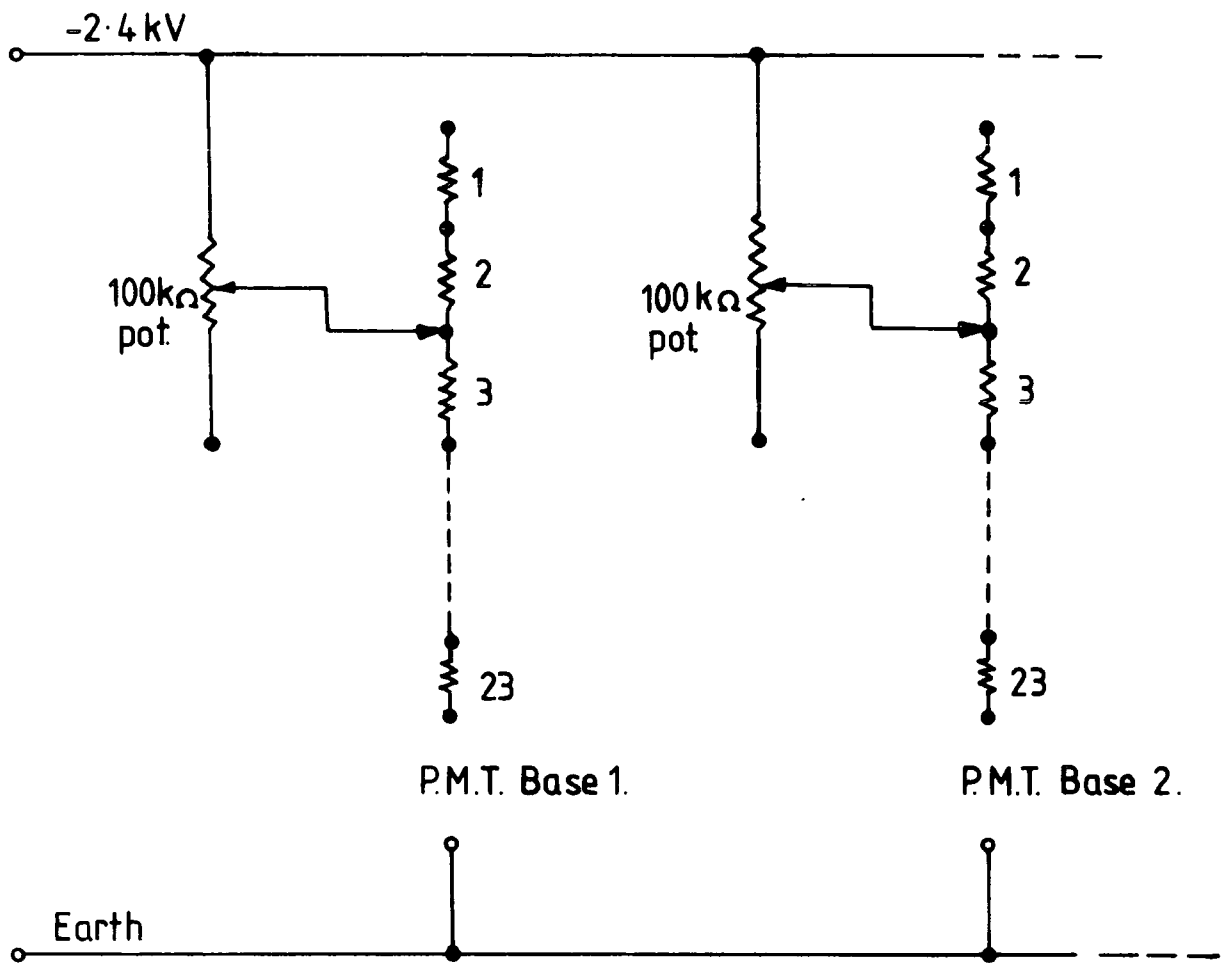
Figure 2.5 : A resistor chain (After Smith, (1976))
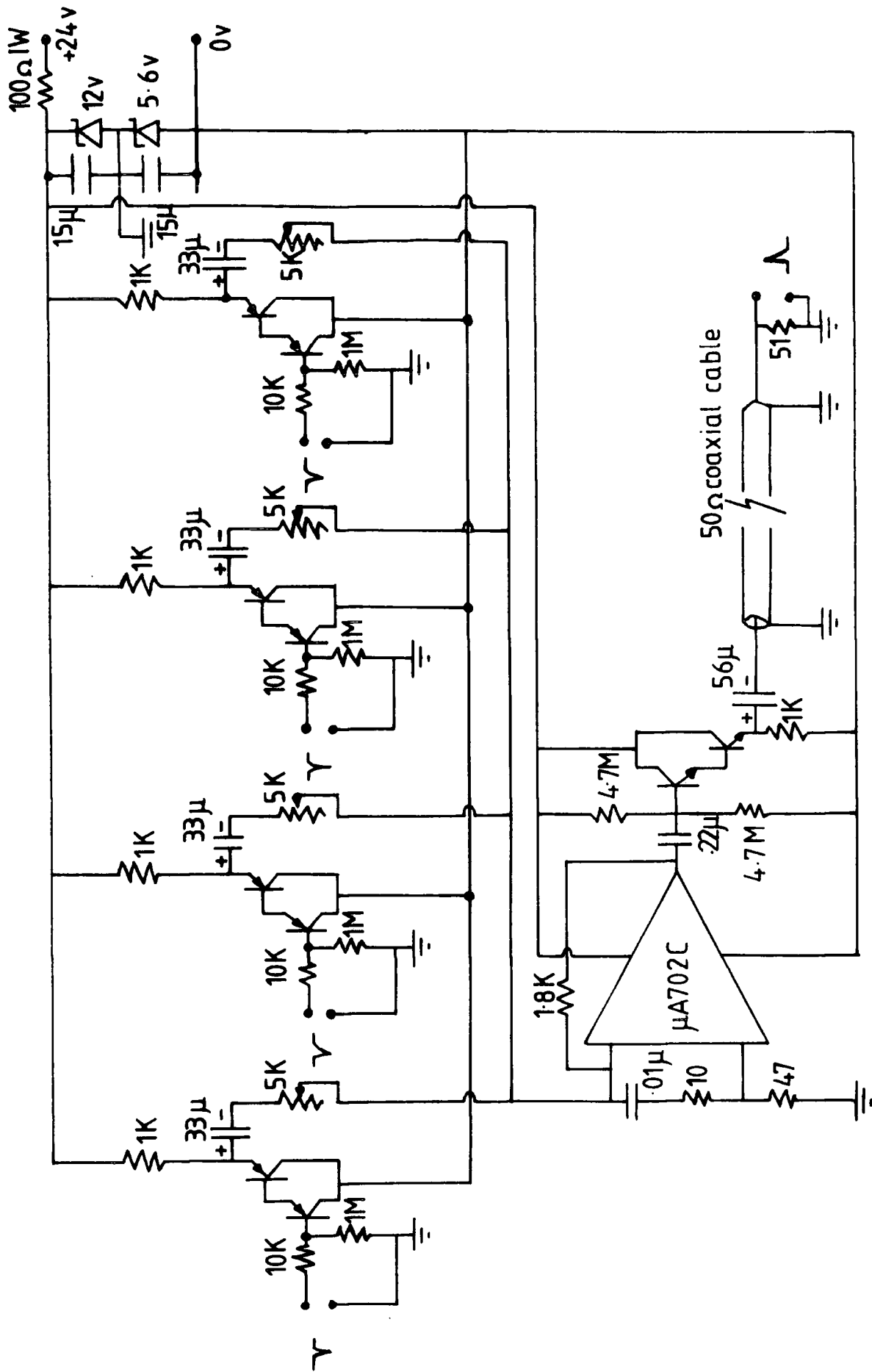
Figure 2.6 : Four input mixer amplifier (After Smith, 1976).

2.3.5 Calibration of the Detectors

A telescope and a multi-channel analyser (M.C.A) are used to calibrate the individual detectors. The telescope consisted of a 23 x 23 x 3 cm plastic scintillator viewed by two photomultipliers (Philips 53 AVP). It was used for the calibration of the density tubes, where the E.H.T. on the tube was adjusted such that the peak of the particle distribution coincides with the desired calibration value, which could be stored and shown on a M.C.A. in the laboratory. The density tubes were adjusted such that after dividing the sum of the overall pulse heights (from 4 tubes) by 100 mV, the number of particles per square metre at the detector is obtained.

2.3.6 The Data Handling Electronics

When an air shower traverses the array and satisfies the triggering condition, all the density and timing data which are now in analogue forms and are presented to an analogue to digital converter. The data are held for 2 ms and in this period each analogue signal is presented in turn to the analogue to digital converter, and the digitised pulse height is then stored in a buffer memory. Eleven events are stored in this way before the contents of the memory are automatically transferred to the magnetic disc of the on-line computer, later to be analysed.

Another set of information which is obtained by the array called "book-keeping" and is as follows :-

1 - the event number
2 - the run number
3 - the triggering mode of the event
4 - the occurrence time of the event

The necessity for this is in the identification of the event.
Figure 2.7 shows a block diagram of the data handling
electronics. More detail information of the data handling
electronics is given by A.C.Smith (1976).
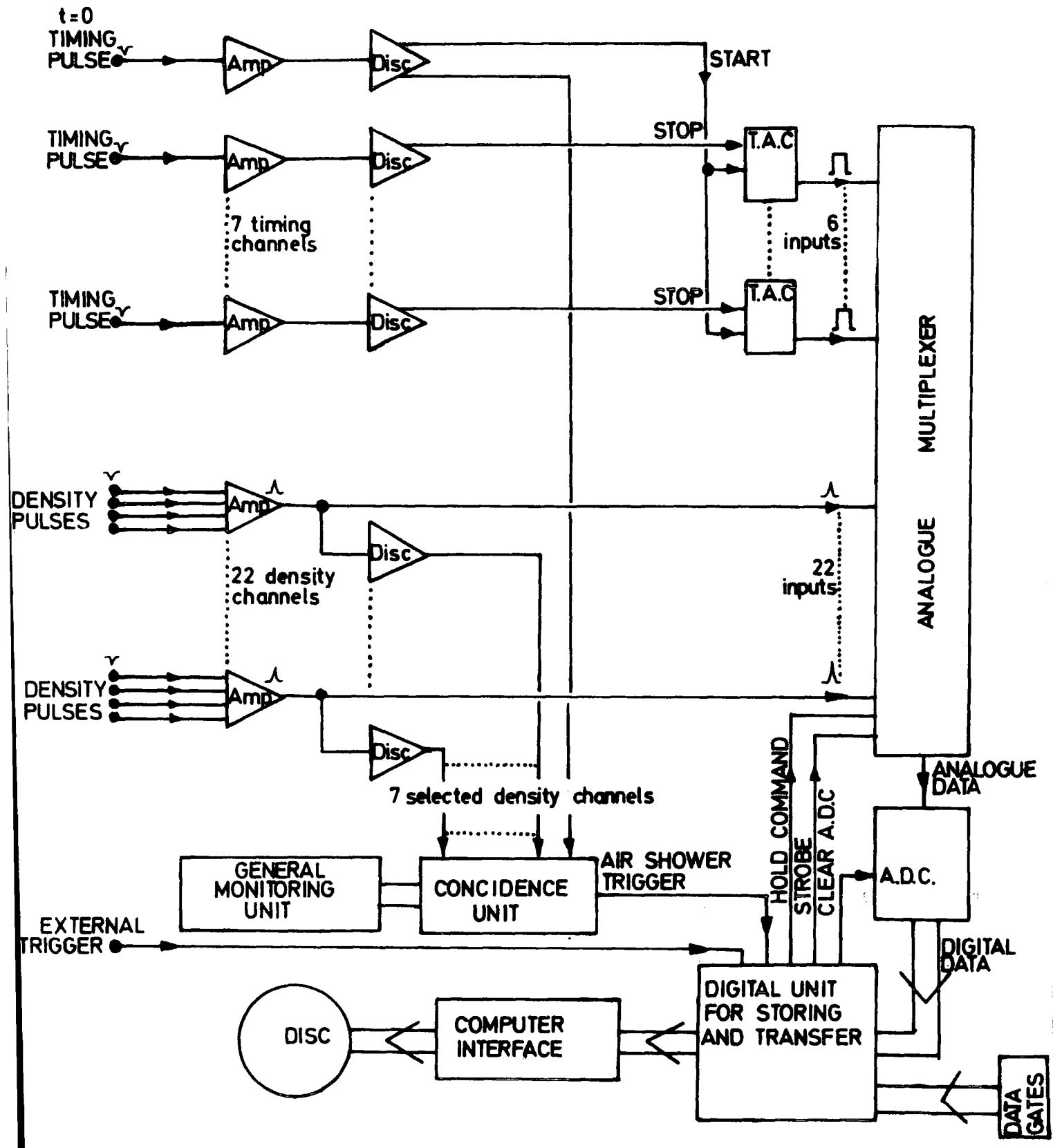
Figure 2.7 : The data handling electronics (After Smith(1976)).

CHAPTER 3

THE ELECTRON COMPONENT OF E.A.S

3.1   INTRODUCTION

Electrons are the most numerous and convenient particles to measure and study than any other existing particles in E.A.S. (i.e. muons and hadrons). The knowledge of this component is essential to get information about the other shower parameters since it provides the initial parameters required for any further measurement in E.A.S. One of the initial parameters is the correct form of the electron lateral structure function which makes it possible to have an accurate method of core location and a measure of the total number of electrons which are a necessity to interpret the shower data.

3.2   THE ELECTRON LATERAL STRUCTURE FUNCTION (E.L.S.F.)

Since the detailed knowledge and appropriate form of the E.L.S.F. is of initial importance in the investigation of E.A.S, it has therefore been the most often repeated experiment. It has been measured using different techniques and has been found that the form of the structure function is slightly dependent on the type of the detectors used. Experiments performed with Geiger-Mulier counters give a good measure of the actual electron density distribution, where the ones performed with scintillation counters give slightly steeper distributions. This is due to the sensitivity of the scintillator to the photon component of the shower.

An empirical formula for the E.L.S.F. has been

suggested by Greisen (1960) which is based on experimental measurements. This formula has the following form :

$$\Delta(N,r) = \frac{0.4\ N}{r_1^2} \left\{\frac{r_1}{r}\right\}^{0.75} \left\{\frac{r_1}{r_1+r}\right\}^{3.25} \left\{1 + \frac{r}{11.4\ r_1}\right\}\ m^{-2}$$

(3.1)

where N is measured in units of single particles and r is in metres. According to Greisen it is valid for sizes from 2.10^3 to 2.10^9 charged particles, core distances 5 cm to 1500 m from the shower axis, and zenith angles less than 55°, r_1 is the Moliere unit (79 metres at sea level).

Hasegawa et al (1962) measured the E.L.S.F. employing an array of scintillators where the result is presented by the following expression

$$\Delta(N,r) = \frac{N}{2\pi\sqrt{120}}\ \frac{e^{-\frac{r}{120}}}{r^{1.5}}\ m^{-2}$$

(3.2)

A detailed analysis of measurements by the scintillation counter is given by Catz et al (1975) in the following form :

$$\Delta(N,r) = 0.15\ N\ \frac{e^{-\frac{r}{120}}}{(r+1)^{1.62}}\ m^{-2}$$

(3.3)

where the function is valid for the distance range of 2 m to at least 70 m from the shower axis. In both these formulae N is measured in units of single particles and r is in metres. For comparison of the above three mentioned forms of structure function, they are presented in Figure 3.2, the Hasegawa et al (1962) measurements show a steeper density distribution than that of Greisen (1960) where the Catz measurements, apart from

small core distances seems to agree rather well with it.
In the present experiment, the showers were recorded by
the Durham E.A.S. array (see previous chapter) where an
E.A.S. selection of the form $\Delta_C(\geq 3.5)$, $\Delta_{13}(\geq 1.5)$, $\Delta_{33}(\geq 1.5)$,
$\Delta_{53}(\geq 1.5)$ was used (the figures in brackets are the number
of particles per square metre at the corresponding detector).
For each E.A.S. event, 10 electron density samples are
normally recorded. Four of these densities have been used
to locate the position of the shower core using the method
of intersecting loci and E.A.S. size has been determined using
the Greisen E.L.S.F,(Eqn. 3.1). For each shower, 6 density
samples are normally available to check the core position to
see whether they are consistent with the assumed E.L.S.F.
In order to present average E.L.S.F. of many events on one
graph, the measured densities have to be normalized to a
fixed size $(10^5$ particles in the present work). Normalization
means the measured densities in a shower of size N, $\Delta(N,r)$
are converted to densities that would have been measured in
a shower of size 10^5 particles, $\Delta(10^5,r)$ using

$$\Delta(10^5,r) = \frac{10^5}{N} \cdot \Delta(N,r) \qquad (3.4)$$

The normalized densities were obtained for a sample of 98
showers and are plotted as a function of core distance, r in
Figure 3.1. From the figure, the average of the densities
obtained over small intervals of core distance was calculated
and the result is shown in Figure 3.2. It is seen that the
average measured densities (representing the average E.L.S.F.
of the showers) are consistent with the Greisen structure
function, especially in the core distance range of $20 < r < 60$ m.

The plot contains the following text labels:

Total no. of showers =98
Total no. of independent density samples =371
Expected no. of independent density samples =564
Difference is due to saturation level of the detectors
and small densities (detectors didn't work)

Catz

Greisen

Catz
Greisen

electron density $\Delta_{e(\times 10^5)}$ (m^2)

core distance r(m)
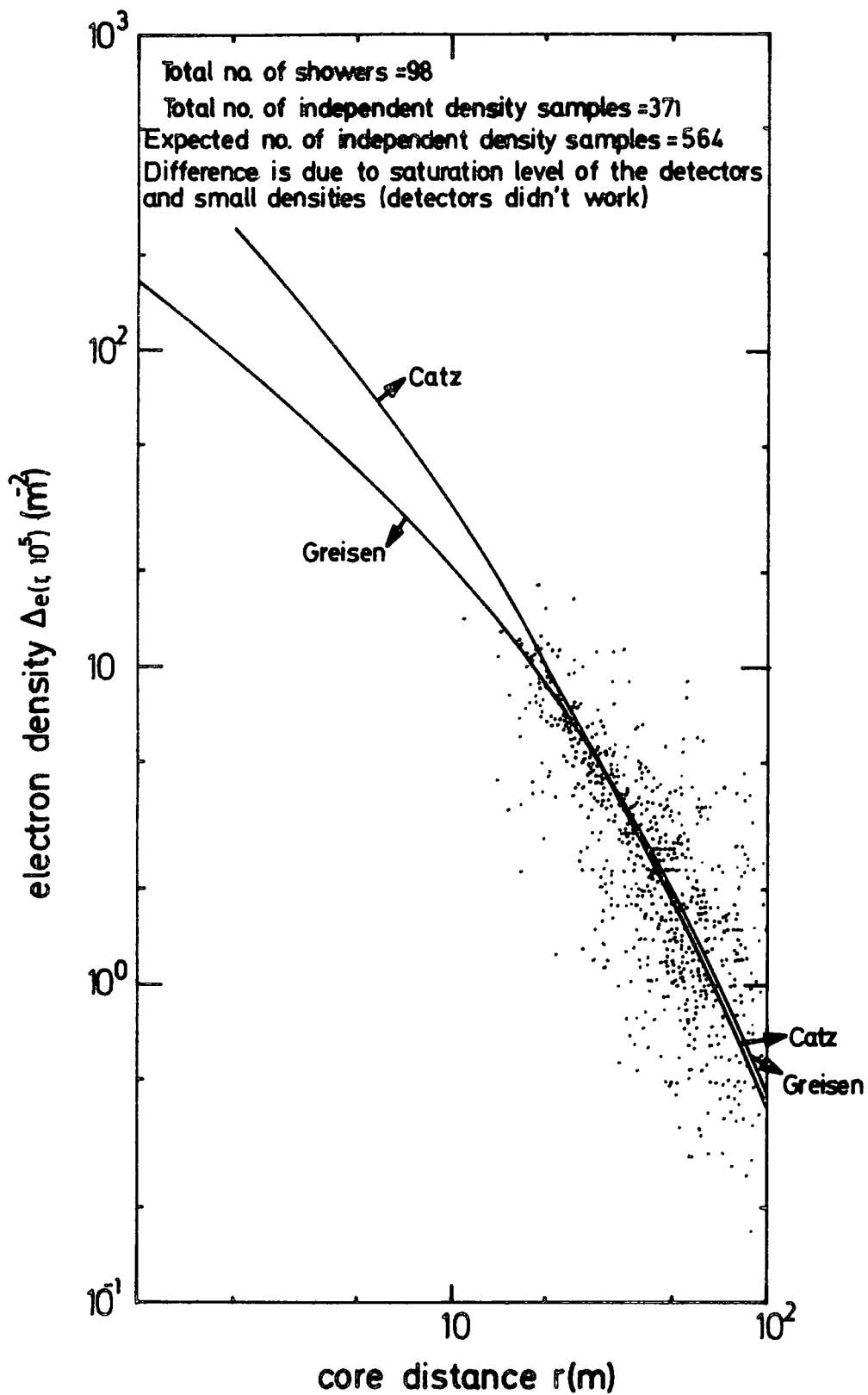
Figure 3.1 : Test of the consistency of the electron densities measured in detectors not used in core position and shower size determination with the Greisen (1960) and Catz et al (1975) lateral structure functions.
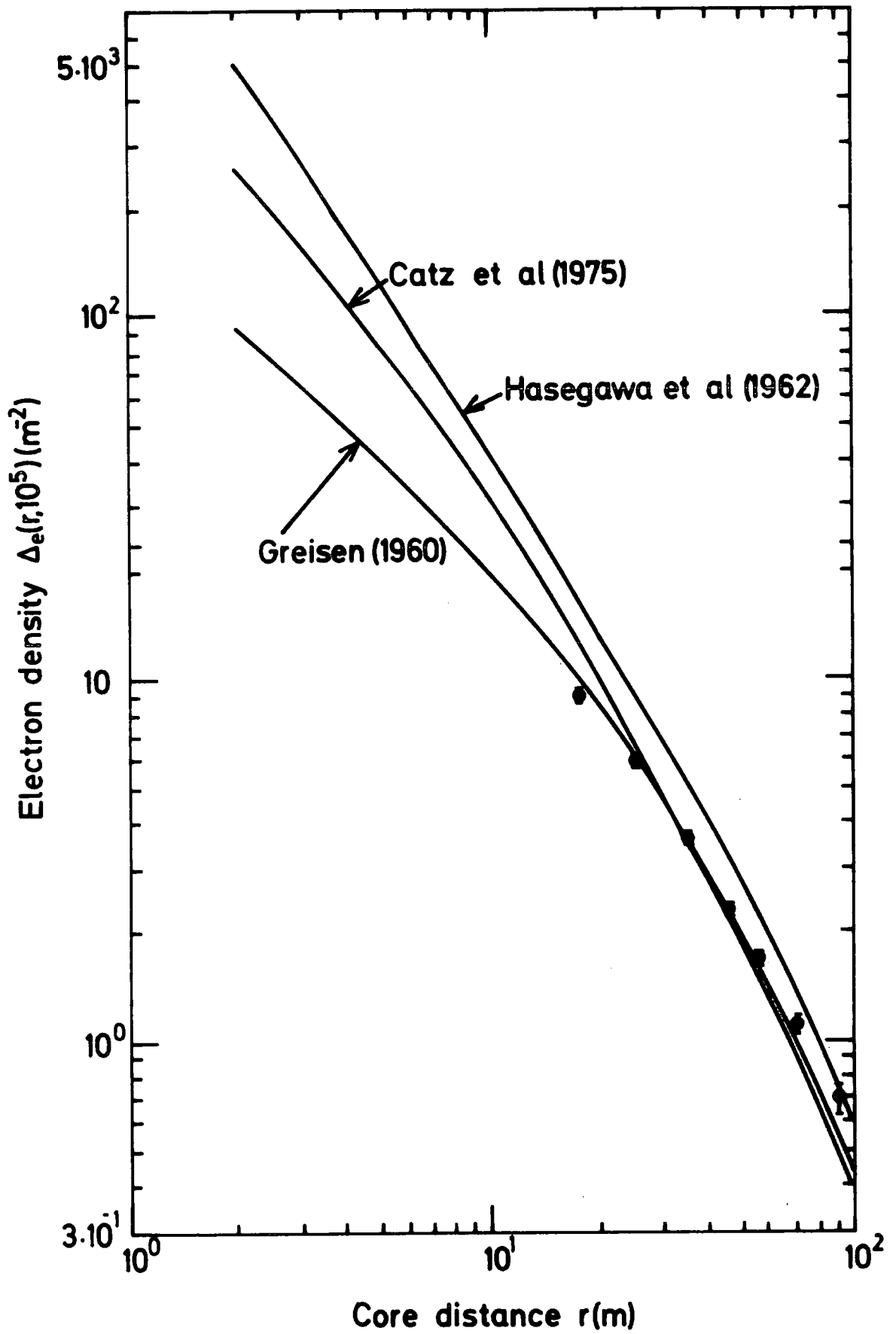
Figure 3.2: The measured average electron lateral structure function and comparison with the result found in other experiments.

The structure function found by the Hasegawa and Catz
E.L.S.F. are also shown in Figure 3.2 for comparison. The
Greisen E.L.S.F. has also been checked with the individual
showers. The redundant densities of the individual shower
were compared to the function. The result obtained showed
that 84 showers were consistent with Greisen structure function
while 6 and 8 showers showed a flatter and a steeper function
respectively.

3.3   METHODS OF CORE LOCATION

The methods available are basically of two types.
The loci curve method which was first introduced by Williams
(1948) and the other method is using a computer when a mini-
mum χ^2 procedure is performed.   For any method of core
location, the sampling densities are used to determine the
core position while an E.L.S.F. is assumed.

3.3.1 Loci Curve Method

In the loci curve method the ratio of the electron
densities from any two detectors is of interest since it
determines a line which is the locus of all the possible
cores falling on the array producing that ratio. Therefore
from a minimum of 3 densities in a shower, two independent
density ratios are obtained, which define two loci curves
whose corresponding ratios intersect in a point which is
the axis of the shower.

In practice, it is not exactly the case, and at least
3 electron density ratios from 4 detectors are used, where
the extra ratio defines a checking locus curve which should
intersect in the core position located by the other two loci
if the E.L.S.F. is correct.   The loci curves so produced for

a number of detectors do not generally intersect at a single point due to density fluctuations and the non-uniqueness of the E.L.S.F.   However the centre of gravity of the over-lapping area provides a good estimate of the core position.

To improve the method and to get a better estimation of core location, the two error limits related to each density ratio was also used to calculate locus curves.   Figures 3.3 and 3.4 show examples of the core position located by this method.   The loci curves corresponding to the error limits are shown by dotted lines.   The errors related to a locus curve with density ratio $y = \dfrac{\Delta_a}{\Delta_b}$ is

$$\frac{\Delta y}{y} = 1.2 \left(\frac{1}{\Delta_a \cdot A} + \frac{1}{\Delta_b \cdot B} \right)^{\frac{1}{2}} \tag{3.5}$$

where Δ_a is the electron density measured by detector a of area A, and Δ_b is the electron density measured by detector b of area B.   The factor 1.2 comes from electron density fluctuation which is found to be $1.2 \sqrt{n}$ (see section 3.5) where n is the number of detected particles.

To prepare a core locating chart for two detectors with distance ℓ apart one chart is obtained when an E.L.S.F. is assumed.   In the present case the Greisen structure function was used which, for a shower falling at core distances of r_a and r_b from the detectors a and b   gives a density ratio of

$$\frac{\Delta_a}{\Delta_b} = \left(\frac{r_b}{r_a} \right)^{0.75} \left(\frac{r_b + r_o}{r_a + r_o} \right)^{3.25} \left(\frac{1 + \dfrac{r_b}{11.4\, r_o}}{1 + \dfrac{r_a}{11.4\, r_o}} \right) \tag{3.6}$$
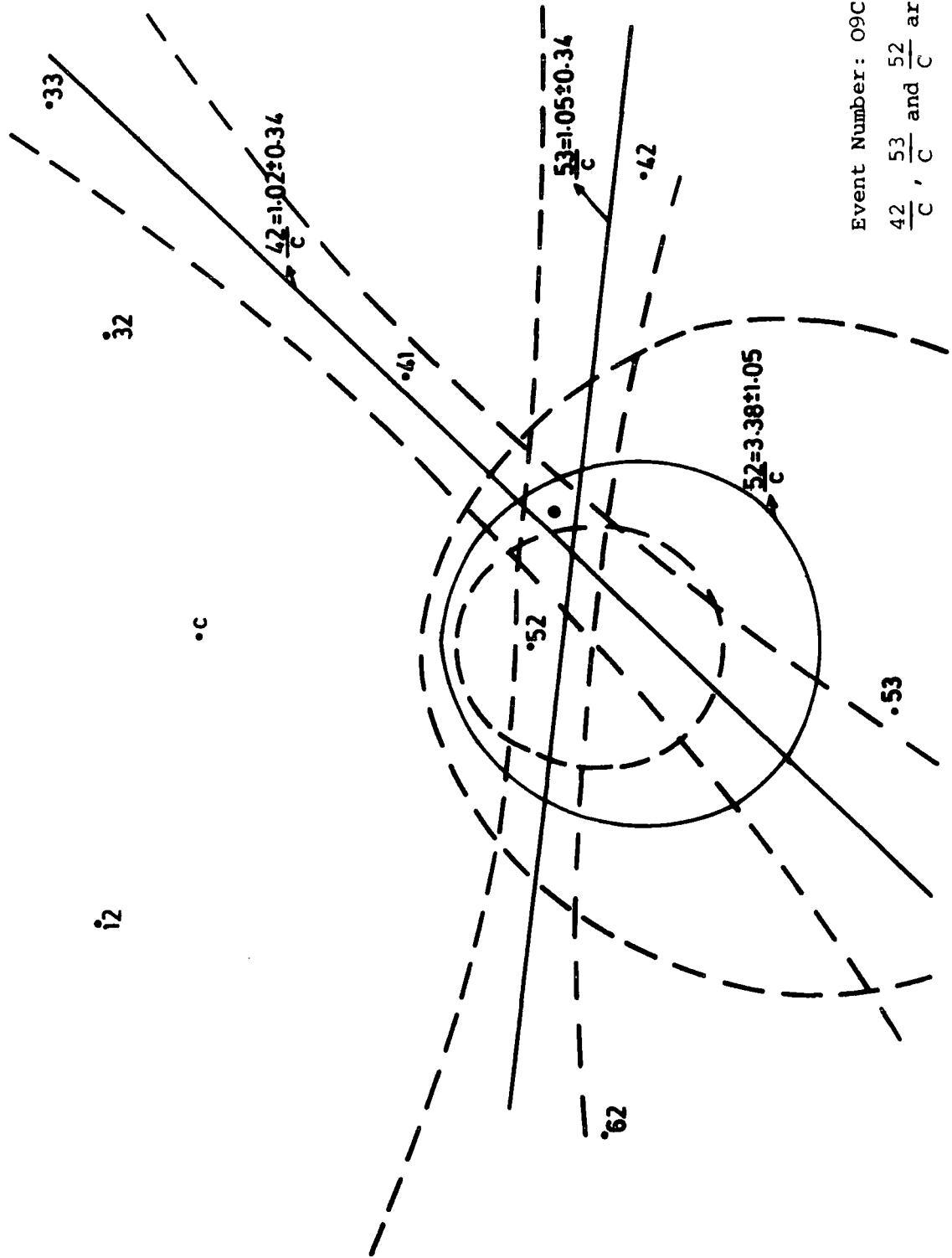
Event Number: 09C567

$\frac{42}{C}$, $\frac{53}{C}$ and $\frac{52}{C}$ are the density ratios of the corresponding detectors.

Figure 3.3 : An example of a shower core located by the loci curve method.
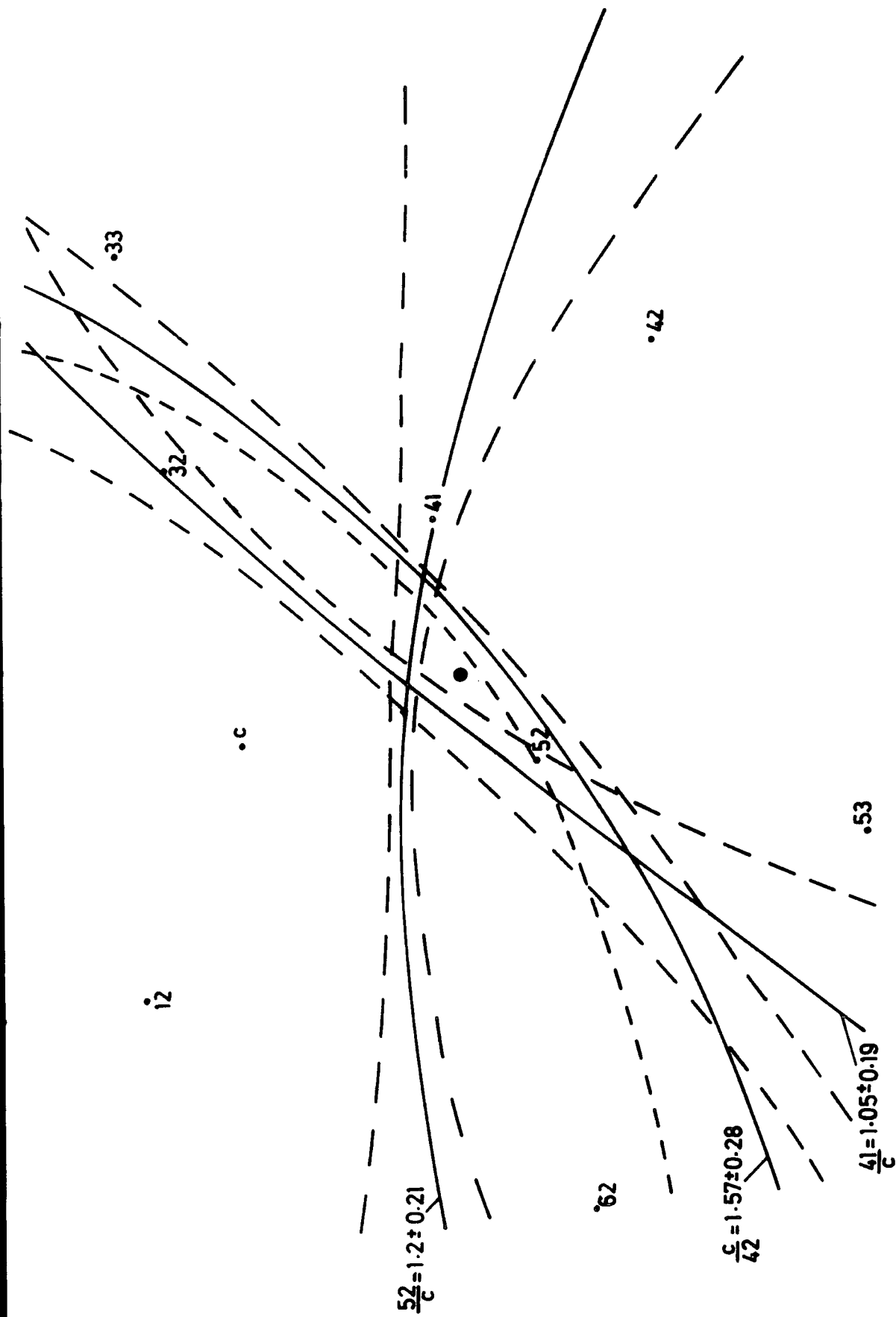
Event Number: 09C566

$\frac{52}{C}$, $\frac{C}{42}$ and $\frac{41}{C}$ are the density
ratios of the corresponding
detectors.

Figure 3.4 : An example of a shower core located by the loci curve method.

Labels on figure:

•33

32

•41

32

•c

•42

i2

•52

•53

•62

$\frac{52}{C}$ = 1.2 ± 0.21

$\frac{C}{42}$ = 1.57 ± 0.28

$\frac{41}{C}$ = 1.05 ± 0.19

where Δ_a and Δ_b are the densities expected in detectors a

and b.   From Eqn. 3.6, for various values of r_a, the density

ratio, $\dfrac{\Delta_a}{\Delta_b}$ is plotted as a function of r_b which are shown in

Figure 3.5.   From the figure, for each density ratio, various

values (r_a, r_b) are obtained and, the locus curve of that

ratio is drawn for any two detectors.   An example of a core

locating chart for loci curves of various density ratios is

shown in Figure 3.6, where detectors C and 62 were chosen.

The loci method is sufficiently accurate provided the shower

core has fallen within or near the array boundary.   For core

distances less than 72 metres from the centre of the array,

simulation work was performed where in simulating the shower

the fluctuation on the number electrons n at a detector

expected by the Greisen E.L.S.F. is assumed to be Poissonian

of standard deviation (S.D) $1.2 \sqrt{n}$ (see section 3.5).   With

this assumption, the S.D. of the difference in true core

distance from the centre of the array, C and the core distance

located by the method of intersecting loci for a sample of

simulated showers was found to be (5.88 ± 0.44)m.

3.3.2 Computer Method of Core Location

For a given set of measured electron densities the

problem is to determine the core position and shower size

assuming the electron lateral structure function is known.

In practice a search is made over a lattice of points and a

minimum X^2 procedure is used to determine the best core position

and shower size

$$X^2 = \sum_i k_i \left(\Delta_i (0) - \Delta_i (P) \right)^2 \qquad (3.7)$$

where K_i is a weight function given by σ_i^{-2} and σ_i is the

standard deviation of the density measurement (see next section).
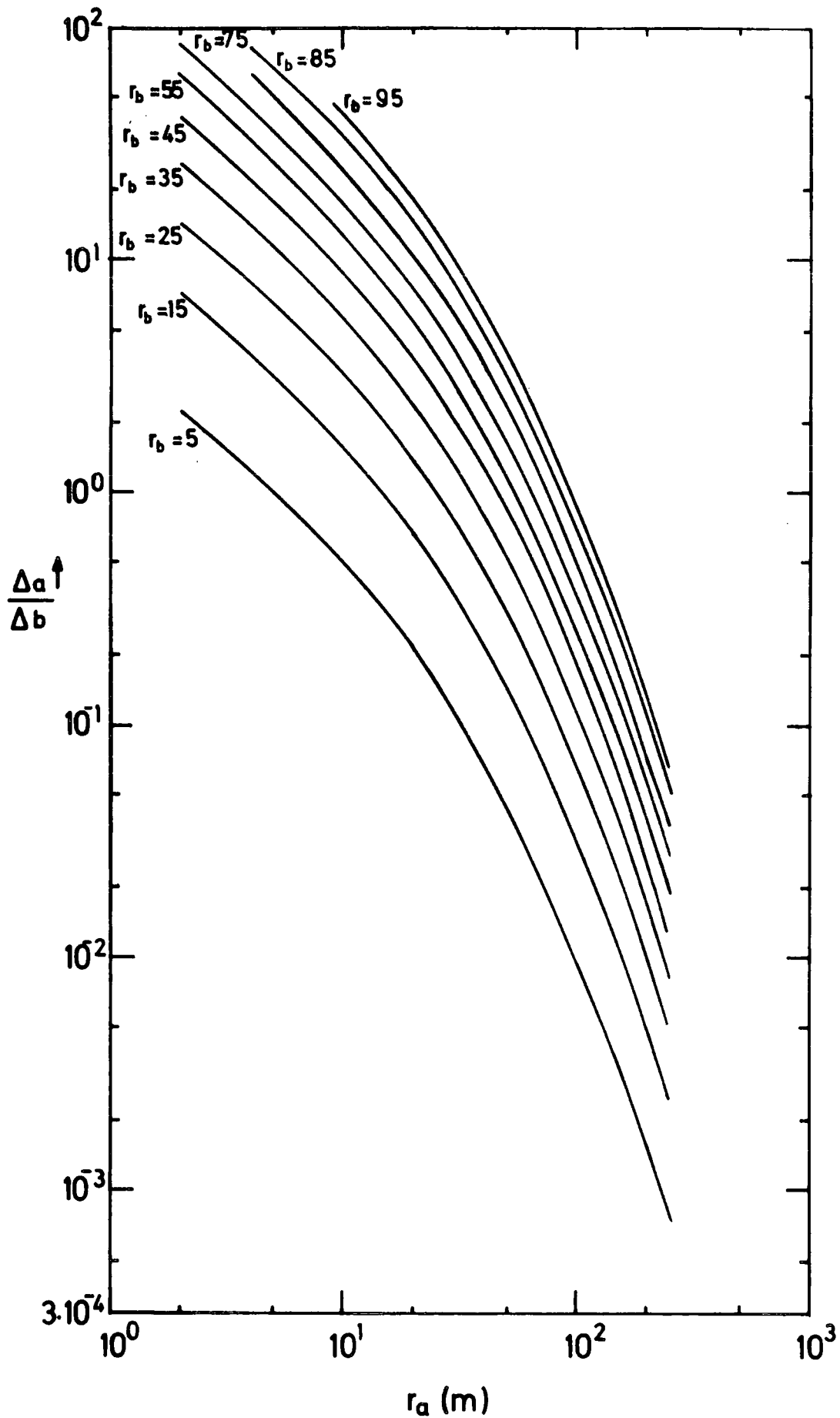
<u>Figure 3.5</u> :   Graph to illustrate the determination of pairs of
values of r_b and r_a that satisfy

$$\frac{\Delta_a}{\Delta_b} = \left\{\frac{r_b}{r_a}\right\}^{0.75} \quad \left\{\frac{r_b + r_0}{r_a + r_0}\right\}^{3.25} \quad \frac{1 + \dfrac{r_b}{11.4 r_0}}{1 + \dfrac{r_a}{11.4 r_0}}$$

where $r_0 = 79m$.

The curves are valid for any separation of detectors if the
condition $r_a + r_b \geqslant$ separation of detectors is noted.

scale 0 ⎿__⏌ 5m
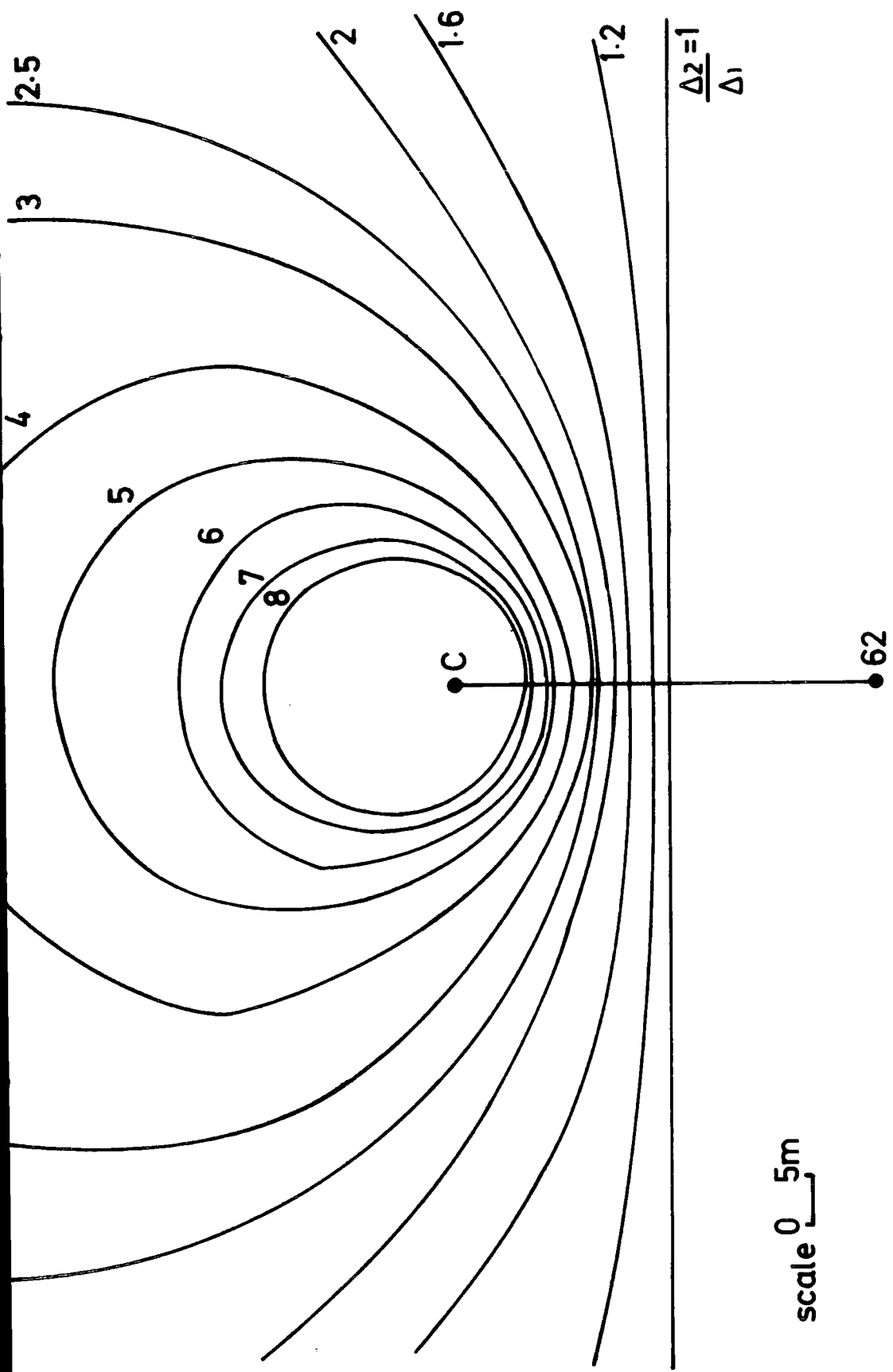
Figure 3.6 : An example of a core locating chart used in the intersecting loci curve method of core location.

$\Delta_i(0)$ is the observed density and $\Delta_i(P)$ is the predicted density from Eqn. 3.3. The χ^2 minimizing procedure normally starts from a point chosen near the highest density detector in the array which gives a good estimation of the core position. By assuming this starting point (X_s, Y_s) the value of N that gives minimum χ^2 is obtained. The χ^2 calculation is repeated over either a lattice of points that cover the array or various random points chosen uniformly around the starting point (X_s, Y_s) where a step size (Δ_x, Δ_y) is taken on any point (X, Y) to shift it to a new position. The χ^2 values of the data are compared to get the real core position and shower size by its corresponding minimum χ^2. The method has been described by Clark et al (1958) and more recently by Evans (1971) and Smith (1976). The present core location analysis was performed by a versatile minimizing package known as MINUIT (James and Roos, 1975). The system has basically the same performance of minimization but with much greater accuracy when the processing time of each event is 2 to 3 seconds to be analysed.

For comparison of the method of loci curves and computer analysis to determine core position, a sample of 189 shower was used where the difference in core distance from C (the centre of the array) located by the two methods was calculated. The difference was found to be Gaussian with S.D. of 3 metres.

3.4   CONCLUSION

For showers of size in the range 10^5-10^6 particles and core distance less than 72m from the centre of the array the error in core position as determined by the method of inter-

secting loci is (5.88 ± 0.44)m.

3.5 ELECTRON DENSITY FLUCTUATION

The loci curves method was applied for an array of
10 electron density sampling detectors where 4 measured
densities were used to locate the core position and determine
shower size assuming the E.L.S.F. is known. The remaining
detectors that give normally 6 measured densities can be taken
both to check whether the assumed form of E.L.S.F. is correct
and also to give information on the magnitude of density
sampling fluctuations. In section 3.2 it was found that the
Greisen formula, Eqn. 3.1, is quite consistent with the experi-
mental density measurement. To get information on sampling
density fluctuation, the observed number of particles n_o at
the detectors of area 0.75 to 2m^2 were plotted versus the
expected number n_e assuming the Greisen formula to be the
correct E.L.S.F. of all showers. Figure 3.7 shows a plot of
n_o versus n_e for density samples in which $n_e \leq 20$ particles.
The data is taken from a sample of 98 E.A.S. of median size
3.10^5 particles whose cores fell at distances < 70m from the
centre of the array. The upper and lower standard deviation
limits are shown in Figure 3.7 assuming Poisson fluctuations.
For $n_e > 10$ these are $n_e + \sqrt{n_e}$ and $n_e - \sqrt{n_e}$ respectively but for
smaller values of n_e the limits given by Regener (1951) are
shown. If the fluctuations are Poisson then 68% of the observed
events should lie in the range $n_e - \sigma_1$ to $n_e + \sigma_2$ where σ_1 and
σ_2 are the S.D. limits. Breaking the data down into 2 ranges
of shower size, and considering observations with $n_e \leq 20$
particles and $n_e > 20$ particles separately, the observed per-
centage of events lying in the range $n_e - \sigma_1$ to $n_e + \sigma_2$ is
compared with expectation in Table 3.1. It is seen that
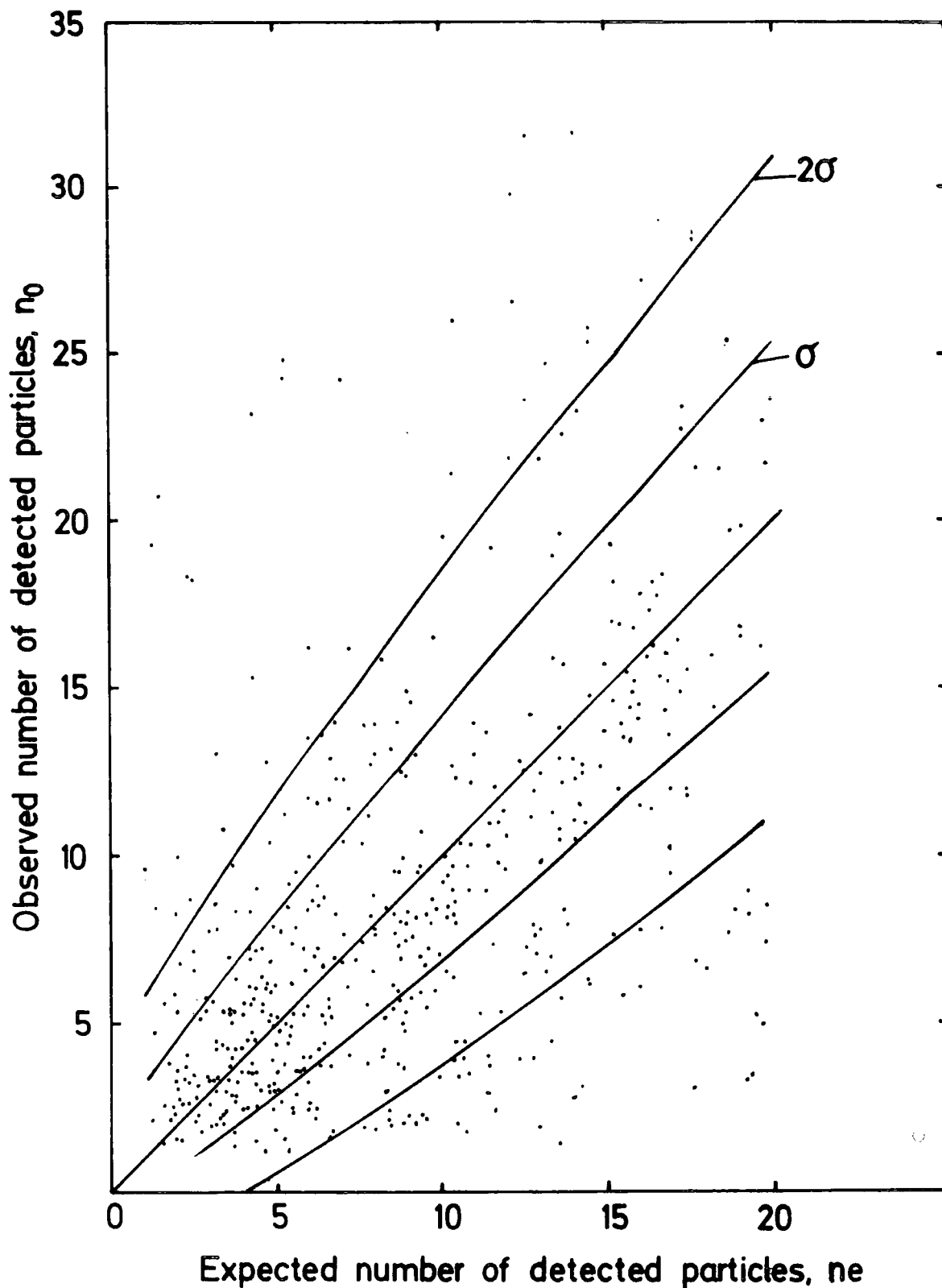
Figure 3.7 : Scatter plot of observed number of detected
particles versus the expected number.
The full lines are the upper and lower standard
deviation limits of a Poisson distribution on
the expected numbers which have been calculated
using the Greisen lateral structure function.

Expected no. of detected particles	Shower size range	No. of density samples	Expected percentage in range $n_e \pm \sigma$ assuming Poisson statistics	Observed percentage in range $n_e \pm \sigma$
$n_e \leqslant 20$	$7.4 \cdot 10^4 < N < 3.3 \cdot 10^5$	342	68%	$(73 \pm 5)\%$
	$3.3 \cdot 10^5 < N < 2.7 \cdot 10^6$	281	68%	$(55 \pm 4)\%$
$n_e > 20$	$7.4 \cdot 10^4 < N < 3.3 \cdot 10^5$	32	68%	$(54 \pm 4)\%$
	$3.3 \cdot 10^5 < N < 2.7 \cdot 10^6$	145	68%	$(47 \pm 6)\%$

TABLE 3.1 : Comparison of the percentage of observed events lying in the range n_e with expectation for different ranges of the expected number of particles n_e and shower size.

there is a suggestion that the observed fluctuations are broader than expected, assuming a Poisson distribution but not considerably so.   If one assumes that the standard deviation limits are given by $n_e - k\sigma_1$ to $n_e + k\sigma_2$ such that 68% of all events lie in this range exactly, then grouping all the data together gives $k = 1.2$.

Brennan et al (1958)and Clark et al (1958,1961) have made a similar study to the present one using showers of size $\sim 10^5$ particles and $\sim 10^5 - 10^8$ particles respectively at sea level.   Clark et al (1961) found $K = 1.15$ at distances $> 50m$ from the core for showers in the range $5.10^5 < N < 10^8$ particles. Kitajima et al (1979) studied density fluctuation of near vertical showers ($\theta < 30^\circ$) at distances of 30m from the core for showers in the range $10^6 < N_e < 4.10^7$ particles.   They found the value of $K = (0.25 + 0.0225 \, \dot{n}_e)^{\frac{1}{2}}$ which indicates the fluctuation gets broader than Poissonian for $n_e > 33$ particles and increases slightly with n_e.   However, if consideration is taken of errors in core location, shower size determination, fluctuation in the shape of the structure function and also in the actual density recording process (e.g. low energy hadron interactions in the scintillators, etc.) then it would seem likely that both in the present work and previous work the true fluctuations in electron numbers sampled by a detector are closely represented by the Poisson distribution.

CHAPTER 4

THE AGE PARAMETER OF E.A.S. AND ITS DEPENDENCE

ON SHOWER SIZE AND ZENITH ANGLE

4.1   INTRODUCTION

4.1.1 The Electromagnetic Cascade Shower

So far, a lot of work has been done on the theory of the electromagnetic cascade. An example is the summary of Cocconi (1961) which discusses the one dimensional development of an electron-photon shower in the air. The calculations used are from Snyder (1949) where the total number of electrons of energy $E \geqslant 0$ initiated by a primary photon of energy W_0 is given as a function of air thickness. The results for various values of W_0 are shown in Figure 4.1, where they can be represented by the following equation due to Greisen (1956).

$$N(W_0, t) = \frac{0.31}{\beta_0^{\frac{1}{2}}} \exp \left[t \left(1 - \frac{3}{2} \log S \right) \right] \qquad (4.1)$$

$t = \dfrac{X}{X_0}$ is the air thickness in radiation units, X_0 (X_0 = 37.7 gr cm^{-2} in air), $\beta_0 = \log \dfrac{W_0}{\epsilon_c}$, ϵ_c is the electron critical energy in air (84.2 MeV) and $S = \dfrac{3t}{t + 2\beta_0}$. The parameter S is known as the age of the shower and is related to the development of shower properties. From Equation 4.1 and Figure 4.1, the shower reaches its maximum development when S = 1 at the thickness of

$$t_{max} = \beta_0 = \log \frac{W_0}{\epsilon_c} \qquad (4.2)$$
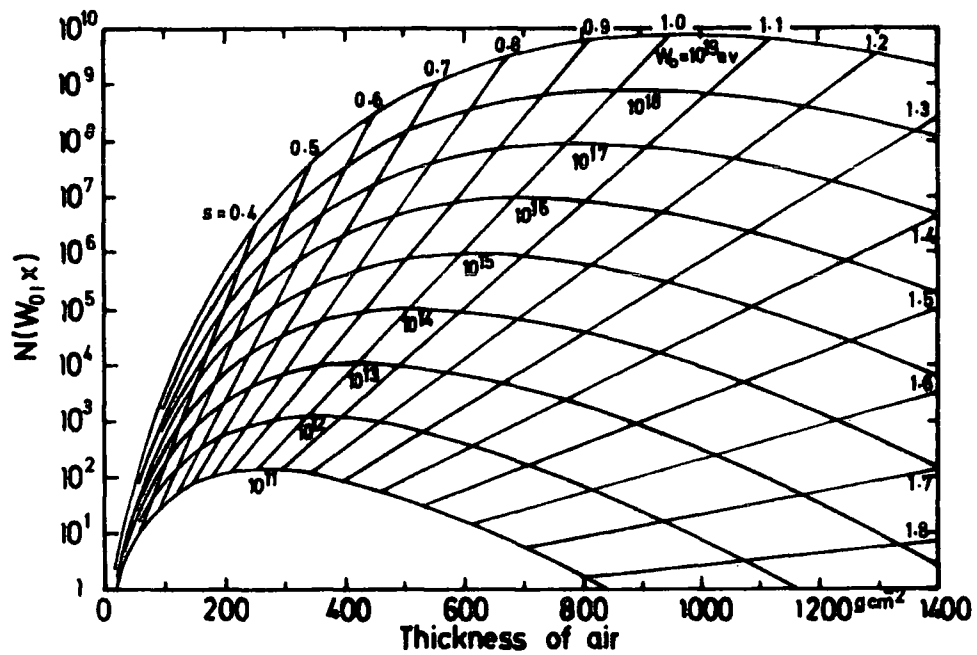
Figure 4.1: The total number of electrons, as a function of the thickness (g cm^{-2}) of air crossed, produced by photons of various energies, W_o, in eV. The parameter s is the age of the shower at different stages of its development, (after Cocconi, 1961).

where before and after its maximum S is less and bigger than one respectively. The relation of age parameter to the number of particles in the shower at any level and the energy of the primary particle is also given by Equation 4.1 as

$$\frac{d \log N}{d \log W_0} = S - \frac{1}{2 \beta_0} \sim S \tag{4.3}$$

(the approximation is for high energy primary particles, i.e. $W_0 >> \epsilon_0$).

4.1.2 The Age Parameter of E.A.S

The behaviour of the electron and photon cascade is well described in terms of cascade shower theory by Nishimura and Kamata (1958). According to this theory, the definition of the age parameter S in shower development is given by

$$S \sim 3t \Big/ (t + 2 \ln (E_0/\epsilon_c) + 2 \ln r/r_0) \tag{4.4}$$

where E_0 is the electron primary energy in ϵ_c units, ϵ_c is the electron critical energy in air, t the atmospheric depth, and r the radial distance from the core (Greisen, 1956). The parameter S represents the age of a shower which increases as it develops, and reaches its maximum when S is equal to one. For S less than one it shows the early stage of development (young shower), and for S greater than one it shows the declining stage of a shower (old shower). Equation (4.4) shows the decrease of S as the distance from the shower axis increases. This corresponds physically to the fact that the maximum of a shower is reached later for the high energy particles near the axis than for the low energy particles far

from the axis. Also in 1952 and 1958, Nishimura and Kamata derived the lateral structure function of E.A.S. particles, which was based on a pure electromagnetic cascade considering the multiple Coulomb scattering of electrons. This function can be simplified by an expression due to Greisen known as the Nishimura-Kamata-Greisen, (N.K.G), function, which is given as

$$F(^r/r_0) = C(s) \ (^r/r_0)^{S-2} \ (\frac{r}{r_0} + 1)^{S-4.5} \qquad (4.5)$$

where r_0 is 79 metres for air at sea level, and $C(s)$ is a normalization factor such that

$$\int_0^\infty 2 \ \pi F(x) \ X \ dx = 1 \ \text{where } X = {}^r/r_0 \qquad (4.6)$$

and can be approximated by (Greisen, 1956)

$$C(s) = 0.443 \ s^2 \ (1.09 - s) \ \text{for} \ S < 1.6$$

$$\text{or} \quad C(s) = 0.366 \ s^2 \ (2.07 - s)^{5/4} \ \text{for} \ S < 1.8$$

Exact values of $C(s)$ according to Wdowczyk (1973) are given in Table 4.1, which are consistent with the last formula

S	0.6	0.8	1	1.2	1.4	1.6	1.8
C(s)	0.22	0.31	0.4	0.44	0.43	0.36	0.25

TABLE 4.1

as shown in Figure 4.2. These values of $C(s)$ were used in the data analysis. Assuming the lateral distribution function
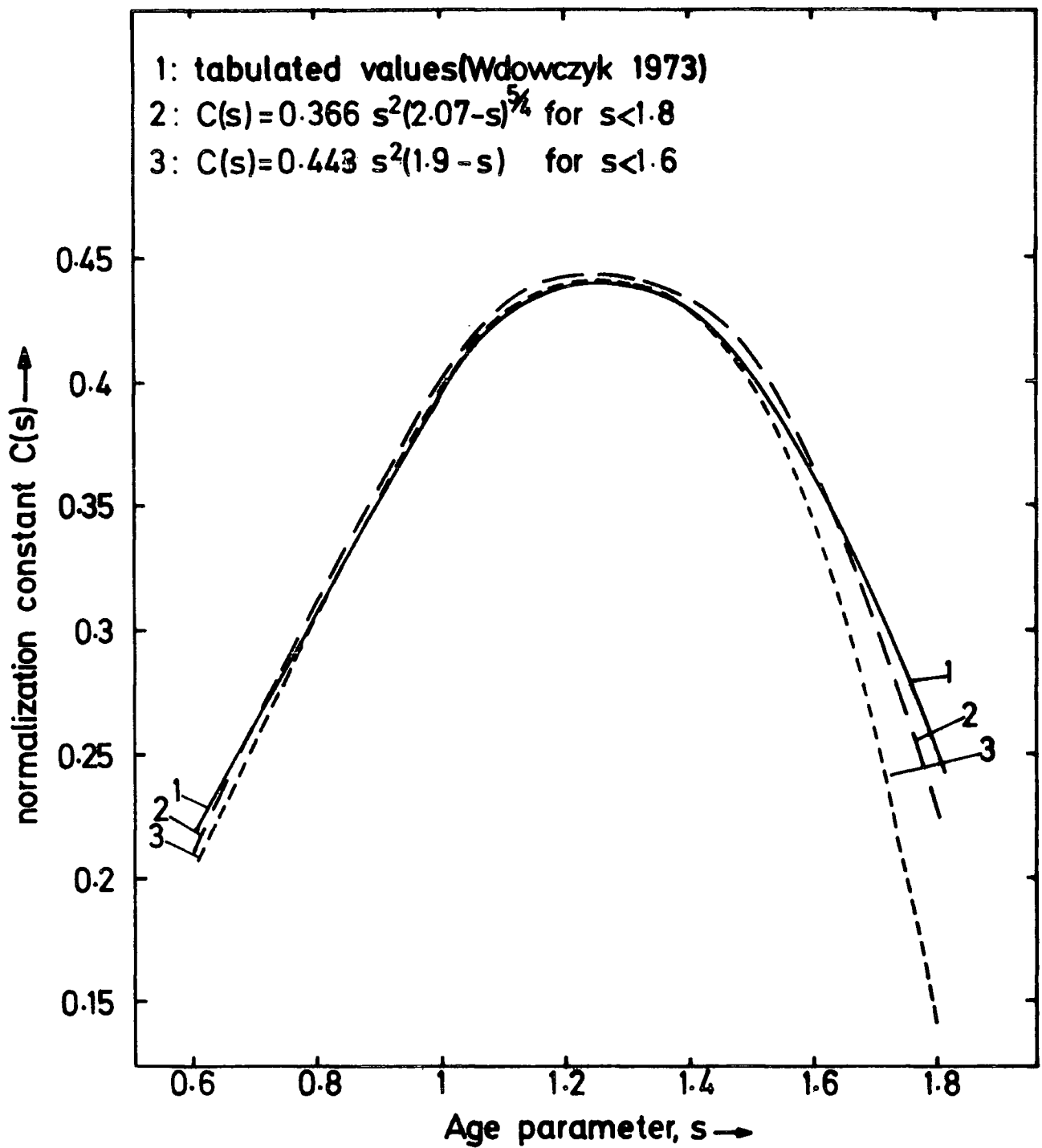
Figure 4.2 : Consistency of the values of normalization factor as a function of age parameter.

is independent of shower size, for a shower with a total of N particles, the electron density at distance r from the core is given by

$$\Delta(r) = \frac{N}{r_0^2} \, F(^r/r_0) \qquad (4.7)$$

Figure 4.3 shows a plot of $\Delta(r)$ versus r for N = 1 and shows how S determines how peaked or flat the structure function of the shower is. Also, the fraction of particles in a shower that fall at a distance greater than r from the core was calculated and the results are given in Appendix $A.A_1$.

4.1.3 Central Density

By assuming the N.K.G. function for the lateral distribution of electrons in different development stages of E.A.S. and measuring the age parameter of individual showers, one may get some information on the shower central density. Central density is a useful parameter due to the fact that it is roughly proportional to the energy per nucleon of the primary particles, whereas the total number of particles represents energy per nucleus (Bray et al, 1964, Thielheim and Beiersdorf, 1970). It was suggested by the Sydney group (Bray et al, 1964) that the distribution of $\Delta c/N$ values of showers (Δ_c - central density in a shower of size N) might contain some information on the chemical composition of the primary particles. For a given size the mean value and fluctuation of this quantity are expected to be smaller for heavy primary particles than for primary protons.

4.2 EXPERIMENTAL ARRANGEMENT AND ANALYSIS

The Durham E.A.S array was previously described in Chapter two and a scale diagram of it is shown in Figure (2.1).
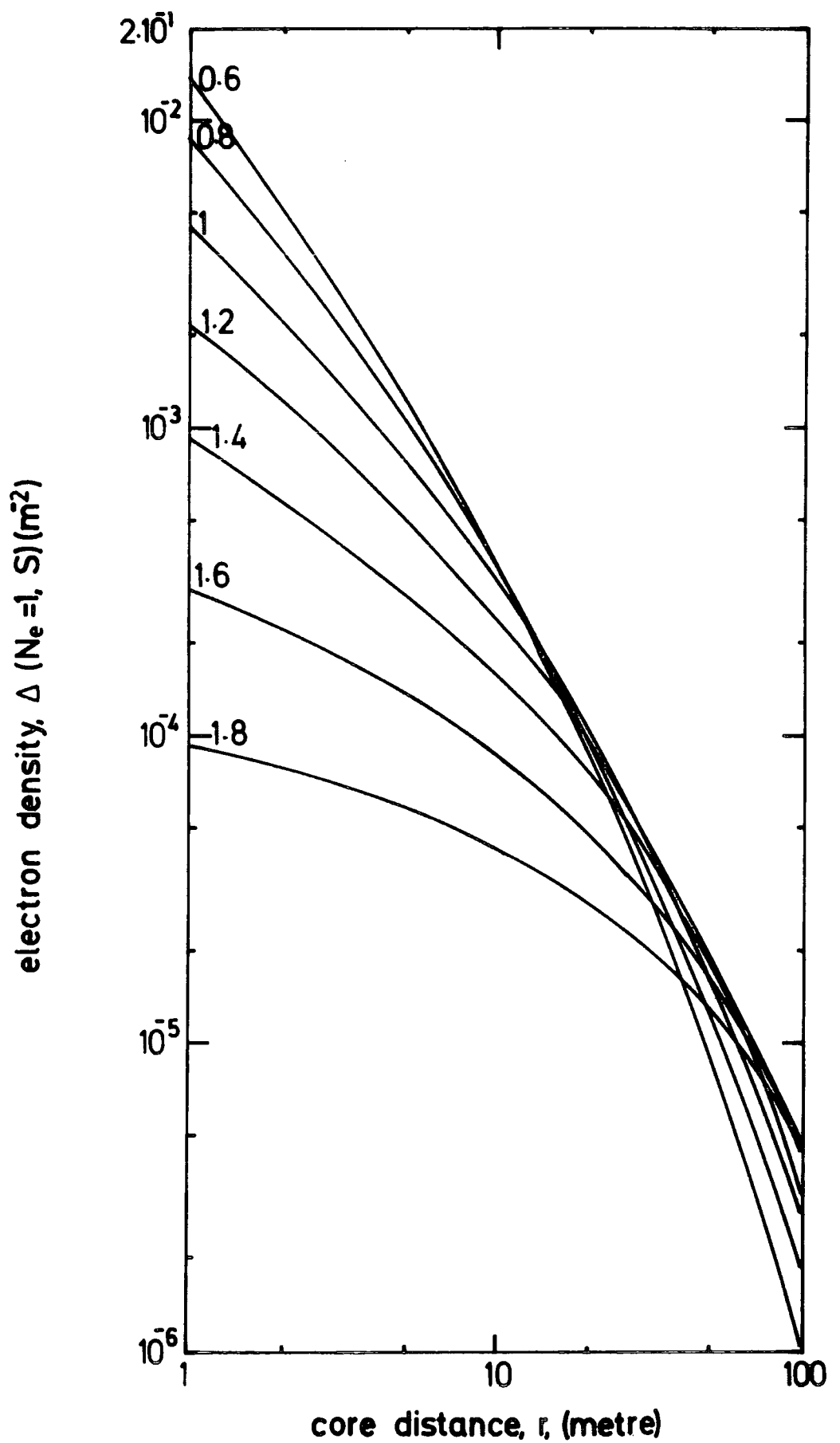
Figure 4.3 : The lateral distribution of electrons in showers of unit size in air at sea level ($r_1 = 79$ m). The number attached to each curve is the age parameter s of the shower.

Air showers were selected by an outer ring Trigger ; a 2

particles m^{-2} coincidence in detectors 13,33,53 with a 4

particles m^{-2} in the central detector C, where the area of

the detectors varies from 2 m^2 to 0.75 m^2. For each event

the sampled electron densities were used to measure the age

parameter of the shower (S was determined by assuming the

core position found using the Greisen structure function was

correct and the best S and N that fitted the measured electron

densities in E.A.S detectors was then found. This was

achieved by computer using the CERN MINUIT program which is

a package for minimizing a function of n parameters. The

program for two parameters, age and shower size, is given in

Appendix $A.A_2$. In deriving the age parameter distribution,

we have to consider the fact that the efficiency of triggering

depends on age for a given shower size. The requirement for

an E.A.S trigger is that the density of particles in each

triggering detector exceeds a certain level. Since the

density given in Equation 4.7 depends on S, the distance from

the axis r is a function of N and S for a given Δ .   Hence

the effective collecting area depends on S as πr^2 (N,S) for

a given triggering level of Δ .   For the present triggering

level, the minimum shower size to produce an outer ring trigger

as a function of age is given in Figure 4.4. Figure 4.4 shows

the minimum size to be triggered by a shower of all ages to

be $2.3.10^5$ particles which is why it was chosen to be the

minimum analysable shower size.   An example of collecting

area for different ages S= 0.6 and S = 1.8 of fixed sizes

5.10^5 and 5.10^6 particles are shown in Figure 4.5a and

Figure 4.5b which gives a bigger collecting area for flatter
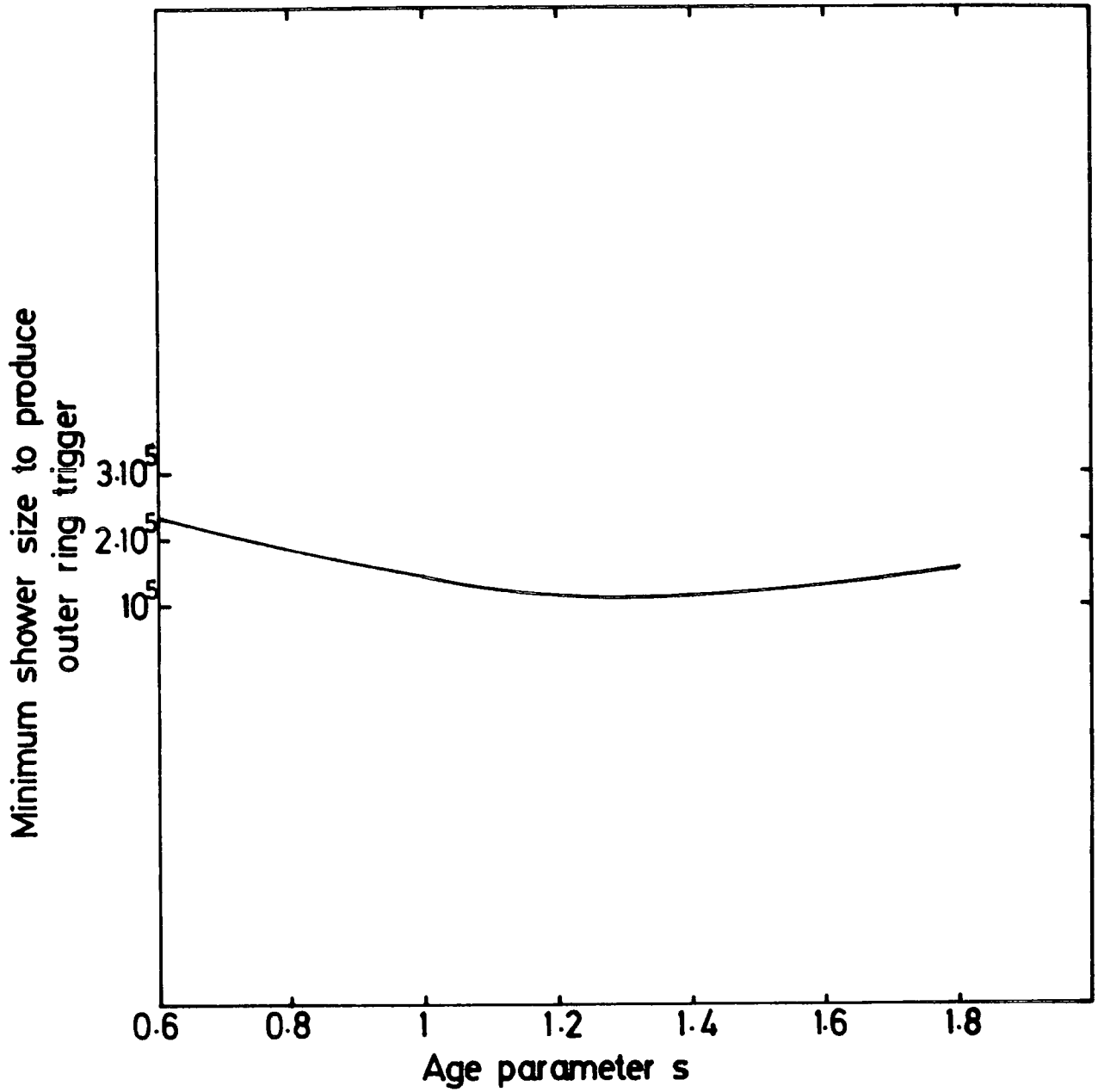
Figure 4.4 : Variation of minimum shower size to produce an outer ring trigger as a function of age parameter.

$Ne = 5 \cdot 10^6$

$\times^{13}$

$Ne = 5 \cdot 10^5$ $\times$ 33

$\times_c$

$\times$ 53
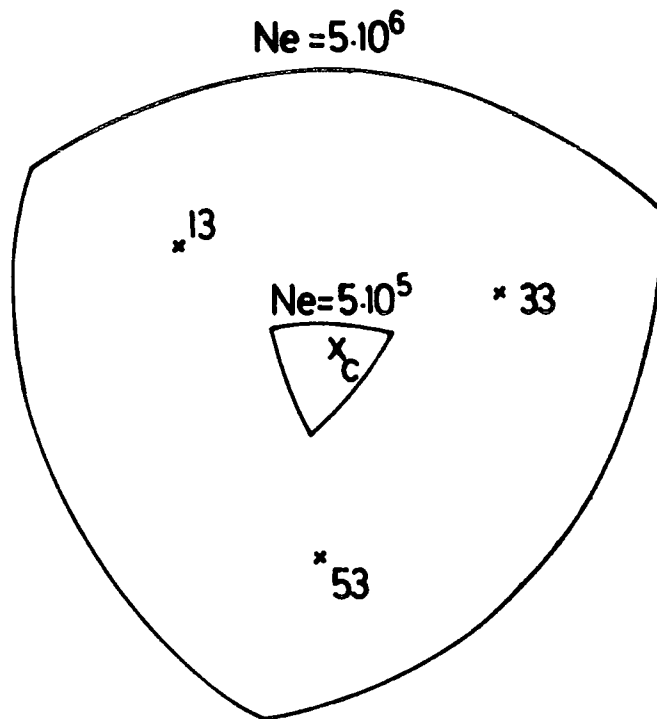
$Area(5 \cdot 10^5) = 5 \cdot 83 \cdot 10^2 \ m^2$

$Area(5 \cdot 10^6) = 2 \cdot 8 \cdot 10^4 \ m^2$

0 ____ 40m

Figure 4.5a : Collecting areas for showers with s = 0.6 and N = 5.10^5 and 5.10^6 particles capable of producing an outer ring trigger.

s=1.8
Vertical shower

$Ne = 5 \cdot 10^6$

$Ne = 5 \cdot 10^5$

×13

×33

×53
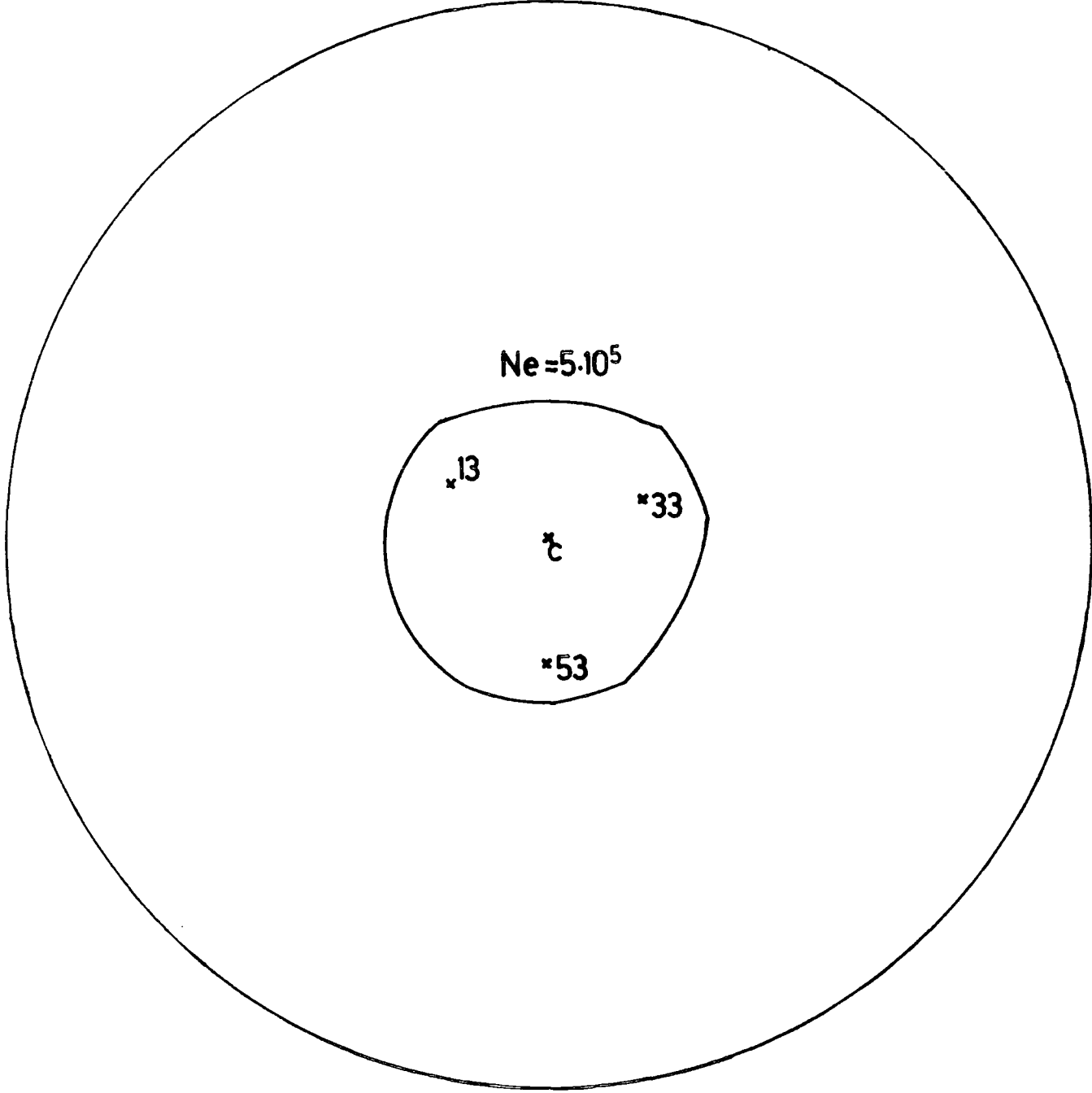
0   40m

$Area(5 \cdot 10^5) = 1 \cdot 41 \cdot 10^4 \, m^2$

$Area(5 \cdot 10^6) = 2 \cdot 12 \cdot 10^5 \, m^2$

Figure 4.5b: Collecting areas for showers with $s = 1.8$ and $N = 5 \cdot 10^5$ and $N = 5 \cdot 10^6$ particles capable of producing an outer ring trigger.

showers (S = 1.8) than steep ones (S = 0.6). The curves
of collecting area as a function of size were calculated
for different age and are shown in Figure 4.6, which will
be used in the data analysis.

656 events were grouped into three ranges of shower
size, $2.3.10^5 - 5.10^5$, $5.10^5 - 5.10^6$ and $5.10^6 - 5.10^7$ particles
which are shown in Table 4.2, where in each size range the
measured distribution of age for showers having orthogonal
core distance of less than 105 metres from C was obtained.
The resulting data was further sub-divided into two ranges of
zenith angle ($\theta < 22^O$ and $\theta \geqslant 22^O$) the results being shown in
Figure 4.7 to Figure 4.12b, the distribution (full lines)
are for the showers triggered by the array. The measured
age distributions were corrected for the variation of collecting
area with shower age as shown by the dashed lines in Figures
4.7, 4.9 and 4.12a, where the orthogonal core distance cut-off
was taken to be 105 metres. This was done by using the curves
of Figure 4.6, which for any shower of fixed size shows the
variation of its collecting area with age which makes it
possible for a given area to obtain the relative collecting
probabilities of a shower of various ages. Practically, to
obtain corrected distribution from the measured distribution
for every interval of age its average age, $\bar{S}$ and size $\bar{N}_e$ were
calculated and by using Figure 4.6 the corresponding collecting
areas $A (\bar{S}, \bar{N}_e)$ were obtained. These areas were used to get
the relative collecting probabilities for all intervals which
were the ratio of their collecting area to a given area, i.e.
area (πr_c^2 : r_c = 105 m) = $3.4.10^4$ m^2. These ratios, or collecting
probability factors, have been multiplied by their corresponding
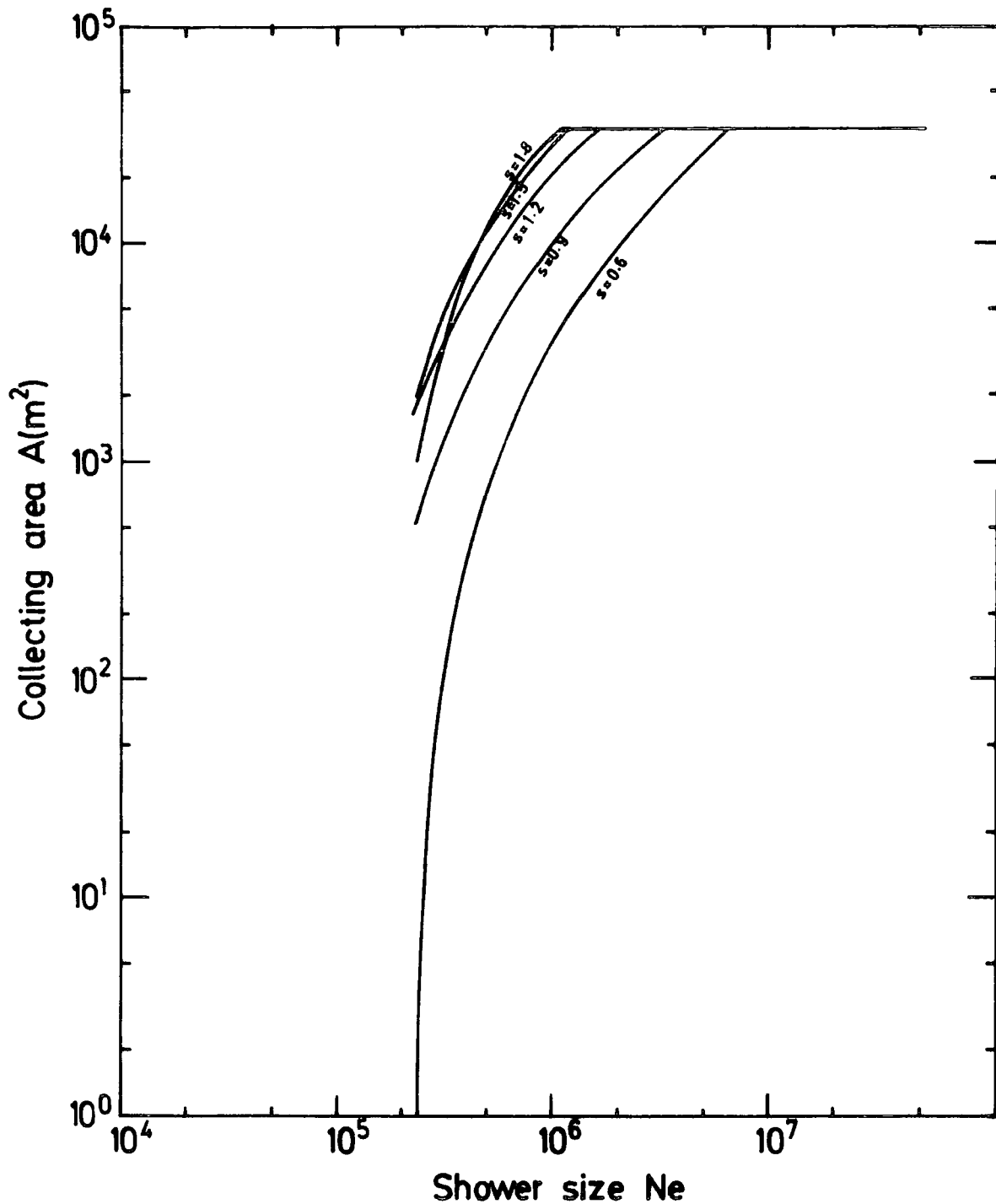
Figure 4.6 : Collecting area as a function of shower
size for showers with different age
parameter detected by an outer ring trigger,
$\Delta_c (\geqslant 4m^{-2})$, $\Delta_{13}(\geqslant 2m^{-2})$, $\Delta_{33}(\geqslant 2m^{-2})$, $\Delta_{53}(\geqslant 2m^{-2})$.
All showers have core distance $\leqslant 105m$ from
the centre of the array.

Size range	$2.3.10^5 - 5.10^5$	$5.10^5 - 5.10^6$	$5.10^6 - 5.10^7$	Total
Total number of events for $\theta < 22^o$	134	186	21	341
Total number of events for $\theta \geqslant 22^o$	123	182	10	315
Total	257	368	31	656

TABLE 4.2 : The total number of analysed events detected by the outer ring trigger for two ranges of zenith angle ($\theta < 22^o$ and $\theta \geqslant 22^o$) and for three different ranges of shower size.

r_c , the core distance from central detector was taken to be less than 105 metres.
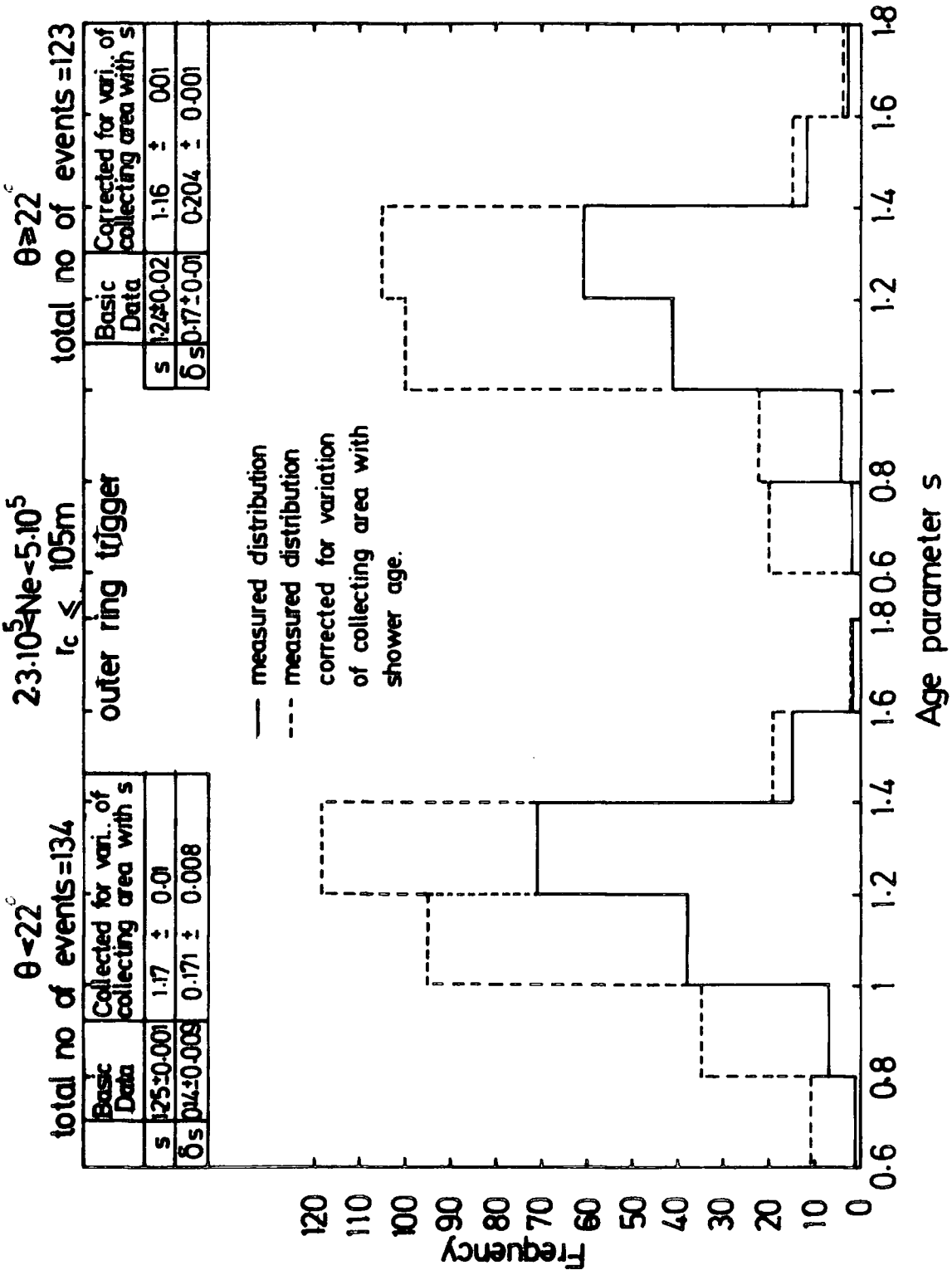
Figure 4.7 : The measured age parameter distribution for the size range of $2.3.10^5 < Ne < 5.10^5$ particles and two zenith angle ranges ($\Theta < 22°$ and $\Theta \geqslant 22°$). The dotted lines are the distribution corrected for variation of collecting area with age.
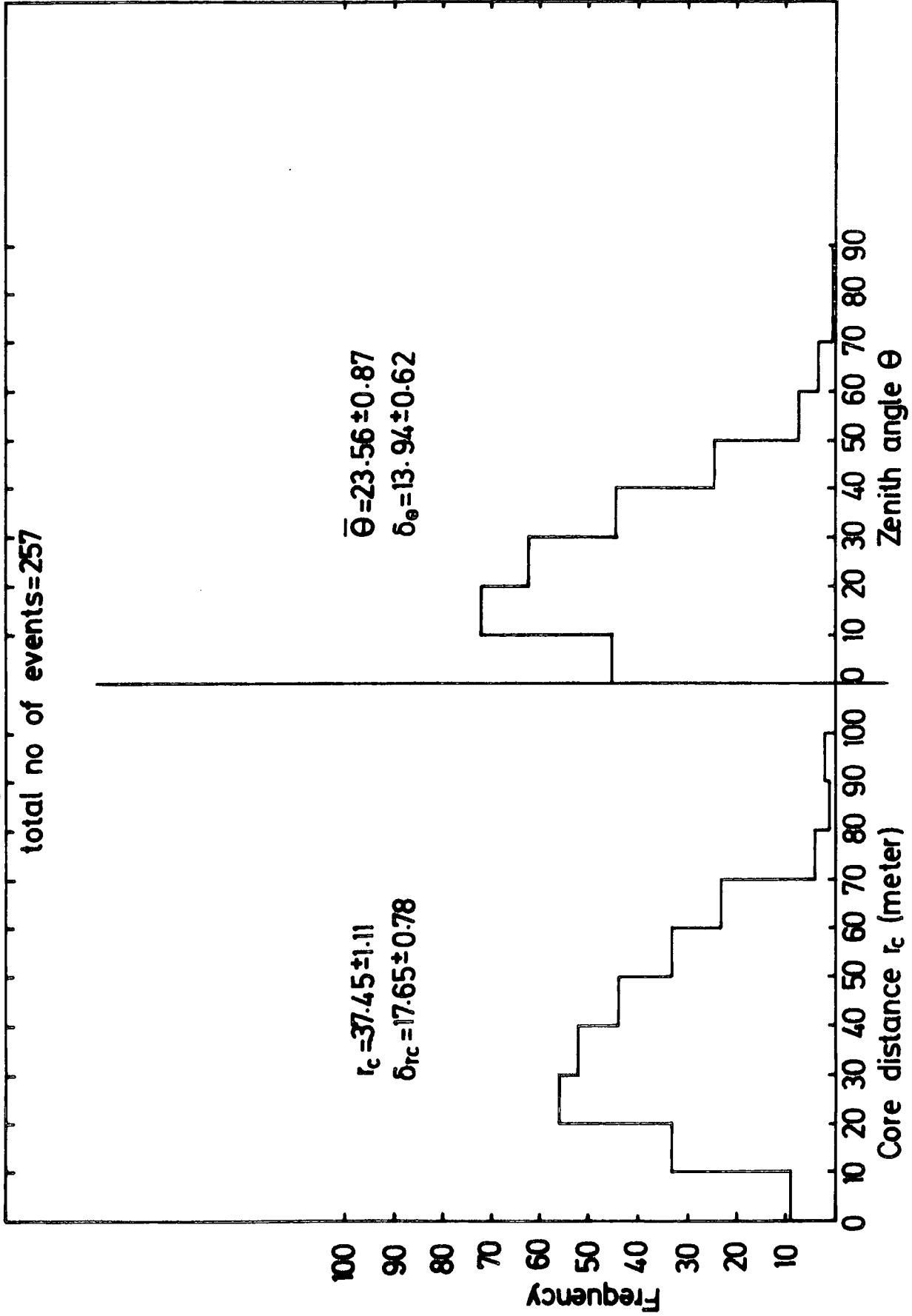
Figure 4.8 : The zenith angle and core distance distribution of events in the size range of $2.3 \cdot 10^5 - 5 \cdot 10^5$ particles.
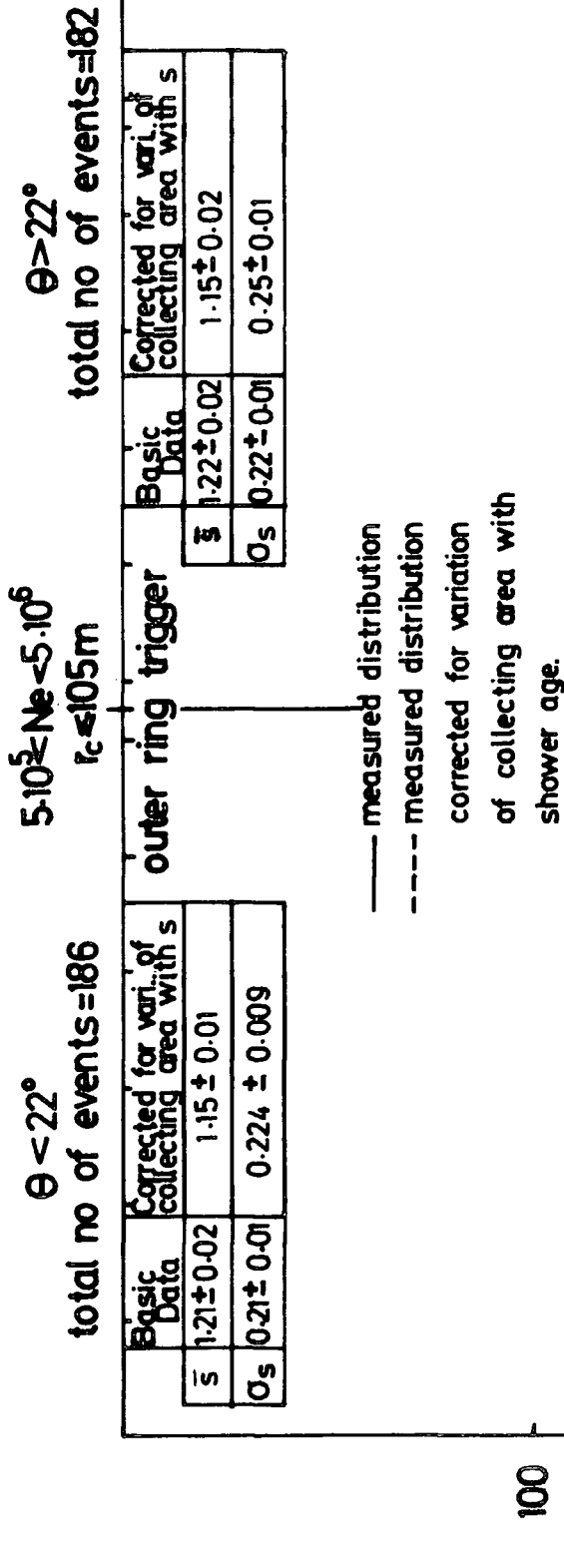
Figure 4.9: The measured age parameter distribution for the size range of $5.10^5 < N_e < 5.10^6$ particles and two zenith angle ranges ($\theta < 22^\circ$ and $\theta \geqslant 22^\circ$). The dotted lines are the distribution corrected for variation of collecting area with age.
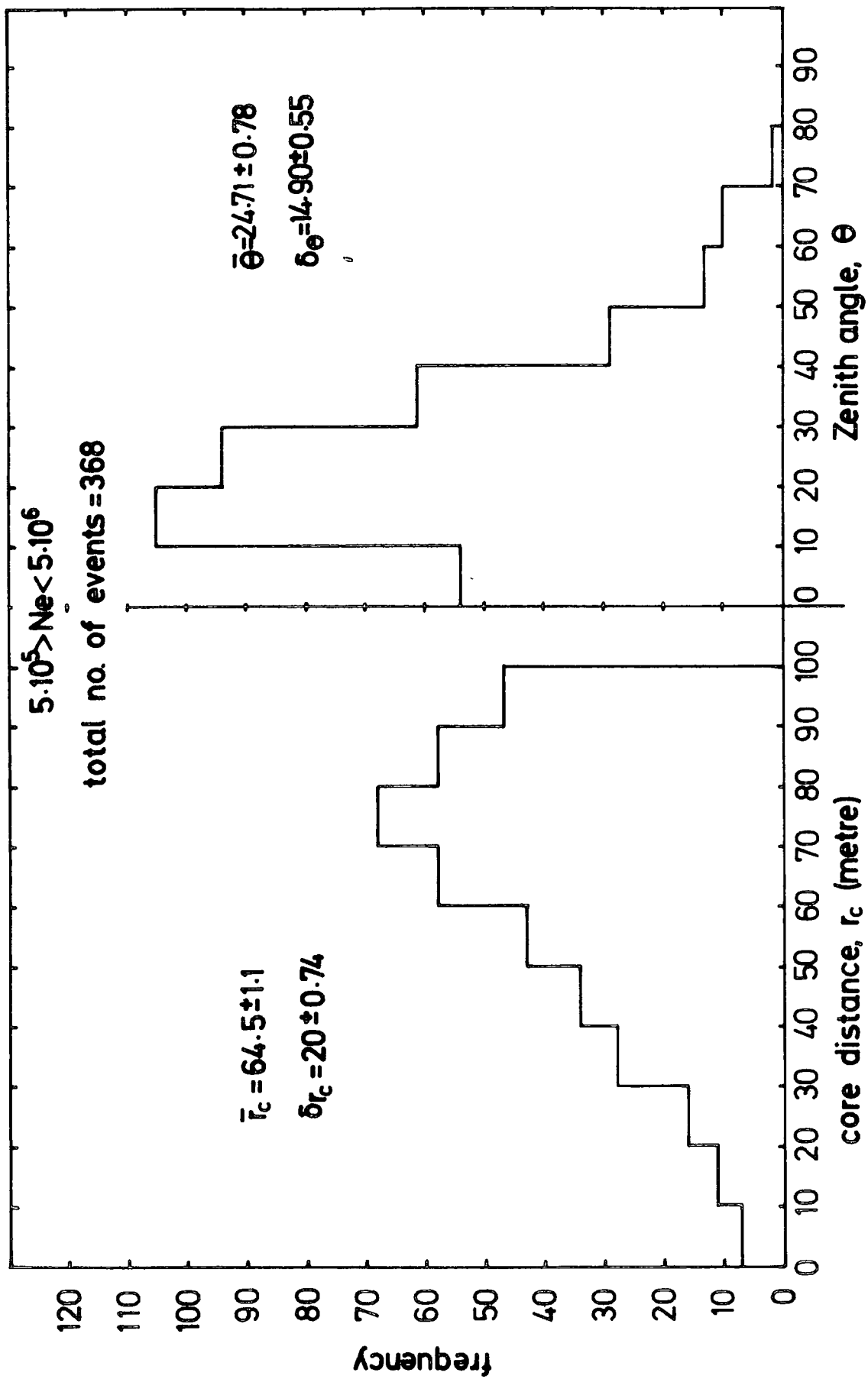
Figure 4.10: The zenith angle and core distance distribution of events in the size range of $5.10^5 - 5.10^6$.
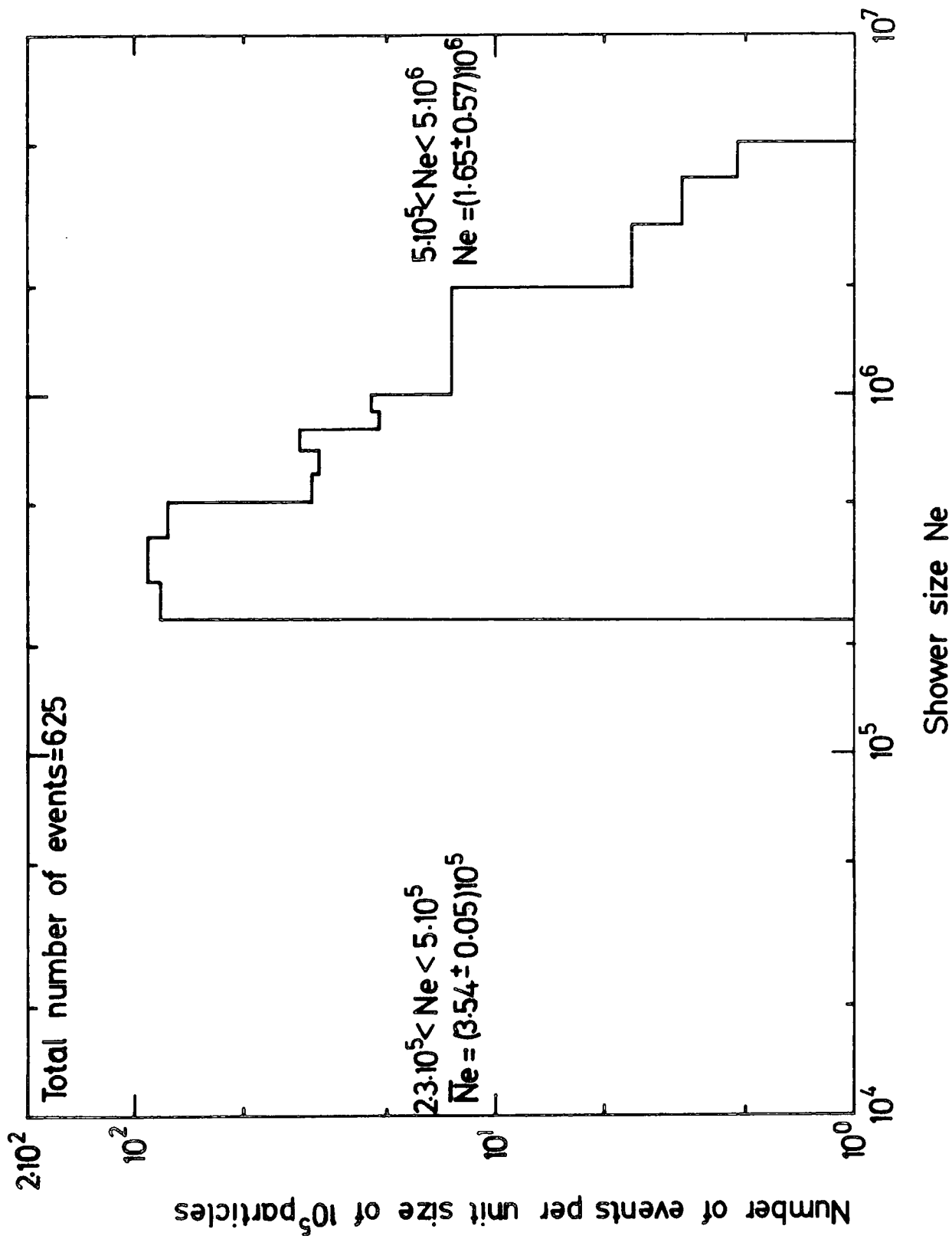
Figure 4.11: The shower size distribution for the size ranges of $2.3 \cdot 10^5 < N_e < 5 \cdot 10^5$ and $5 \cdot 10^5 < N_e < 5 \cdot 10^6$ particles.
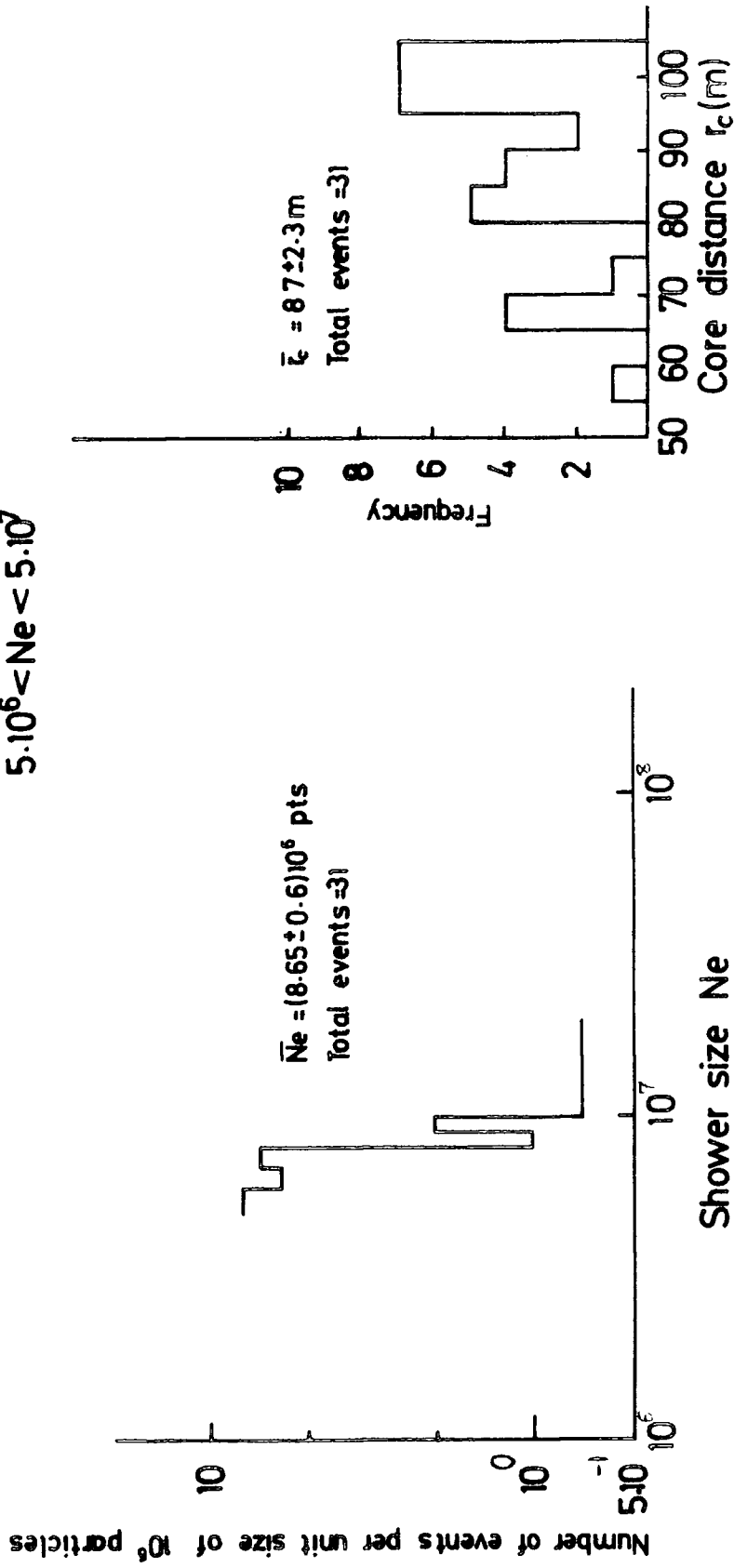
Figure 4.12a : The shower size and core distance distribution of events in the size range of 5.10^6 - 5.10^7 particles.
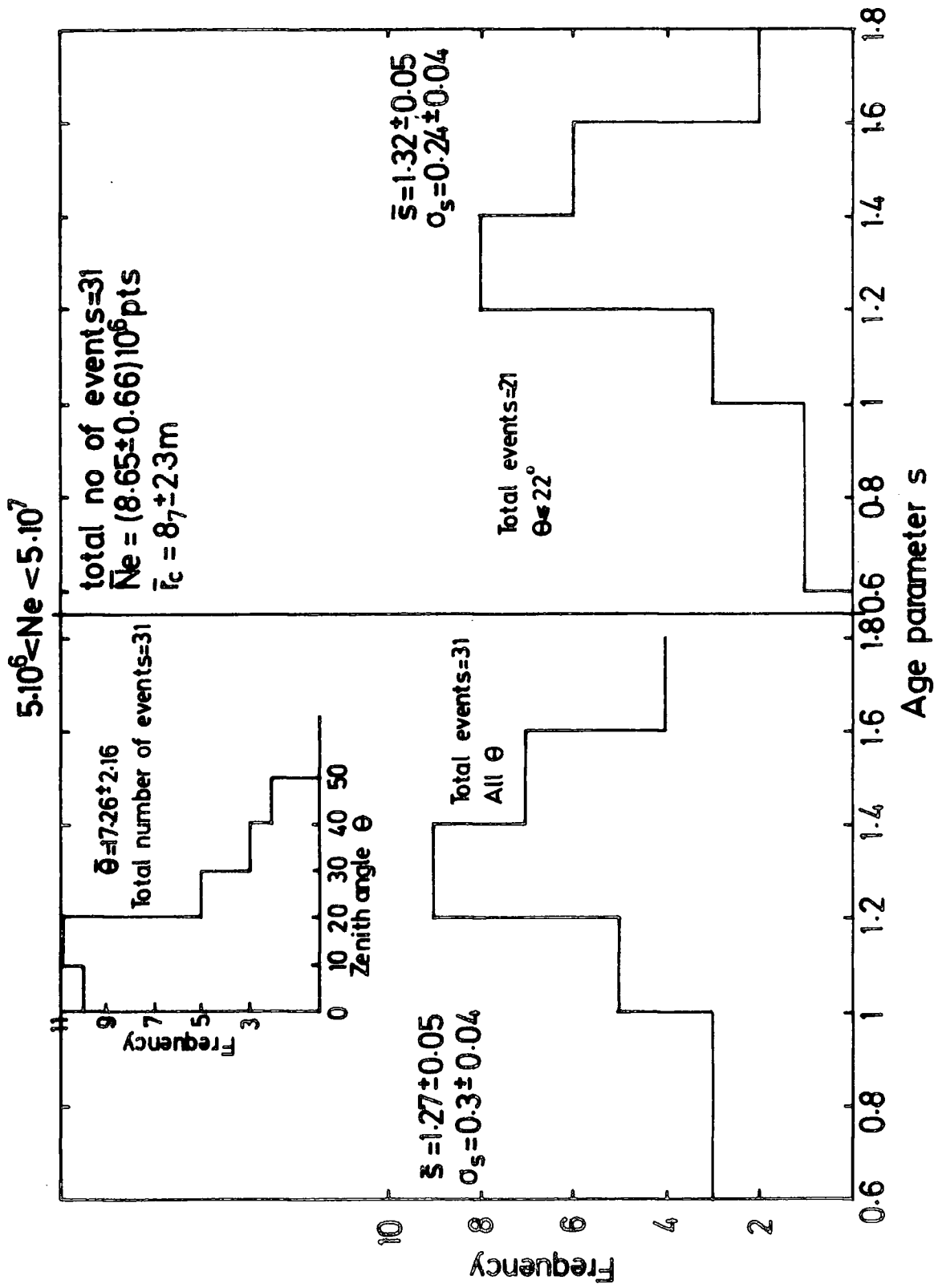
Figure 4.12b : The measured age parameter distribution for the size range of $5.10^6 < Ne < 5.10^7$ particles and two zenith angle ranges of ($\theta \geqslant$ and $\theta \leqslant 22^\circ$).

frequency of measured age intervals to obtain the corrected

frequency of every interval which are shown by the dashed

lines. These dashed lines form the corrected distribution

of age parameter for the three mentioned ranges of shower

size where, in each range, an example of showers with various

age parameter are given in Figures 4.13a, 4.13b and 4.13c.

4.3   THE RESULTS AND PREVIOUS MEASUREMENTS

4.3.1 The Shower Size and Zenith Angle Dependence

Theoretical predictions of the age parameter depend-

ence on shower size and zenith angle of E.A.S were given

by Karakula (1968), where the standard model of E.A.S.

development was used. The results are given in Figure 4.15,

after Udowczyk (1973), which shows a small decrease of age

parameter with increasing shower size, where the decrease is

more pronounced for less inclined showers. The simulation

work of Acharya et al (1979) on the size-age dependence of

E.A.S is also shown in the figure where a greater average age

parameter for primary iron showers than primary proton showers

is found. For comparison they presented their experimental

results for small showers ($(1-4)10^4$ particles) at an atmos-

pheric depth of 920 grms/cm^2 which are consistent with primary

protons.

Experimentally it is of interest to note that while

most of the measurements do not give any size age dependence

(Greisen, 1960) there is some evidence which suggests that

not only does the age parameter depend on shower size but also

for higher shower size the average age parameter increases with

shower size. The experimental points of Vernov et al (1970)

at sea level and Miyake et al (1973) at mountain altitude,
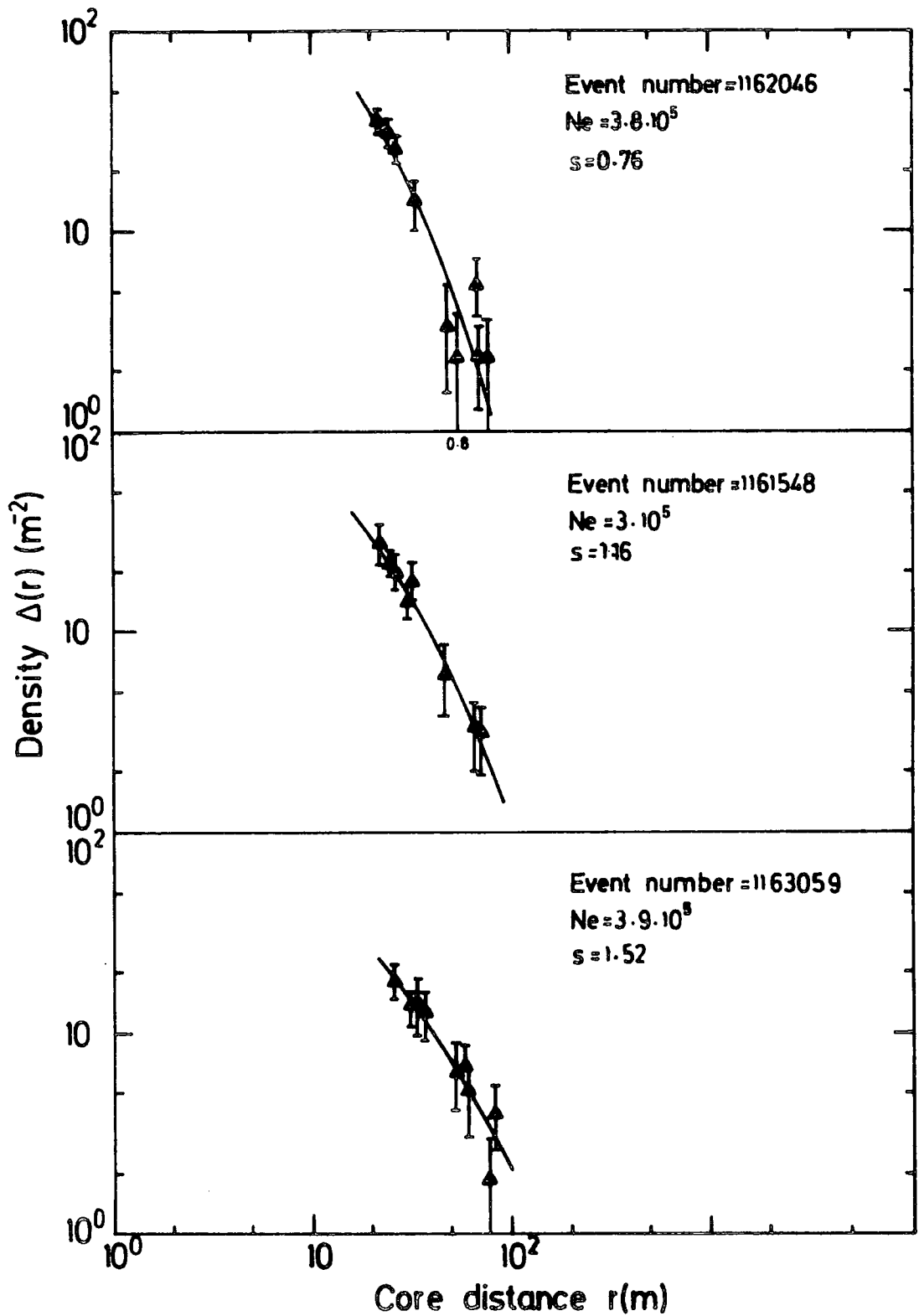
Figure 4.13a :   Examples of the lateral structure of
typical E.A.S. events in the size range
of $2.3.10^5 - 5.10^5$ particles.
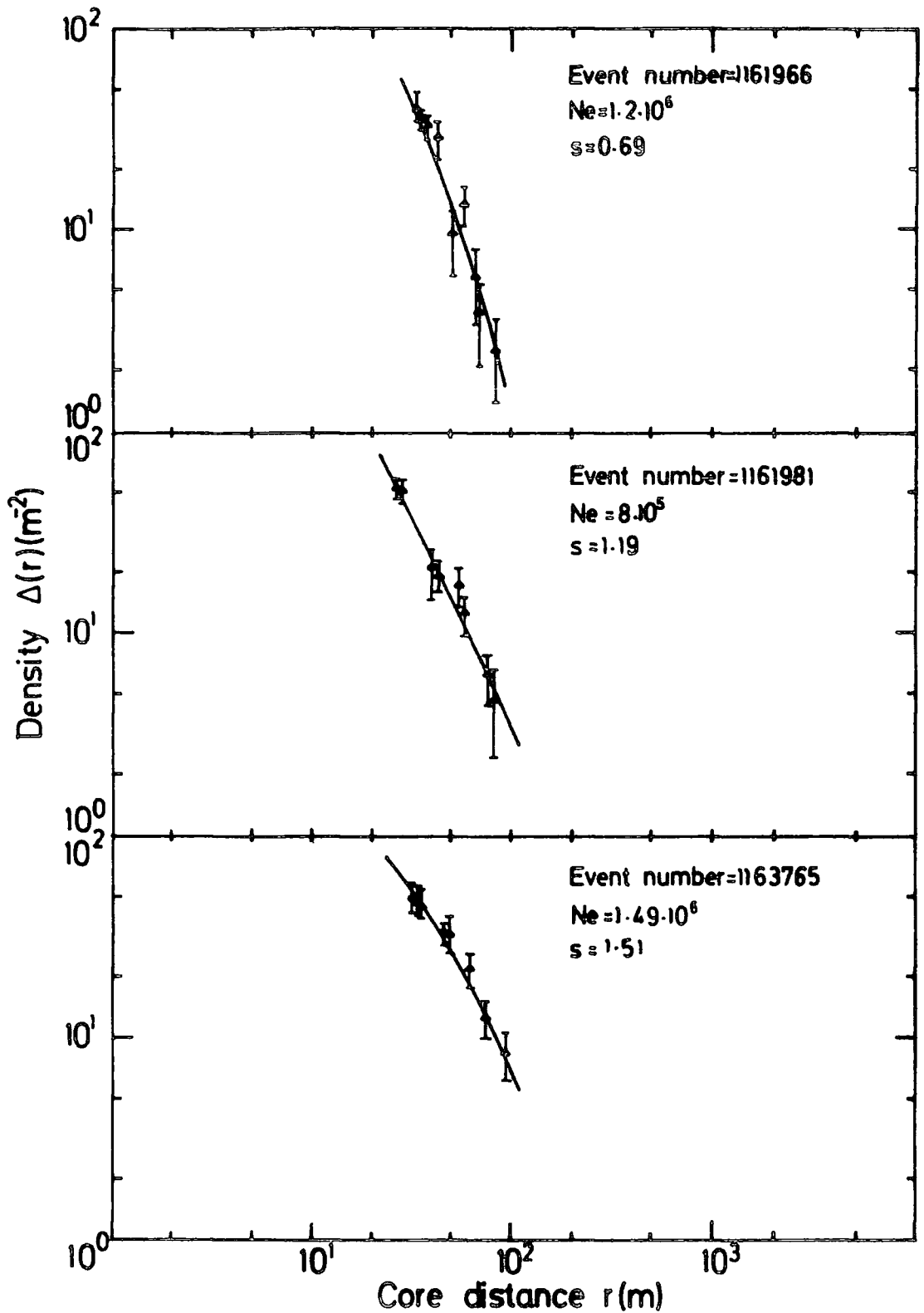
Figure 4.13b :   Examples of the lateral structure of
typical E.A.S. events in the size range
of $5 \cdot 10^5 - 5 \cdot 10^6$ particles.
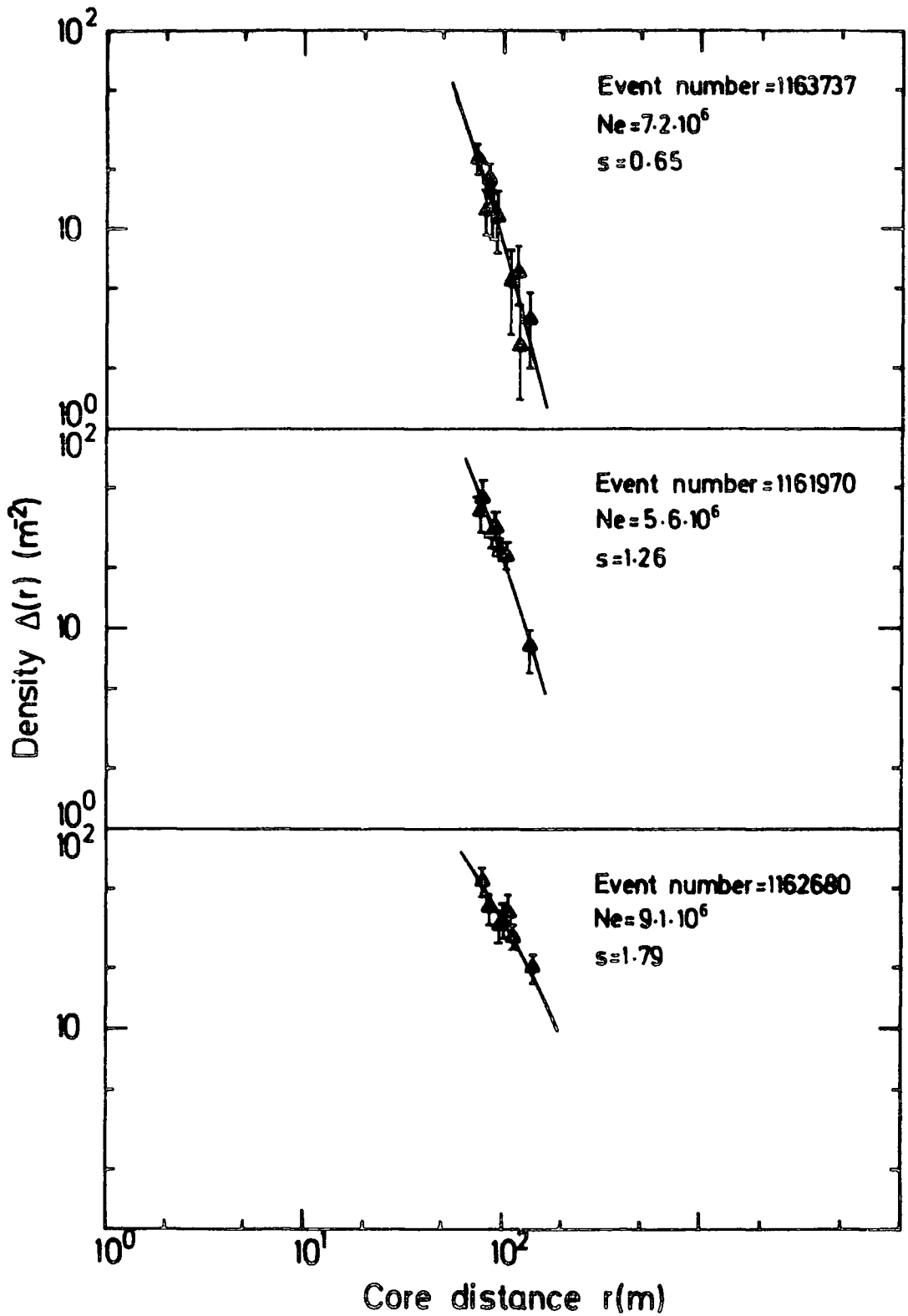
Figure 4.13c :   Examples of the lateral structure of
typical E.A.S. events in the size range
of $5.10^6 - 5.10^7$ particles.

present this dependence which is shown in Figure 4.14. It shows that the average age parameter at sea level and mountain altitude shows an increase at an equivalent primary energy of about 3.10^{16} eV. Miyake et al (1973) suggested that the increase of age in this energy region could be due to a change in the composition of the primary cosmic rays or in the properties of high energy nucleon-nucleon collisions. Since then efforts have been made to clarify the difference. One approach is the central density measurements which are sensitive to the mass composition of primary particles (Peters, 1961 ; Tramper et al, 1971 ; Samorski et al, 1979). This will be discussed in the next section.

A more detailed age parameter study is the work of Chudako et al, 1979, in which they studied the correlation of age parameter with core distance. In two core distance ranges of (1-15)m and (6-45)m for $N_e \geqslant 2.10^5$ particles on the average they found no significant increase of age with core distance, where the mean lateral distribution function is well approximated by a single N.K.G. function.

The present result of the shower size-age parameter dependence is shown in figure 4.15 and is for three ranges of shower size with means, $3.5.10^5$, $1.6.10^6$ and 8.10^6 particles. The average age parameter for the first two size ranges decrease from 1.17 to 1.15 as predicted by the cascade shower theory, since at the level of observation, the maximum development of a shower comes down with primary energy. In the third size range an increase of age parameter was observed which is in the same primary energy region as obtained by Vernov et al,(1970) and Miyake et al, (1973).
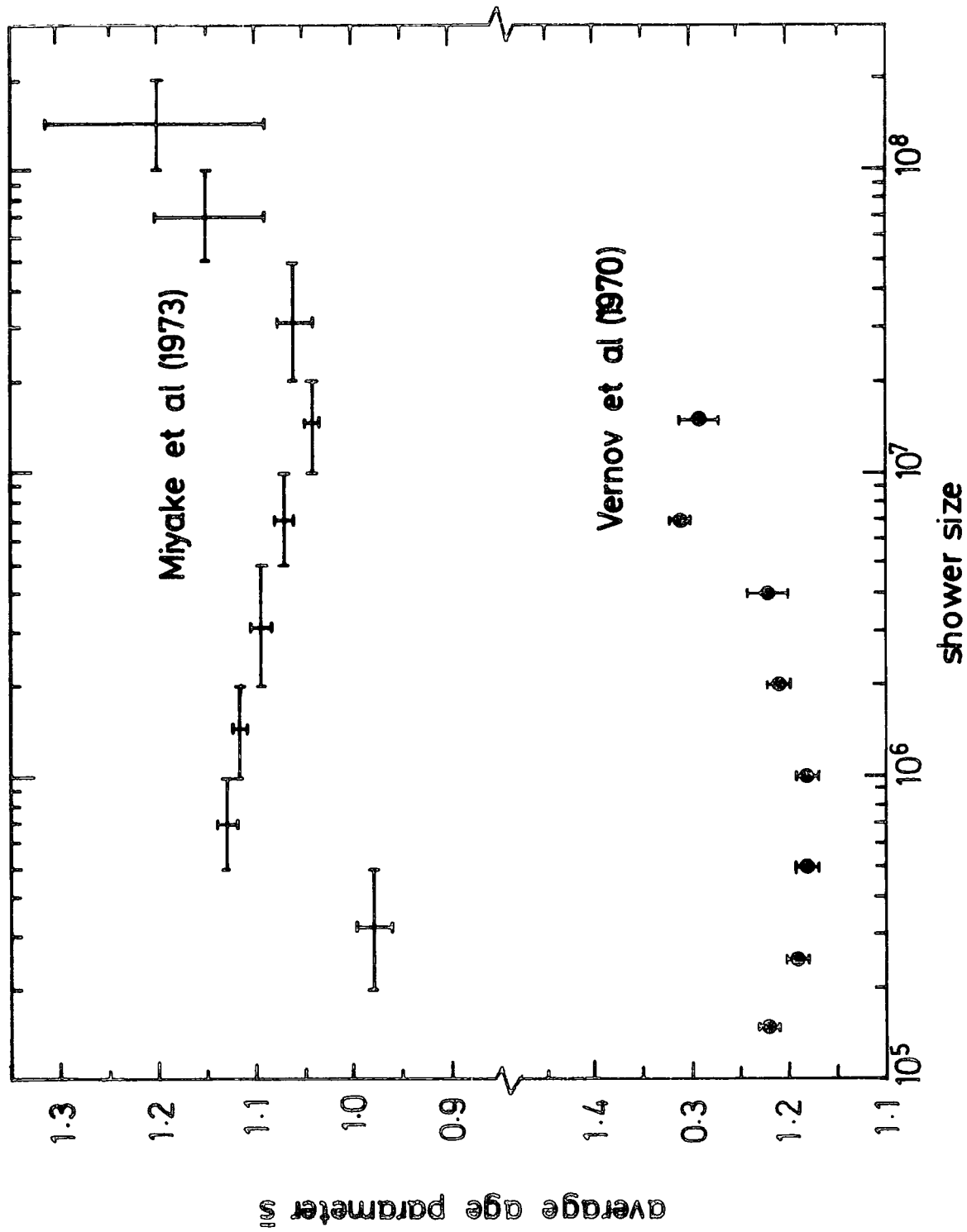
Figure 4.14 : The dependence of average age parameter as a function of shower size measured by Vernov et al (1970) at sea level and by Miyake et al (1973) at 2770 m. elevation.
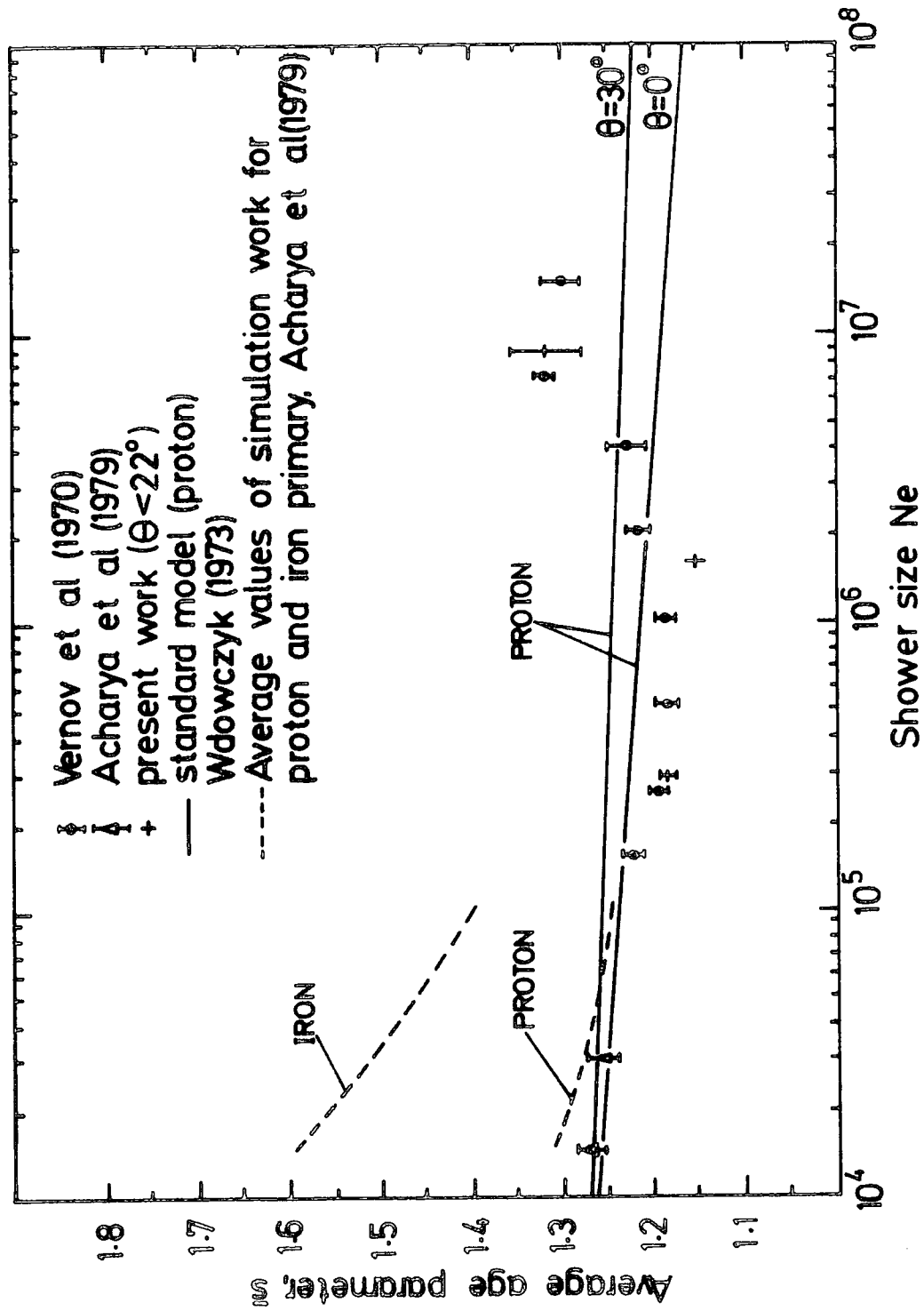
Figure 4.15a: Dependence of the average age parameter on shower size. The experimental points of Acharya et al (1979) are the averages of their raw data uncorrected for bias.
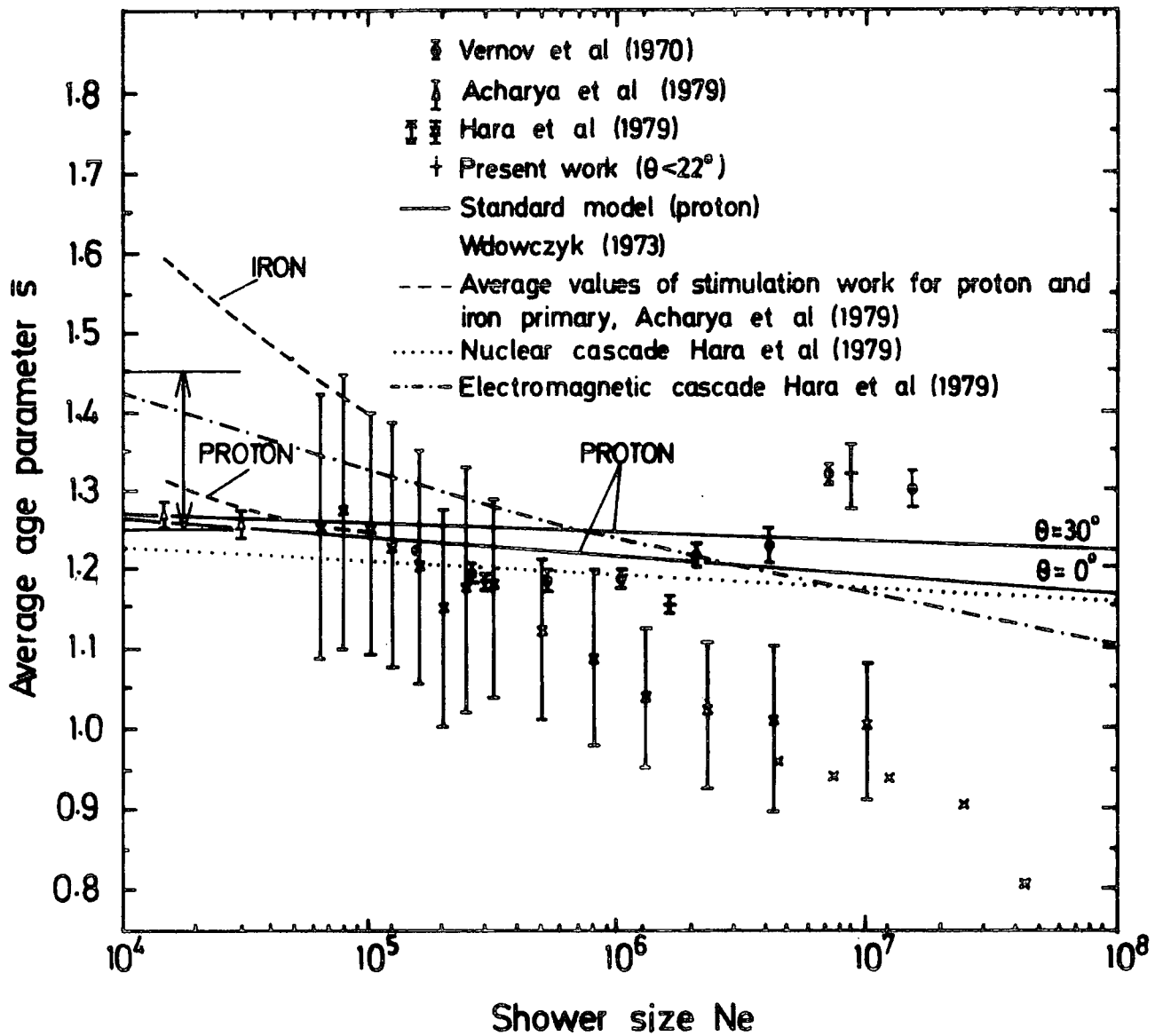
Figure 4.15b : Similar to Figure 4.15a except that the preliminary
results obtained using the Japanese Akano EAS array
(atmospheric depth 927 g cm^{-2}) are also shown.

The dependence of age parameter on zenith angle was also considered by dividing the showers into two ranges of less and bigger than 22° for three ranges of shower size as shown in figures 4.7, 4.9 and 4.12a. The result shows that the average age parameter is independent of θ in the limit of statistical error. It is of interest to mention that at a different altitude and different range of shower size the consistency of zenith angle-age has also been observed. Aguirre et al (1973) at 5200 m.a.s.l, found no correlation for showers bigger than 3.10^7 particles in the zenith angle ranges of $\theta < 20^O$, $20^O \leqslant \theta < 40^O$ and $40^O < \theta \leqslant 60^O$.

4.3.2 The $\Delta c/N$ Measurements

Measurements concerning central density to get information about the chemical composition of cosmic rays started after Peters (1961) proposed the possibility of a greater number of heavy primaries at an energy $> 3.10^{15}$ eV. The Sydney group (McCusker et al, 1968,1969) measured the $\frac{\Delta_c}{N}$ distribution (Δ_c central density, N shower size) and compared it with the result of Monte Carlo calculations which indicated the primary cosmic ray beam has a mixed chemical composition at around 10^{15} eV which becomes richer in heavy nuclei above 3.10^{15} eV up to 10^{17} eV. However, the Sydney result was not confirmed by other measurements (Trumper, 1969) in the same energy region. The Keil group (Trumper et al, 1971) using a 32 m^2 hodoscope, have also performed the same comparison of the $\Delta c/N$ distribution. They concluded that the chemical composition at corresponding energies can not be much different from a pure proton or mixed composition. More recent work of the Kiel group (Samorski et al, 1979) on the central electron

densities also shows a significant proportion of protons

for the primaries in the shower size range of $2.10^5 \leq N \leq 2.10^6$

particles. In the present work to obtain the central density,

N.K.G functions (Equation 4.7) were used, where the number of

particles in an area of $F = 0.215 \, m^2$ centred on the core was

defined as the central particle number n_c. Values of n_c

corresponding to different age parameter were calculated and

the results are shown in Table 4.3 which, for any shower of

size N_e, makes it possible to calculate its central density

when its age parameter is known. The integral distribution

of the normalized central density $\Delta_c = (\frac{n_c}{F} \cdot \frac{10^5}{N_e})$ was found

from the measured age parameter of individual showers and the

result obtained is shown in Figure 4.16 for all θ and

Figure 4.17 for $\theta < 22^\circ$. This was done for the size range of

previous work (Samorski et al, 1971) $3.10^5 - 10^6$ pts as well

as for the three ranges of shower size chosen for the present

study, and particularly the higher size range of $5.10^6 - 5.10^7$

pts which the increase of average S have been observed. The

calculated distribution of the central density for a pure

primary composition $A = 1$ (proton) and $A = 56$ (iron) is given

by the Sydney group (McCusker et al, 1968, 1969) and the Kiel

group (Thielheim and Beiersdorf, 1970 ; Samorski et al, 1971)

which are also shown in the figure. Figures 4.16 and 4.17

show the present results which give a broader distribution of

central density than previous work. The flattening can be

understood from the recent measurements of central density by

the Kiel group (Samorski et al, 1979) where a very large neon

hodoscope was used to measure the electron density from 10 up

to 0.1 metre to the core centre. They found that the distri-

S, Age Parameter	0.6	0.7	0.8	0.9	1	1.1	1.2	1.3	1.4	1.5	1.6	1.7	1.8
n_c/N_e	7.10^{-2}	$4.2.10^{-2}$	$2.4.10^{-2}$	$1.4.10^{-2}$	$8.2.10^{-3}$	$4.4.10^{-3}$	$2.4.10^{-3}$	$1.2.10^{-3}$	$6.3.10^{-4}$	$3.1.10^{-4}$	$1.5.10^{-4}$	$6.5.10^{-5}$	3.10^{-5}

TABLE 4.3 : $\dfrac{n_c}{N_e} = \dfrac{1}{r^2} \displaystyle\int_{10^{-3}}^{2.6.10^{-1}} 2\pi r\, F(r,S)\, dr$ where n_c is the electron number in the central core region of area $0.215\ m^2$ with size and age parameter, N_e and S.
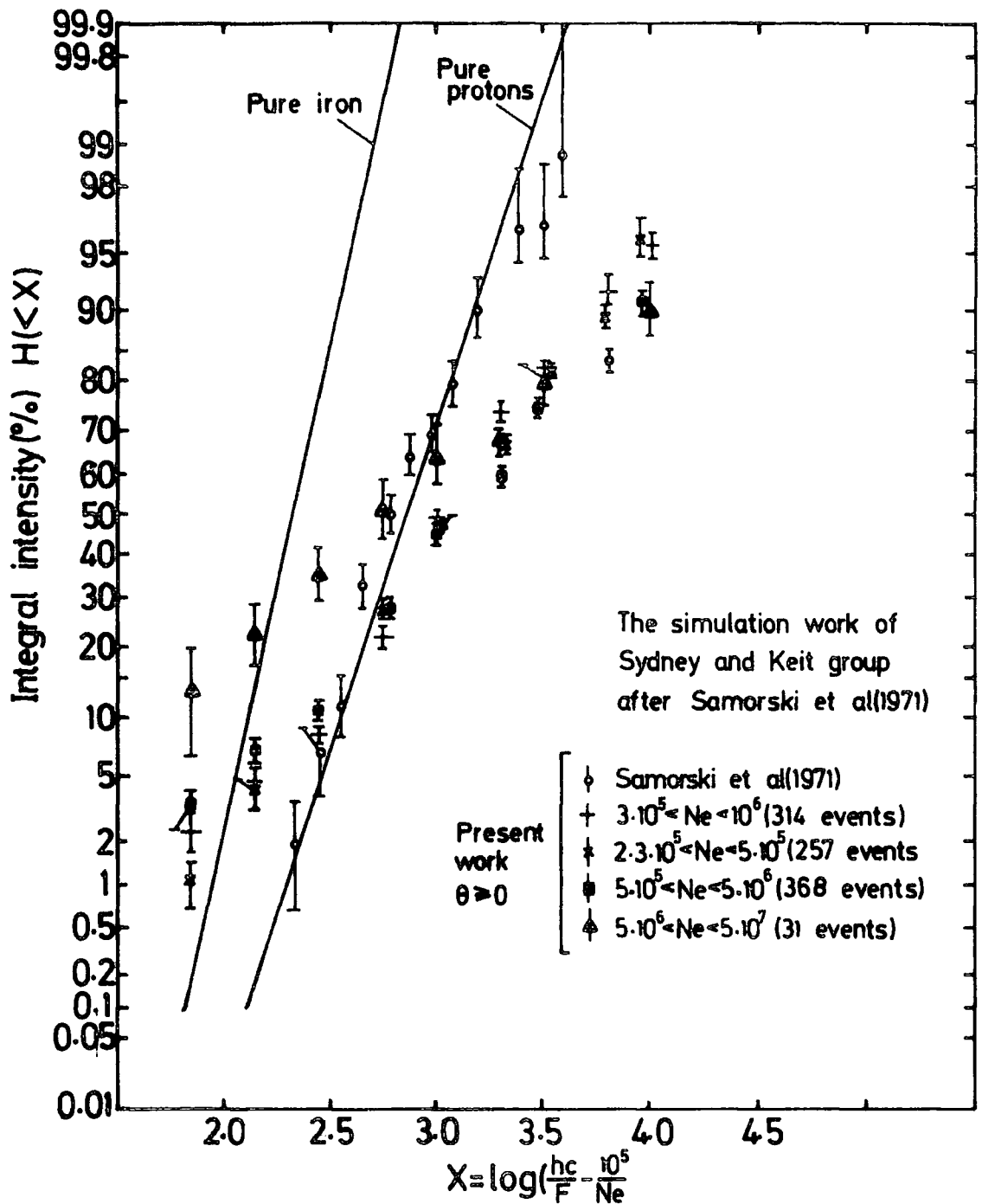
Figure 4.16 : Comparison of the distribution of the normalized central density $\Delta_c = \left(\dfrac{n_c}{F} \cdot \dfrac{10^5}{Ne} \right)$ for different ranges of shower size and the expected distributions assuming pure protons and pure iron (Samorski et al, 1971). n_c is the number of charged particles observed in an area of $F = 0.215$ m^2 around the centre of the shower core. Previous measurements of the Kiel group are also shown.
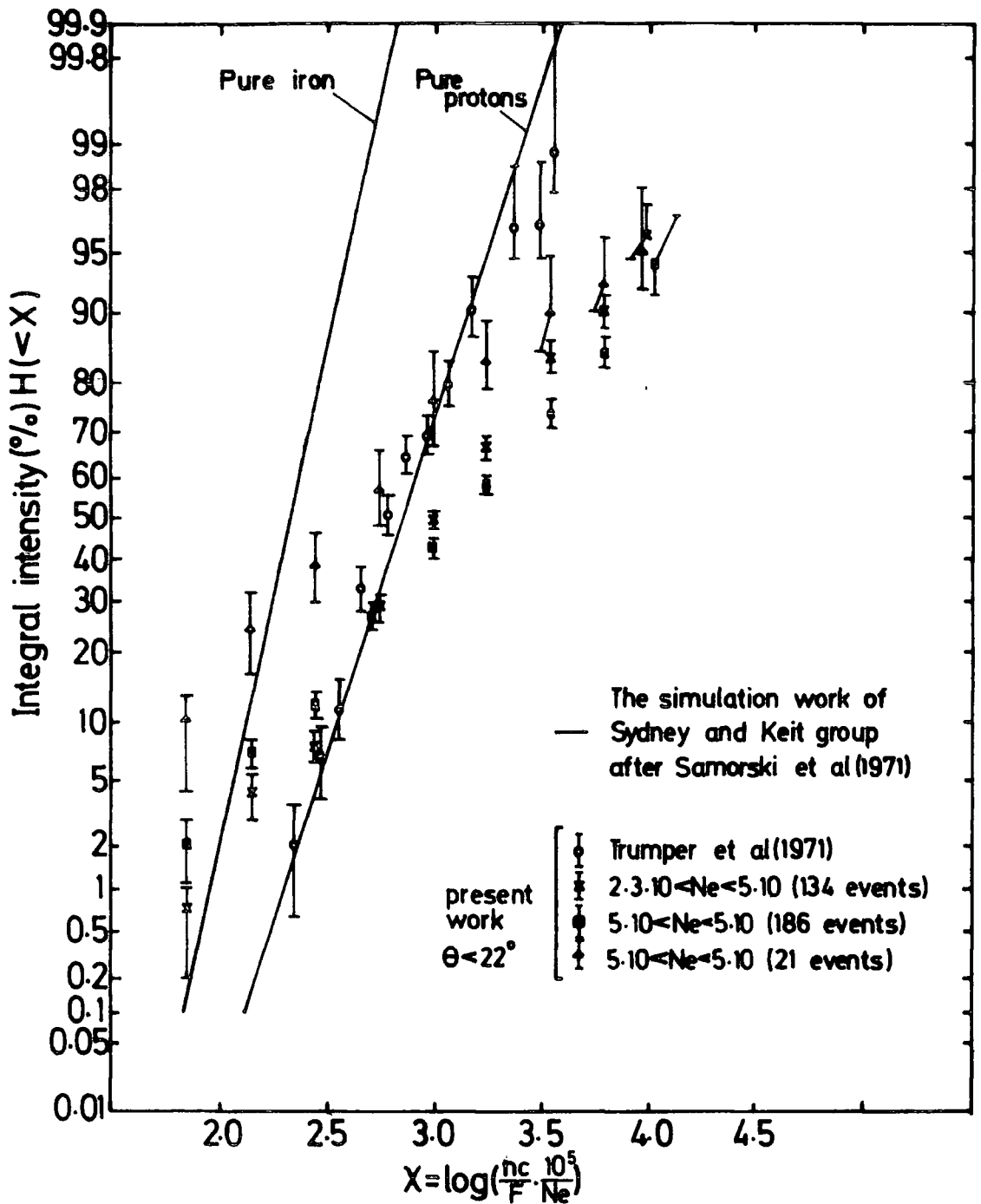
Figure 4.17 : Comparison of the distribution of the normalized central density $\Delta_c = \left(\dfrac{n_c}{F} \quad \dfrac{10^5}{Ne} \right)$ for different ranges of shower size and the expected distributions assuming pure protons and pure iron. Present work is for $\theta < 22°$.

bution of E.A.S electrons becomes on average progressively flatter than an N.K.G. function when approaching the shower core centre (see Figure 4.18). Therefore, determining the central density using N.K.G functions (i.e. age parameter) gives a greater percentage of young showers or on the other-hand a bigger percentage of higher central density than previous work which implies the flatter observed distributions. The interesting feature of the present results is its size dependence. For the size range of $5.10^6 - 5.10^7$ particles, the central density distribution is relatively flatter than the other size ranges (see Figure 4.17). Therefore, knowing that lower central density is produced by a shower of large S (flat shower) the results indicate a bigger percentage of flat showers in the higher energy range.

4.4   CONCLUSION

For a given shower size at sea level both the mean age parameter and the standard deviation of the age parameter distribution are independent of zenith angle. The result obtained for the mean age parameter $\bar{S}$ is consistent with previous work, but the standard deviation is larger than the result quoted by Wdowczyk (1973), $\frac{\delta_S}{\bar{S}} = 0.09$. In the next stage of analysis, an age parameter-shower size dependence was found, particularly the surprising change and increase of age parameter at large size is noticed, which is in the same primary energy region as previous work, (Vernov et al, (1970) and Miyake et al, (1973)). The increase indicates that the position of the maximum development of E.A.S does not move down in the atmosphere as the primary energy increases as is expected from cascade shower theory assuming the chemical
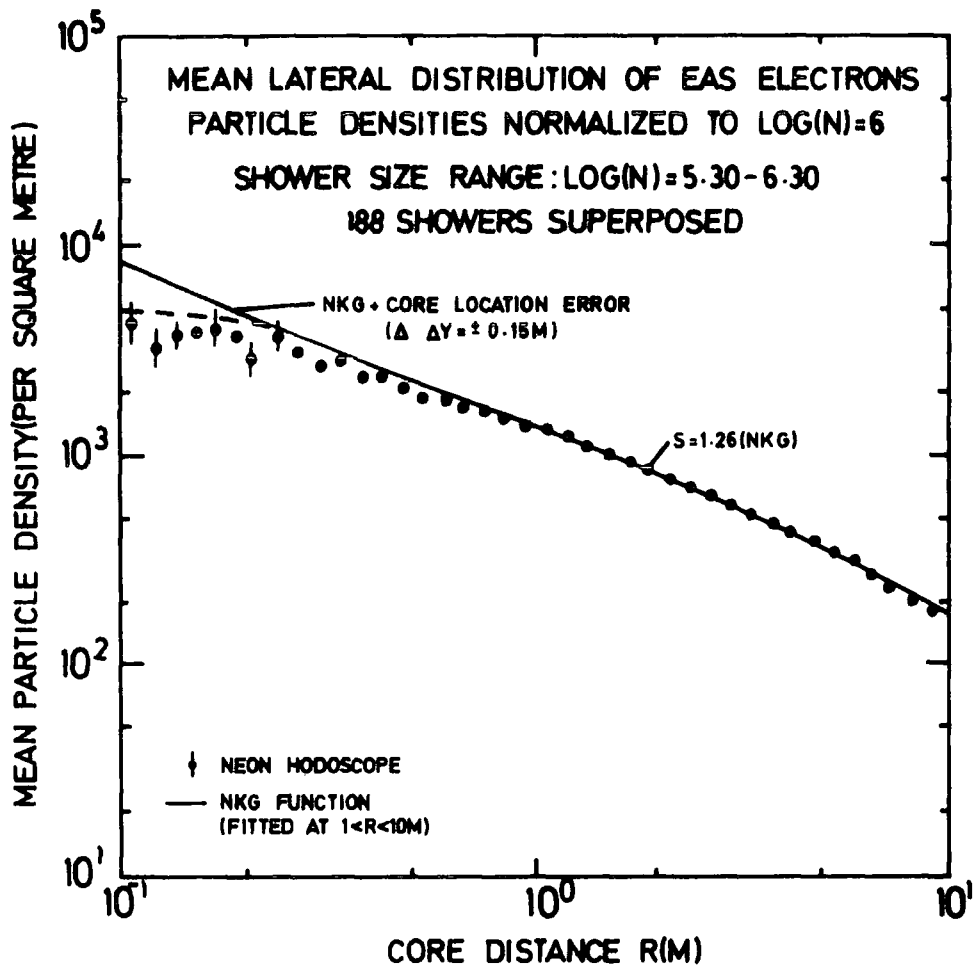
Figure 4.18 : The lateral distribution of electrons for core distance range of $0.1 \le r \le 10$ metre, (after Samorski, 1979).

composition of the primaries does not change throughout the energy range studied. Since heavy primaries are expected to produce a greater average age parameter than primary protons, it is possible that the chemical composition of the primary radiation changes at a primary energy of $\sim 5.10^{16}$ eV such that the primary radiation contains a greater percentage of heavy nuclei. However, as measurements of the primary energy spectrum show no significant change in slope in this energy range, it is thought that a more likely explanation is a change in the characteristics of the nucleon-nucleon interaction at an energy of $\sim 5.10^{16}$ eV.

CHAPTER 5

SIZE SPECTRUM OF E.A.S. AT SEA LEVEL TAKING

INTO ACCOUNT THE AGE PARAMETER OF THE SHOWER

5.1   INTRODUCTION

The interest in investigating the size spectrum is

the information it contains about the energy spectrum of

the primary high energy cosmic rays, while a comparison of

spectra measured at different altitudes above sea level with

other information on E.A.S. may also produce a picture of

their evolution in the atmosphere.

The method used to obtain the size spectrum of vertical

showers is by using the measured size distribution of the

showers at different ranges of zenith angle taking the

zenith-angle dependence of the showers as

$$I(\theta) = I(o)\cos^{n}\theta \qquad (5.1)$$

The size distribution and the electron lateral distribution

are closely connected.

The determination of the size and collecting area of

a shower is dependent on the structure function, and the

precise location of the core. Too steep a structure function

causes an overestimation in the size of the shower and an

underestimation in the collecting area of the shower. Many

electron lateral distribution functions for different types

of detector have been used. The most popular form that fits

the experimental data is defined by Nishimura-Kamata-Greisen

(N.K.G) which is dependent on s, the age parameter of the

shower. The function is

$$\triangle (N,s,r) = C(s) \ \frac{N}{r_1^2} \ (1 + \frac{r}{r_1})^{s-4.5} (\frac{r}{r_1})^{s-2} (1 + \frac{r}{11.4 \ r_1})$$

$$(5.2)$$

where r_1 is the Moliere unit, 79 m at sea level (see Chapter 4).
Although the measurement of the size spectrum is commonly
obtained by assuming the same electron lateral structure
function for all the showers (e.g. Catz et al, 1975, Ashton
et al, 1979a, Crouch et al, 1980), to determine the size
spectrum accurately, the age parameter of individual showers
should be taken into account in order to get an accurate deter-
mination of size and collecting area.

Only Vernov et al, 1968, have carried out the latter
approach and concluded that the spectrum had the same shape
but lower intensity by an average factor of 0.77 than the
spectrum determined using an average electron lateral structure
function. The present experiment is a check and continuation
of this work.

5.2   PREVIOUS MEASUREMENTS OF THE NUMBER SPECTRUM

The two ways that have been used to determine the
number or size spectrum of E.A.S. are (a) the more reliable
one which is derived from measuring the frequency, size and
angular distribution of showers (direct method), (b) from
density spectrum measurements (indirect method). The deter-
mination of the density spectrum is the frequency of showers,
$P(\Delta)d\Delta$ which give densities within the range Δ to $\Delta + d\Delta$
particles per unit area at a particular point and is known
to have the form $H(>\Delta) = K \ \Delta^{-\beta}$. In both cases, apart from

knowing the location of the shower axis and its arrival direction, the electron structure function and its size dependence is necessary.

Over many years, the number spectrum has been measured by many workers with different types of detector. Hillas (1970) calculated the best estimate number spectrum from the available data of all reliable experiments. His summary of the number spectrum at sea level is formulated as follows :

$$R(\geqslant N) = 52 \ N^{-1.5} \quad m^{-2} \ s^{-1} \ st^{-1} \quad \text{for} \quad N \leqslant 5.10^5$$

$$R(\geqslant N) = 36920 \ N^{-2} \quad m^{-2} \ s^{-1} \ st^{-1} \quad \text{for} \quad 5.10^5 \leqslant N \leqslant 3.10^7$$

$$R(\geqslant N) = 6.76 \ N^{-1.5} \ m^{-2} \ s^{-1} \ st^{-1} \quad \text{for} \quad N \geqslant 3.10^7$$

where $R(\geqslant N)$ is the integral rate of showers of size more than N particles. It is plotted in Figure 5.22 (Curve a). Some more recent experiments are summarised by the Australian group, Crouch et al (1980), see Figure 5.23. The size spectrum is characterised as ;

(i) having a sharp break or "knee" around size 5.10^5 particles at sea level and 2.10^6 particles at mountain altitude.

(ii) an increase of the exponent of the slope above the "knee".

A determination of the size spectrum from the measured density spectrum has been described by Parvaresh (1975). The experiment consisted of a proportional counter and three large area liquid scintillators. The former was employed to measure the density spectrum of E.A.S, and the latter to select E.A.S. The number spectrum was derived from the density spectrum measured over the density range of $40 \ m^{-2} < \Delta < 5000 \ m^{-2}$, where the kink was at $\Delta \sim 1000 \ m^{-2}$. The best estimation of the

integral number spectrum at sea level was derived as,

$$R(>N) = 3. \, N^{-1.3} \qquad m^{-2} \, s^{-1} \, st^{-1} \qquad N \leqslant 7.10^5$$

$$R(>N) = 36920 \, N^{-2} \qquad m^{-2} \, s^{-1} \, st^{-1} \qquad 7.10^5 \leqslant N < 3.10^7$$

$$R(>N) = 6.76 \, N^{-1.5} \qquad m^{-2} \, s^{-1} \, st^{-1} \qquad N > 3.10^7$$

The spectrum has approximately the same form as that given by Hillas except for $N_e < 7.10^5$ where a smaller rate is predicted (Figure 5.22 (Curve b)). In spite of a suggestion of slope flattening of the integral number spectrum for $N_e \geqslant 10^7$ by Khristiansen et al (1974), it has not been clearly investigated. A change in the slope of the density or number spectrum reflects a sharper change in the form of the primary energy spectrum, that is in the energy interval $E \sim 10^{15}-10^{16}$ eV. Around the break the exponent of the slope changes from -1.7 to -2.3, two possible interpretations of the sharp break in the energy spectrum may be (a) the break of energy spectrum of primary cosmic rays itself (a genuine change) or (b) a sudden change of nature of nuclear inter-action at an energy around 5.10^{15} eV. Generally, the form of the primary energy spectrum is of particular interest from the point of view of the theory of the origin of the cosmic radiation.

5.3 PRESENT EXPERIMENT

5.3.1 The Trigger Modes of the E.A.S.Array

The Durham E.A.S. array consists of 14 plastic scintillators, and E.A.S. are recorded by two types of selection system each triggered by C, the Central detector, and either detectors 11, 31, 51 that are close to the centre

of the array (inner ring) or 13, 33, 53 the outer ring detectors. The triggering condition of the array is satisfied by a density of $\geqslant$ 4 particles per m^2 at C and $\geqslant$ 2 particles per m^2 at the other three mentioned detectors. On changing the trigger mode from the inner ring to the outer ring the detection sensitivity of the array changes from a small to a larger shower size range. Overall it is from size 2.10^4 to 3.10^7 particles (present experiment).

n, the power of the assumed zenith angle distribution of the shower (Eqn. 5.1) has been calculated to be n = 8.0 $\pm$ 0.3 and n = 8.5 $\pm$ 0.2 for the inner and outer ring trigger modes respectively was shown in Figure 5.4.

5.3.2 The Collecting Area of E.A.S. and the Shower Age

One of the important parameters required to determine the size spectrum is the collecting area of showers of a given size. This is the area within which the shower axes have to fall to be detected. The requirement for detecting an E.A.S. is that the density of particles in the selection detectors should exceed the respective triggering levels. Since the density is given by Δ = N $F(r,s)$, the maximum allowed distance of the axis from a given trigger detector is a function of N, Δ and s. Hence the collecting area depends on s, as $\pi r^2(N,s)$ for a given triggering detector. In the present work the collecting areas have been calculated for three equi-number groups of showers having age parameter ranges of 0.6< s <1.1, 1.1< s <1.3, 1.3 <s< 1.8 with means 0.95, 1.2 and 1.45. The result is shown for the three zenith angle ranges of 0-10°, 10-20°, 20-30° with means 5°, 15° and 25° respectively, in Figures 5.16 to 5.18 for both the inner and outer ring triggers.

The dependence of age on collecting area can be explained with the help of Figure 4.3. It shows that the density at small core distances ($r \lesssim 20m$) in a shower of small age is larger than for showers with a bigger value of s, whereas at larger core distances the reverse is true. This is reflected in the variation of the collecting area of the shower with the age parameter. For fixed large shower sizes the collecting area of the shower increases with its age, as shown in Figure 5.13. However, for smaller shower sizes concerning smaller core distances this may not be the case. The example in Figure 5.14 shows that as the age parameter of E.A.S. increases, the collecting areas for a fixed size first increases and then decreases as s increases. The variation of collecting area with size for the three mean age parameter ranges of 0.95, 1.2 and 1.45 are shown in Figure 5.15 where showers were assumed to be vertical.

5.3.3 Effect of Zenith Angle on Collecting Area

Each scintillator in the array is calibrated by determining the average pulse height v produced by relativistic muons traversing it at normal incidence. If a pulse height V is produced by a shower of particles traversing a scintillator of area s at normal incidence, the particle density Δ is given by

$$\Delta = \frac{V}{v \, s} \quad m^{-2} \tag{5.3}$$

Consider the same particle density traversing the scintillator at zenith angle θ. The actual number of particles that traverse the scintillator is $\Delta \cdot s \cos\theta$ but each particle will produce a larger pulse height $v/\cos\theta$ because of its longer

track length in the phospor. The pulse height produced is

thus, $\Delta .s \cos \theta . \dfrac{v}{\cos \theta} = \Delta .sv = V$ from Equation 5.3.

Thus if a pulse height V is observed from any detector and

v is the average pulse height produced by normally incident

muons, the particle density at the detector is correctly given

by $\dfrac{V}{v}$ for any incident zenith angle.

Consider a detector of area s situated at O as shown

in Figure 5.1a and initially assume showers can only fall

anywhere along the line OX. If an electronic requirement of

$> n$ particles m^{-2} is required for triggering then vertical

showers of size N will only trigger the detector if they fall

at distance $\leqslant r$ from O in the direction of OX where r is found

from solving the equation $N F(r) = n$, where $F(r)$ is the electron

lateral distribution function. For showers of size N incident

at A at zenith angle θ their orthogonal core distance from O

is not r but the smaller value $r \cos \theta$. only at the larger

distance $r/\cos \theta$ from O is their orthogonal core distance

from O equal to r as illustrated in Figure 5.1b. Thus the

maximum distance from O along the line OX at which showers

of size N can trigger the detector at O increases as their

zenith angle increases.

In the case of three triggering detectors situated in

a plane, they will be simultaneously triggered by a shower of

size N, only if it falls in an area (collecting area) which

is approximately given by ;

$$A \simeq \pi (r-d)^2 \qquad \text{for vertical showers} \qquad (5.4a)$$

$$B \simeq \pi (r/\cos \theta -d)^2 \text{ for inclined showers} \qquad (5.4b)$$

d is the distance of an outer detector from C (assumed to

be the same for all three triggering detectors) and r is the

maximum core distance that a shower of size N incident vertically can fall from a triggering detector to satisfy the electron density triggering requirement (see Figure 5.2). Taking the present outer ring trigger detectors with $d \sim 58m$ and various collecting areas, say $A = 1$, 10^2 and 10^3 m^2 (corresponding to three increasing shower sizes each incident vertically) r is found by solving equation (5.2a) to be $r = 58.56$, 63.6 and $75.8m$ for each collecting area. To see the effect of zenith angle θ on collecting area we consider showers of the same size (i.e. they have collecting areas 1 1, 10^2 and 10^3 m^2 when incident vertically) but with zenith angle θ. The maximum distance that their cores can fall in the horizontal plane to satisfy the selection criteria is increased from r to $r_1 = r/\cos\theta$, for $\theta = 15^o$, $r_1 = r/\cos\theta = 1.035$ r or $r_1 = 60.62$, 65.42 and $78.47m$ which from equation (5.2b) gives collecting areas of 21.5, $1.72.10^2$ and $1.31.10^3$ m^2. This shows that the collecting area of showers with collecting areas 1, 10^2 and 10^3 m^2 when incident vertically increases by factors of 21.5, 1.72 and 1.31 when incident with $\theta = 15^o$. It is seen that the importance of this effect is very large close to the triggering threshold but becomes less important as the collecting area (shower size) increases. The variation of collecting area with shower size for different zenith angles are shown in Figures 5.16 to 5.18 for the inner and outer ring triggers of the E.A.S. array.

5.3.4 Analysis of the Data

A total number of 4814 triggers in a running time of 511.27 hours were analysed and the shower information : shower size N_e, core distance r_c and zenith angle θ and also age

(a)

(b)
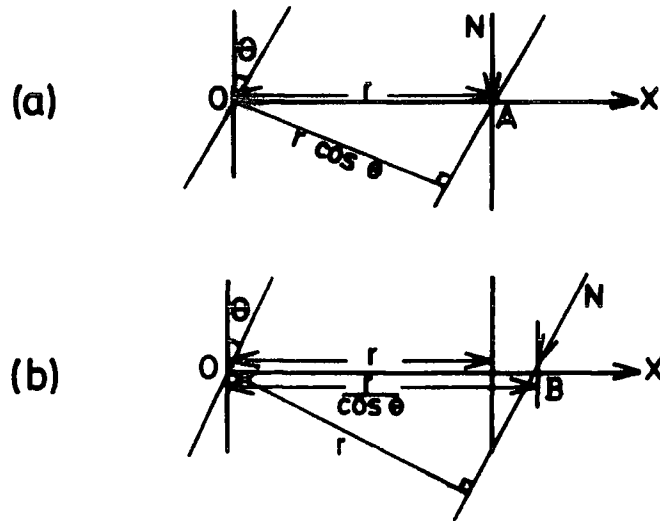
Figure 5.1 : To be detected by a given local density detector situated
at O the maximum distance from O along OX at which showers
of a given size can fall is r as shown in Fig.(5.1a) if the
showers are incident vertically. For showers incident at zenith
angle Θ the maximum distance is r/cosΘ as shown in Fig.(5.1b).
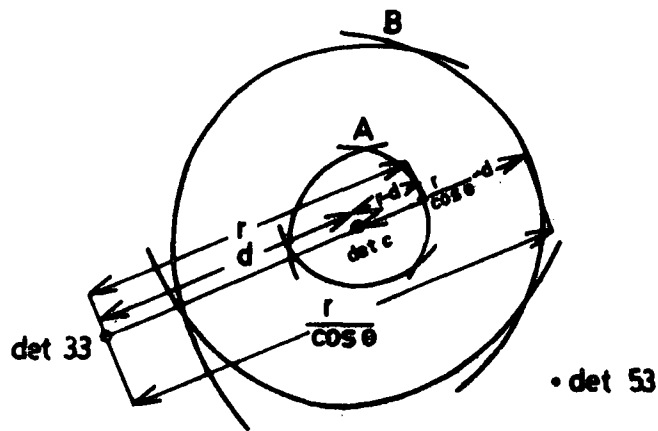
Figure 5.2 : The dependence of collecting area on zenith angle for showers
of a given size. A is the collecting area for a vertical shower
and B is the collecting area for the same shower incident at
zenith angle Θ.

parameter s and shower size $N_e(s)$ were obtained. N_e and
$N_e(s)$ are sizes obtained using the Catz and N.K.G. (i.e.age
parameter) structure functions respectively. Figure 5.3 shows
the minimum shower size that showers of given age must have to
produce a trigger. It is seen that the minimum size of a
shower to trigger the array is 7.10^4 and 2.10^5 particles for
the inner and outer ring triggers respectively. Table 5.1
shows the basic data used in the determination of the size
spectrum for both the inner and outer ring triggers used in
the present work. In this table the quoted shower sizes are
$N_e(s)$. The observed and expected zenith angle distributions
of recorded E.A.S. are shown in Figure 5.4, where the exponent
n (see equation 5.1) for best to the data was calculated to be
n = 8.0 $\pm$ 0.3 and 8.5 $\pm$ 0.2 for the inner and outer ring
triggers respectively. The age parameter and shower size
distributions are given in Figures 5.5 to 5.7. A comparison
of N_e with $N_e(s)$ for showers with $\theta < 30^o$ are given in
Figures 5.8 to 5.10 where the average percentage difference
$\frac{N_e(s) - N_e}{N_e(s)}$ is + (36.1 $\pm$ 1.8)% for $10^4 < N_e < 4.10^4$ - (0.6 $\pm$ 1.0)%
for $4.10^6 < N_e(s) < 10^6$ and +(15.1 $\pm$ 6.7)% for $N_{e(s)} > 4.10^6$ particles.
Overall, it is seen that for very small and large shower sizes
there is a significant difference between the correct size
$N_e(s)$ and the value obtained if a unique electron structure
function is assumed for all showers. The distribution of
orthogonal core distance from the central detector C is given
with a comparison with (X,Y) plane core distances in
Figures 5.11 and 5.12. For showers with $\theta < 30^o$ the average
percentage difference $\frac{r_{xy} - r_{orth}}{r_{xy}}$ is (3.9 $\pm$ 0.02)%.

E.A.S. Selection	Run time (hrs)	Total No. of Triggers	Trigger rate (hr^{-1})	Total No.of Analyzable Showers	No. of Triggers with $\theta<30^\circ$, $r_c<75m$ $N<4.10^6$	No. of Triggers with $\theta<30^\circ$, $r_c<105$ $N<4.10^6$
Inner ring Trigger : $\Delta_c(\geq 4m^{-2})$, $\Delta_{11}(\geq 2m^{-2})$, $\Delta_{31}(\geq 2m^{-2})$, $\Delta_{51}(\geq 2m^{-2})$	128	2683	20.96+0.40	2608	1802	9
Outer ring Trigger; $\Delta_c(\geq 4m^{-2})$, $\Delta_{13}(\geq 2m^{-2})$, $\Delta_{33}(\geq 2m^{-2})$, $\Delta_{53}(\geq 2m^{-2})$	383.27	2131	5.56 $\pm$ 0.12	2042	1149	33

TABLE 5.1 : Summary of experimental data used in the analysis.
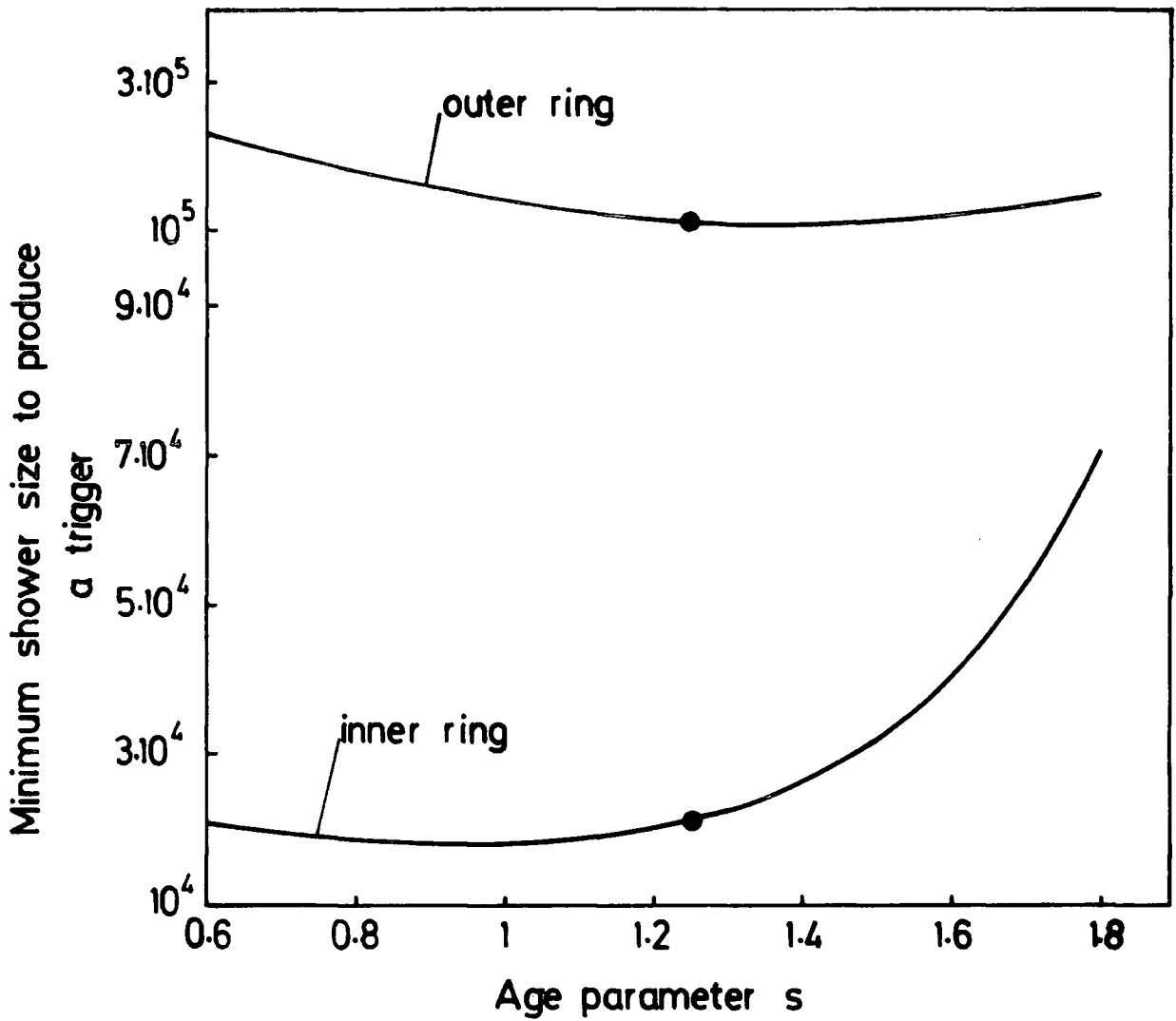
Figure 5.3 : The dependence of minimum shower size on the
shower age parameter for showers to satisfy
the inner ring trigger and the outer ring trigger
of the Durham E.A.S. array. Values calculated
assuming all showers obey the Greisen average
electron structure function are indicated by
the solid circles.
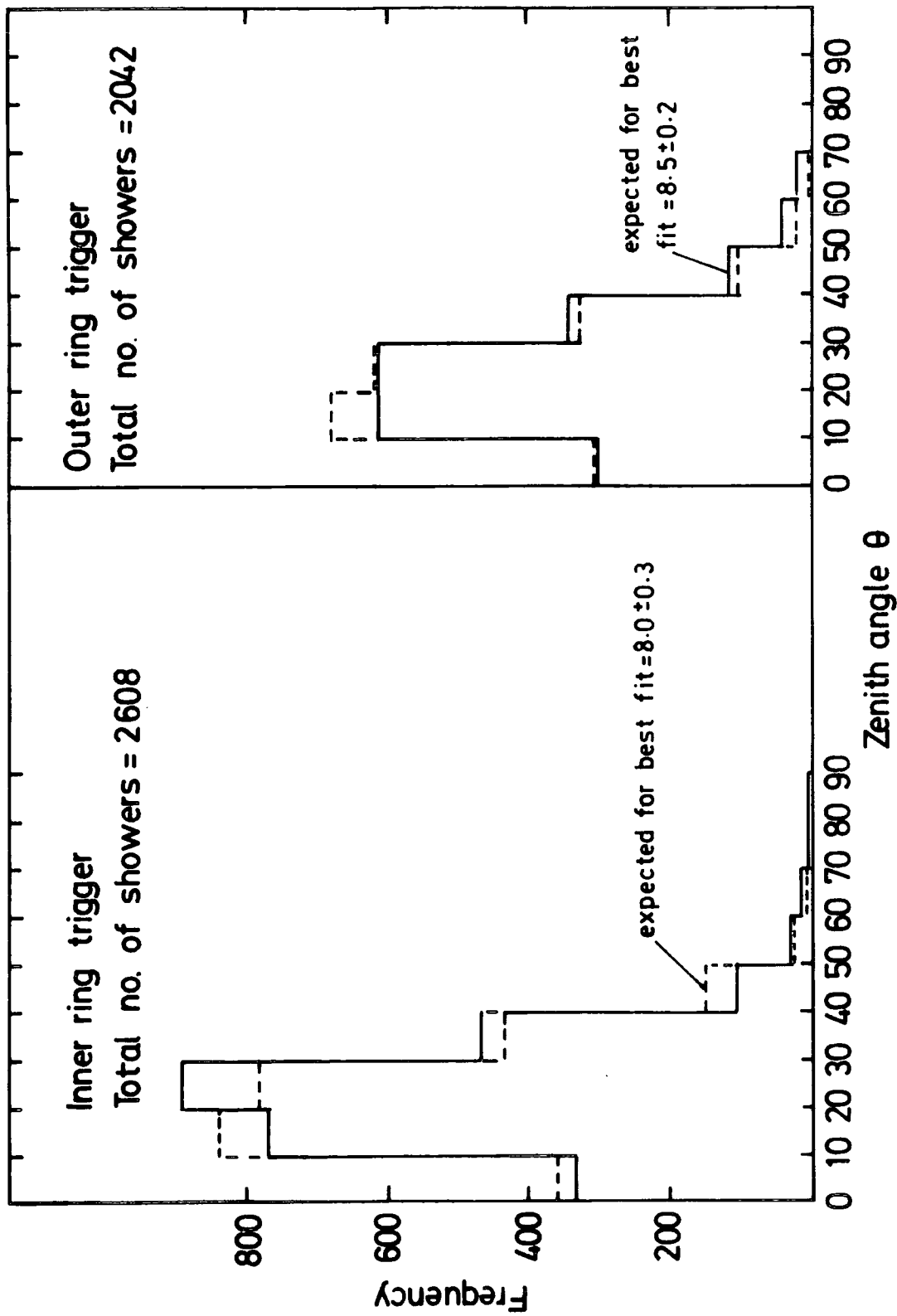
Figure 5.4 : The measured zenith angle distributions of the data, where the dashed lines are a fit to the data according to $I(\theta) = I(o) \cos^n\theta$.
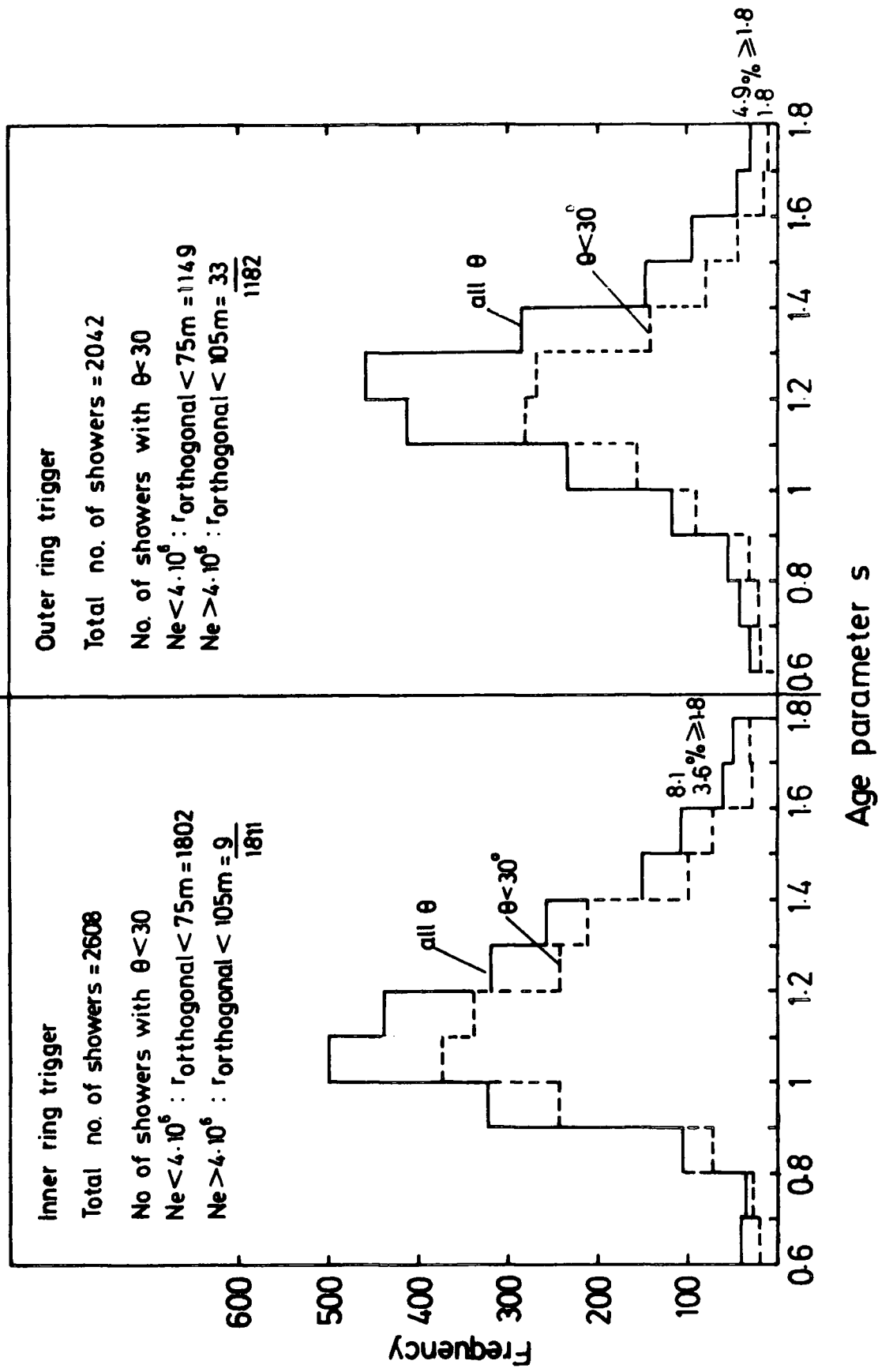
Figure 5.5 : The measured age parameter distributions of all showers and those with zenith angle less than 30°.

The plot contains the following annotations:

Inner ring triggers
Total no of showers = 2608

No of showers with $\theta < 30°$
$Ne(s) < 4 \cdot 10^6$: $r_{orthogonal} < 75m = 1802$
$Ne(s) > 4 \cdot 10^6$: $r_{orthogonal} < 105m = \dfrac{9}{1811}$

all θ

$\theta < 30°$

Y-axis: no of showers

X-axis: Shower size Ne(s)
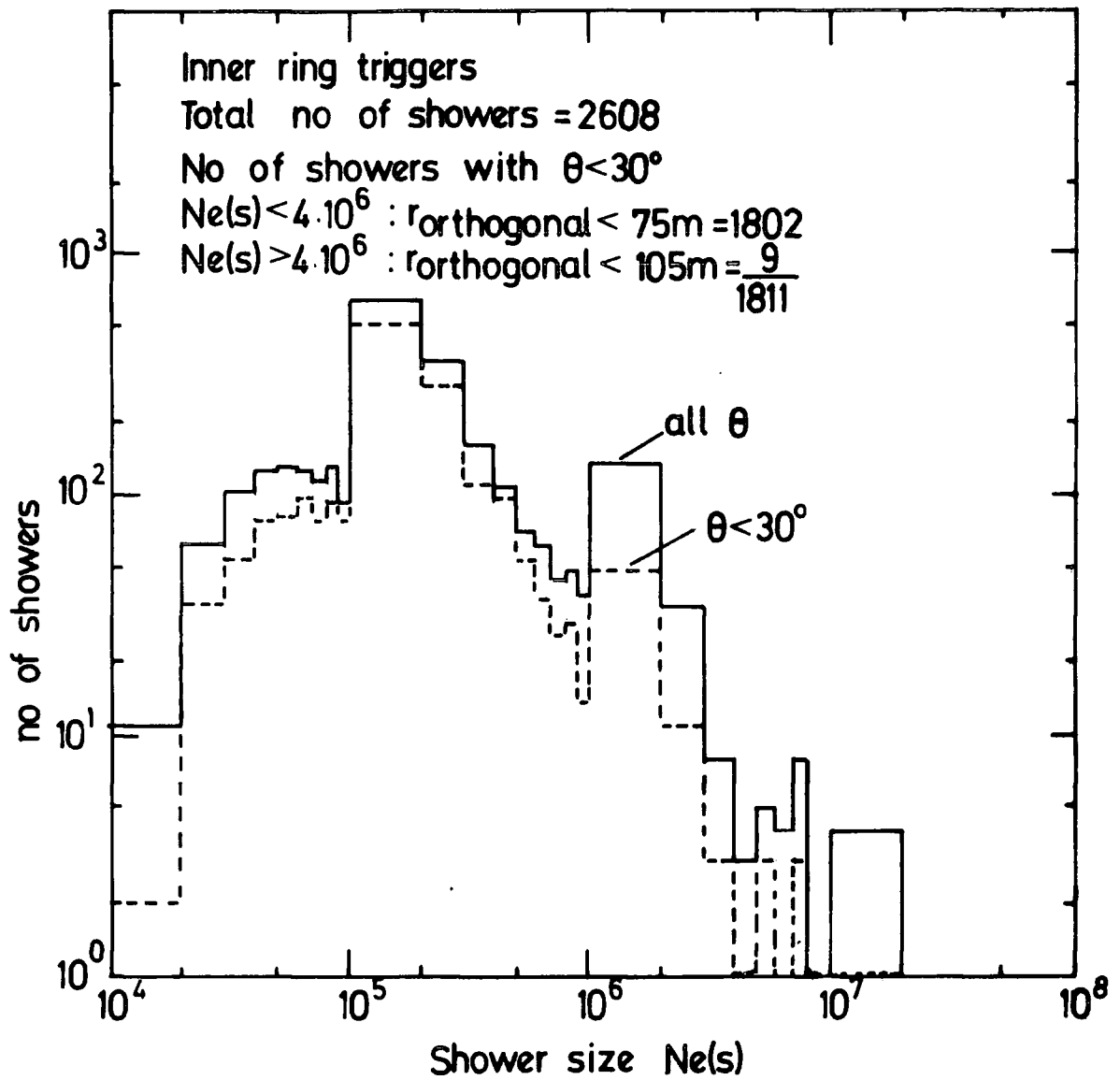
Figure 5.6 : The size distributions of all showers and those with $\theta < 30°$ used in the data analysis.
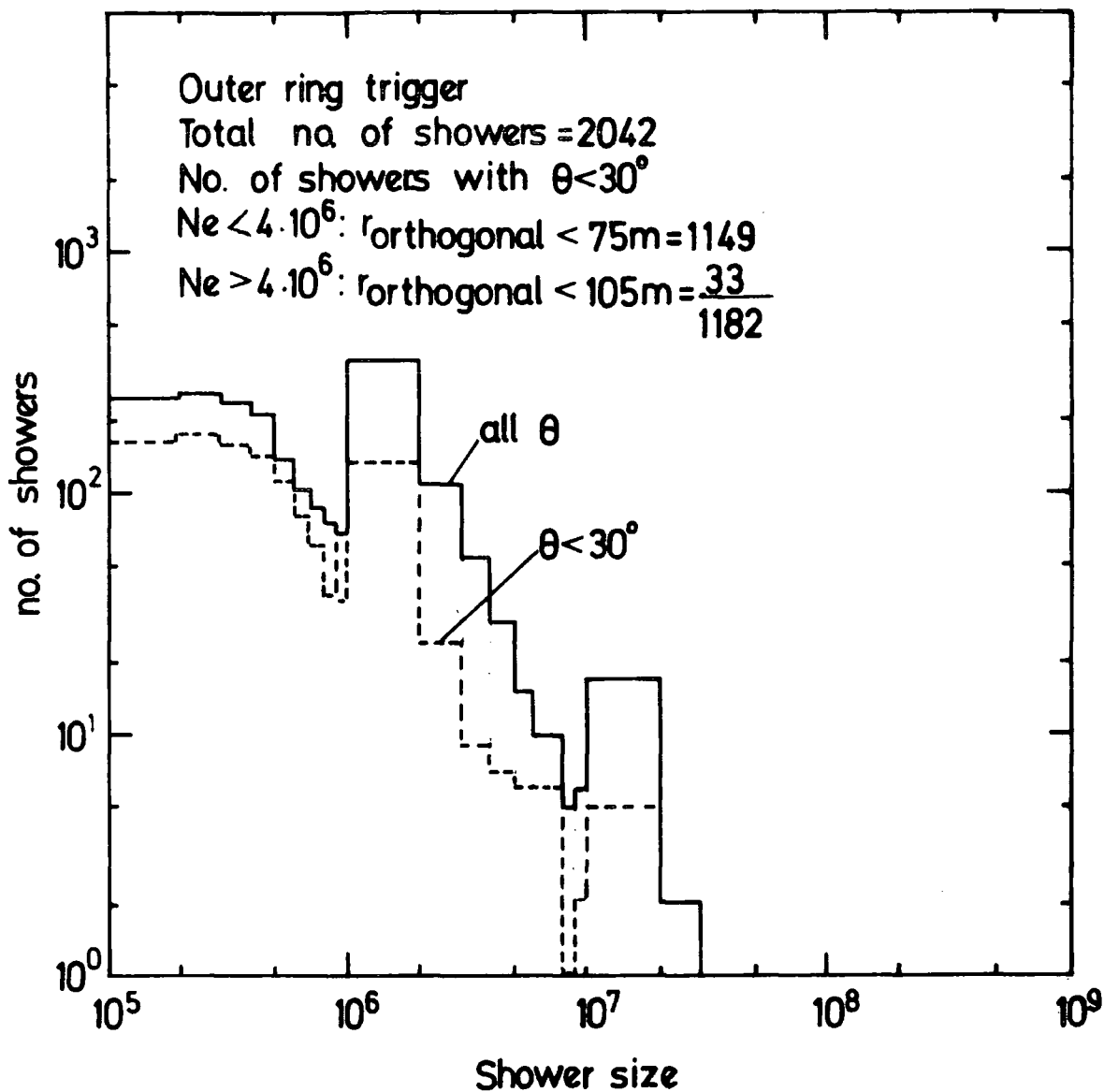
Figure 5.7 : The size distributions of all showers and those with θ< 30° used in the data analysis.
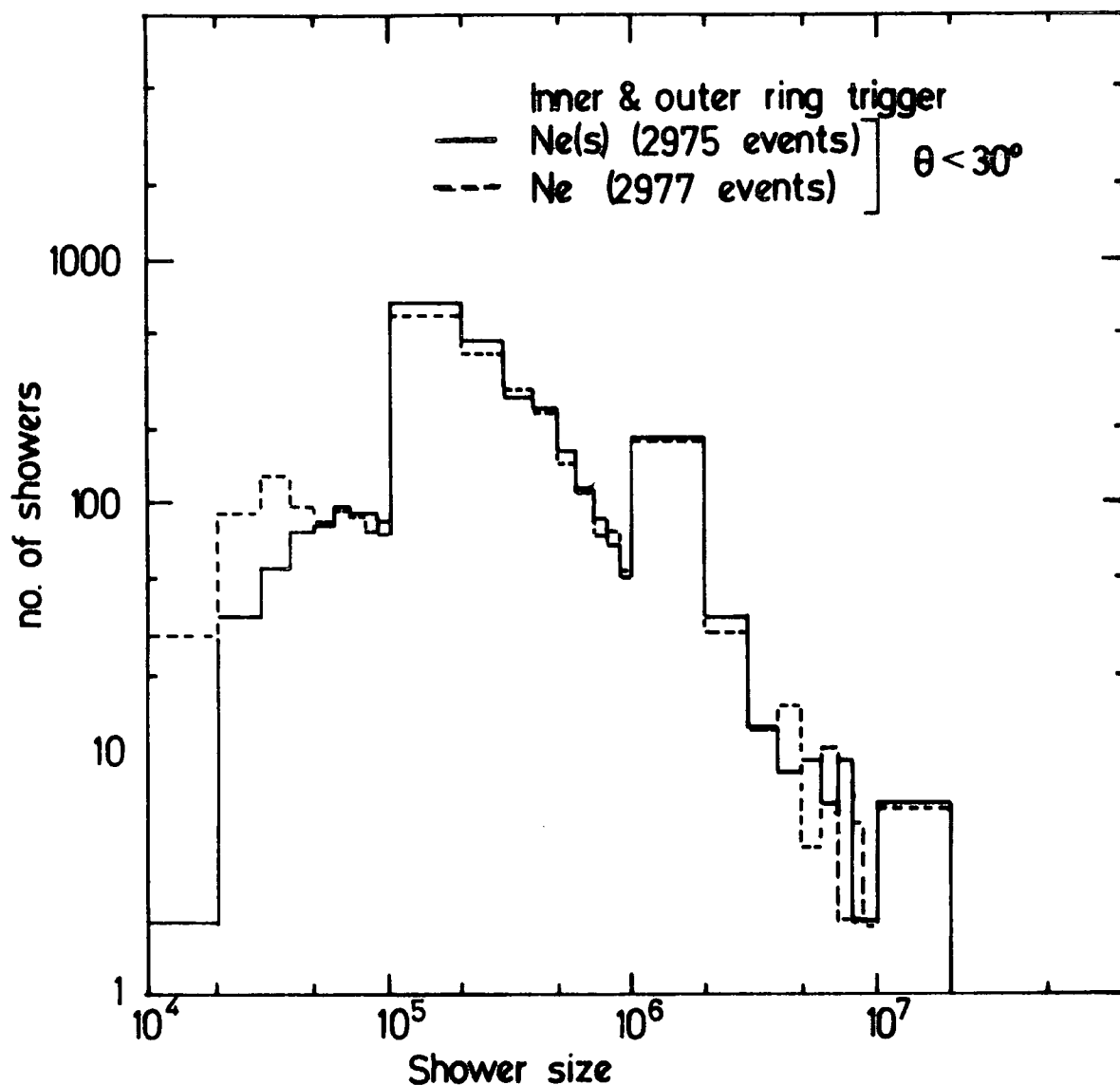
Figure 5.8 : A comparison of the measured distributions
of shower size N_e and N_e (s) for showers
with zenith angles of less than 30^0 used in
the determination of the size spectrum. Two
events (not plotted in the histogram) have
$N_e(s) = 7.10^3$ and 9.10^3 particles.
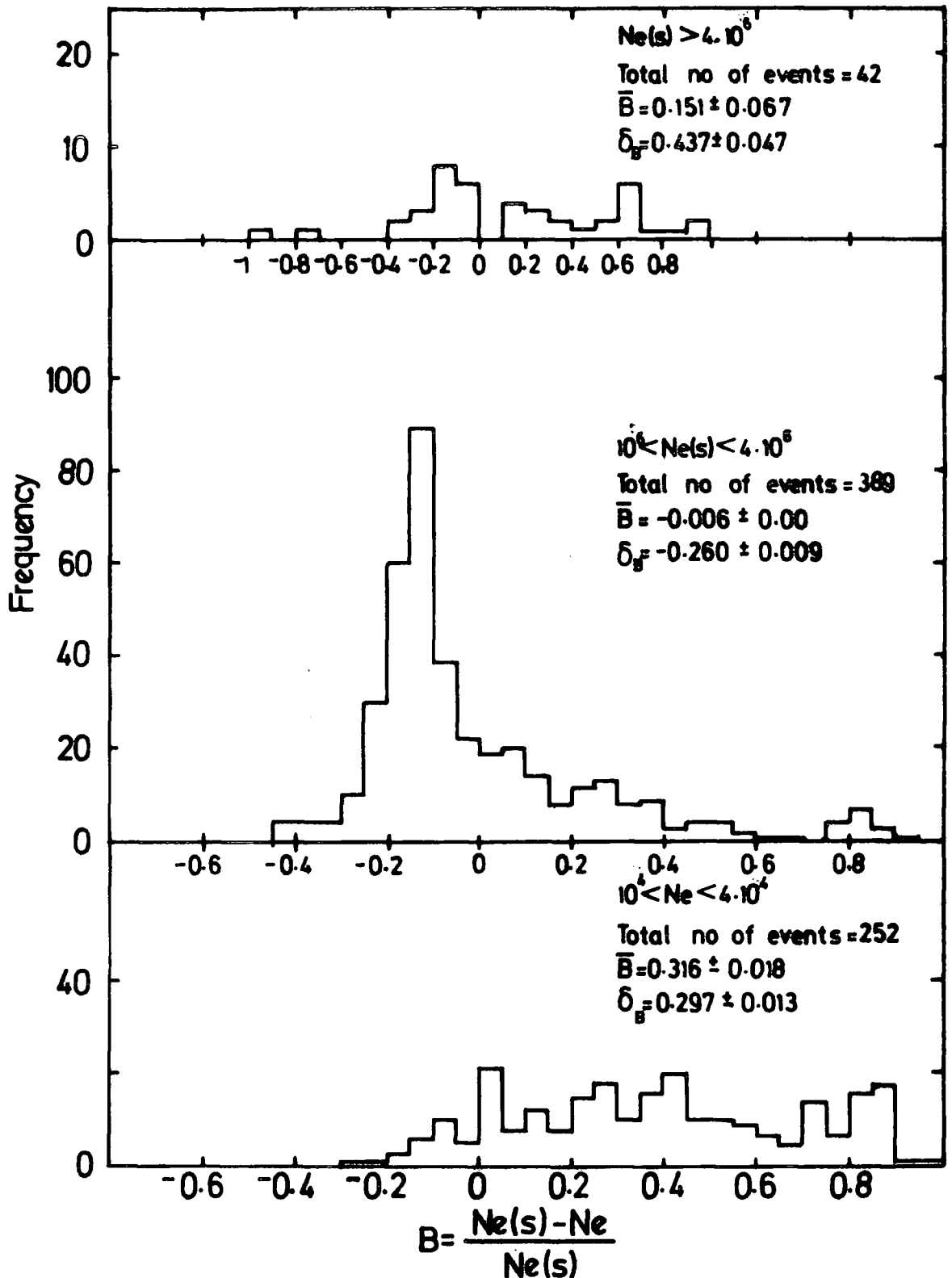
Figure 5.9 : The fractional difference between the correct shower size, $N_e(s)$ taking the age parameter of individual showers into account and the shower size N_e determined assuming all showers obey the Catz average electron structure function for showers in different size ranges.

The plot is labeled with:

$Ne(s) < 10^6$
total no. of events=486
$\bar{B} = -0.030 \pm 0.008$
$\delta_B = 0.190 \pm 0.006$

The y-axis is labeled "Frequency" with values 20, 40, 60, 80, 100, 120, 140.

The x-axis is labeled $B = \dfrac{Ne(s) - Ne}{Ne(s)}$ with values -0.8, -0.6, -0.4, -0.2, 0, 0.2, 0.4, 0.6, 0.8.
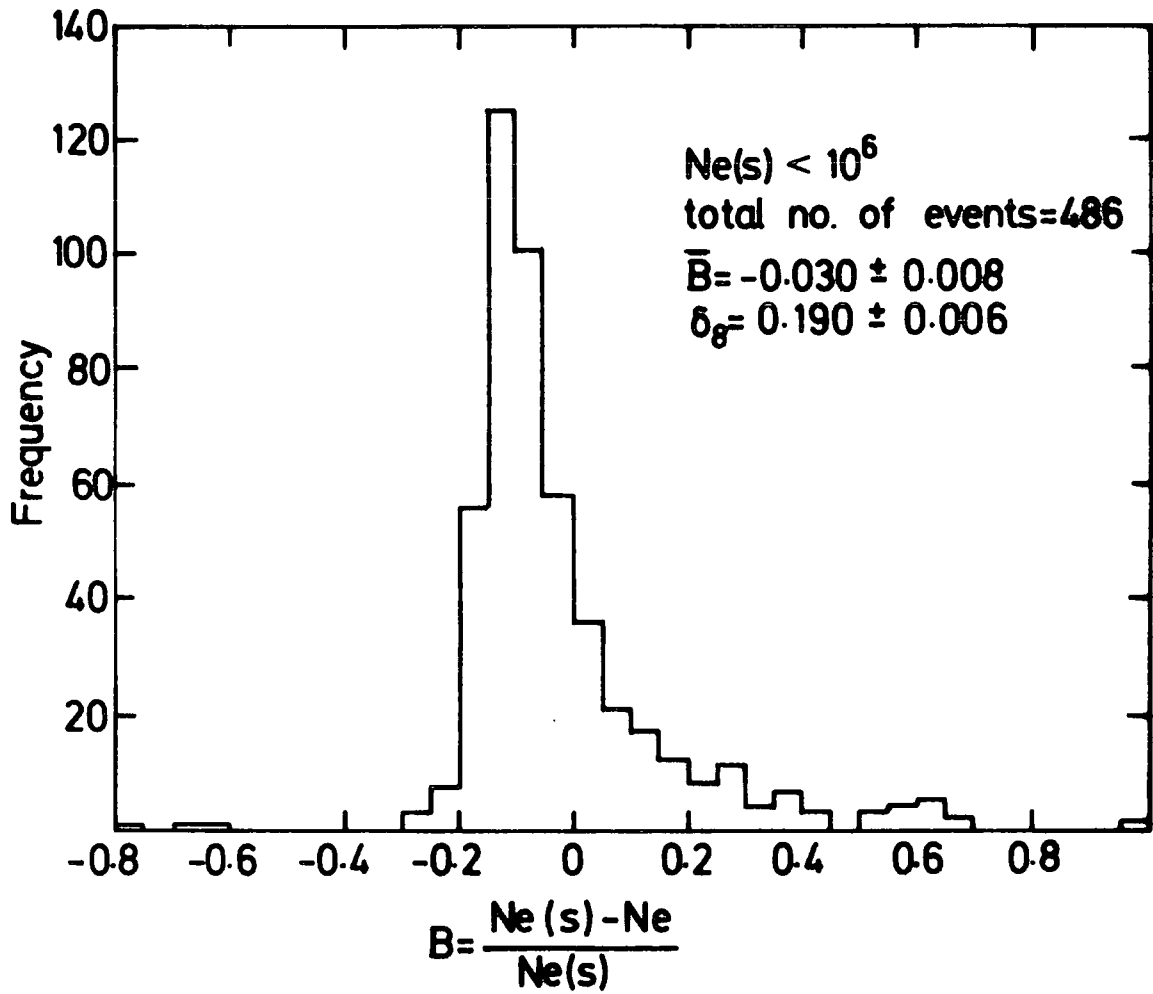
Figure 5.10:   The fractional difference between $N_e(s)$
and N_e for showers in the size range of
less than 10^6 particles.
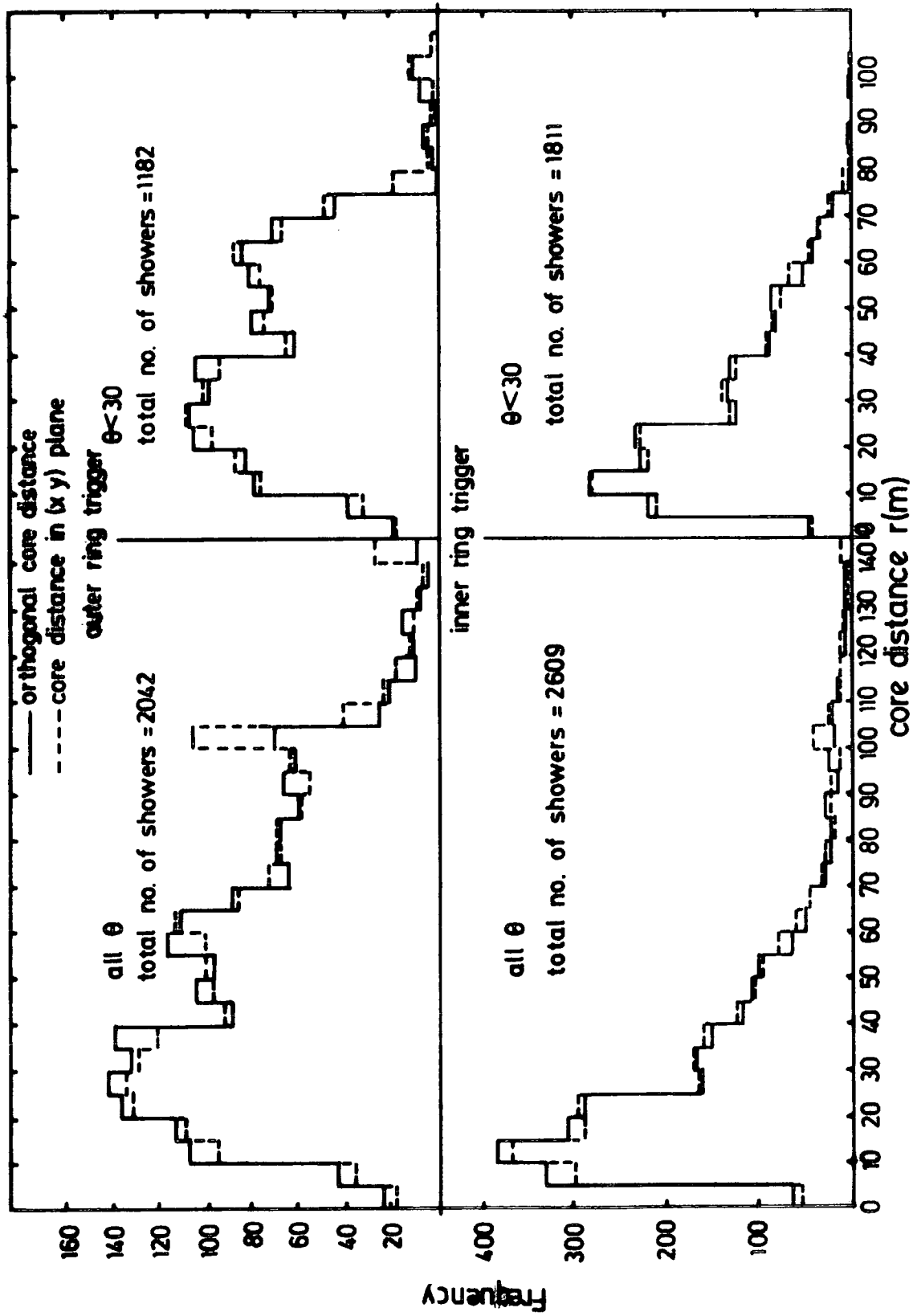
Figure 5.11 : A comparison between orthogonal and (x,y) plane core distances from the central detector C.
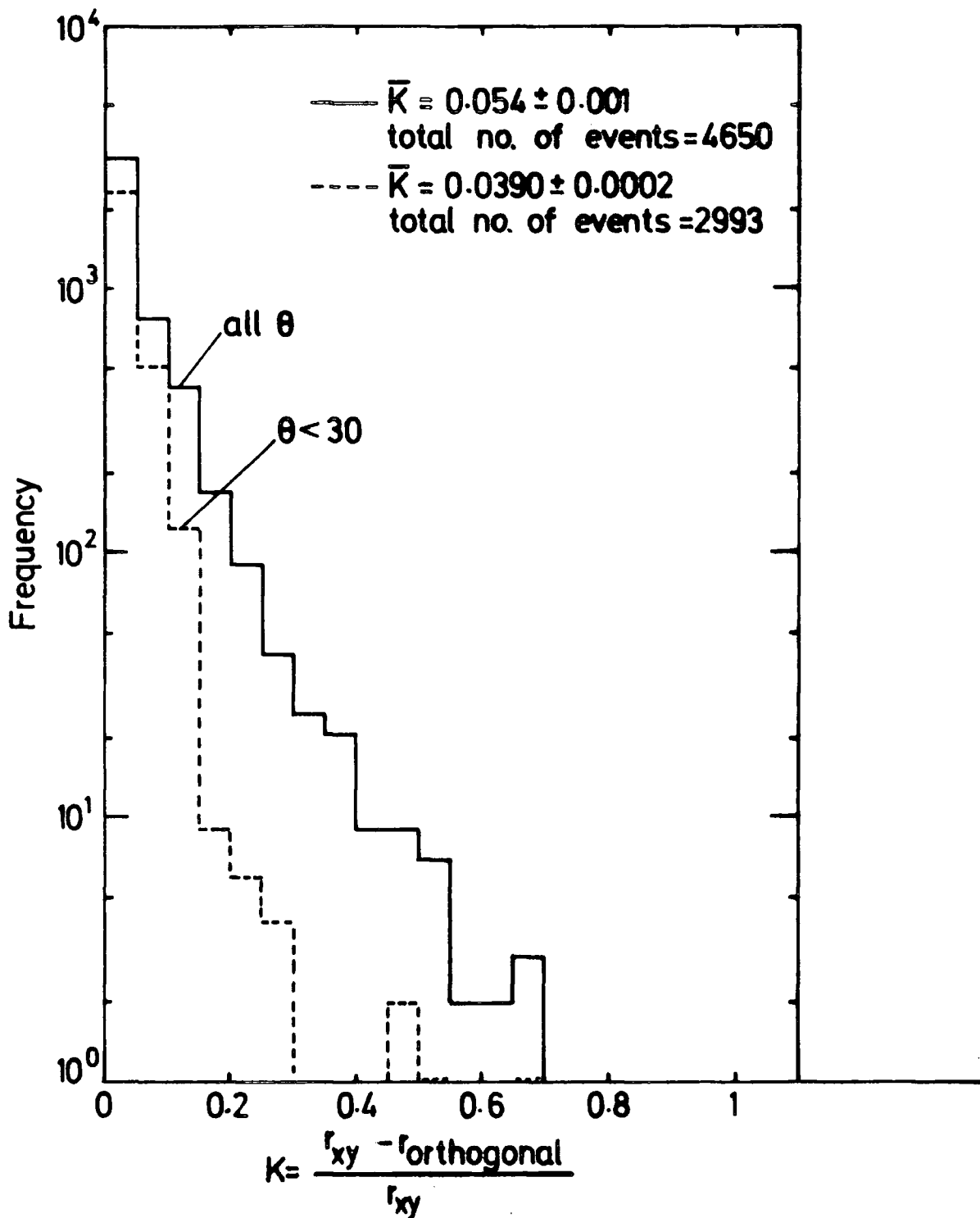
Figure 5.12 : The fractional difference between the orthogonal and (x,y) plane core distances from the central detector C for all the showers and those with zenith angle less than 30°.

In determining the size spectrum the dependence of collecting area on shower age is of importance. For showers with zenith angle less than 30°, the data was grouped into approximately three equinumber ranges of age parameter with mean ages of s = 0.95, 1.2 and 1.45, where each age range was subgrouped into three zenith angle ranges of $0-10^O$, $10-20^O$ and $20-30^O$ with mean zenith angles 5°, 15°, 25°. An example of collecting areas for vertical showers with different values of age are shown in Figures 5.13 and 5.14. The dependence of collecting area on shower size for vertically incident showers with different age parameter is shown in Figure 5.15 for the inner and outer ring triggers. The dependence on zenith angle θ is shown in Figures 5.16 to 5.18. Figure 5.19 shows that for vertical showers, on average, variation of collecting area with size does not depend strongly on the assumed electron lateral structure function. The structure functions considered are the structure function relevant to the age parameter of individual showers, the Catz and the Greisen structure function.

To obtain the vertical differential size spectrum $R(N,0)$ from the experimental data it was assumed that the differential size spectrum at zenith angle θ is given by ;

$$R(N,\theta) = R(N,0) \cos^n\theta \quad m^{-2} \ s^{-1} \ st^{-1}/\text{unit N}$$

The number of showers X of size N/unit N traversing a collectting area $A(\theta)$ in the horizontal plane in time t that have

Ne = 3·10⁵ particles
Vertical shower

33

S=1.45
S=1.2
S=0.95

×C

53

13

20m
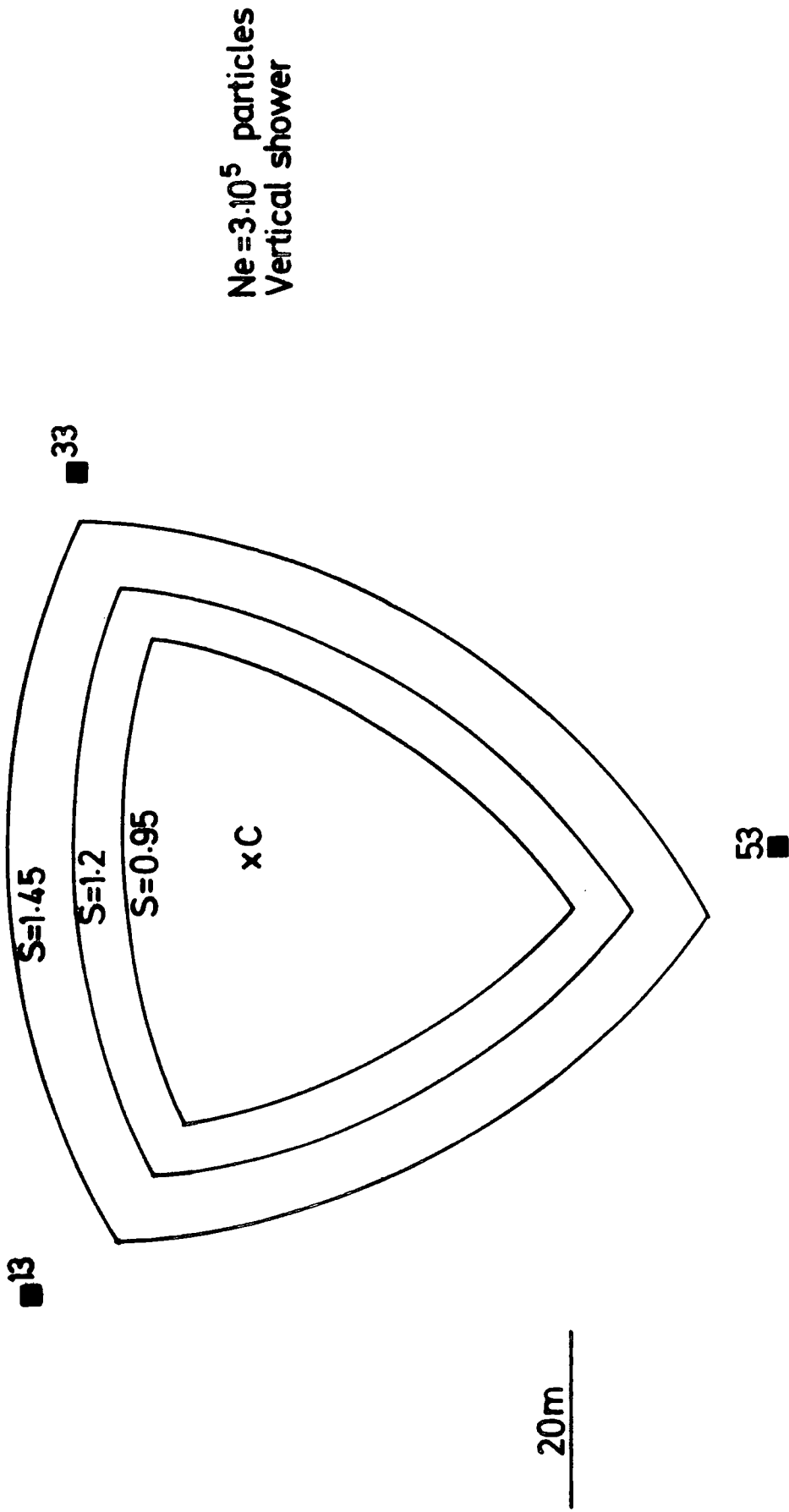
Figure 5.13 : An example of the variation of acceptance area of showers with size 3.10^5 particles for different values of the shower age parameter.

S=1.2

S=1.45

S=0.95

■C

Ne=2.10^5 particles
Vertical shower

20m

53
■
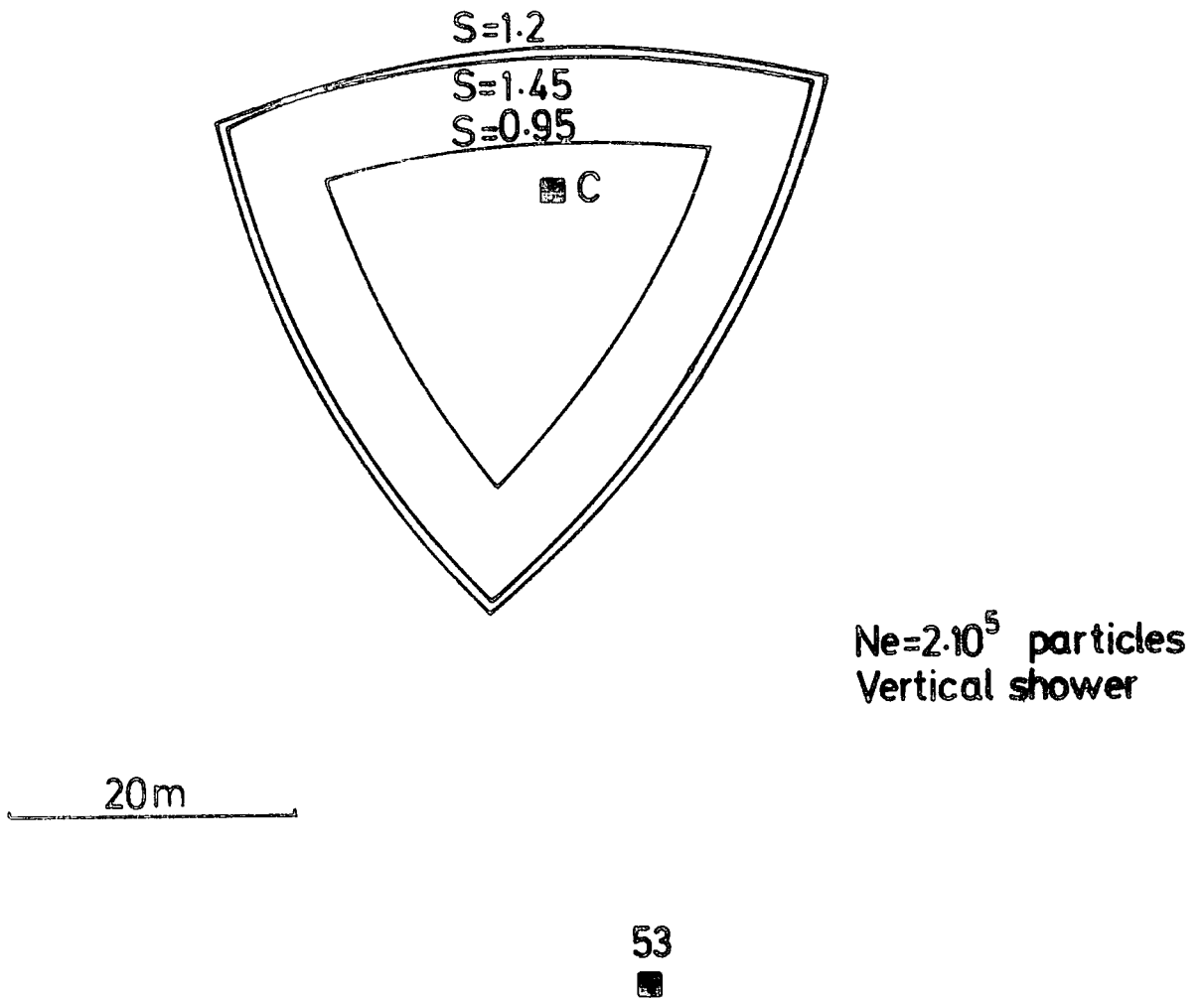
Figure 5.14 : An example of the variation of acceptance area

of showers with size 2.10^5 particles for

different values of the shower age parameter.
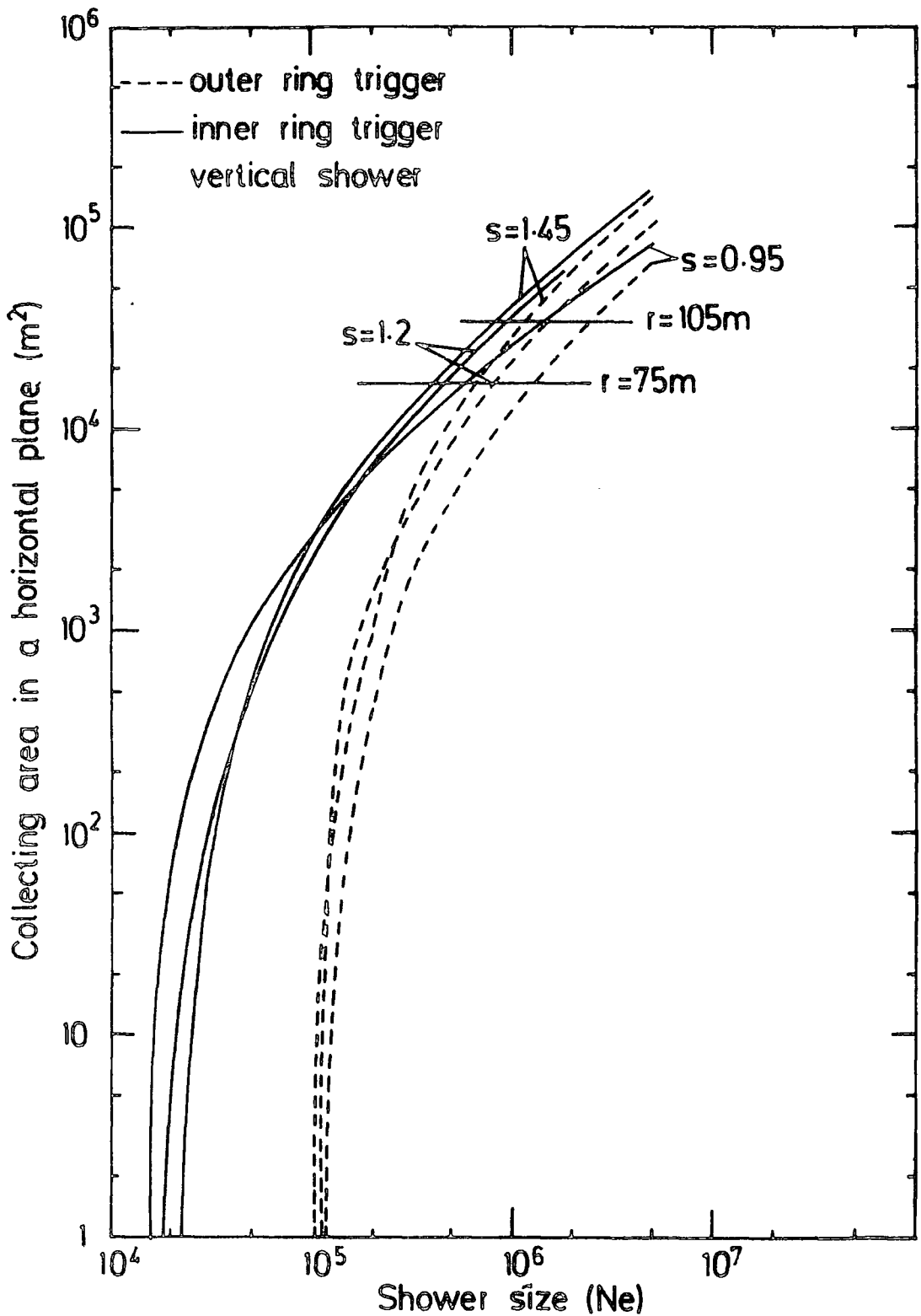
Figure 5.15 : Dependence of collecting area on shower size
for vertically incident showers with different
age parameter for the inner and outer ring
triggers. The curve for showers which obey
the Greisen average electron structure function
has s = 1.25 and is close to the curve labelled
s = 1.20 in the figure.
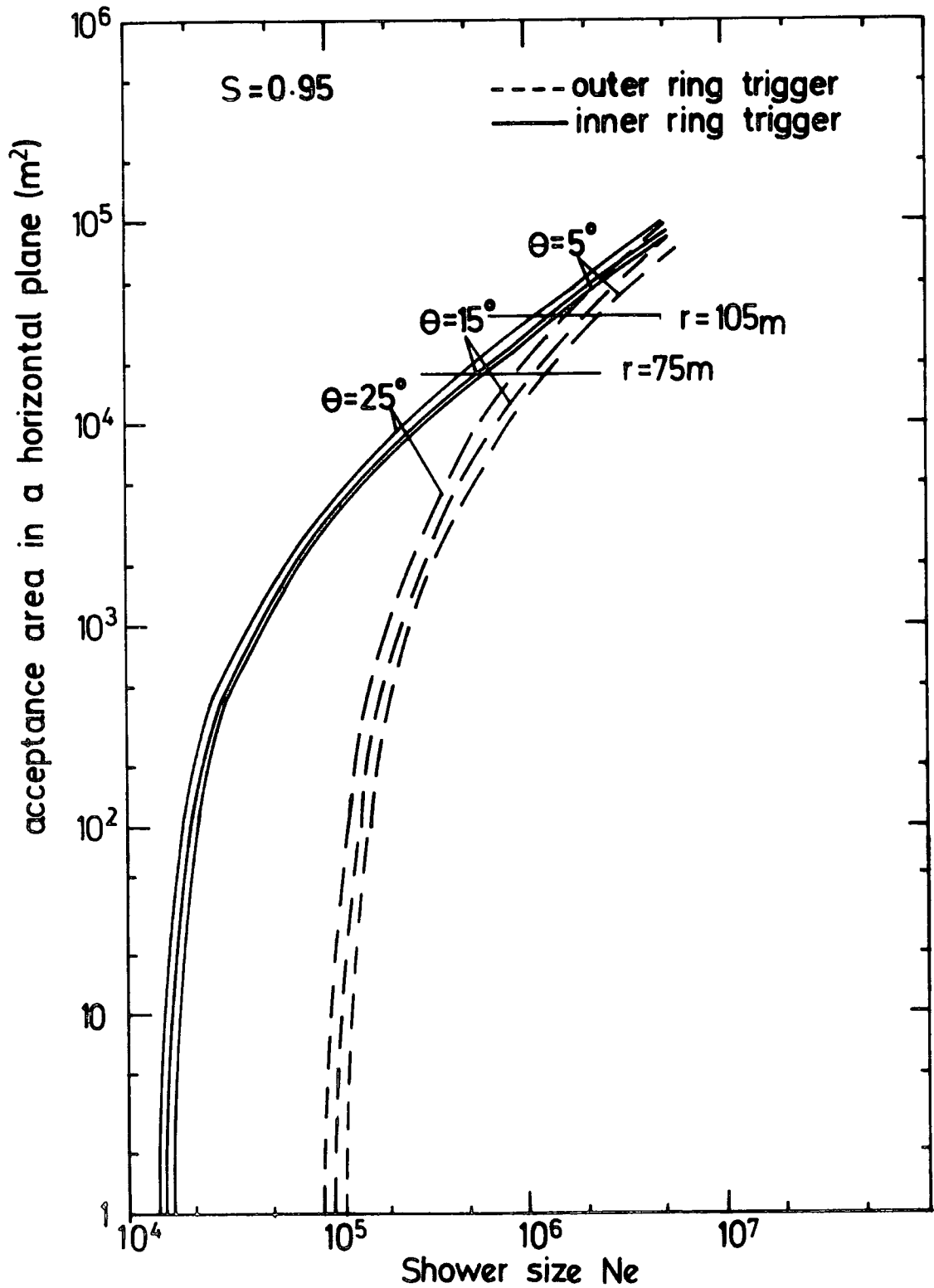
Figure 5.16 : The dependence of collecting area on shower size for showers with age parameter s = 0.95 and different values of zenith angle.
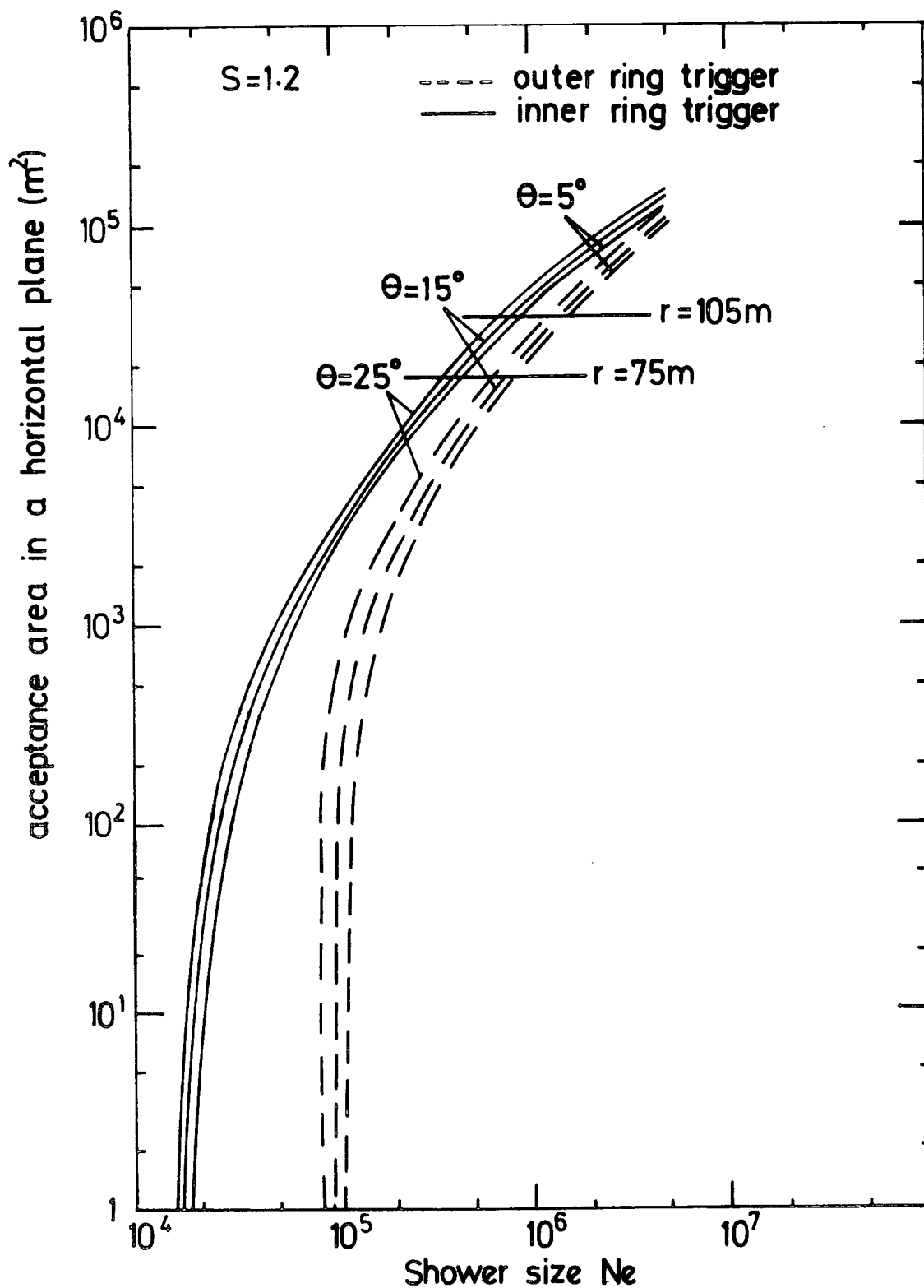
figure 5.17 : The dependence of collecting area on shower size for showers with age parameter s = 1.2 and different values of zenith angle.
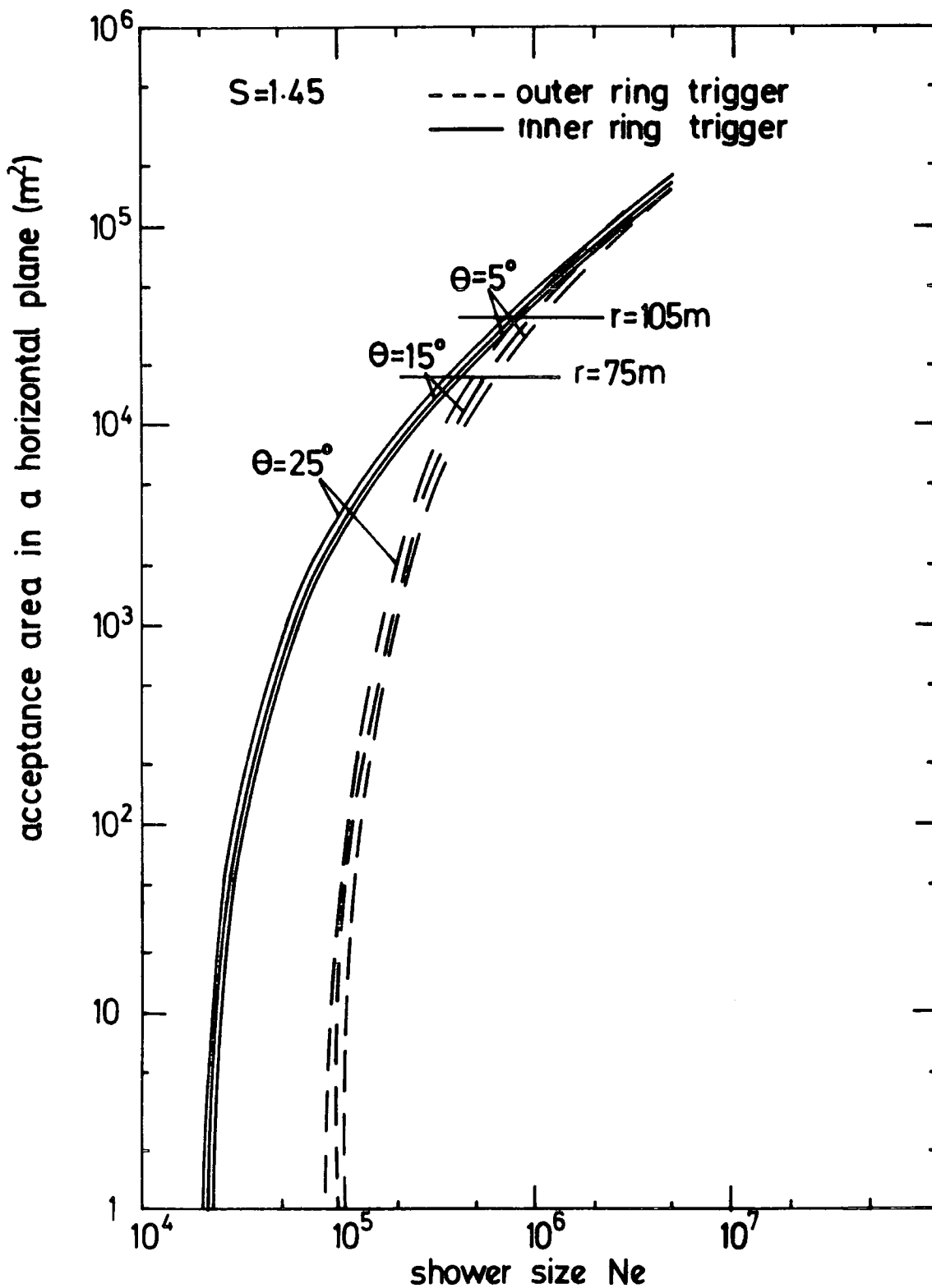
Figure 5.18 : The dependence of collecting area on shower
size for showers with age parameter s = 1.45
and different values of zenith angle.
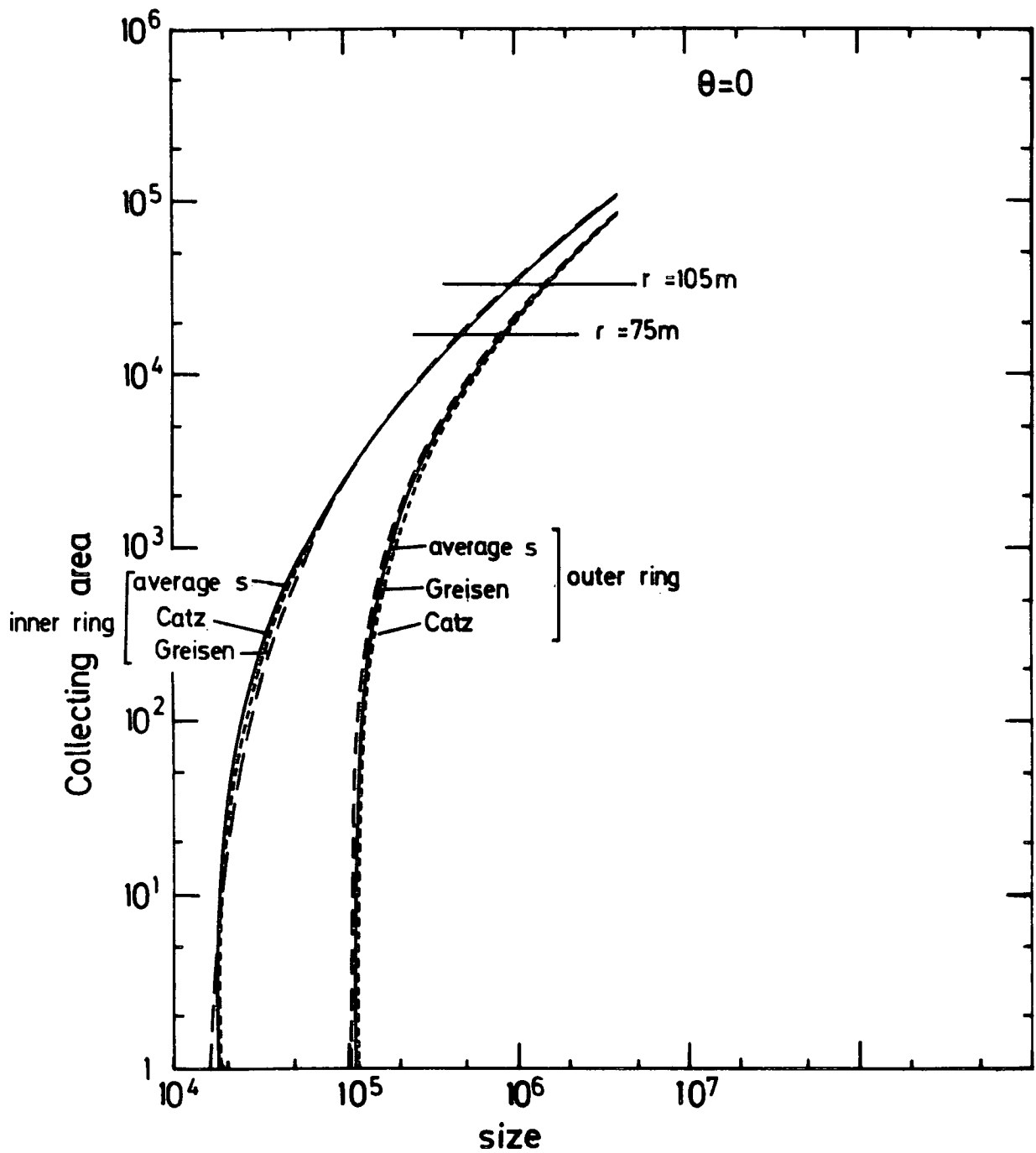
Figure 5.19 : Collecting area-shower size dependence for vertically incident showers with different average electron lateral structure functions.

zenith angle θ is given by

$$X = \int_0^\theta R(N,\theta) \cdot A(\theta) \cos\theta \cdot t \cdot 2\pi\sin\theta d\theta$$

from which $R(N,0) = \dfrac{X}{t \cdot 2\pi \int_0^\theta A(\theta) \cos^{n+1}\theta \sin\theta \, d\theta}$ \hfill (5.5)

Using the shower size and age dependence of $A(\theta)$ obtained from the curves of Figures 5.16 to 5.18 and using $n = 8.0$ and 8.5 for the inner and outer ring triggers, equation 5.5 was evaluated for showers in the three stated age parameter ranges. Adding the three resulting rates together gives the total differential rates of showers of N/unit N incident vertically at sea level. This was done when $N_e(s)$ and N_e were used for showers with zenith angle less than 30°. For near vertical showers, when $A(\theta) = A = $ a constant, equation 5.5 becomes

$$R(N,0) = \dfrac{X}{t + 2\pi \cdot A \left\{ \dfrac{1 - \cos^{n+2}\theta}{n+2} \right\}}$$

5.3.5 The Results and Conclusion

The size spectrum determined assuming all showers obey the same Catz electron structure function and using the resulting N_e sizes is given in Table 5.2a. To be more precise, in determining the size spectrum, the age parameter of the individual showers has been taken into account and the resulting size spectrum using $N_e(s)$ for three stated ranges of age parameter has been found. The result for each range of age and the total result as a final size spectrum are

given in Tables 5.2b to 5.2f. The results are plotted in Figures 5.20 and 5.21 where the work of Hillas (1970), Curve a and Parvaresh (1975), Curve b, are also plotted for comparison. From these figures it is seen that apart from very small and large sizes the size spectrum obtained using $N_e(s)$ is consistent with the previous work of Parvaresh and also with the spectra obtained using N_e. The result for the integral size spectrum is shown in Figures 5.22 and 5.23 where it is compared with some recent measurements (Catz et al, 1975, Ashton et al, 1979a, Crouch et al, 1980). The significant rate difference at small sizes ($<4.10^4$) shown in Figure 5.22, is due to a loss of showers with large age parameter since the minimum size of a shower of all ages to trigger the inner ring trigger is $> 7.10^4$ particles (see Figure 5.3). The difference at large sizes $> 10^7$ particles is due to an increase of age parameter with shower size which results in a larger average size when individual shower ages are taken into account than when an average electron structure function is assumed.

Size Range	Core distance range	$\bar{N}$	Inner ring	Outer ring	inner and outer ring triggers	Inner ring	Outer ring	Inner ring (unit N^{-1})	Outer ring (unit N^{-1})	ring triggers
$(2-3)10^4$	<75m	$2.5.10^4$	92		92	$4.4.10^1$		$6.56.10^{10}$		$(3.45 \pm 0.19)10^{10}$
$(3-4)10^4$		$3.5.10^4$	131		131	2.10^2		$2.73.10^{10}$		
$(4-5)10^4$		$4.5.10^4$	97		97	$3.8.10^2$		$1.07.10^{10}$		
$(5-6)10^4$		$5.5.10^4$	84		84	7.10^2		$5.47.10^{11}$		$(4.85 \pm 0.36)10^{11}$
$(6-7)10^4$		$6.5.10^4$	94		94	$1.02.10^3$		$4.24.10^{11}$		
$(7-8)10^4$		$7.5.10^4$	81		81	$1.3.10^3$		$2.83.10^{11}$		$(2.83 \pm 0.31)10^{11}$
$(8-9)10^4$		$8.5.10^4$	77		77	$1.6.10^3$		$2.31.10^{11}$		$(2.03 \pm 0.17)10^{-11}$
$(9-10)10^4$		$9.5.10^4$	65		65	$1.95.10^3$		$1.75.10^{11}$		
$(1-2)10^5$		$1.5.10^5$	408	168	576	$3.9.10^3$	$5.4.10^2$	$5.48.10^{12}$	$4.4.10^{12}$	$(5.16 \pm 0.22)10^{12}$
$(2-3)10^5$		$2.5.10^5$	237	175	413	$7.6.10^3$	$2.2.10^3$	$1.67.10^{12}$	$1.43.10^{12}$	$(1.56 \pm 0.08)10^{12}$
$(3-4)10^5$		$3.5.10^5$	118	176	294	$1.3.10^4$	$4.3.10^3$	5.10^{-13}	7.10^{13}	$(6.20 \pm 0.36)10^{13}$
$(4-5)10^5$		$4.5.10^5$	74	158	233	$1.65.10^4$	$6.6.10^3$	$2.50.10^{13}$	$4.7.10^{13}$	$(3.98 \pm 0.26)10^{13}$
$(5-6)10^5$		$5.5.10^5$	42	107	149	$1.76.10^4$	$9.1.10^3$	$1.42.10^{13}$	$1.65.10^{13}$	$(1.58 \pm 0.13)10^{13}$
$(6-7)10^5$		$6.5.10^5$	36	75	111	$1.76.10^4$	$1.17.10^4$	$1.21.10^{13}$	$1.15.10^{13}$	$(9.93 \pm 0.73)10^{-14}$
$(7-8)10^5$		$7.5.10^5$	28	46	74	$1.76.10^4$	$1.45.10^4$	$9.9.10^{-14}$	$7.1.10^{-14}$	
$(8-9)10^5$		$8.5.10^5$	27	50	77	$1.76.10^4$	$1.7.10^4$	$9.06.10^{-14}$	$7.5.10^{-14}$	$(6.8 \pm 0.60)10^{-14}$
$(9-10)10^5$		$9.5.10^5$	18	35	53	$1.76.10^4$	$1.76.10^4$	$6.11.10^{-14}$	$5.3.10^{-14}$	
$(1-2)10^6$		$1.5.10^6$	48	134	182	$1.76.10^4$	$1.76.10^4$	$1.69.10^{-14}$	$2.06.10^{-14}$	$(1.96 \pm 0.14)10^{-14}$
$(2-3)10^6$		$2.5.10^6$	14	16	30	$1.76.10^4$	$1.76.10^4$	$4.7.10^{-15}$	$2.6.10^{-15}$	$(3.58 \pm 0.65)10^{-15}$
$(3-4)10^6$	<75m	$3.5.10^6$	3	9	12	$1.76.10^4$	$1.76.10^4$	$1.06.10^{-15}$	$1.7.10^{-15}$	$(1.54 \pm 0.44)10^{-15}$
$(4-7)10^6$	<105m	$5.5.10^6$	3	26	29	$3.46.10^4$	$3.46.10^4$	$9.39.10^{-16}$	$4.68.1.10^{-16}$	$(5.16 \pm 0.95)10^{-16}$
$(0.7-2)10^7$	<105m	$1.1.10^7$	4	11	15	$3.46.10^4$	$3.46.10^4$	$1.25.10^{-16}$	$9.92.10^{-17}$	$(1.06 \pm 0.27)10^{-16}$
			1782	1186	2968					

TABLE 5.2a : Differential size spectrum of showers with θ <30° assuming all showers obey the Catz average electron lateral structure function.

Size Range	Core distance range	$\bar{N}$	Catz No.of showers with θ <30	N.K.G. No. of Showers in S Range						Inner & Outer ring used for all S
				0.6<S<1.1		1.1<S<1.3		1.3<S<1.8		
				Inner ring	Outer ring	Inner ring	Outer ring	Inner ring	Outer ring	
$(2-3)10^4$	<75	$2.5.10^4$	92	25		9		1		35
$(3-4)10^4$		$3.5.10^4$	131	36		14		4		54
$(4-5)10^4$		$4.5.10^4$	97	38		23		17		78
$(5-6)10^4$		$5.5.10^4$	84	39		24		18		81
$(6-7)10^4$		$6.5.10^4$	94	50		23		23		96
$(7-8)10^4$		$7.5.10^4$	81	41		18		19		78
$(8-9)10^4$		$8.5.10^4$	77	38		27		26		91
$(9-10)10^4$		$9.5.10^4$	65	34		29		13		76
$(1-2)10^5$		$1.5.10^5$	576	185	54	155	73	168	36	671
$(2-3)10^5$		$2.5.10^5$	413	97	50	88	85	94	44	458
$(3-4)10^5$		$3.5.10^5$	294	46	38	33	80	30	45	272
$(4-5)10^5$		$4.5.10^5$	233	33	33	35	78	27	37	243
$(5-6)10^5$		$5.5.10^5$	149	20	29	23	53	11	30	166
$(6-7)10^5$		$6.5.10^5$	111	12	20	17	33	8	27	117
$(7-8)10^5$		$7.5.10^5$	74	9	13	11	31	6	17	87
$(8-9)10^5$		$8.5.10^5$	77	9	8	11	22	9	8	67
$(9-10)10^5$		$9.5.10^5$	53	4	7	8	20	2	9	50
$(1-2)10^6$		$1.5.10^6$	182	12	39	23	58	13	39	184
$(2-3)10^6$		$2.5.10^6$	30	2	9	3	9	6	6	35
$(3-4)10^6$	<75	$3.5.10^6$	12	0	4	2	3	1	2	12
$(4-7)10^6$	<105	$5.8.10^6$	29	2	6	1	5	1	8	23
$(0.7-2)10^7$	<105	$1.01.10^7$	15	1	4	1	2	3	8	19
										2993

TABLE 5.2b :   The number of showers in different ranges of shower size assuming
(1) all showers obey the Catz electron structure function and
(2) taking the age parameter of individual showers into account.

Range	Core dist. range		Inner ring	Outer ring	Total	Inner ring	Outer ring	Inner ring	Outer ring	outer ring triggers $m^{-2} sec^{-1} st^{-1}$ unit N^{-1}
$(2-3)10^4$		$2.5.10^4$	25		25	$2.2.10^2$		$4.4.10^{-11}$		$(4.4 \pm 0.88)10^{-11}$
$(3-4)10^4$	< 75	$3.5.10^4$	36		36	$5.4.10^2$		$2.92.10^{-11}$		$(2.92 \pm 0.48)10^{-11}$
$(4-5)10^4$		$4.5.10^4$	38		38	$8.9.10^2$		$2.02.10^{-11}$		$(2.02 \pm 0.32)10^{-11}$
$(5-6)10^4$		$5.5.10^4$	39		39	$1.27.10^3$		$1.62.10^{-11}$		$(1.62 \pm 0.26)10^{-11}$
$(6-7)10^4$		$6.5.10^4$	50		50	$1.65.10^3$		$1.62.10^{-11}$		$(1.63 \pm 0.23)10^{-11}$
$(7-8)10^4$		$7.5.10^4$	41		41	$2.07.10^3$		$9.4.10^{-12}$		$(9.40 \pm 1.46)10^{-12}$
$(8-9)10^4$		$8.5.10^4$	38		38	$2.45.10^3$		$8.12.10^{-12}$		$(8.12 \pm 1.31)10^{-12}$
$(9-10)10^4$		$9.5.10^4$	34		34	$2.85.10^3$		$6.39.10^{-12}$		$(6.39 \pm 1.09)10^{-12}$
$(1-2)10^5$		$1.5.10^5$	185	54	239	5.10^3	8.10^1	$2.04.10^{-12}$	7.10^{-12}	$(3.1 \pm 0.2)10^{-12}$
$(2-3)10^5$		$2.5.10^5$	97	50	147	$8.3.10^3$	10^3	$6.13.10^{-13}$	$9.6.10^{-13}$	$(7.31 \pm 0.60)10^{-13}$
$(3-4)10^5$		$3.5.10^5$	46	38	84	$1.1.10^4$	$2.35.10^3$	$2.27.10^{-13}$	$3.2.10^{-13}$	$(2.69 \pm 0.29)10^{-13}$
$(4-5)10^5$		$4.5.10^5$	33	33	66	$1.35.10^4$	$3.8.10^3$	$1.38.10^{-13}$	$1.92.10^{-13}$	$(1.65 \pm 0.2)10^{-13}$
$(5-6)10^5$		$5.5.10^5$	20	29	49	$1.6.10^4$	$5.4.10^3$	$6.77.10^{-14}$	$1.15.10^{-13}$	$(9.57 \pm 1.37)10^{-14}$
$(6-7)10^5$		$6.5.10^5$	12	20	32	$1.76.10^4$	7.10^3	$4.53.10^{-14}$	$5.98.10^{-14}$	$(5.43 \pm 0.96)10^{-14}$
$(7-8)10^5$		$7.5.10^5$	9	13	22	$1.76.10^4$	$8.6.10^3$	$3.20.10^{-14}$	$3.11.10^{-14}$	$(3.14 \pm 0.67)10^{-14}$
$(8-9)10^5$		$8.5.10^5$	9	8	17	$1.76.10^4$	$1.05.10^4$	$3.15.10^{-14}$	$1.57.10^{-14}$	$(2.41 \pm 0.58)10^{-14}$
$(9-10)10^5$		$9.5.10^5$	4	7	11	$1.76.10^4$	$1.25.10^4$	$1.25.10^{-14}$	$1.41.10^{-14}$	$(1.35 \pm 0.41)10^{-14}$
$(1-2)10^6$		$1.5.10^6$	12	39	51	$1.76.10^4$	$1.76.10^4$	$4.14.10^{-15}$	$5.7.10^{-15}$	$(5.33 \pm 0.74)10^{-15}$
$(2-3)10^6$	< 75	$2.5.10^6$	2	9	11	$1.76.10^4$	$1.76.10^4$	$7.56.10^{-16}$	$1.22.10^{-15}$	$(1.13 \pm 0.34)10^{-15}$
$(3-4)10^6$		$3.5.10^6$	0	4	4	$1.76.10^4$	$1.76.10^4$	0	$5.92.10^{-16}$	$(5.92 \pm 2.96)10^{-16}$
$(4-7)10^6$	<105	$6.2.10^6$	2	6	8	$1.76.10^4$	$3.46.10^4$	10^{-16}	$1.22.10^{-16}$	$(1.16 \pm 0.41)10^{-16}$
$(0.7-2)10^7$	<105	$1.1.10^7$	1	4	5	$1.76.10^4$	$3.46.10^4$	$1.75.10^{-17}$	$2.9.10^{-17}$	$(2.67 \pm 1.19)10^{-17}$

TABLE 5.2c : Differential size spectrum of showers with $\theta < 30^\circ$ and $0.6 < S < 1.1$

Range	Co dist		Inner ring	Outer ring	Total ring	Inner ring	Outer ring	Inner ring	Outer ring	$m^{-2}sec^{-1}st^{-1}$ unit N^{-1}
$(2-3)10^4$		$2.5.10^4$	9		9	$4.3.10^1$		$4.36.10^{11}$		$(4.36 \pm 1.45)10^{-11}$
$(3-4)10^4$	< 75	$3.5.10^4$	14		14	$1.8.10^2$		$2.32.10^{11}$		$(2.32 \pm 0.62)10^{-11}$
$(4-5)10^4$		$4.5.10^4$	23		23	$3.8.10^2$		$2.24.10^{11}$		$(2.24 \pm 0.49)10^{-11}$
$(5-6)10^4$		$5.5.10^4$	24		24	7.10^2		$1.34.10^{11}$		$(1.34 \pm 0.27)10^{-11}$
$(6-7)10^4$		$6.5.10^4$	23		23	$1.02.10^3$		$9.8.10^{-12}$		$(9.8 \pm 2.04)10^{-12}$
$(7-8)10^4$		$7.5.10^4$	18		18	$1.3.10^3$		$6.04.10^{-12}$		$(6.04 \pm 1.42)10^{-12}$
$(8-9)10^4$		$8.5.10^4$	27		27	$1.6.10^3$		$6.91.10^{-12}$		$(6.91 \pm 1.32)10^{-12}$
$(9-10)10^4$		$9.5.10^4$	29		29	$1.95.10^3$		$7.14.10^{-12}$		$(7.14 \pm 1.31)10^{-12}$
$(1-2)10^5$		$1.5.10^5$	154	73	227	9.10^3	$5.4.10^2$	$1.90.10^{12}$	$1.73.10^{-12}$	$(1.84 \pm 0.12)10^{-12}$
$(2-3)10^5$		$2.5.10^5$	88	85	173	$7.6.10^3$	$2.35.10^3$	$5.6.10^{-13}$	$6.62.10^{-13}$	$(6.1 \pm 0.47)10^{-13}$
$(3-4)10^5$		$3.5.10^5$	33	80	113	$1.3.10^4$	$4.6.10^3$	$1.38.10^{-13}$	$3.4.10^{-13}$	$(2.81 \pm 0.26)10^{-13}$
$(4-5)10^5$		$4.5.10^5$	35	78	113	$1.65.10^4$	7.10^3	$1.18.10^{-13}$	$2.2.10^{-13}$	$(1.88 \pm 0.17)10^{-13}$
$(5-6)10^5$		$5.5.10^5$	23	53	76	$1.76.10^4$	$9.7.10^3$	$7.8.10^{-14}$	$1.13.10^{-13}$	$(1.02 \pm 0.12)10^{-13}$
$(6-7)10^5$		$6.5.10^5$	17	33	50	$1.76.10^4$	$1.24.10^4$	$5.44.10^{-14}$	$5.82.10^{-14}$	$(5.69 \pm 0.81)10^{-14}$
$(7-8)10^5$		$7.5.10^5$	11	31	42	$1.76.10^4$	$1.5.10^4$	$3.56.10^{-14}$	$4.93.10^{-14}$	$(4.57 \pm 0.71)10^{-14}$
$(8-9)10^5$		$8.5.10^5$	11	22	33	$1.76.10^4$	$1.7.10^4$	$3.43.10^{-14}$	$3.32.10^{-14}$	$(3.35 \pm 0.58)10^{-14}$
$(9-10)10^5$		$9.5.10^5$	8	20	28	$1.76.10^4$	$1.7.10^4$	$2.62.10^{-14}$	$2.96.10^{-14}$	$(2.86 \pm 0.54)10^{-14}$
$(1-2)10^6$		$1.5.10^6$	23	58	81	$1.76.10^4$	$1.7.10^4$	$7.57.10^{-15}$	$7.05.10^{-15}$	$(7.19 \pm 0.80)10^{-15}$
$(2-3)10^6$		$2.5.10^6$	3	9	12	$1.76.10^4$	$1.7.10^4$	$1.05.10^{-15}$	$1.27.10^{-15}$	$(1.21 \pm 0.35)10^{-15}$
$(3-4)10^6$	< 75	$3.5.10^6$	2	3	5	$1.76.10^4$	$1.7.10^4$	$6.2.10^{-16}$	$4.56.10^{-16}$	$(5.21 \pm 2.32)10^{-16}$
$(4-7)10^6$	<105	$5.5.10^6$	1	5	6	$3.46.10^4$	$3.46.10^4$	5.10^{-17}	$5.6.10^{-17}$	$(5.50 \pm 2.24)10^{-17}$
$(o.7-2)10^7$	<105	$8.5.10^6$	1	2	3	$3.46.10^4$	$3.46.10^4$	$3.75.10^{-17}$	$2.6.10^{-17}$	$(2.98 \pm 1.72)10^{-17}$

TABLE 5.2d : Differential size spectrum of showers with $\theta < 30^o$ and $1.1 < s < 1.3$

range	$\bar{N}$	Core distance range	Inner ring	Outer ring	Total ring	Inner ring	Outer ring	Inner ring	Outer ring	Outer ring triggers $m^{-2} sec^{-1} st^{-1}$ unit N^{-1}
$(2-3)10^4$	$2.5 \cdot 10^4$		1		1	8		$4.53 \cdot 10^{-11}$		$(4.53 \pm 4.53)10^{-11}$
$(3-4)10^4$	$3.5 \cdot 10^4$	<75	4		4	$1.3 \cdot 10^2$		$1.53 \cdot 10^{-11}$		$(1.53 \pm 0.76)10^{-11}$
$(4-5)10^4$	$4.5 \cdot 10^4$		17		17	$3.5 \cdot 10^2$		$2.04 \cdot 10^{-11}$		$(2.04 \pm 0.49)10^{-11}$
$(5-6)10^4$	$5.5 \cdot 10^4$		18		18	$6.4 \cdot 10^2$		$1.19 \cdot 10^{-11}$		$(1.19 \pm 0.28)10^{-11}$
$(6-7)10^4$	$6.5 \cdot 10^4$		23		23	10^3		$8.17 \cdot 10^{-12}$		$(8.17 \pm 1.7)10^{-12}$
$(7-8)10^4$	$7.5 \cdot 10^4$		19		19	$1.4 \cdot 10^3$		$5.73 \cdot 10^{-12}$		$(5.73 \pm 1.35)10^{-12}$
$(8-9)10^4$	$8.5 \cdot 10^4$		26		26	$1.8 \cdot 10^3$		$6.87 \cdot 10^{-12}$		$(6.87 \pm 1.35)10^{-12}$
$(9-10)10^4$	$9.5 \cdot 10^4$		13		13	$2.4 \cdot 10^3$		$2.50 \cdot 10^{-12}$		$(2.50 \pm 0.69)10^{-12}$
$(1-2)10^5$	$1.5 \cdot 10^5$		168	36	204	$5 \cdot 10^3$	$2.4 \cdot 10^2$	$1.72 \cdot 10^{-12}$	$2.54 \cdot 10^{-12}$	$(1.86 \pm 0.13)10^{-12}$
$(2-3)10^5$	$2.5 \cdot 10^5$		94	44	138	$9.7 \cdot 10^3$	$2.15 \cdot 10^3$	$5.05 \cdot 10^{-13}$	$3.37 \cdot 10^{-13}$	$(4.53 \pm 0.38)10^{-13}$
$(3-4)10^5$	$3.5 \cdot 10^5$		30	45	75	$1.4 \cdot 10^4$	$6.25 \cdot 10^3$	$1.06 \cdot 10^{-13}$	$1.48 \cdot 10^{-13}$	$(1.31 \pm 0.15)10^{-13}$
$(4-5)10^5$	$4.5 \cdot 10^5$		27	37	64	$1.76 \cdot 10^4$	10^4	$8.86 \cdot 10^{-14}$	$7.93 \cdot 10^{-14}$	$(8.32 \pm 1.04)10^{-14}$
$(5-6)10^5$	$5.5 \cdot 10^5$		11	30	41	$1.76 \cdot 10^4$	$1.41 \cdot 10^4$	$3.68 \cdot 10^{-14}$	$5 \cdot 10^{-14}$	$(4.64 \pm 0.72)10^{-14}$
$(6-7)10^5$	$6.5 \cdot 10^5$		8	27	35	$1.76 \cdot 10^4$	$1.75 \cdot 10^4$	$2.74 \cdot 10^{-14}$	$3.95 \cdot 10^{-14}$	$(3.67 \pm 0.62)10^{-14}$
$(7-8)10^5$	$7.5 \cdot 10^5$		6	17	23	$1.76 \cdot 10^4$	$1.76 \cdot 10^4$	$1.87 \cdot 10^{-14}$	$2.54 \cdot 10^{-14}$	$(2.36 \pm 0.49)10^{-14}$
$(8-9)10^5$	$8.5 \cdot 10^5$		9	8	17	$1.76 \cdot 10^4$	$1.76 \cdot 10^4$	$2.93 \cdot 10^{-14}$	$1.23 \cdot 10^{-14}$	$(2.13 \pm 0.52)10^{-14}$
$(9-10)10^5$	$9.5 \cdot 10^5$		2	9	11	$1.76 \cdot 10^4$	$1.76 \cdot 10^4$	$6.24 \cdot 10^{-15}$	$1.22 \cdot 10^{-14}$	$(1.11 \pm 0.33)10^{-14}$
$(1-2)10^6$	$1.5 \cdot 10^6$		13	39	52	$1.76 \cdot 10^4$	$1.76 \cdot 10^4$	$4.18 \cdot 10^{-15}$	$5.77 \cdot 10^{-15}$	$(5.37 \pm 0.74)10^{-15}$
$(2-3)10^6$	$2.5 \cdot 10^6$	<75	6	6	12	$1.76 \cdot 10^4$	$1.76 \cdot 10^4$	$1.87 \cdot 10^{-15}$	$8.63 \cdot 10^{-16}$	$(1.36 \pm 0.39)10^{-15}$
$(3-4)10^6$	$3.5 \cdot 10^6$		1	2	3	$1.76 \cdot 10^4$	$1.76 \cdot 10^4$	$3.12 \cdot 10^{-16}$	$2.72 \cdot 10^{-16}$	$(2.85 \pm 1.64)10^{-16}$
$(4-7)10^6$	$5.7 \cdot 10^6$	<105	1	8	9	$3.46 \cdot 10^4$	$3.46 \cdot 10^4$	$6.8 \cdot 10^{-17}$	$1.5 \cdot 10^{-16}$	$(1.4 \pm 0.4)10^{-16}$
$(0.7-2)10^7$	$1.7 \cdot 10^7$	<105	3	8	11	$3.46 \cdot 10^4$	$3.46 \cdot 10^4$	$9.22 \cdot 10^{-17}$	$9.4 \cdot 10^{-17}$	$(9.35 \pm 2.81)10^{-17}$

TABLE 5.2e : Differential size spectrum of showers with $\theta < 30°$ and of $1.3 < S < 1.8$

Range	Cor. distance range	N	$0.8 < s < 1.1$	$1.1 < s < 1.3$	$1.3 < s < 1.6$	$1.6 < s < 1.8$	all s $m^{-2} sec^{-1} st^{-1}$ unit N^{-1}
$(2-3)10^4$	< 75	$2.5 \cdot 10^4$	$(4.4. \pm 0.88)10^{-11}$	$(4.36 \pm 1.45)10^{-11}$	$(4.53 \pm 4.53)10^{-11}$		$(9.78 \pm 0.68)10^{-11}$
$(3-4)10^4$		$3.5 \cdot 10^4$	$(2.92 \pm 0.48)10^{-11}$	$(2.32 \pm 0.62)10^{-11}$	$(1.53 \pm 0.76)10^{-11}$		
$(4-5)10^4$		$4.5 \cdot 10^4$	$(2.02 \pm 0.32)10^{-11}$	$(2.24 \pm 0.49)10^{-11}$	$(2.04 \pm 0.49)10^{-11}$		$(3.78 \pm 0.28)10^{-11}$
$(5-6)10^4$		$5.5 \cdot 10^4$	$(1.62 \pm 0.26)10^{-11}$	$(1.34 \pm 0.27)10^{-11}$	$(1.19 \pm 0.28)10^{-11}$		
$(6-7)10^4$		$6.5 \cdot 10^4$	$(1.63 \pm 0.23)10^{-11}$	$(9.80 \pm 2.04)10^{-12}$	$(8.17 \pm 1.7)10^{-12}$		$(2.11 \pm 0.23)10^{-11}$
$(7-8)10^4$		$7.5 \cdot 10^4$	$(9.40 \pm 1.46)10^{-12}$	$(6.04 \pm 1.42)10^{-12}$	$(5.73 \pm 1.35)10^{-12}$		
$(8-9)10^4$		$8.5 \cdot 10^4$	$(8.12 \pm 1.31)10^{-12}$	$(6.91 \pm 1.32)10^{-12}$	$(6.87 \pm 1.35)10^{-12}$		$(1.90 \pm 0.15)10^{-11}$
$(9-10)10^4$		$9.5 \cdot 10^4$	$(6.39 \pm 1.09)10^{-12}$	$(7.14 \pm 1.31)10^{-12}$	$(2.50 \pm 0.69)10^{-12}$		
$(1-2)10^5$		$1.5 \cdot 10^5$	$(3.1 \pm 0.2)10^{-12}$	$(1.84 \pm 0.12)10^{-12}$	$(1.86 \pm 0.13)10^{-12}$		$(6.80 \pm 0.26)10^{-12}$
$(2-3)10^5$		$2.5 \cdot 10^5$	$(7.31 \pm 0.60)10^{-13}$	$(6.1 \pm 0.47)10^{-13}$	$(4.53 \pm 0.38)10^{-13}$		$(1.79 \pm 0.08)10^{-12}$
$(3-4)10^5$		$3.5 \cdot 10^5$	$(2.69 \pm 0.29)10^{-13}$	$(2.81 \pm 0.26)10^{-13}$	$(1.31 \pm 0.15)10^{-13}$		$(6.81 \pm 0.41)10^{-13}$
$(4-5)10^5$		$4.5 \cdot 10^5$	$(1.65 \pm 0.2)10^{-13}$	$(1.88 \pm 0.18)10^{-13}$	$(8.32 \pm 1.04)10^{-14}$		$(4.36 \pm 0.28)10^{-13}$
$(5-6)10^5$		$5.5 \cdot 10^5$	$(9.57 \pm 1.37)10^{-14}$	$(1.02 \pm 0.12)10^{-13}$	$(4.64 \pm 0.72)10^{-14}$		$(2.44 \pm 0.19)10^{-13}$
$(6-7)10^5$		$6.5 \cdot 10^5$	$(5.43 \pm 0.96)10^{-14}$	$(5.69 \pm 0.81)10^{-14}$	$(3.67 \pm 0.62)10^{-14}$		$(1.24 \pm 0.09)10^{-13}$
$(7-8)10^5$		$7.5 \cdot 10^5$	$(3.14 \pm 0.67)10^{-14}$	$(4.57 \pm 0.71)10^{-14}$	$(2.36 \pm 0.49)10^{-14}$		
$(8-9)10^5$		$8.5 \cdot 10^5$	$(2.41 \pm 0.58)10^{-14}$	$(3.35 \pm 0.58)10^{-14}$	$(2.13 \pm 0.52)10^{-14}$		$(6.60 \pm 0.61)10^{-14}$
$(9-10)10^5$		$9.5 \cdot 10^5$	$(1.35 \pm 0.41)10^{-14}$	$(2.86 \pm 0.54)10^{-14}$	$(1.11 \pm 0.33)10^{-14}$		
$(1-2)10^6$		$1.5 \cdot 10^6$	$(5.33 \pm 0.74)10^{-15}$	$(7.19 \pm 0.80)10^{-15}$	$(5.37 \pm 0.74)10^{-15}$		$(1.79 \pm 0.13)10^{-14}$
$(2-3)10^6$		$2.5 \cdot 10^6$	$(1.13 \pm 0.34)10^{-15}$	$(1.21 \pm 0.35)10^{-15}$	$(1.36 \pm 0.39)10^{-15}$		$(3.70 \pm 0.62)10^{-15}$
$(3-4)10^6$	< 75	$3.5 \cdot 10^6$	$(5.92 \pm 2.96)10^{-16}$	$(5.21 \pm 2.32)10^{-16}$	$(2.85 \pm 1.64)10^{-16}$		$(1.40 \pm 0.40)10^{-15}$
$(4-7)10^6$	<105	$5.8 \cdot 10^6$	$(1.16 \pm 0.41)10^{-16}$	$(5.50 \pm 2.24)10^{-17}$	$(1.4 \pm 0.4)10^{-16}$		$(3.11 \pm 0.64)10^{-16}$
$(0.7-2)10^7$	<105	$1.4 \cdot 10^7$	$(2.67 \pm 1.19)10^{-17}$	$(2.98 \pm 1.72)10^{-17}$	$(9.35 \pm 2.81)10^{-17}$		$(1.50 \pm 0.34)10^{-16}$

TABLE 5.2f : Final differential size spectrum of showers with $\theta < 30°$ for all values of the age parameter s.
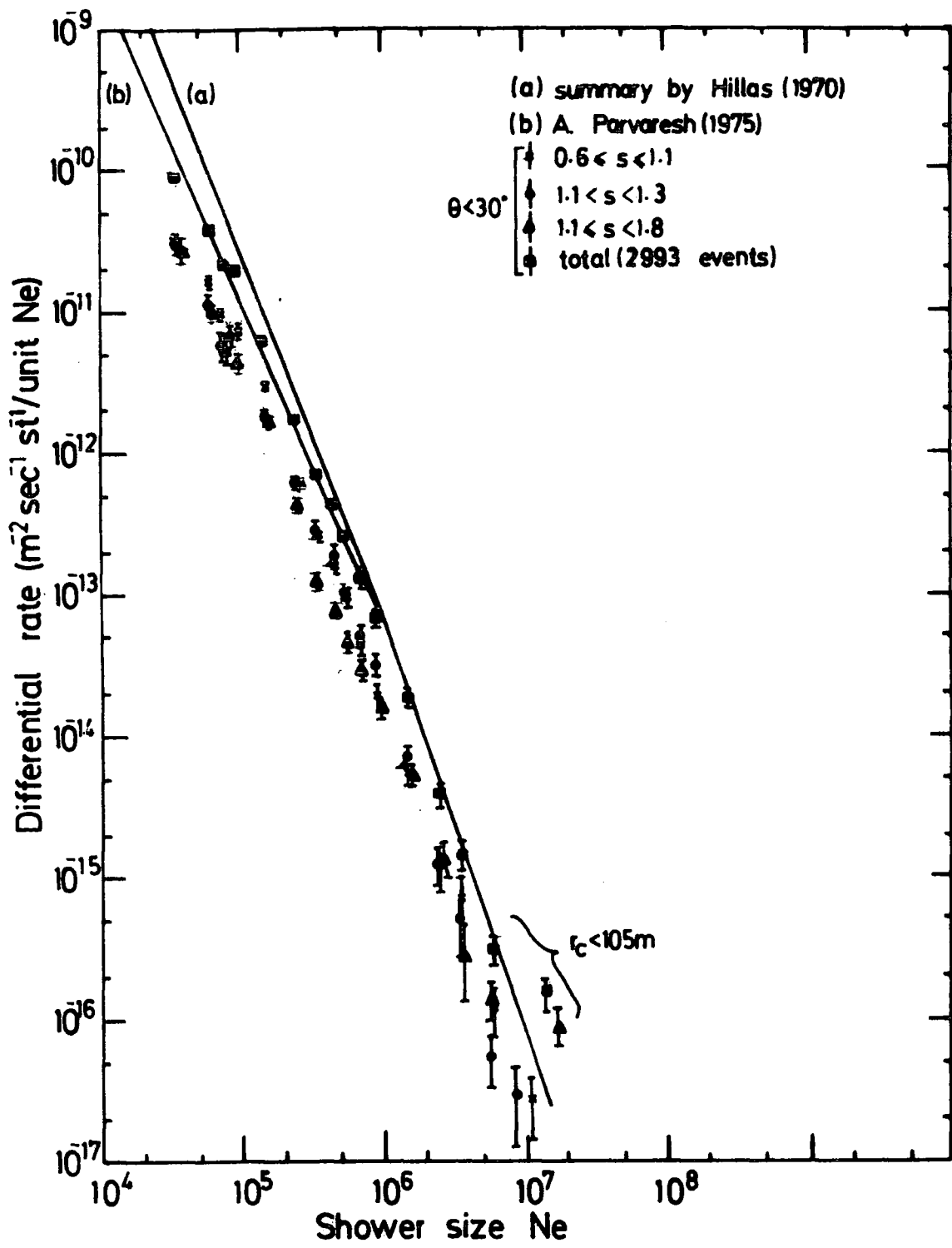
Figure 5.20 : The vertical differential size spectrum of E.A.S. at sea level for showers with different values of the age parameters. The total rate for showers of all age parameter is also shown. The work of Hillas (1970) and Parvaresh (1975) are also plotted for comparison.
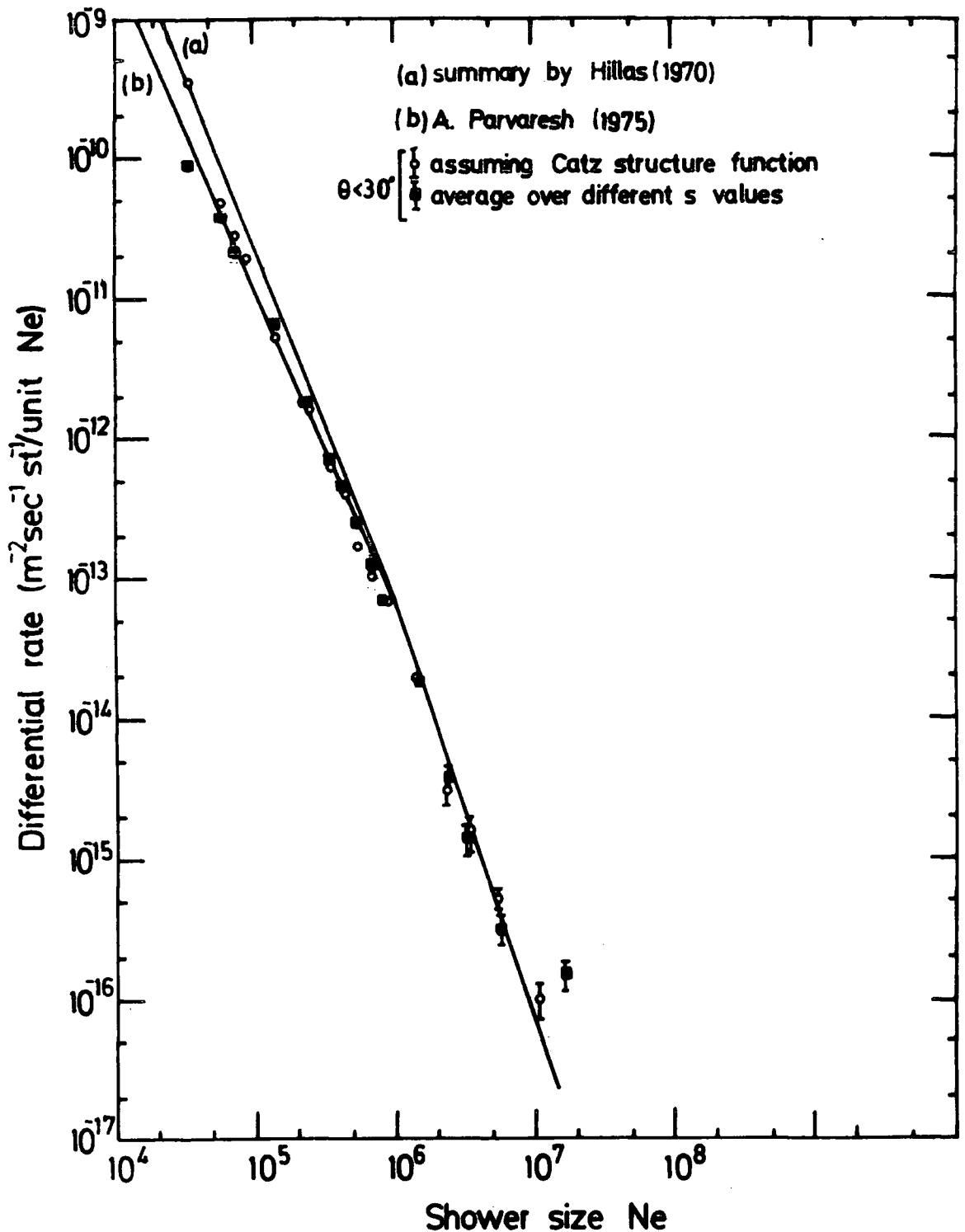
Figure 5.21 :   Comparison of the vertical differential size spectrum
of E.A.S. at sea level assuming that all showers obey
the Catz average electron lateral structure function
(open circles), with the more accurate evaluation
taking the age parameter of individual showers into
account (solid points). The full lines are the previous
work of Hillas (1970) and Parvaresh (1975).
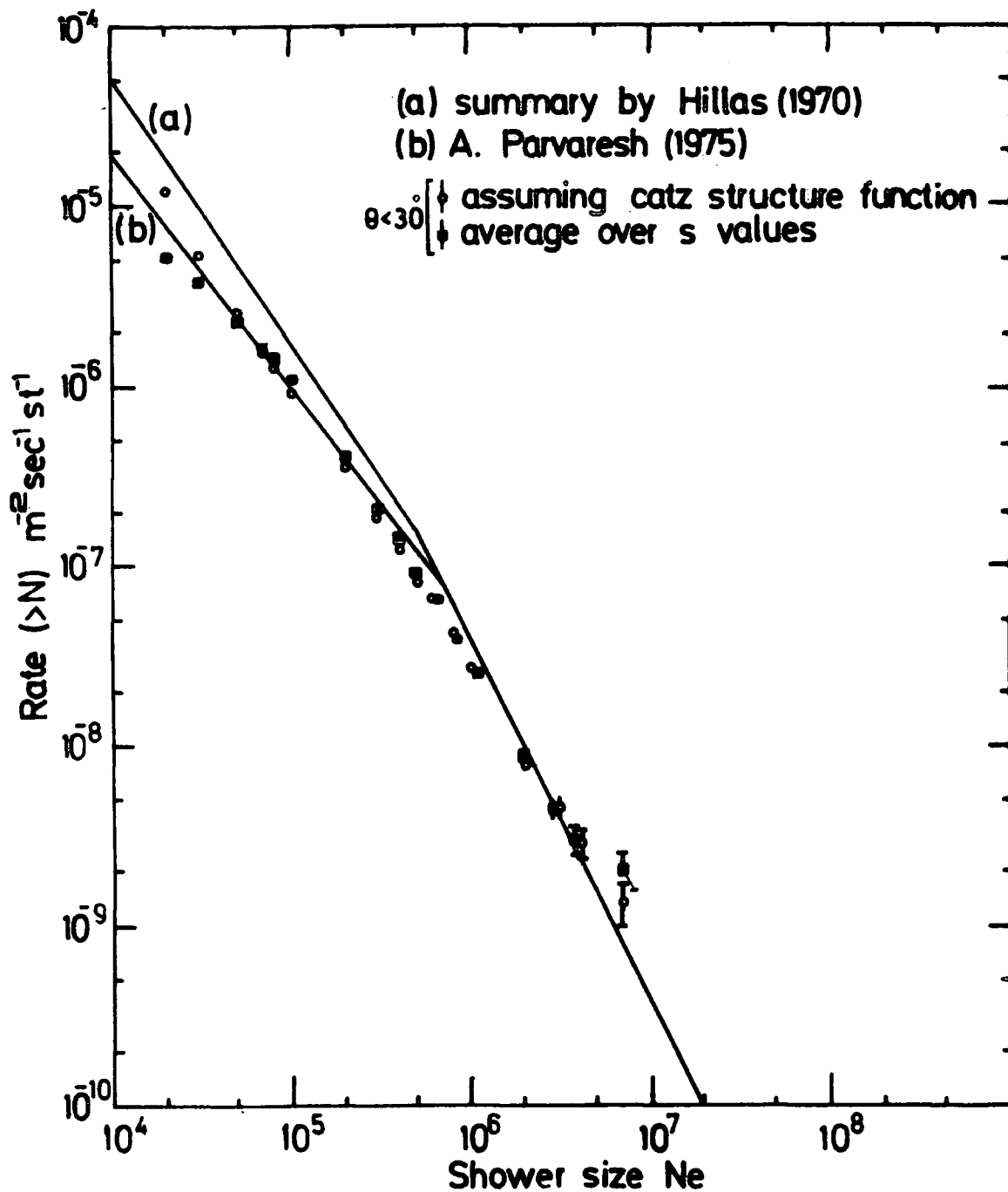
Figure 5.22 : Comparison of the vertical integral size spectrum
of E.A.S. at sea level assuming that all showers
obey the Catz average electron lateral structure
function (open circles) with the more accurate
evaluation taking the age parameter of individual
showers into account (solid points). The full
lines are the previous work of Hillas (1970) and
parvaresh ·1975)
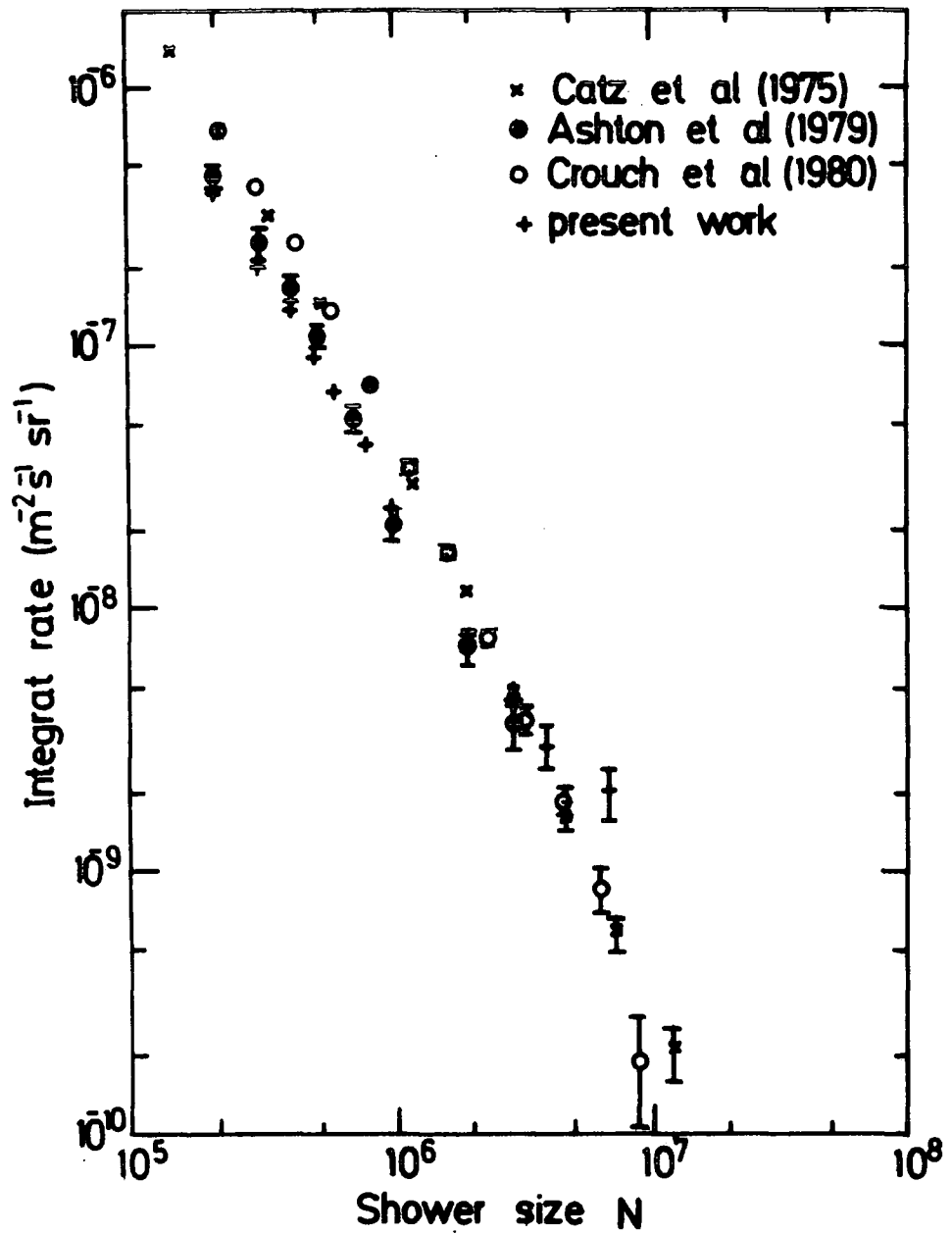
Figure 5.23 :   Comparison of the vertical integral size
                spectrum of E.A.S. at sea level taking
                into account the age parameter of individual
                showers with other recent measurements.

CHAPTER 6

LATERAL DISTRIBUTION OF MUONS

IN E.A.S. AT SEA LEVEL

6.1   THE MUON COMPONENT

The muon component of extensive air showers (E.A.S.) has been investigated by numerous workers because of its close link to the nuclear cascade and nuclear interactions. From a practical viewpoint, this component is easier to study than the more fundamental particles of the nuclear cascade, because it can be isolated with relative certainty from the other components of the shower. Also, muons are of interest because of their weak interaction with matter. As penetrating particles they carry information about the early stages of E.A.S. development, and about the primary particles and their mechanism of interaction. The average muon energy in a typical shower is much more than that of the electron component. At sea level, they carry much more total energy than the electrons, therefore this energy is a good measure of the primary energy.

An important parameter of the muon component is its lateral distribution, which is of great importance since it provides information about the transverse momenta of the parent pions and the height of origin of the muons in the atmosphere. The height of origin is dependent on the rate of development of the nuclear cascade in the atmosphere which is related to the multiplicity of secondary particle production in high energy interactions.

In practice, measuring the lateral distributions of muons is difficult because of the low number of muons relative to the number of electrons present in the shower. It is necessary to construct a large and well-shielded muon detector to obtain accurate measurements. The muon detector is usually operated in conjunction with an E.A.S. array to provide information about the other shower parameters. The total number of muons with energy greater than E_μ in a shower, $N_\mu (> E_\mu)$, is obtained by integrating average $2\pi r dr$ x the average density distribution function over all core distances, where E_μ is the muon threshold energy defined by the detector absorber thickness.

In a shower, the total number of muons is not proportional to the number of electrons, N_e, but $N_\mu = A N_e^\alpha$ where α is a constant less than one. A measured variation of the exponent, α in the shower size range $10^5 - 10^6$ particles could be associated with a possible increase of heavy nuclei in the primary cosmic radiation in the region 10^{15} eV (N.v. Kabonov, et al, 1973).

6.2   THE MUON LATERAL DISTRIBUTION

As muons represent the emission direction of their parent pions rather well, the lateral spread of muons in E.A.S. is mainly due to the acquired transverse momentum of mesons at their generation. A small additional contribution to the lateral spread is produced by a combination of Coulomb scattering and geomagnetic deflection. These are not important except for highly inclined showers, because the path lengths of muons are large in this case. The measurement of the lateral distribution of muons is performed above a

particular energy threshold for various radial distances from the shower core. The early experimental result on the form of distribution was given by Clark et al (1958). Muons of energy greater than one GeV for showers in the size range of $2.10^5 - 2.10^8$ particles were studied. Their results were reduced by Greisen (1960) to the following empirical form :

$$\Delta_\mu (N_e, r) = 18 \left(\frac{Ne}{10^6} \right)^{0.75} . r^{-0.75} . \left(1 + \frac{r}{320} \right)^{-2.5} \quad (6.1)$$

where $\Delta_\mu (N_e, r)$ is the muon density (m^{-2}) at a core distance of $r(m)$ in a shower of size N_e.

A more complete form of the lateral distribution of muons for various threshold energies E in the size range of 10^3-10^7 particles was proposed by Bennett and Greisen (1962). The empirical formula is :

$$\Delta_\mu (N_e, r, \geqslant E) = 14.4 \left(\frac{N}{10^6} \right)^{0.75} r^{-0.75} \left(1 + \frac{r}{320} \right) \left(\frac{51}{E_\mu + 50} \right) \left(\frac{3}{E_\mu + 2} \right)^{0.14r^{0.37}} \quad (6.2)$$

where E_μ is in GeV and the formula is valid for muons of energies of 1-10 GeV. No serious deviation of experimental results from the above formula has been observed up to the present time. Figure (6.1) shows the prediction of formula (6.2) for muons with energies, $E_\mu > 1$ GeV, compared with the results of various experiments. It is seen that the measured muon densities at small core distances are lower than expected. This was interpreted to be due to errors in core location and to the effect of normalizing the measured results to a fixed shower size of 2.10^7 particles. The previous result for the
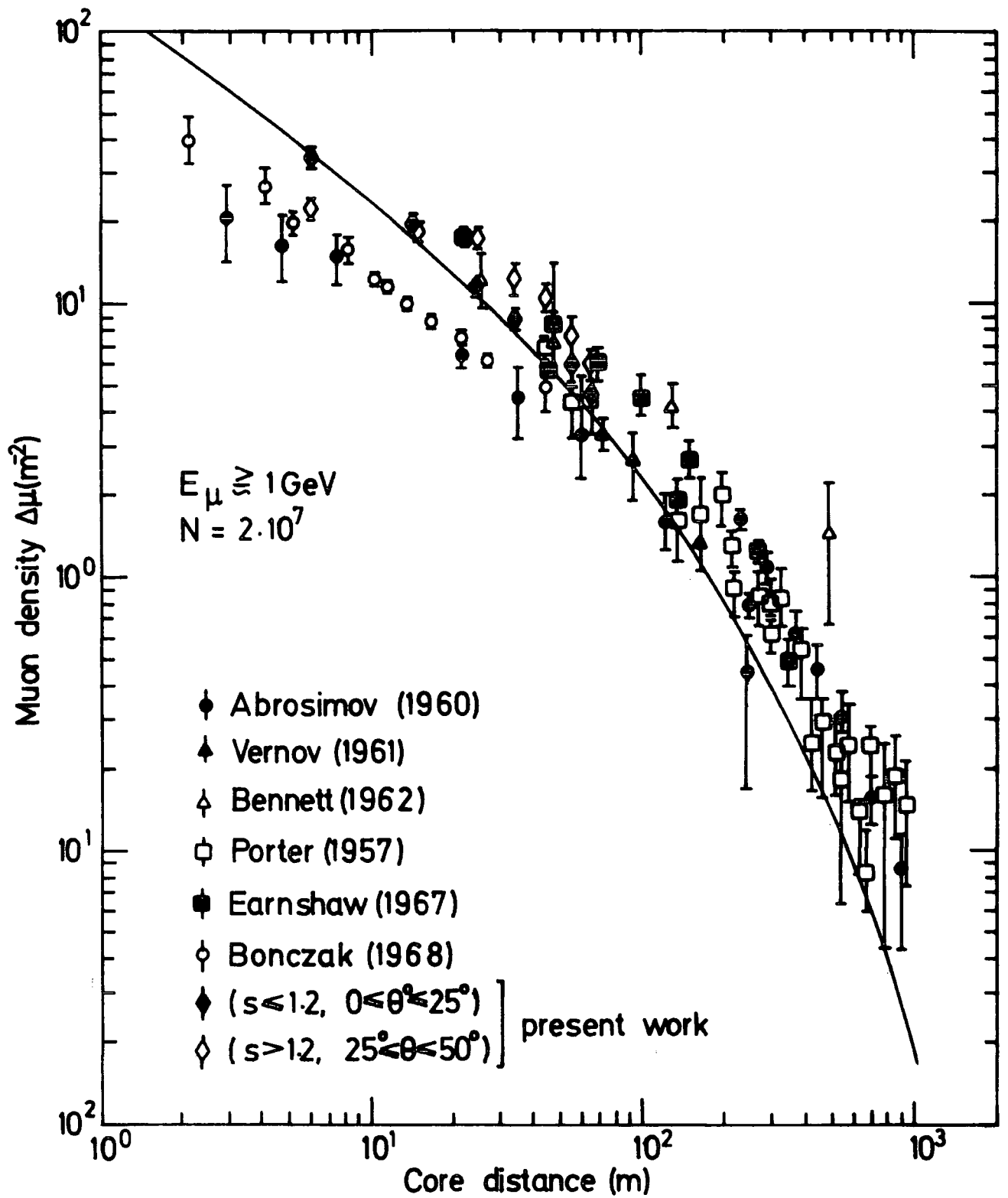
Figure 6.1 : The muon lateral distribution for 1 GeV energy threshold. All data are normalized to a shower size $N = 2.10^7$ particles. The continuous curve was calculated according to Greisen's formula (After Wdowczyk, 1973).

lateral distribution of muons of different threshold energy, shower size, zenith angle and core distance ranges and also its correlation with the electron component (represented by the age parameters of the shower) are considered in the next section, where a comparison is made between the theoretical standard cascade model and the experimental data observed by several workers.

6.3   PREVIOUS MEASUREMENTS

6.3.1 Allan et al (1968).

The muon detector consisted of four scintillation detectors, of total area 10 m^2, shielded by a sheet of lead 20 cm thick. The detector was located at the central position of the Haverah Park E.A.S. array so that it could be operated in conjunction with all three sub arrays of radius 50 m, 150 m and 500 m respectively. The shower sizes to which these arrays were sensitive were 2×10^5 to 4.10^6, 10^6 to 10^7 and 5.10^6 to 10^8 particles respectively. In this work the lateral distribution of the muon component and the variations of the total number of muons with shower size have been studied. The variation of the number of muons was found to be governed by the relationship

$$N_\mu \; \alpha \; N^{0.75 \pm 0.1} \tag{6.3}$$

where the exponent 0.75 is constant over the whole range of shower sizes $N_e = 3.10^5$ to 10^8 particles with zenith angles of less than 27 degrees. In particular, there was no evidence for a discontinuity in the exponent with changing N, which could arise from a change in composition of the primary cosmic radiation.   The observed muon densities were normalized to $N_e = 2.10^7$ particles with the aid of equation (6.3), to estimate

the lateral distribution of muons with energy greater than 0.3 GeV. From the 50 m and 150 m arrays the variation of muon density with shower size, N_e and core distance, r was found to be

$$\Delta_\mu = K_1 \left(\frac{N}{2 \times 10^7} \right)^{\beta_1} \frac{\exp\ (-\ r/320)}{(r/320)^{\alpha_1}} \tag{6.4}$$

with $K_1 = 2.5\ m^{-2}$ $3 \times 10^5 < N < 4.10^6$

$\alpha_1 = 0.8 \pm 0.01$ $10\ m\ <\ r < 80\ m$

$\beta_1 = 0.73 \pm 0.05$ $E_\mu > 0.3\ GeV$

The choice of $N = 2.10^7$ as normalization size was made to facilitate comparisons with showers recorded by the 500 m array. The lateral distribution of muons for large sizes ($N_e > 4.10^6$ particles) was also performed with the 500 m array. Overall, the measured lateral distribution was found to be in essential agreement with Greisen's formula (1960) where the densities were about 15% larger. The dependence of the distribution on r for r > 250 m was a power law of the form r^{-n}. The exponent, n, was observed to decrease with increasing Θ , implying a greater lateral spreading of the muons under a greater thickness of air. The evidence that n changes with Θ suggests that a similar dependence should be observed for changes in N, since both N and Θ control the age of the shower (i.e. its distance from maximum development) at the level of observation. In this experiment, the statistical evidence was too weak to demonstrate this dependence.

6.3.2 Khristiansen et al (1975)

An underground muon detector, consisting of hodoscoped Geiger-Müller counters with a total area of 37 m^2 was used in conjunction with an E.A.S. array to investigate the muon component and its correlation with s, the age parameter of the shower. In their early work, Khristiansen et al (1968) studied the correlation between the lateral distribution of muons with energy greater than 10 GeV and the form of the electron lateral distribution, i.e. the parameter s. This result showed that within a core distance range of 10 to 50 m, a muon flux in old showers (S $\geqslant$ 1.3) was 1.64 $\pm$ 0.2 times a muon flux in young showers.

With the improved statistics of the present work and also their division into two groups of data with s $\leqslant$ 1 and s $\geqslant$ 1.3, respectively, the muon lateral distribution was obtained for shower sizes in the range 2.10^5 to 10^6 particles. Figure (6.2) represents the experimental results which are normalized to N_e = 10^6 particles with the aid of the relation Δ_μ = A $N^{0.78}$. The result in the figure can be approximated by a function of the form :

$$\Delta_\mu = B \, r^{-n} \, \exp\left(- \frac{r}{80}\right)$$

where n = 0.7 $\pm$ 0.07   for   s $\leqslant$ 1

n = 0.5 $\pm$ 0.07   for   s $\geqslant$ 1.3

which shows its correlation up to a distance of 50 m from the shower axis. For large showers, with sizes N_e = 10^7-7.10^7 particles, the correlation between the lateral distribution of muons and the age parameter, s was studied up to 100 m

from the shower core. In this range, two groups of data with $s \leqslant 1.2$ and $s \geqslant 1.4$ were selected and each group was normalized to $N_e = 2.10^7$ particles. These are shown in Figure (6.3). It was found that lateral structure functions with different values of s are of the same form and the relation

$$\frac{\Lambda_\mu (S \geqslant 1.4)}{\Delta_\mu (S \leqslant 1.2)}$$

has a value of 3.0 ± 0.2 averaged over all core distances. Figures (6.2) and (6.3) show that the total number of muons is clearly lower in young showers and that their lateral distribution is steeper. The distributions for larger showers are also clearly steeper.

6.3.3 Wdowczyk et al (1973)

Some theoretical considerations of experimental observations were carried out for muons of energy greater than 5 GeV. The experiment was performed at sea level with a large underground muon detector consisting of G-M counters in conjunction with an E.A.S. array. The parameters investigated here were the muon lateral distribution, muon to electron ratio in E.A.S. and fluctuations of the ratio. To obtain the lateral distribution, muon densities in individual detectors of area, about 12 m^2, were measured and plotted as a function of the distance between the shower core and the centre of the detector.

The measured lateral distribution of muons for shower sizes of about 10^5 particles resulted in a much wider distribution than expected on the basis of the E.A.S. standard model (multiplicity α $E^{\frac{1}{4}}$) calculated by de Beer et al, (1966). The
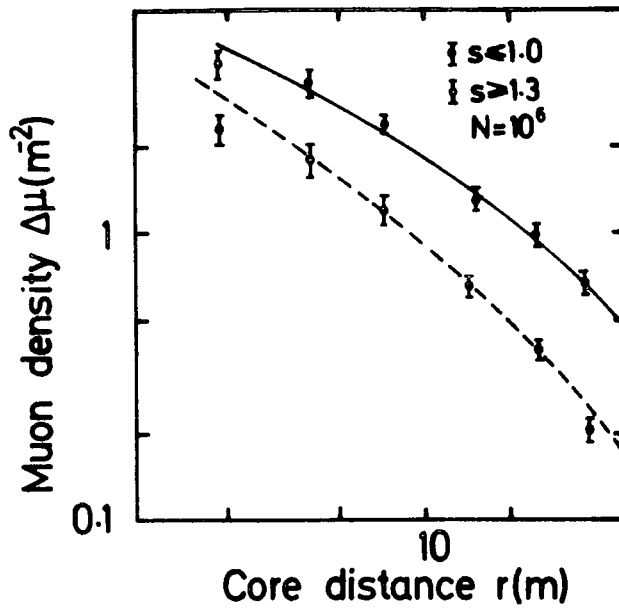
Figure 6.2 : Sea level muon lateral distribution for showers with
two different age parameters and a fixed size of 10^6
particles (After Khristiansen et al (1975)).
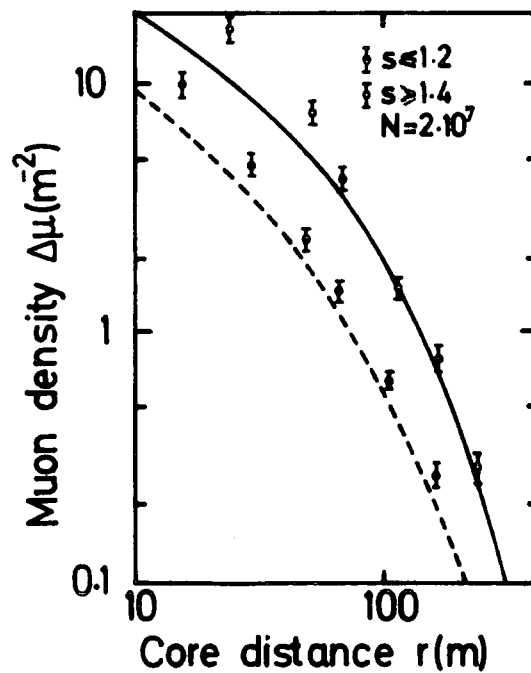
Figure 6.3 : Sea level muon lateral distribution for showers with
two different age parameters and fixed size 2×10^7
particles. The curves were taken from Fig.6.2 and
renormalised under the assumption that $N_\mu \sim N_e\, 0.78$
(After Khristiansen et al, 1975).

widening of the distribution was interpreted to be more likely due to a high multiplicity of secondary particle production in extremely high energy interactions. The possibility that it could be due to an increase in the mean transverse momentum was not favoured since at those muon energies, the transverse momenta of their parent pions should be normal.

This effect was also reported by a Moscow group, Khristiansen et al (1971). The high multiplicity indicates the fact that a high level of muon production should be due to rapid decrease of the mean energy of secondary hadrons with penetration through the atmosphere. The consistency of the observed fluctuations of the ratio of muon to electron densities versus muon shower size with the theoretical predictions of De Beer et al (1968) for showers of primary mixed composition and of pure proton primary composition indicates that the increase of multiplicity is not caused by a rapid increase of the mean primary mass.

6.3.4 Rozhdestvensky et al (1975)

A magnetic spectrometer was used to study relatively high energy muons in the range (10-90) GeV. The apparatus consisted of the magnetized iron body placed between arrays of wide-gap spark chambers of area 1 m^2. In order to obtain the density and energy of muons from this experiment, photo-graphs of the spark chambers were scanned and the trajectories of muons before and after the magnet were digitised and fed into a computer. The spectrometer was located at a depth of 40 meters water equivalent (m.w.e) underground at the centre of the E.A.S array of Moscow University in order to investigate muons in the core distance range of 6 to 100 m and the shower

size range of $N_e = 3.10^4 - 10^6$ particles. Using the data on muon energy spectra at various distances from the shower core and the absolute muon density measured in the previous work for all muons registered underground (i.e. $E_\mu \geq 10$ GeV, see Kulikov et al, 1974). The lateral distribution of muons of energies 20, 50 and 90 GeV respectively as shown in Figure (6.4) were obtained. These distributions are compared with theoretical predictions from a standard model which are shown by the full lines in Figure (6.4). It is seen that the experimental lateral distributions are clearly wider than those predicted as was the case in the previous experiment. The widening of the distribution could be due either to a higher transverse momentum than assumed or to a higher level of muon origin in the atmosphere. An alternative explanation is to assume that the energy of the particles in the initial stages of the shower development are degraded at a faster rate. For example, a higher multiplicity law with $n_s \alpha E^{\frac{1}{2}}$ may be assumed in contrast with the standard law, $n_s \alpha E^{\frac{1}{4}}$.

6.3.5 Discussion of Previous Work

The experimental work on the muon component of E.A.S. at sea level can be summarised as follows :

(i) The lateral distribution of muons depends on zenith angle, especially for large distances (r > 200m) from the shower axis. The function tends to be a power law of the form, r^{-n}, where the exponent n decreases with increasing zenith angle, θ. This indicates a greater spread of muons about the shower axis for showers traversing a greater thickness of the atmosphere.

(ii) No significant change in the shape of the lateral
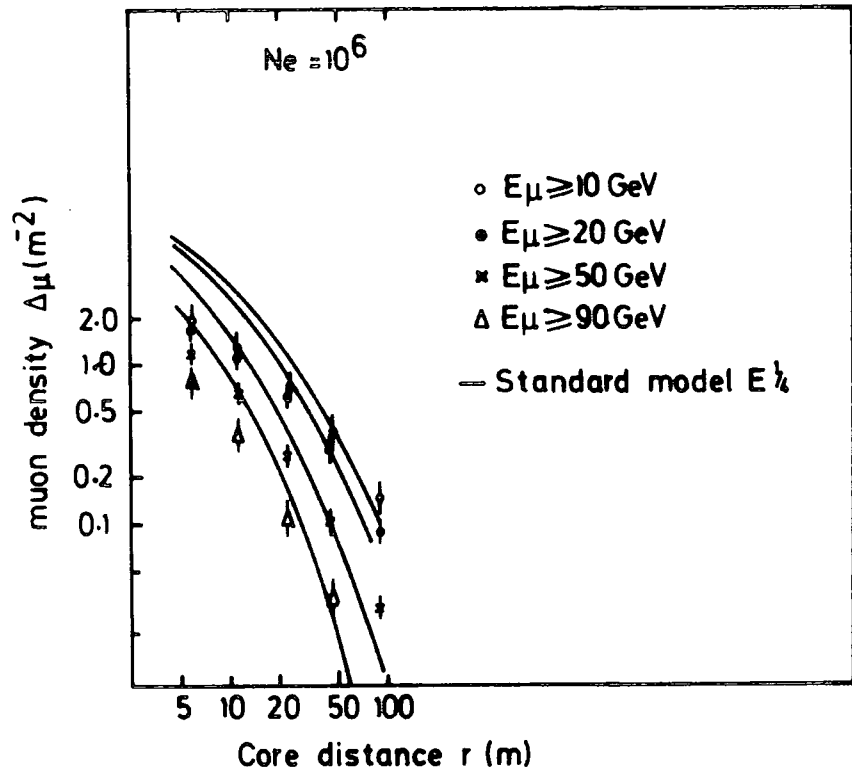
Figure 6.4 : The muon lateral distributions of Rozhdesivensky et al, 1975.

distribution of muons with increase of shower size in the range $10^4 - 10^8$ particles has been observed.

(iii) There is a clear correlation between the lateral distribution of muons and the age parameter of the electron photon component. Young showers give a steeper lateral distribution and a greater number of muons than old showers.

(iv) When measured muon lateral distributions are compared with theoretical predictions of a standard model the measured distributions are found to be flatter than expected. This result is interpreted as being caused by a higher multiplicity of secondary particles than the assumed relationship, $n_s \propto E^{\frac{1}{4}}$.

(v) The Greisen formula of equation (6.2) is the best function that fits the experimental results obtained for muon energies.in the range (1-10)GeV. This formula has been used in the present experiment for comparison purposes.

6.4   PRESENT WORK

6.4.1 The Muon Detector

The muon detector used in the present experiment was a flash tube chamber of sensitive area 2.95 m^2 which was triggered by the Durham E.A.S array. It was shielded above by a 15 cm lead absorber and also a 15 cm iron absorber. The lead absorber was designed to cut out the soft component (electrons and photons) whereas the iron absorber was placed to separate the muons from the nuclear active particles. The chamber is situated in a tunnel of rectangular cross-section with 30 cm thick barytes concrete walls. This also acts as a filter by

absorbing the soft component.

The detailed description of the chamber and the array are given in Chapter 2, and a scale diagram of the front view of the chamber is shown in Figure (6.5).

Events occurring in the chamber were recorded photographically by an automatic camera. For each event triggered, the timing and density information of the air shower were recorded by the array. The array information was used to determine, shower size, core location, arrival direction (zenith angle, θ, and azimuth angle ϕ), and the age parameter of the shower. Where the chamber data made it possible to investigate the muon component, the procedure of chamber event analysis consisted of projecting the negative of the film onto a scanning sheet of a size reduced in the ratio of 1:13 of the actual size. An example of this is presented in Figure (6.5) showing the passage of muons through the middle of the chamber (AB), which was defined as a reference level to measure acceptable muon tracks. For each event, the number of acceptable muon tracks was counted and the muon density obtained. An acceptable event was defined as one which satisfied the following criteria ;

(i) the muons passed through the reference level taken as the middle of the chamber.

(ii) the muons were parallel to each other to within $\pm 5^{o}$ in the projected plane.

(iii) the muons had a track length of $\geqslant 60$ cm in real space.

These criteria ensured that the tracks counted were due to muons and it excluded any bias due to background muons and
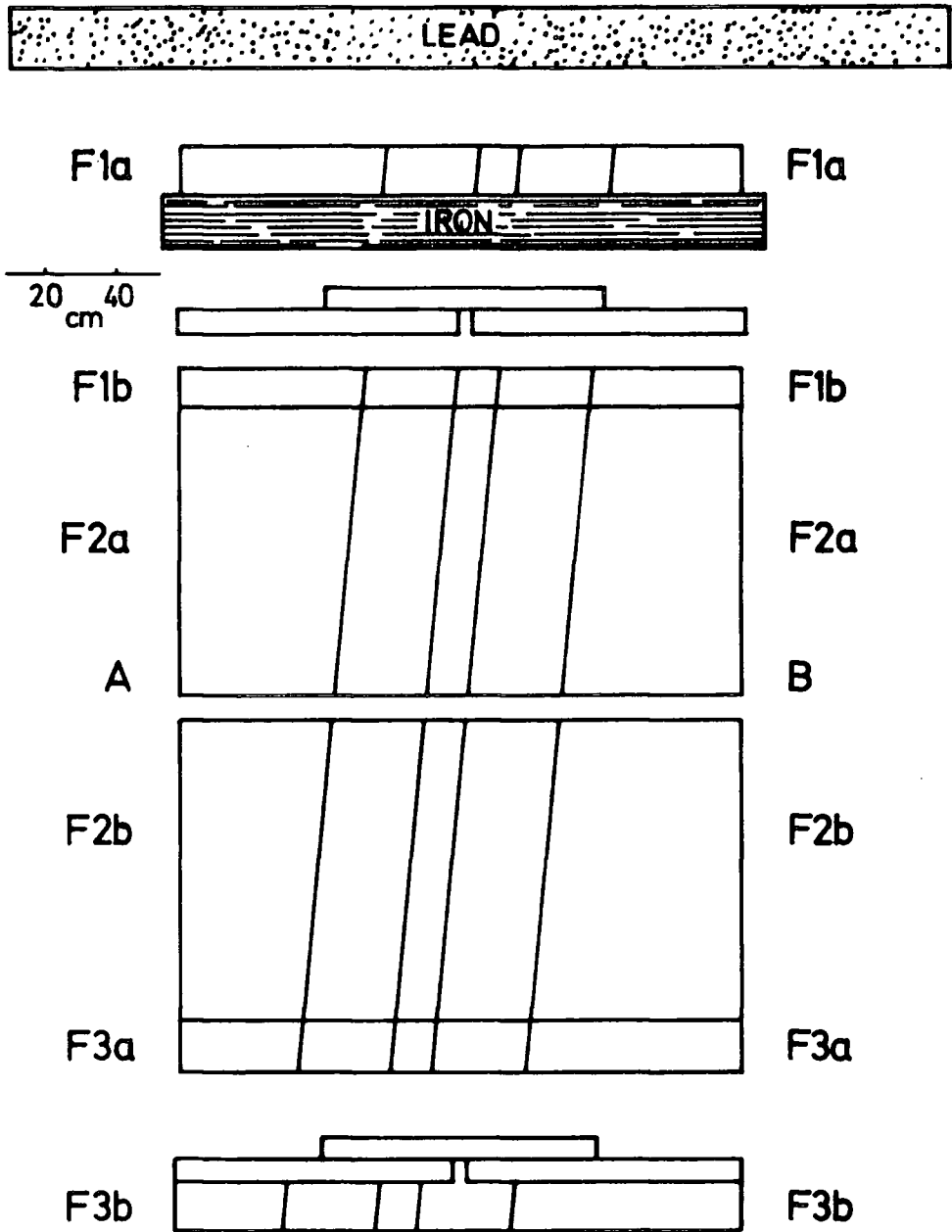
Figure 6.5 : A scale diagram showing the passage of muons through the middle AB of the chamber.

any other unreal tracks (i.e. small tracks due to diffused electrons). Events, for which the whole or part of the chamber was obscured by bursts so that measurement was impossible or inaccurate, have been rejected in the analysis of the data.

6.4.2 Data Analysis

Evidence for a change in slope of the size spectrum in the shower size range of 10^5-10^6 particles has been described in Chapter 5. It is of interest to investigate if there is any observed effect of this change of slope on the lateral distribution of muons. A total of 3387 triggers with both chamber and array information available were analysed, and are shown with the basic data in Table (6.1). The electron structure function was initially assumed to be the same for all the events. With this assumption, the core location and the size (N_e) of each shower was obtained. In the second step of the analysis, the sampling densities of each shower were re-analysed by computer, to find the best N.K.G. function and hence age parameter s as well as the best shower size $N_e(s)$ that fitted the measurements. The average difference of the two sizes (N_e and $N_e(s)$ was found to be about 10 per cent. Measurement of the average lateral distribution of muons raises the problem of the normalisation of the muon densities, $\Delta_\mu(N,r)$ in a shower of size, N at core distance, r. Generally, the relationship $\Delta_\mu(N,r) = F(N) \ F(r)$ is anticipated, where $F(N)$ is of the form $F(N) = A \ N^\alpha$ as found in previous work. If it is further assumed that $F(r)$ is the same for all N, α can be found from a scatter plot of the number of muons including zeros detected in the chamber as a function of shower size for showers whose cores fall within a given distance of

E.A.S. Selection	Total No. of Shower Triggers	No. of analysable shower triggers with $\Theta<50^{\circ}$ and no cut on core distance	No. of analysable shower triggers with $\Theta<50^{\circ}$ when flash tube chamber operational and no cut on core distance	No.of analysable shower triggers with $\Theta<50^{\circ}$, orthogonal core distance from flash tube chamber <70m and chamber operational
Inner ring trigger ; $\Delta_c(\geq 4m^{-2})$, $\Delta_{11}(\geq 2m^{-2})$ $\Delta_{31}(\geq 2m^{-2})$, $\Delta_{51}(\geq 2m^{-2})$	2683	2572	2263	2060
Outer ring trigger ; $\Delta_c(\geq 4m^{-2})$, $\Delta_{13}(\geq 2m^{-2})$ $\Delta_{33}(\geq 2m^{-2})$, $\Delta_{53}(\geq 2m^{-2})$	2131	2014	1798	1327
Total	4814	4586	4061	3387

TABLE 6.1 : Summary of experimental data used in the analysis. The cut in core distance used was r< 70m from the centre of the flash tube chamber.

the chamber. Using the value of α found in this way by Nejabat (1980) α = 0.69 $\pm$ 0.08, all measured muon densities have been normalised to a standard shower size of 3.10^5 using the relation

$$\Lambda_\mu (3.10^5, r) = \Lambda_\mu (N, r) \left(\frac{3.10^5}{N} \right)^\alpha \tag{6.5}$$

6.4.3 The Results of the Present Experiment

The lateral distribution of muons for a sample of 3,387 events was measured for two different zenith angle ranges, $0 < \theta \leqslant 25$ and $25^o < \theta \leqslant 50^o$, respectively. The results are shown in Figures (6.6) and (6.7), where a comparison is also made with the analytical expression given by Greisen (1962), (Equation 6.2), which is evaluated for muon energies of more than 500 MeV in showers of size 3.10^5 particles.

The distribution for nearly vertical showers, $0 < \theta \leqslant 25^o$, shows reasonable agreement with Greisen's prediction. For the other zenith angle range, $25 < \theta \leqslant 50^o$, the distribution is significantly flatter. The previous experimental results of Nejabat (1980) are also shown on the same plots and they are consistent with the present result. The consistency is also valid when the shower size, $N_e(s)$ is used instead of N_e. The age parameter distributions, shower size, and zenith angle distributions, of the total number of events analysed, are shown in Figures (6.8a),(6.8b)and (6.9) ; only showers with zenith angle of less than 50° being used in the analysis. In the next step, the dependence of the lateral muon distribution on shower size was investigated for the size range intervals of $10^4 - 3.10^5$ and $3.10^5 - 4.10^6$ particles respectively. This was
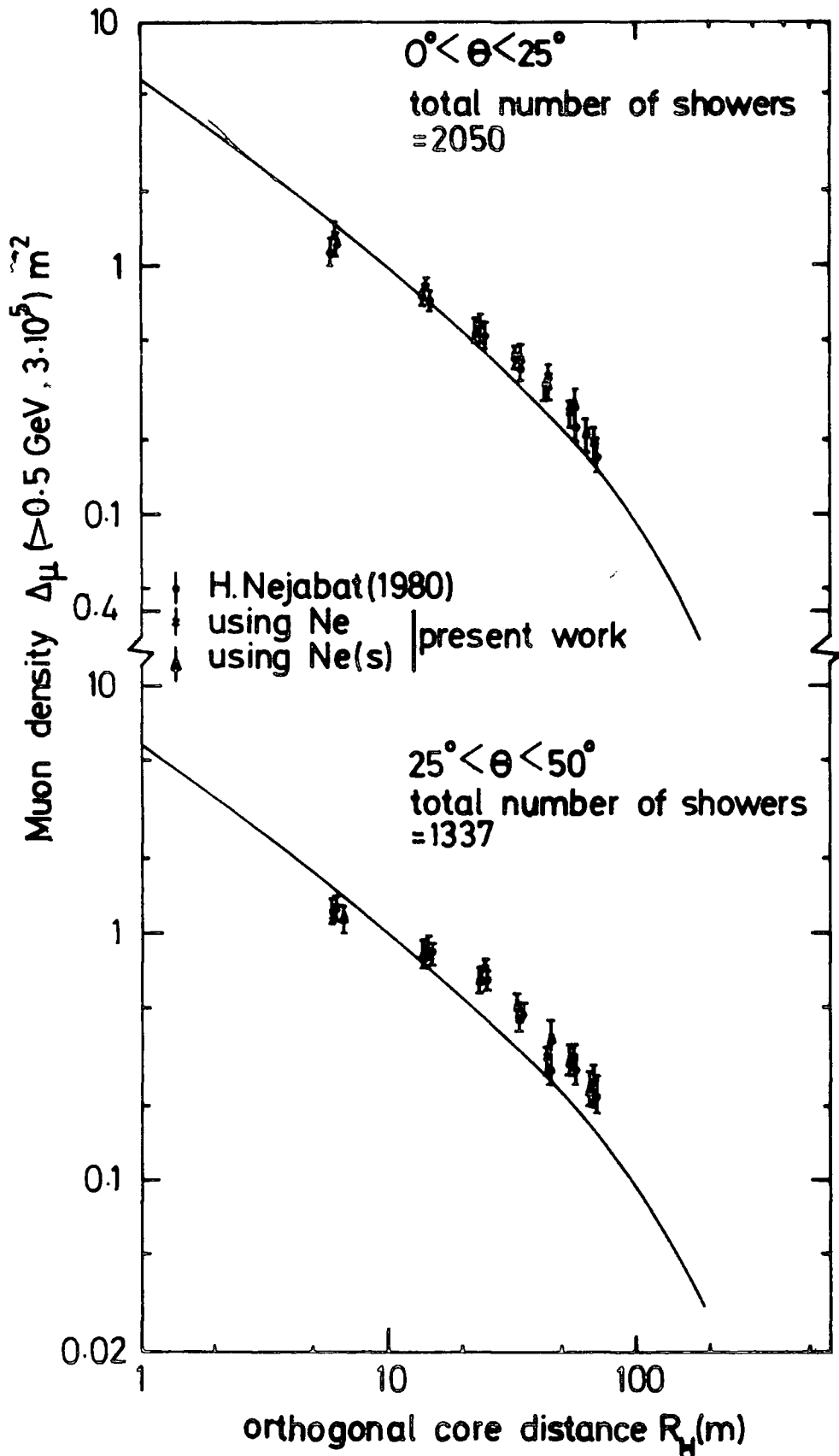
Figure 6.6 & 6.7 : The lateral distribution of muons for 500 MeV energy threshold and different ranges of zenith angle. All data are normalized to a shower size $N = 3.10^5$ particles. The solid curve was calculated according to Greisen's formula (eqn. 6.2).
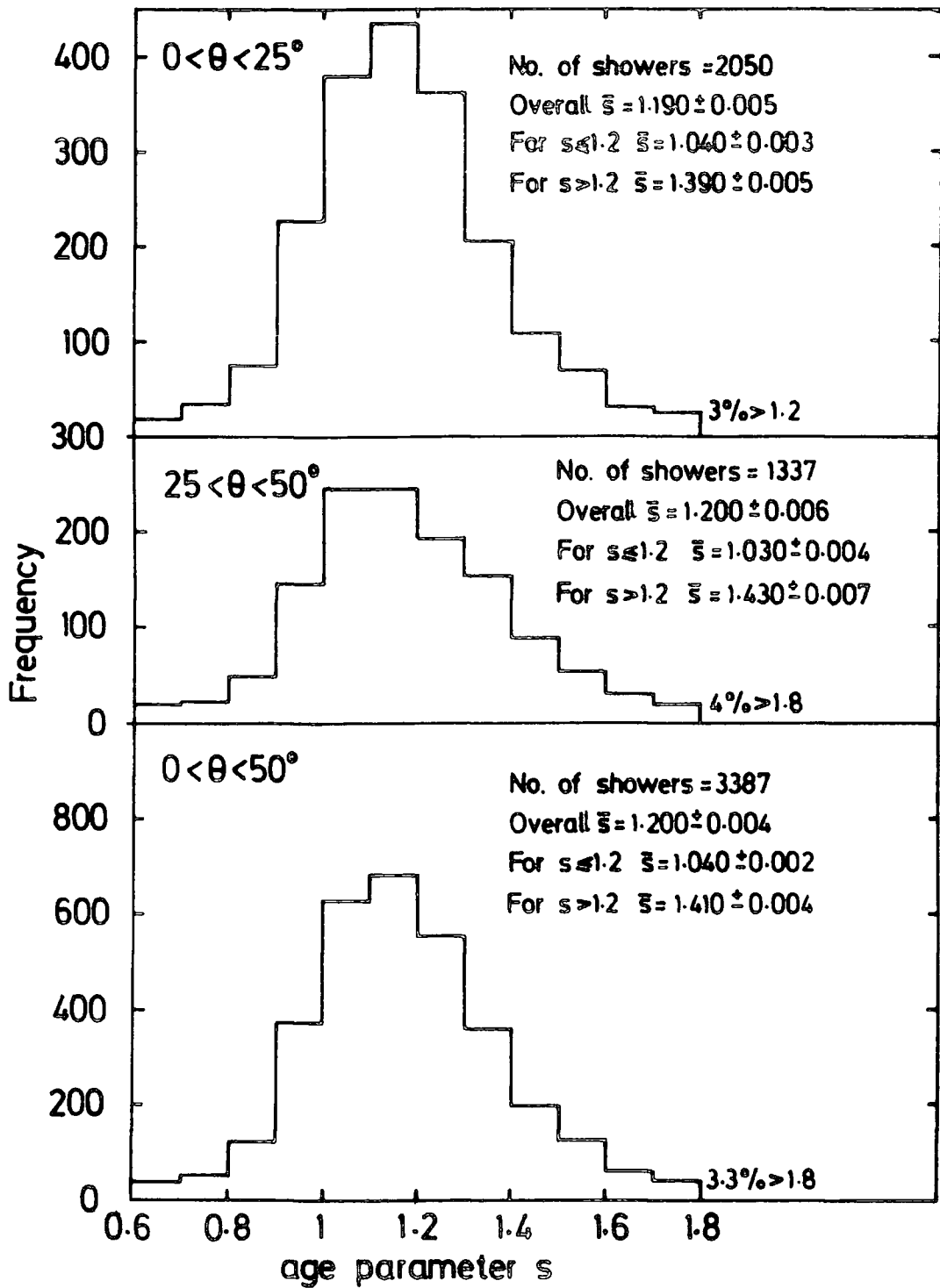
Figure 6.8a :   Age parameter distributions of the data for different

ranges of zenith angle.   The percentage of showers that

could not be fitted with a value of S in the range

0.6 - 1.8 is   0<θ<25°, 3% ;   25<θ<50°, 4% ;

0<θ<50°, 3.3%.
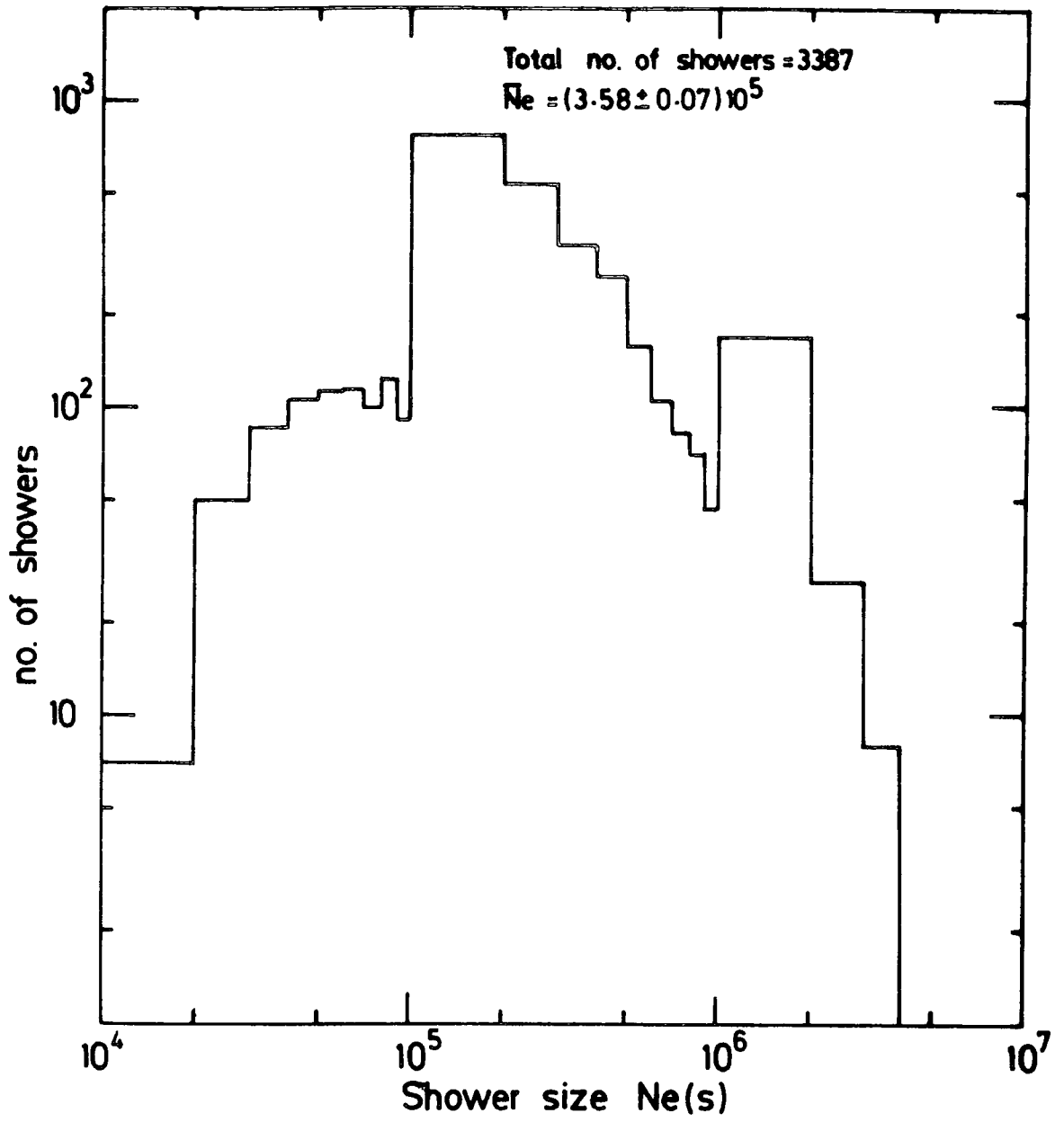
Figure 6.8b :   Shower size distribution of the showers used in the
                present analysis.

No. of showers = 3387
$\bar{\theta} = 21 \cdot 27 \pm 0 \cdot 18$
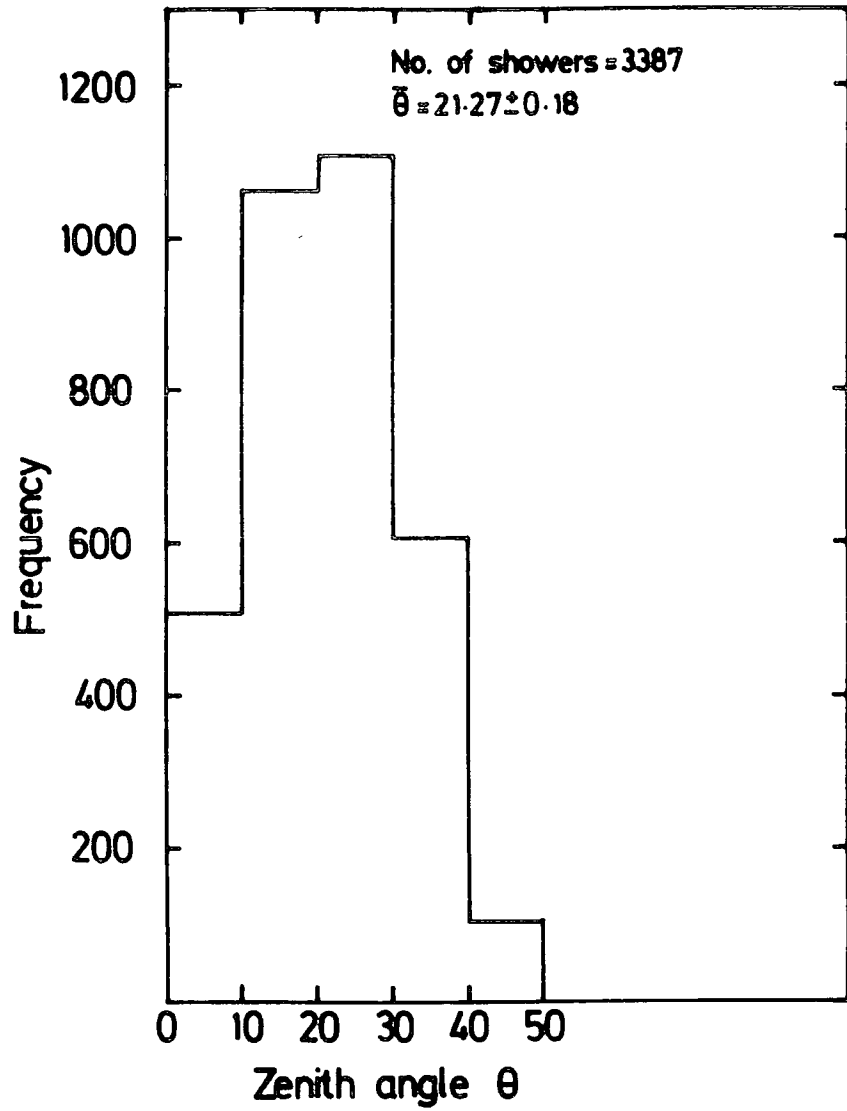
Figure 6.9 : Zenith angle distribution of the showers used in the present analysis.

carried out for different ranges of zenith angle, θ , and age parameter, and comparison was made with the predictions of Greisen's formula. The results are shown in Figures (6.10), (6.11), (6.12) and (6.13). They show no significant dependence of the lateral distribution of muons on shower size in the size range $10^4 - 4.10^6$ particles. This is also true for zenith angle and age parameter ranges of $0 \leqslant \theta \leqslant 50^O$ and $0.6 < s \leqslant 1.8$ respectively.

The correlation of the lateral distribution of muons with the age parameter was investigated for nearly vertical showers and a large zenith angle range where the age parameter ranges of less than, and greater than, the average age value $s = 1.2$ were considered. The results are shown in Figures (6.14) and (6.15). It seems that for showers with a larger age parameter (old showers), the distribution is flatter than for young showers with smaller age values. The muon density at small distances from the core of old showers seems to be smaller than for young showers, where for relatively larger core distances (greater than 20 m) the case is the inverse. This gives the overall result that there are more muons in old showers than young showers of the same size, which will be discussed later in this section. Besides, it should be mentioned that the shape of the lateral distribution of muons apart from the sample for young and nearly vertical showers (the results for which are in very good agreement with the predictions of Greisen), is flatter than predicted, especially for the case of inclined, old showers ($25^O < \theta \leqslant 50^O$ and $S \geqslant 1.2$) see Figure (6.1).
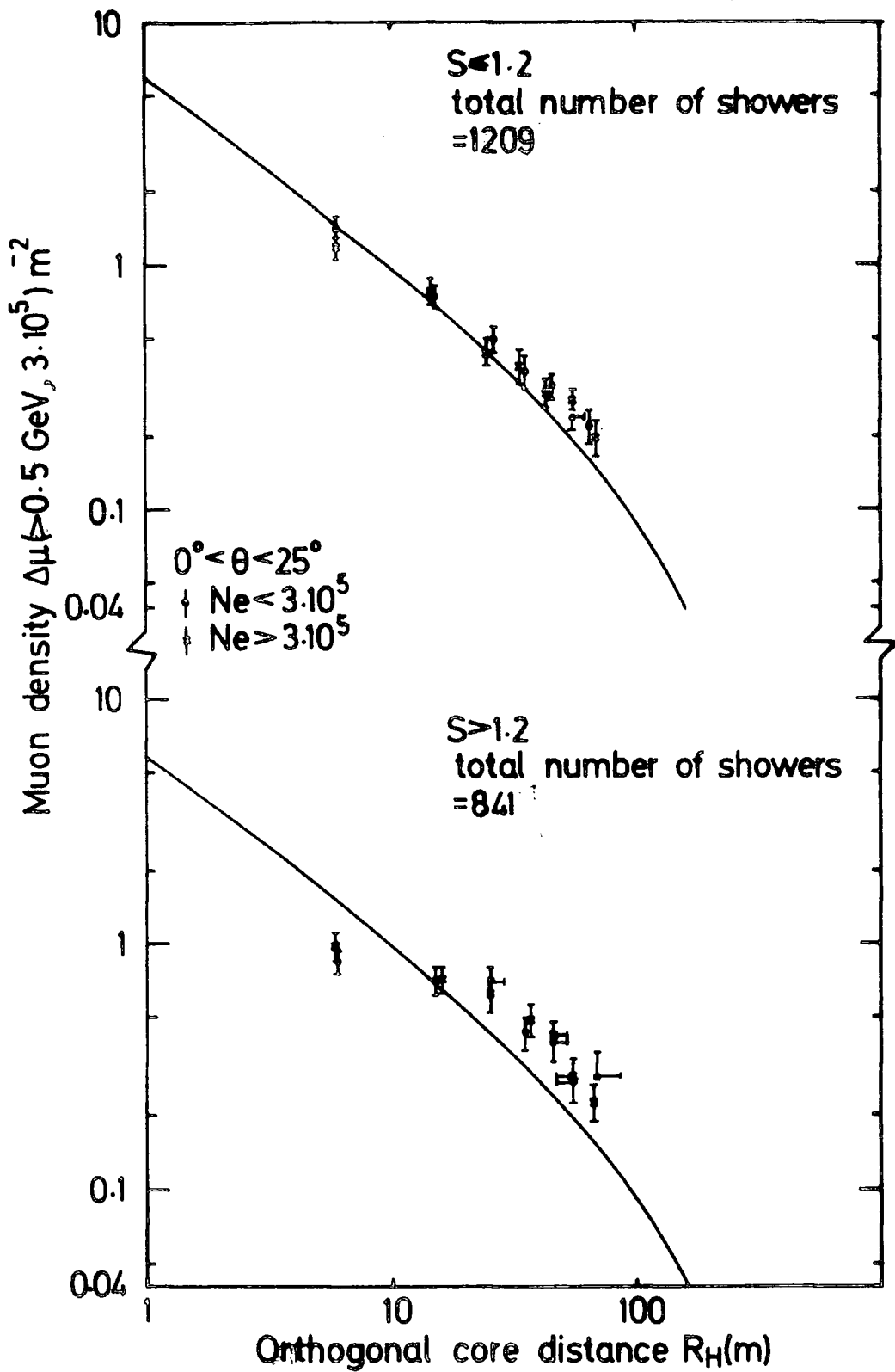
Figure 6.10 & 6.11 : The dependence of the lateral distribution of muons on shower size for different ranges of zenith angle and age parameter.
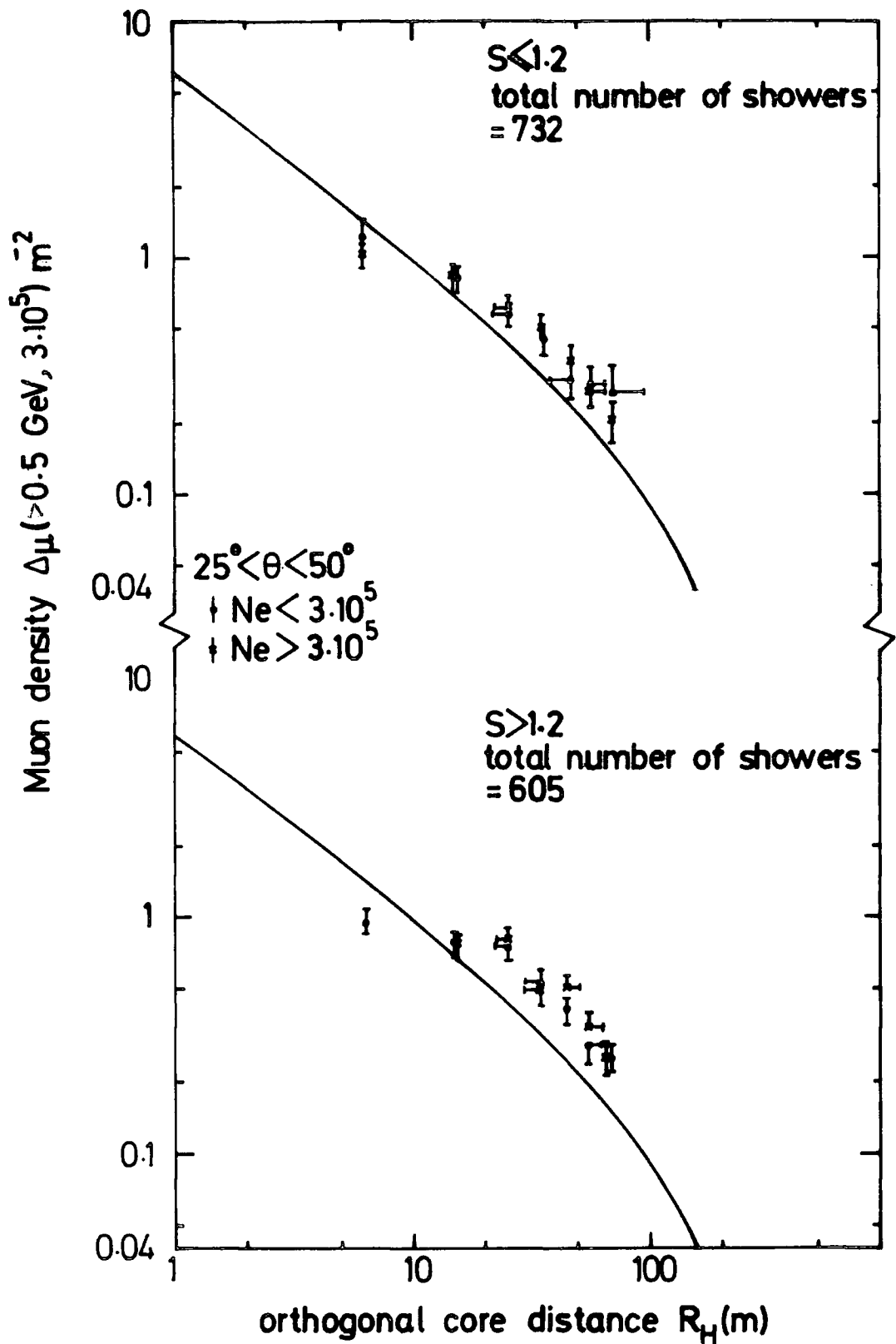
Figure 6.12 & 6.13 : The dependence of the lateral distribution of muons on shower size for different ranges of zenith angle and age parameter.
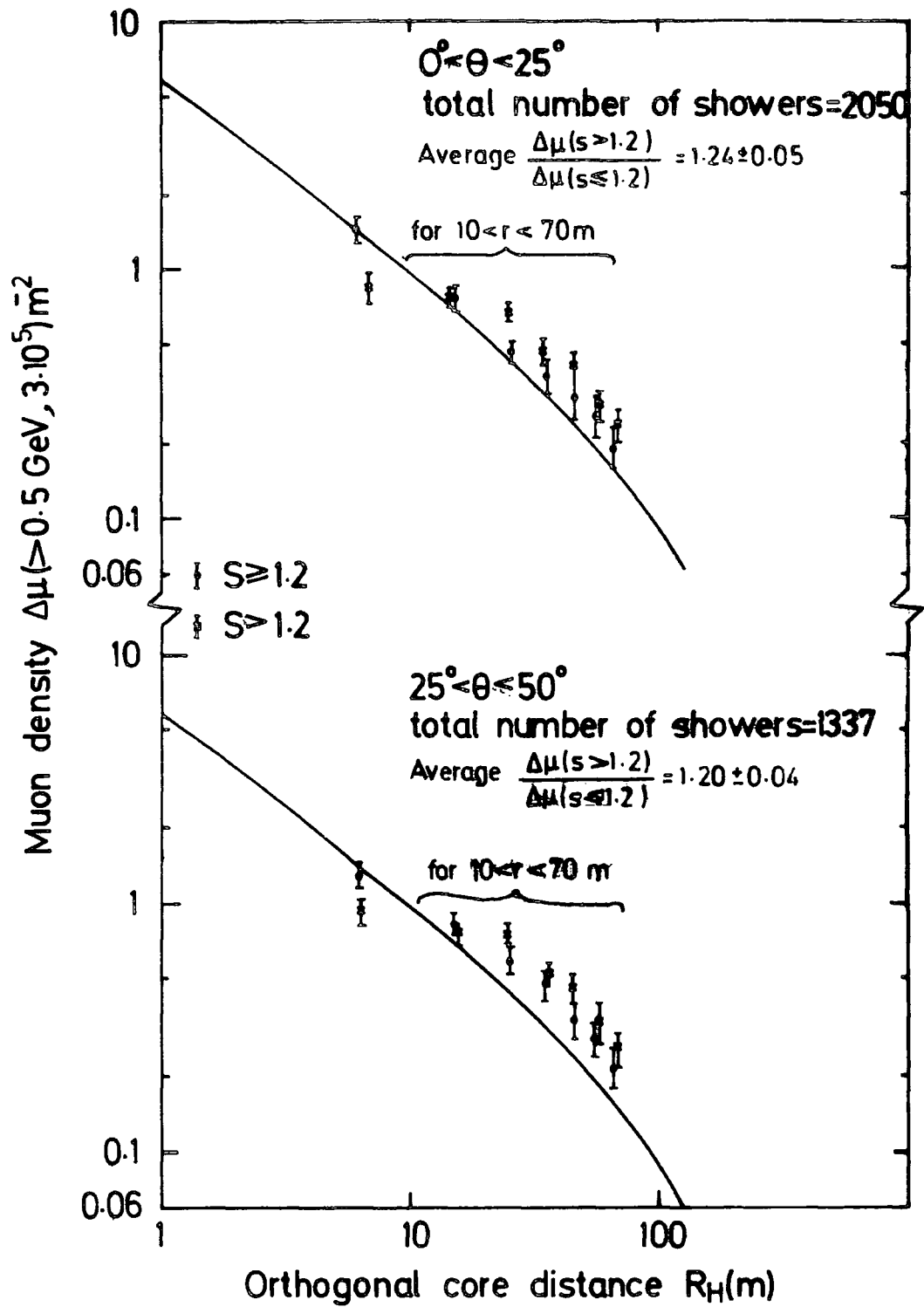
Figure 6.14 & 6.15 :   The dependence of the lateral distribution of muons on age parameter for different ranges of zenith angle.

To obtain the value of the exponent, α in the relation $\bar{N}_\mu \sim N_e^\alpha$ where $\bar{N}_\mu$ is the observed mean number of muons including zeros, in the chamber a scatter plot of N_μ versus N_e was made. Finding $\bar{N}_\mu$ for a given range of N_e, the exponent, α was measured from the slope of the line fitted to the experimental points of the $\bar{N}_\mu$ -N_e relation, which in turn was measured for different ranges of core distance and age parameter as is shown in figures (6.16) and (6.17). The values obtained for α are tabulated in Table (6.2) for core distance ranges of less than 40 m. As deduced from the table, two points are of considerable importance. The first is the smooth decrease of the exponent α with increase of core distance for old and young showers respectively. The mean shower size for every range of core distance happened to be nearly the same for old and young shower intervals ($S \leqslant 1.2$ and $S > 1.2$). The second point is that the average exponent over the core distance range 10-40m is greater for old showers than for young showers provided that the mean shower size is the same. This indicates that the number of muons in old showers is greater than in young showers.

6.5   CONCLUSION

From the results of the previous section, it is concluded that there is no evidence for a significant change of the muon lateral structure function with shower size over the size range of 10^4-4.10^6 particles at sea level. The measured lateral distribution of muons in showers with zenith angle $\geqslant 25°$ and age parameter $S \geqslant 1.2$ is significantly flatter than suggested by the empirical analytic expression of Greisen (1962), whereas for near vertical and young showers
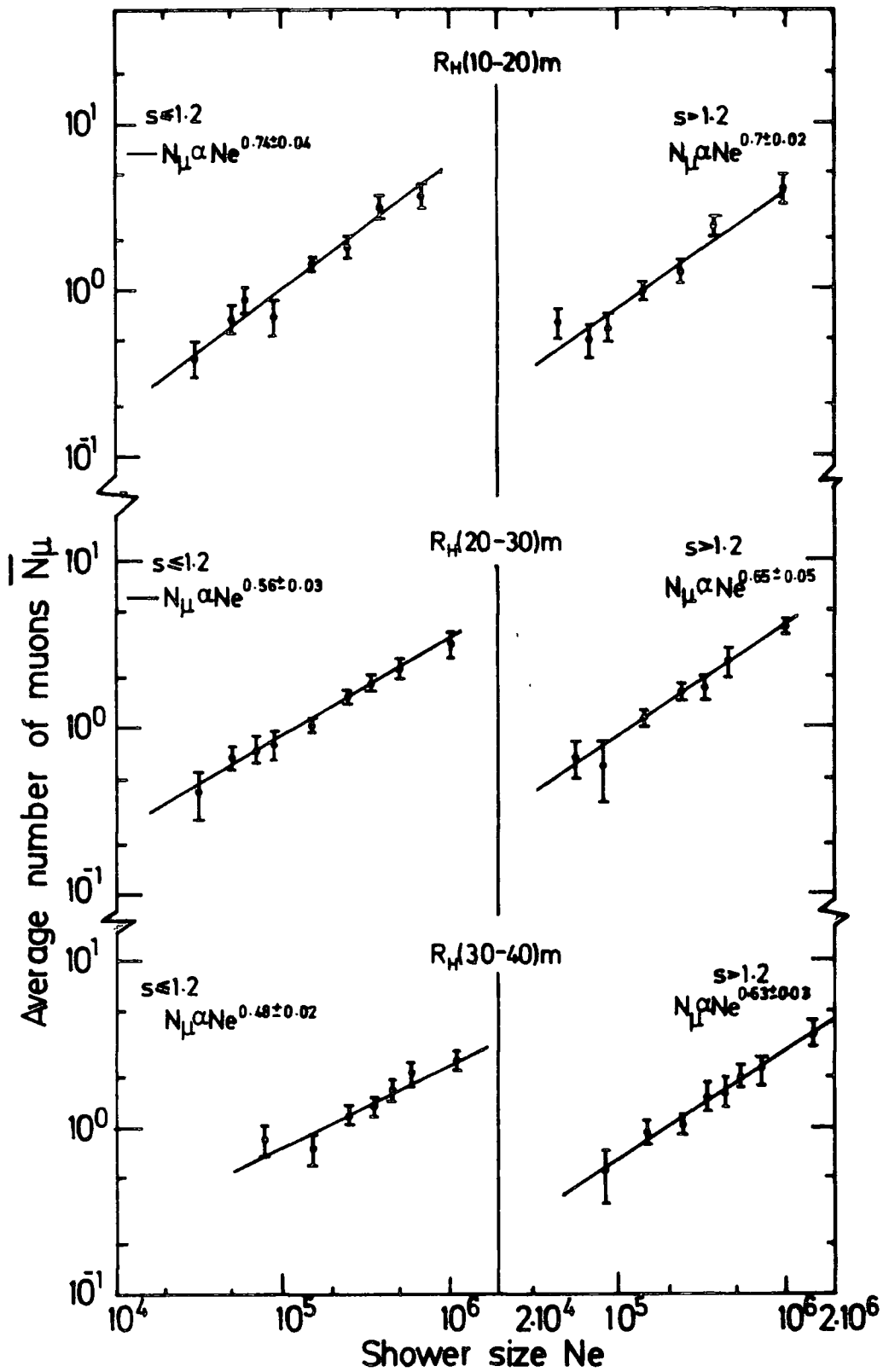
Figure 6.16 & 6.17 :   Size dependence of the average number of muons
observed in the chamber for different ranges of
core distance and age parameter.

s	≤ 1.2			> 1.2		
r (metres)	(10-20)	(20-30)	(30-40)	(10-20)	(20-30)	(30-40)
N_e	$(1.84\pm0.08)10^5$	$(2.18\pm0.1)10^5$	$(3.71\pm0.15)10^5$	$(1.87\pm0.12)10^5$	$(2.91\pm0.17)10^5$	$(4.13\pm0.23)10^5$
α	0.74±0.04	0.56±0.03	0.43±0.02	0.7 ± 0.02	0.65 ± 0.05	0.63 ± 0.03
$\bar{N}_e$	$(2.58 \pm 0.11)10^5$			$(2.97 \pm 0.17)10^5$		
$\bar{\alpha}$	0.59 ± 0.03			0.66 ± 0.03		

TABLE 6.2: The values of α in $\Delta_\mu (r) = A N_e^\alpha$ for different ranges of core distance and age parameter. N_e is the average shower size for showers falling in the given range of r. and $\bar{N}_e$ the overall average.

($S \leqslant 1.2$) it is consistent with the formula. The total number

of muons in old showers seems to be greater than for young

showers, which was also observed in previous work,

Khristiansen, et al (1975).

CHAPTER 7

SEARCH FOR QUARKS CLOSE TO THE CORE

OF. E.A.S

7.1   THE CONCEPT OF QUARKS

Since the discovery of pions (1947) and many other
so-called elementary particles, attempts have been made to
understand them in terms of elementary sub-units.
Historically, Fermi and Yang (1949) proposed the hypothesis
that the π-meson may not be elementary but composite formed
by the association of a nucleon and anti-nucleon assuming
the existence of a strong binding force between them.
However, this hypothesis could not account for all strongly
interacting particles as another sub-unit carrying a strange-
ness quantum number was needed. Sakata (1956) proposed the
triplet of proton, neutron, lambda zero and their anti-
particles, as sub-units to fill up this gap. By then, the
model was able to describe the structure of the octet and
singlet meson multiplets but it failed to be consistent with
the observed octet and decuplet multiplets of baryons when
their properties became firmly established experimentally.

The next development in the theory was by Gell-Mann
and Zweig (1964), independently. They noticed that although
from the group theory viewpoint, the Sakata model gives the
wrong multiplet structure of baryons 3 $\otimes$ 3 $\otimes$ 3 = 15 $\oplus$ 6 $\oplus$ 3 $\oplus$ 3.
But instead the form 3 $\otimes$ 3 $\otimes$ 3 = 10 $\oplus$ 8 $\oplus$ 8 $\oplus$ 1 agrees with
the experimental observations. ($\otimes$ means direct product and
$\oplus$ means direct sum). They also pointed out that all the

hadronic particles (baryons and mesons), could be built up
from three types of fundamental entity called quarks (q).
They are named as p,n,λ, (or u,d,s) each having spin $1/2\hbar$.
They are also characterized by quantum numbers ; isospin (I)
and strangeness (S) which are conserved in strong inter-
actions.   The isospin, I, is defined by the (2I + 1) charge
substates (labelled I_3) of a particle, in analogy with
angular momentum.   As it has already been hinted, the hadrons
are of two types : baryons with baryon number B = 1, and mesons
with B = 0 .   However any of their states,(I,S), may be built
up from combinations of p,n, λ quarks and their antiparticles.
The hadronic charge, isospin and strangeness quantum numbers
are related to each other by : $Q = I_3 + \dfrac{B + S}{2} = I_3 + Y/2$ (7.1)
which is called the Gell-Mann/Nishijima formula.   Here, Y is
the hypercharge quantum number.   These quantum numbers are
tabulated in Table 7.1.

Triplet particles	I_3	B	S	Y	Q	Spin($\hbar$)
p	$\frac{1}{2}$	$\frac{1}{3}$	0	$\frac{1}{3}$	2/3	$\frac{1}{2}$
n	$-\frac{1}{2}$	$\frac{1}{3}$	0	$\frac{1}{3}$	$-\frac{1}{3}$	$\frac{1}{2}$
λ	0	$\frac{1}{3}$	-1	-2/3	$-\frac{1}{3}$	$\frac{1}{2}$

TABLE 7.1

It is seen in this table that the baryon number assigned
to each quark is fractional. A consequence of this is
that the expected electric charge of quarks is also fractional.

The above theory of quarks predicts that all the
hadronic states are made up either by combining a single
quark (q) with a single antiquark ($\bar{q}$), i.e. (q.$\bar{q}$) or by
making combinations of three quarks (qqq). In the simplest
quark model, therefore, the particle states of the baryons
and mesons could be grouped into multiplets. For instance,
the baryon multiplets consist of octets and decuplets of states
with a particular spin (j) and parity (p), i.e. j^p. Fig.7.1
below shows octet states of baryons of spin parity $j^p = \frac{1}{2}^+$.
Here the quark combination (e.g. ppn) of each state in the
Gell Mann/Zweing model is also indicated.
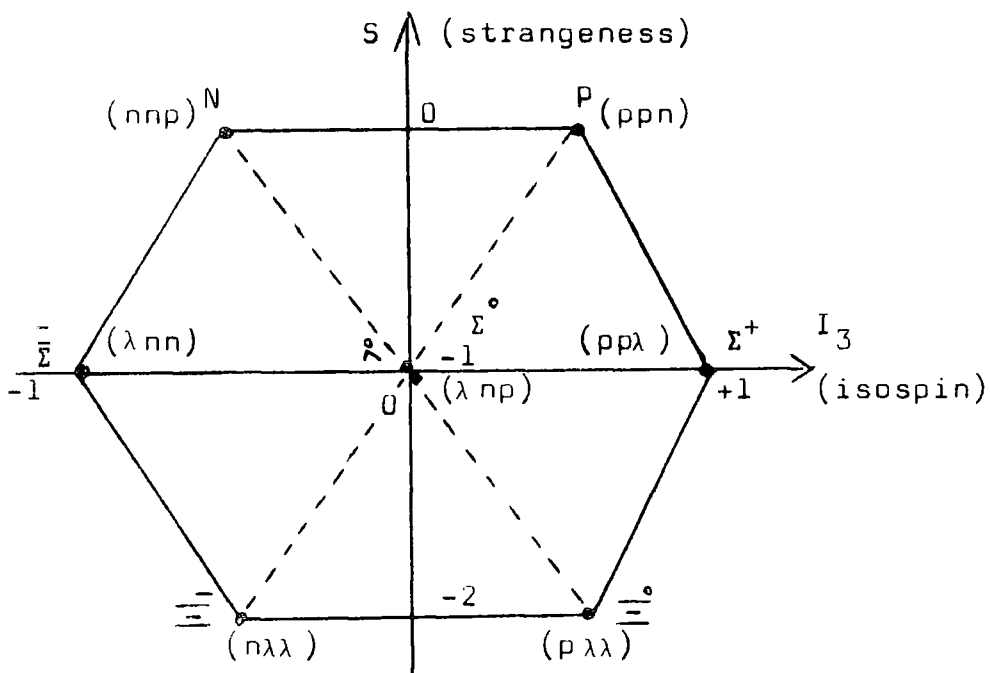
Fig.7.1 : Baryon octet, spin parity $j^p = \frac{1}{2}^+$

The quark model can account for all known strongly particle states. However, on the ground of previous experimental observation of the so known "elementary" particles such as electron, nucleon, pion, we could expect that the proposed quarks ought to be detectable if they exist as free particles. So far the result of experimentation in this direction has led to the following expected properties of them.

(a) Mass of quark

Comparing the known masses of elementary particles and their corresponding combination of quarks, it is found that $M_p \simeq M_n = M$ and $M_\lambda = M + M_\pi$. But if mesons are quark-antiquark systems, then a crude estimation of quark or anti-quark mass could be in the range of 5 GeV/C^2 to several tens of GeV/C^2.

(b) Decay scheme

A possible decay scheme of quark is shown in Table 7.2 below and it seems that only the p type quark is stable.

Quark	Decay Scheme	Lifetime
p	stable	infinite
n	$n \rightarrow p + \bar{e} + \bar{\nu}_e$	$\sim$ sec
λ	$\lambda \nearrow p + \bar{\pi}$ $\searrow \pi + \pi^0$	$\sim 10^{-10}$ sec

TABLE 7.2

(c) Some possible reactions producing quarks

If quarks exist as elementary particles, then they will be

produced in the interaction of high energy nucleon-nucleon

collisions (Ashton et al, 1973a) as follows :

$$(1) \quad N + N \longrightarrow N + N + q + \bar{q}$$

$$(2) \quad N + N \longrightarrow N + 3q \qquad\qquad (7.2)$$

$$(3) \quad N + N \longrightarrow 3q + 3q$$

The interaction will produce either a quark and its anti-

particle or the three constituent quarks of the nucleon.

Therefore, it should be possible to detect stable quarks

experimentally.

7.2 QUARK SEARCH METHODS

7.2.1 Searches at Accelerators

Accelerators have been applied to investigate quarks

that could be produced by some of reaction of eqn.(7.2). In

this method, a target is bombarded by the high energy

accelerated particle beam. A secondary beam is selected

according to the momentum in a given angle with respect to

the primary beam. This method is considered to measure the

mass and the charge of quarks or any other new particles.

To identify the secondary particles a set of electronic and

visual detectors is used as the detection system. To measure

the charge, a scintillation counter or bubble chamber is used.

In the case of employing scintillation counters, a set of them

is needed to reduce the fluctuation in determination of the

charge. Also, time of flight measurements are used independ-

ently of the charge to determine the mass of particles as well

as Cerenkov counters to measure the velocity at fixed
momentum. So far, particle accelerators show no positive
evidence for the existence of fractionally charge particles
but two sensitive experiments that have been reported are
now described. D. Antreasyan (1977), searched for non-
integer charged particles produced with large transverse
momentum in 400 GeV P-Cu collision. The motivation was that
a quark might physically be knocked out of a nucleon in a high
$p_\perp$ collision. They gave an upper limit for the invariant
production cross-section per nucleon for charge $-\frac{1}{3}$ and charge
2/3 as $8.8 \cdot 10^{-39}$ and $1.3 \cdot 10^{-39}$ cm^2 GeV^{-2} respectively. Also,
a search for tungsten ions having an additional charge of
$-\frac{1}{3}$ e has been performed by R.N.Boyd (1977). An ultra-sensitive
mass spectrometer was used to investigate the mass range of
182-192 a.m.u. No tungsten ions having fractional electron
charge were found above a level of 1 part in 1×10^{12} of the
tungsten sample over the mass range covered.

7.2.2 Searches in Stable Matter

If quarks were produced by cosmic rays, they would be
absorbed in some depth x the earth's crust or the oceans.
Over the age of the earth, $T = 4 \cdot 10^9$ years, there should be
an accumulated density of quarks in the stable matter of the
earth, which is proportional to the cosmic ray flux, j,
$(cm^{-2} s^{-1} st^{-1})$. Then, the quark density of the matter is
given by the formula,

$$\Delta(\text{quarks/nucleon}) = \frac{\pi \, j \, T}{N \, x} \qquad (7.3)$$

where N is Avogadro's number and π comes from integrating over
the flux. Taking eqn.(7.3) gives an estimation of the quark

density as 48 quarks per gram in the water of the oceans, where x = 3 km and j $\sim 5.10^{-11}$ cm^{-2} s^{-1} st^{-1}. Some methods of searching for quarks in stable matter are now described. One method is the modified Millikan (1910) oil drop experiment. The purpose is to measure the charge on a droplet of oil which is determined by its motion under the influence of gravity and electric fields in the presence of viscous drag. In the Millikan experiment, the electric and the gravitational forces on the droplet should be comparable in order to measure the precise charge. That is why for a heavier sample an improved technique is required, which is the levitation method. In this method, the test body is placed in a magnetic potential well and the charge on the body is measured by the body's motion under the influence of an electric field. Using the levitation method, Larue et al (1977) reported observing fractional charges in a total of eight heat treated niobium balls. Two balls showed a charge of $(0.377 \pm 0.09)e$ and $(-0.331 \pm 0.07)e$, where the mass of each ball was 90 µg, (Table 7.3). However, to be more confident of these results, confirmation by other workers is required. A recent summary of quark searches in stable matter by the method of oil drops and the levitometer is given by L.Jones (1977) shown in Table 7. 3 . Notice that the upper limits of the quark flux shown in the table using different techniques varies widely.

^{a}Sample "rubbed" on spheres of polyethylene to transfer quarks to spheres.

^{b}An enrichment factor is included in this figure.

^{c}Values given are upper limits except last three entries.

^{d}Flux values given assuming Eq.(5.2) ($y = 5 \times 10^7$ g cm^{-2}) as well as a smaller value of y, smaller than that corresponding to the existing oceans ($y = 5 \times 10^1$ g cm^{-2}).

^{e}One pellet of q = 1/3 e reported, although systematic uncertainties precluded quark claim.

^{f}Most pellets appeared to show residual q = 1/3 e, although systematic uncertainties precluded quark claim.

^{e}Two pellets of residual charge q = (+ 0.337 $\pm$ 0.009)e and q = (-0.331 $\pm$ 0.070)e reported. Positive evidence for existence of fractional charge on matter claimed.

TABLE 7.3 : Stable matter quark searches. Oil drops, levitometer (After Jones,(1977)).

Reference	Technique	Source material	Sample mass (gm)	No. of samples	Quarks per nucleon ρ	Corresponding quark flux upper limits ϕ $(cm^2\ sr\ sec)^{-1}$
Millikan, 1910	Oil drop	Water	10^{-11}	~100	$<10^{-13}$	
Chapka, Schiffer, and Stephens, 1966	Oil drop	Sea water,[a] air	6×10^{-11}	1000	$<10^{-14}$ [b]	
Gallinaro and Morpurgo, 1966	Diamagnetic levitometer	Graphite	10^{-9}	70	$<10^{-18}$	$10^{-4}-10^{-7}$
Stover, Moran, and Trischka, 1967	Ferromagnetic levitometer	Iron	10^{-6}	2	$<10^{-19}$	$10^{-5}-10^{-8}$
Rank, 1968	Oil drop	Mineral oil, soy bean oil, cod liver oil, peanut oil	10^{-10}	46 45 17 20	$<10^{-20}$ [b]	$10^{-6}-10^{-9}$
Braginskii et al, 1968	Diamagnetic levitometer	Graphite and sample mixed	10^{-8}	36	$<10^{-17}$	$10^{-3}-10^{-6}$
Johnston, 1969	Superconducting levitometer	Niobium	9×10^{-6}	2	$<10^{-19}$	$10^{-5}-10^{-8}$
Morpurgo, Gallinaro, and Palmieri, 1970	Diamagnetic levitometer	Graphite	5×10^{-7}	75	$<5\times10^{-19}$	$5\times10^{-5}-5\times10^{-8}$
Hebard and Fairbank, 1971	Superconducting levitometer	Niobium	7×10^{-5}	2	2×10^{-20} [e]	$2\times10^{-6}-2\times10^{-9}$
Garris and Ziock, 1974	Ferromagnetic levitometer	Iron	3×10^{-5}	12	5×10^{-20} [f]	$5\times10^{-6}-5\times10^{-9}$
LaRue, Fairbank, and Hebard, 1977	Superconducting levitometer	Niobium	9×10^{-5}	8	2×10^{-20} [g]	$2\times10^{-6}-2\times10^{-9}$
Gallinaro, 1977	Ferromagnetic levitometer	Iron	2×10^{-4}	3	$<3\times10^{-21}$	$3\times10^{-7}-3\times10^{-10}$

7.3   COSMIC RAY SEARCHES

Since the proposal of quarks by Gell-Mann (1964), searches in cosmic rays have been of interest as they contain a much higher range of particle energy than is produced by the accelerators. Experiments have been performed at different depths in the atmosphere and underground using different techniques. A summary of the progress in the subject is given by L. Jones (1977).

7.3.1 Single Particle Searches

One of the most numerous types of quark searches is by using a vertically arranged set of detectors in coincidence. It has been done by using scintillation counters in such a way that the recorded pulse height of the detectors is sensitive to the fractional charge ionization of single particles. Searches have been done at mountain altitudes, e.g.Krider(1970) and underground, e.g. Briatore (1968), respectively.   The problem with these experiments is to distinguish the recorded spurious events that are produced, for instance, by a low energy electron shower, hitting the side of the detectors and giving small relevant pulses and also statistical fluctuations. This problem could be reduced by increasing the number of the detectors or by using track detectors such as a flash tube chamber (Ashton et al, 1968) or spark chambers (Chin, 1971), to ensure that the events are indeed single and specified.

The combination of the independent single particle experiments, assuming they are all equivalent gives the overall flux limits of quarks as $j \lesssim 1.1.10^{-11}$ $(cm^{-2} \ sec^{-1} \ st^{-1})$ for e/3, and $j \lesssim 2.4.10^{-11}$ $(cm^{-2} \ sec^{-1} \ st^{-1})$ for 2e/3 with 90% confidence level (see L. Jones, 1977).

7.3.2 Search in E.A.S.

Since extensive air showers are produced by the inter-action of energetic primary particles ($E_p \geq 10^{14}$ eV) with air nuclei, it is likely that quarks may exist as secondary particles of the shower. Many searches have been made for quarks in E.A.S, especially near the core of the shower using different techniques, often visual detectors. One exciting result was reported by McCusker et al (1969) which claimed to have observed quarks. They used a cloud chamber and found five possible quark events which gave a flux of $5.5.10^{-10}$ cm^{-2} sec^{-1} st^{-1} with charges $2e/3$. After their claim for the events to be genuine, questions were raised by a number of workers (Rahm et al.(1970) ; Kiraly et al (1970) ; Frauenfelder (1970). The criticism concerned whether the droplet count along the tracks was anomalously low due to technical problems associated with the cloud chamber technique. McCusker et al continued to repeat the experiment with somewhat improved technique. However, for a longer running time, no confirmation of the detected quarks was obtained.

The other positive result was reported by Chu et al, (1970) using film obtained from a heavy shielded liquid bubble chamber. They identified two tracks as quarks corresponding to a flux of 10^{-7} cm^{-2} sec^{-1} st^{-1}, which was sharply criticised by Allison et al (1970), and the Michigan group which designed and built the chamber (Sinclair, 1970). Their flux was quite high and in disagreement with many convincing negative results. However, the rest of the experiments searching for quarks give negative results and so far there is no strong evidence that shows quarks exist.

7.4 PRESENT EXPERIMENT

7.4.1 Introduction

In this experiment the flash tube chamber was used as the quark detector in conjunction with the E.A.S. Array which has been described in Chapter 2. Some relevant properties of the chamber are now described. The efficiency-time delay variation of the flash tubes is theoretically given in terms of the parameter afQ (Lloyd, 1960), where a is the tube radius, f is the average probability that a single electron produces a flash and Q is the average number of initial electrons produced per unit length in the neon gas. The Lloyd parameter (afQ) was empirically measured (Ashton et al, 1973) to have the value 9 ± 1 for the best fitted curve to the points (Fig.7.2) and also the curve for the particles of charge e/3 corresponding to $afQ = (\frac{1}{3})^2 .9 = 1$ is presented. It is apparent from Figure 7.2 that the difference between the efficiency for e and e/3 particles increases as T_D increases but for finding the optimum T_D for the experiment a limit is set when an e/3 track has so few flashes that it is not distinguished from random background flashes. There-fore, the time delay was chosen to be $T_D = 20$ μsec as it gives a reasonable separation in the distribution of the number of flashes along the particle tracks between charges e and e/3.

The chamber does give a good resolution to particles of charge e/3 but does not to particles of charge 2e/3 as will be shown in the following section. It is assumed that the median momentum of the muons measured in the chamber is 2.1 Gev/c, which was calculated from the muon spectrum of Hayman and Wolfendale (1962). Further, it is assumed that
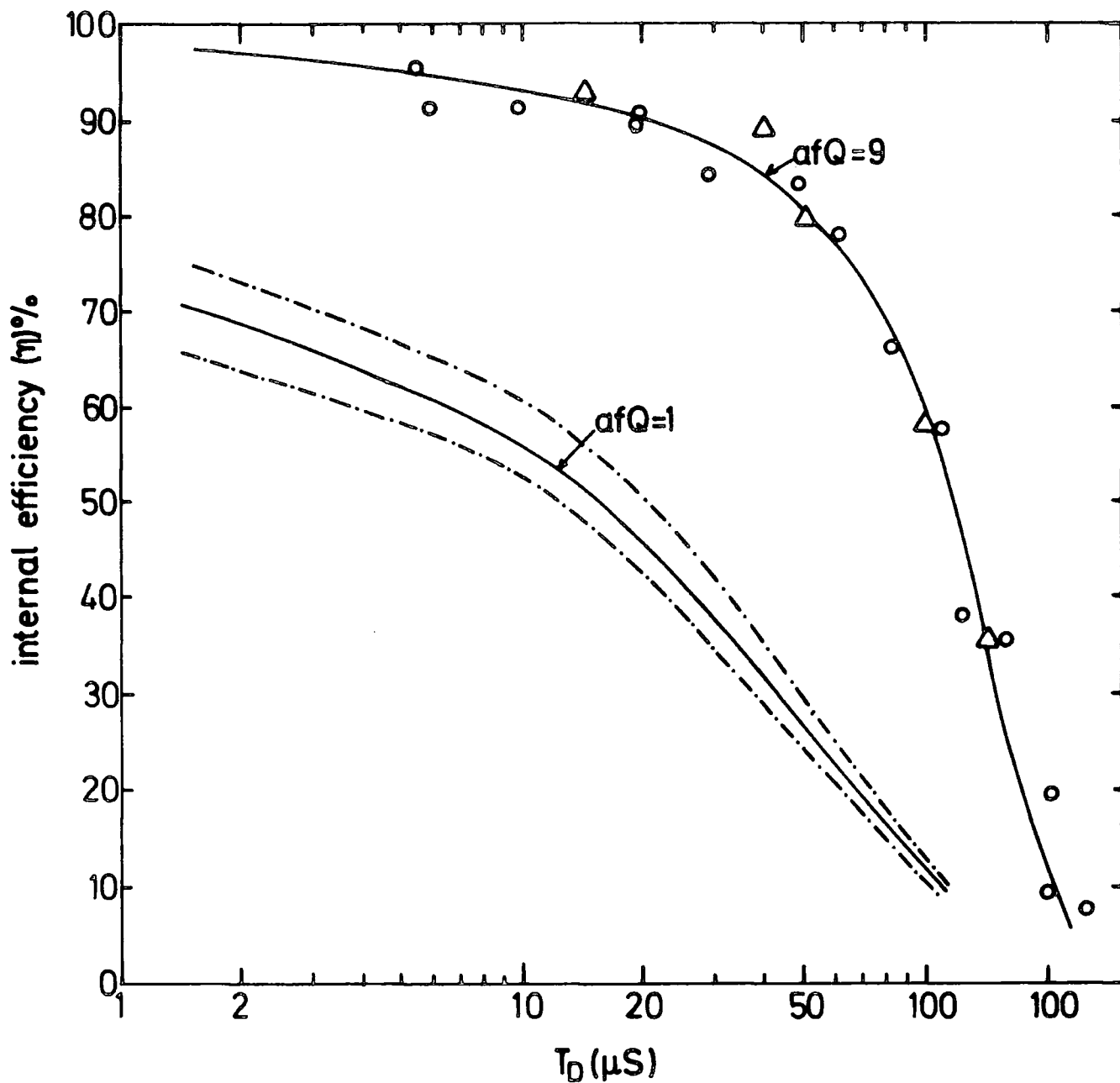
Figure 7.2 : The variation of the internal efficiency of the flash tubes
as a function of time delay, T_D. The full curve represents
the theoretical prediction with afQ = 9 as a best fit to the
experimental points. The curve with afQ = 1.0 corresponds
to a particle of charge $e/_3$. The curves —.— indicate the
latitude of uncertainty, (after Ashton et al, 1973).

the curve given by Crispin and Fouler (1970), describes the variation of the most probable ionization loss in neon as a function of muon momentum. This makes it possible to obtain $\frac{I}{I_m}$ and $\frac{I_p}{I}$ ratios which are 1.14 and 0.69 respectively, where l_m and I_p are minimum and plateau ionization losses. Taking these ratios, the values of afW for I_m and I_p are calculated to be $\frac{9^{\pm}1}{1.14} = 7.9 \pm 0.9$ and $\frac{9^{\pm}1}{0.69} = 11.3 \pm 1.3$ respectively when T_D is 20 μsec. However, these afW values are for particles of charge e,and for charge e/3 and 2e/3 they are expected to be 1/9 and 4/9th of its value as shown in Table 7. 4 . Knowing afW values makes it possible to obtain the internal efficiency at fixed T_D which is related to the expected number flashes in (F2a and F2b) which contains 96 layers of tubes as shown in Table 7.4 considering particles of charge e, e/3 and 2e/3 and also the minimum and plateau ionization regions. In column 7 the expected standard deviation (S.D.) of the expected number of flashes about the mean taking various T_D is shown (Saleh, 1975). However, considering the last two columns of the table gives the e/3 quark track efficiency to be in the range F2a and F2b = 28-50 flashes and the corresponding ranges for particles of charge 2e/3 and e are (60-70) and (70-82) flashes. Therefore, it can be seen that the chamber could not resolve 2e/3 quarks because it cannot distinguish them from particles of charge e, but it is possible to resolve e/3 quarks, if any.

Charge	Ionisation Loss	af_1Q_1	Internal efficiency (%) η_I (for $T_D = 20\ \mu s$)	Layer efficiency (%) $\eta_L = 0.873\ \eta_I$	Expected No. of flashes in F2a + F2b (96 layers)	Expected standard deviation of the distribution of number of flashes about mean = 96 n_L
e	I_p	11.3 ± 1.3	92 ± 1	80.0 ± 0.9	77.1 ± 0.9	± 4.5
e	I_m	7.9 ± 0.9	89 ± 1	77.6 ± 0.9	74.5 ± 0.9	± 4.7
$e/3$	I_p	1.26 ± 0.15	52 ± 3	45.4 ± 2.6	43.5 ± 2.6	± 5.9
$e/3$	I_m	0.88 ± 0.1	41 ± 3	35.8 ± 2.6	34.4 ± 2.5	± 5.8
$2e/3$	I_p	5.04 ± 0.6	84.5 ± 1.8	73.7 ± 1.6	70.9 ± 1.5	± 4.9
$2e/3$	I_m	3.52 ± 0.4	78 ± 2	68.0 ± 1.7	65.2 ± 1.6	± 5.3

TABLE 7.4 : The expected number of flashes produced by plateau and minimum ionising (I_p and I_m) e particles, $e/3$ and $2e/3$ quarks in F2a and F2b layers for time delay $T_D = 20\ \mu s$ (after Saleh, 1975).

7.4.2 The Basic Data and Analysis

The basic data of the flash tube (F/T) chamber for all E.A.S. triggers are 4547 events which, with the details concerning running time and the number of charge e/3 quark candidates, are presented in Table 7.5. The flash tube film events were scanned and copied on a special skeleton diagram of the chamber. The number of flashes were counted along the track of every event showing a measurable track. A measurable track is one that passes through the regions F2a (48 layers of tubes) and F2b (48 layers of tubes) with the added requirement that at least one flashed tube must occur on the track in each of the defining layers F1a(8 layers of tubes), F1b (6 layers), F3a (8 layers) and F3b(8 layers) -see Figure 6.5 . The number of triggers with 0,1,2 etc. measurable tracks for the two E.A.S. selection triggers are shown in Table 7.6, and the distribution of their number of flashes in the defined (F2a & F2b) layers of the flash tube chamber is shown in Figure 7. 3 . In the tail of the distributions, in the e/3 quark region (less than fifty flashed tubes) two quark-like tracks are observed which are presented in Figure 7.4a and 7.4b, where the full details of the two events are also given in Table 7.7. The above measurements are again performed for all analysable shower where the shower information of every event N_e, r_H, θ and ϕ are known (Table 7.6 and Figure 7.5). The shower size and core distance distributions for these events are shown for the two E.A.S. selection triggers in Figure 7.6a and 7.6b. The next step in the analysis of the data was by dividing it in two different core distance ranges of less or bigger

	Total No. of Shower Triggers	Run Time hr	Trigger Rate hr^{-1}	No. of Shower Triggers with F/T Chamber Working	No. of quark Candidates with F2a & F2b in range 17-50 regardless of whether r,N,Θ,ϕ, known	No. of shower triggers with F/T Chamber working and information available for r,N,Θ,ϕ, known	No. of quark Candidates with F2a & F2b in range 17-50 and r,N,Θ,ϕ, known
Inner Ring Trigger	2683	128	20.96$\pm$0.40	2552	2	2299	1
Outer Ring Trigger	2131	383.27	5.56$\pm$0.12	1995	0	1826	0
Total	4814	511.27		4547	2	4125	1

TABLE 7. 5   Summary of the basic data.

No. of triggers with n measurable tracks in Chamber	Inner ring trigger		Outer ring trigger	
	Frequency	Frequency xn	Frequency	Frequency xn
0	2100 (1887)	0 (0)	1606 (1457)	0 (0)
1	354 (321)	354 (321)	271 (254)	271 (254)
2	77 (71)	154 (142)	86 (83)	172 (166)
3	16 (15)	48 (45)	20 (20)	60 (60)
4	4 (4)	16 (16)	7 (7)	28 (28)
5	1 (1)	5 (5)	3 (3)	15 (15)
6	0 (0)	0 (0)	1 (1)	6 (6)
7	0 (0)	0 (0)	1 (1)	7 (7)
8	0 (0)	0 (0)	0 (0)	0 (0)
	Total No. of triggers = 2552 (2299)	Total No. of tracks = 577 (529)	Total No. of triggers = 1995 (1826)	Total No. of tracks = 559 (536)

TABLE 7.6 : The frequency distribution of observing n measurable tracks for E.A.S. selected by the inner ring and outer ring trigger respectively. The figures refer to all E.A.S. triggers and those in brackets to E.A.S. in which the core position, shower size, and arrival direction are known.
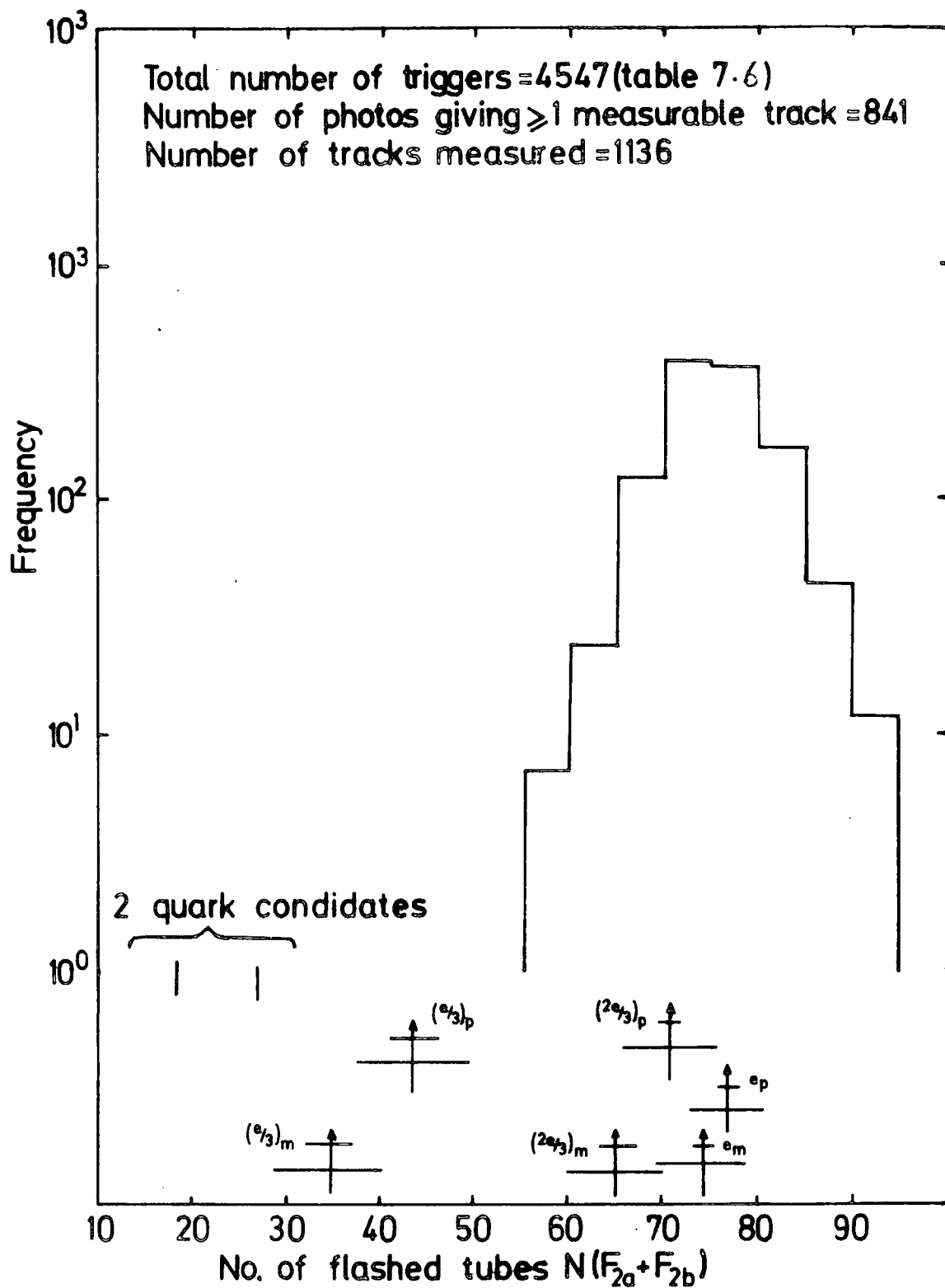
Figure 7.3 :   Frequency distribution of the observed number of
flashed tubes in F2$_a$ + F2$_b$. The arrows indicate the
expected number of flashes for minimum ionising and
plateau ionising charge e, 2e/3 and e/3 pts.   The
small bars indicate the uncertainty in the position of
the arrow and the large bars, the expected standard
deviation of the distribution.

Figure 7.4a :   Event M53 - 11E419 (inner ring trigger)

A low efficiency track

N (F2a & F2b)   =   17

r_H =   27 m

N_e = $1.4.10^5$ pts

θ = 8.5^O

ϕ = 263°

Measured projected zenith angle, α_m = -16.5^O

Predicted projected zenith angle, α_p = $+1.04^O$
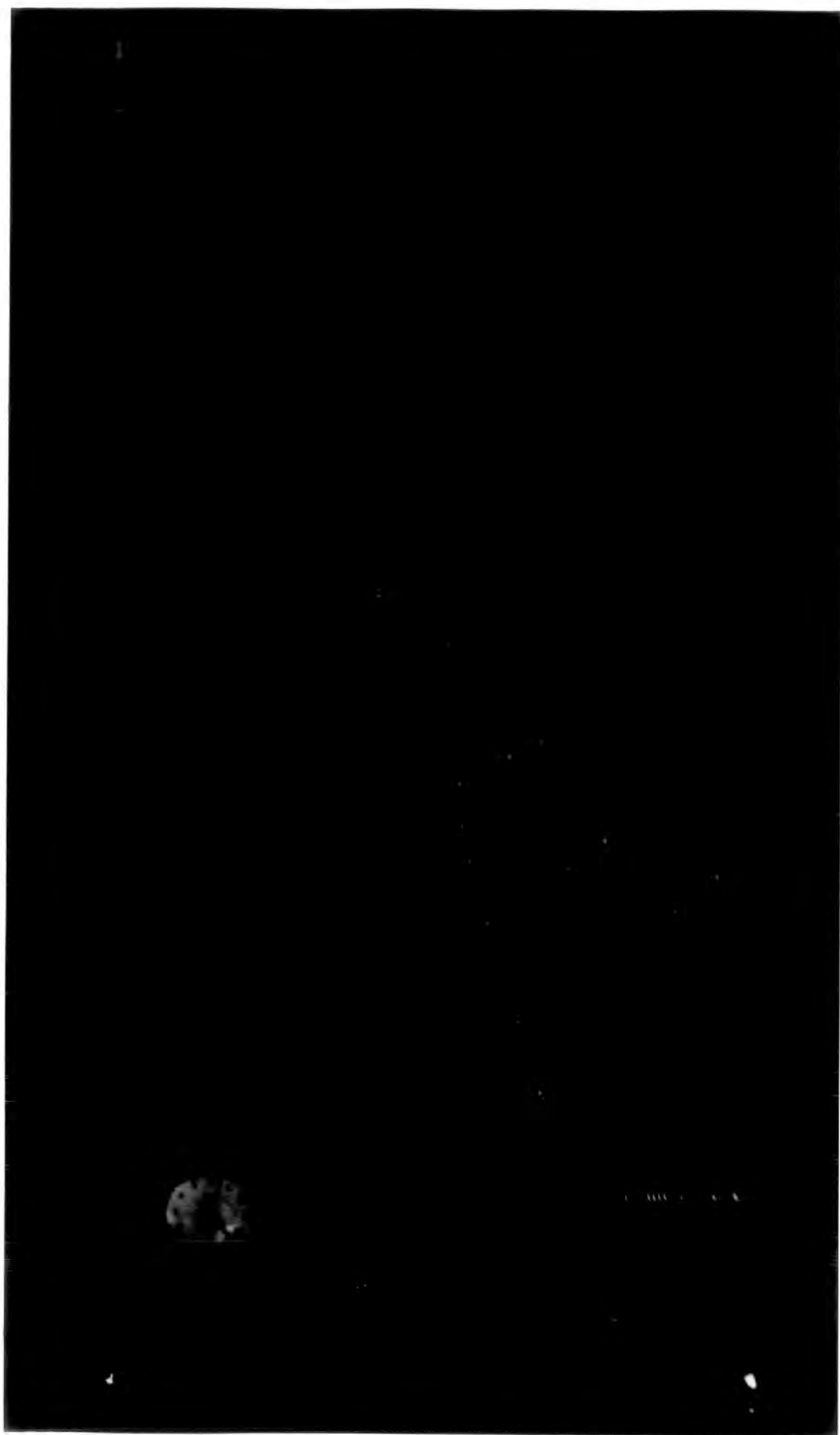
Figure 7.4b :   Event M57 - 11EA9C (inner ring trigger)

A quark candidate

$$N \; (F_{2a} \; \& \; F_{2b}) \qquad\qquad = \quad 26$$

$$r_H \qquad\qquad = \quad 4.6 \; m$$

$$N_e \qquad\qquad = \quad 1.5.10^4 \; pts$$

Measured projected zenith angle, $\alpha_m \quad = \quad +7^O$

no timing data
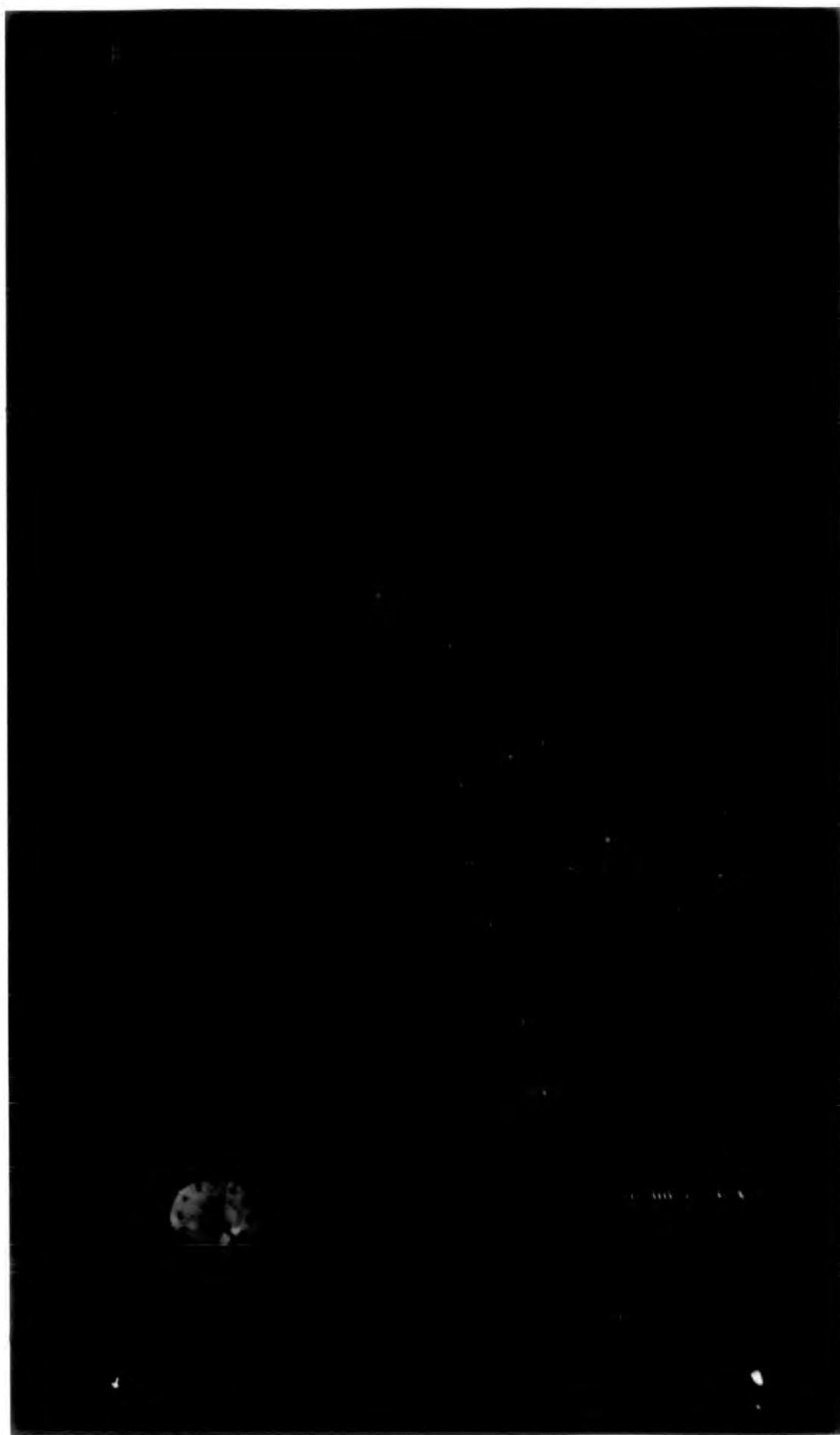
Quark Candidate	α measured	α expected	r_H (m)	Θ	ϕ	N	No. of other tracks in photo	Measured projected zenith angle of other tracks	No. of flashes on quark candidate track
Event 1	-16.5°	$+1.04^\circ$	27	8.5°	263°	$1.4 \cdot 10^5$	0	–	17
Event 2	$+7^\circ$	No timing data	4.6	–	–	$1.5 \cdot 10^4$	1	-10	26

TABLE 7.7 : Details of the two quark candidate events. α(measured) is the measured projected zenith angle of the quark candidate track in the front view of the flash tube chamber and α(expected) is the expected projected zenith angle assuming that real quark tracks are closely parallel to the E.A.S. arrival direction determined from the E.A.S. array fast timing measurements. r_H is the distance of the E.A.S. core from the centre of the flash tube chamber. Θ, ϕ, N are the zenith angle, azimuth angle and shower size of the E.A.S.
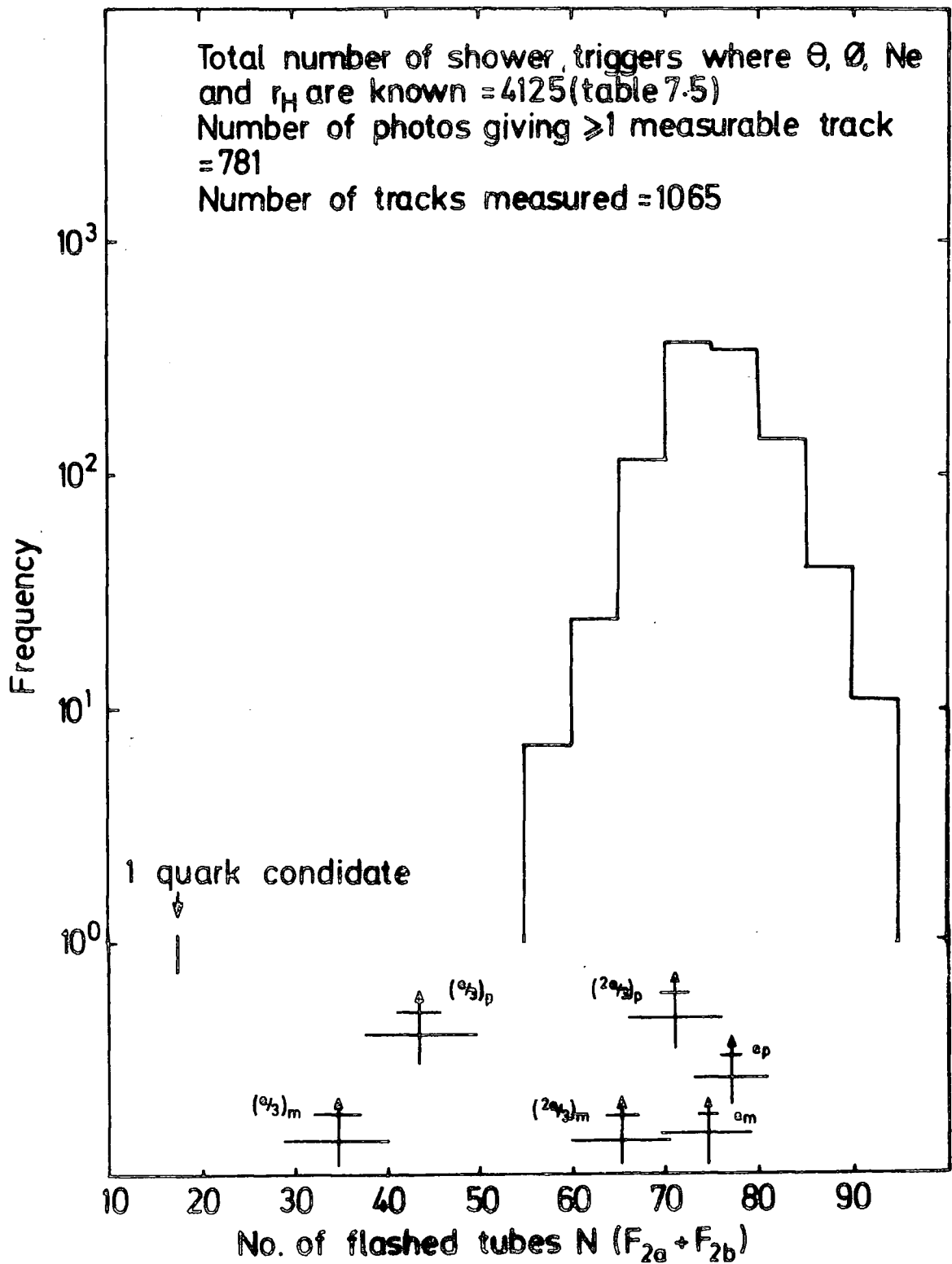
Figure 7.5 : Frequency distribution of the observed number of flashes in $F2_a$ + $F2_b$ where all shower information r_H, N_e, θ and ϕ are known. The arrows indicate the expected number of flashes for minimum ionising and plateau ionising charge e, 2e/3 and e/3 pts. The small bars indicate the uncertainty in the position of the arrow and the large bars, the expected standard deviation of the distribution.
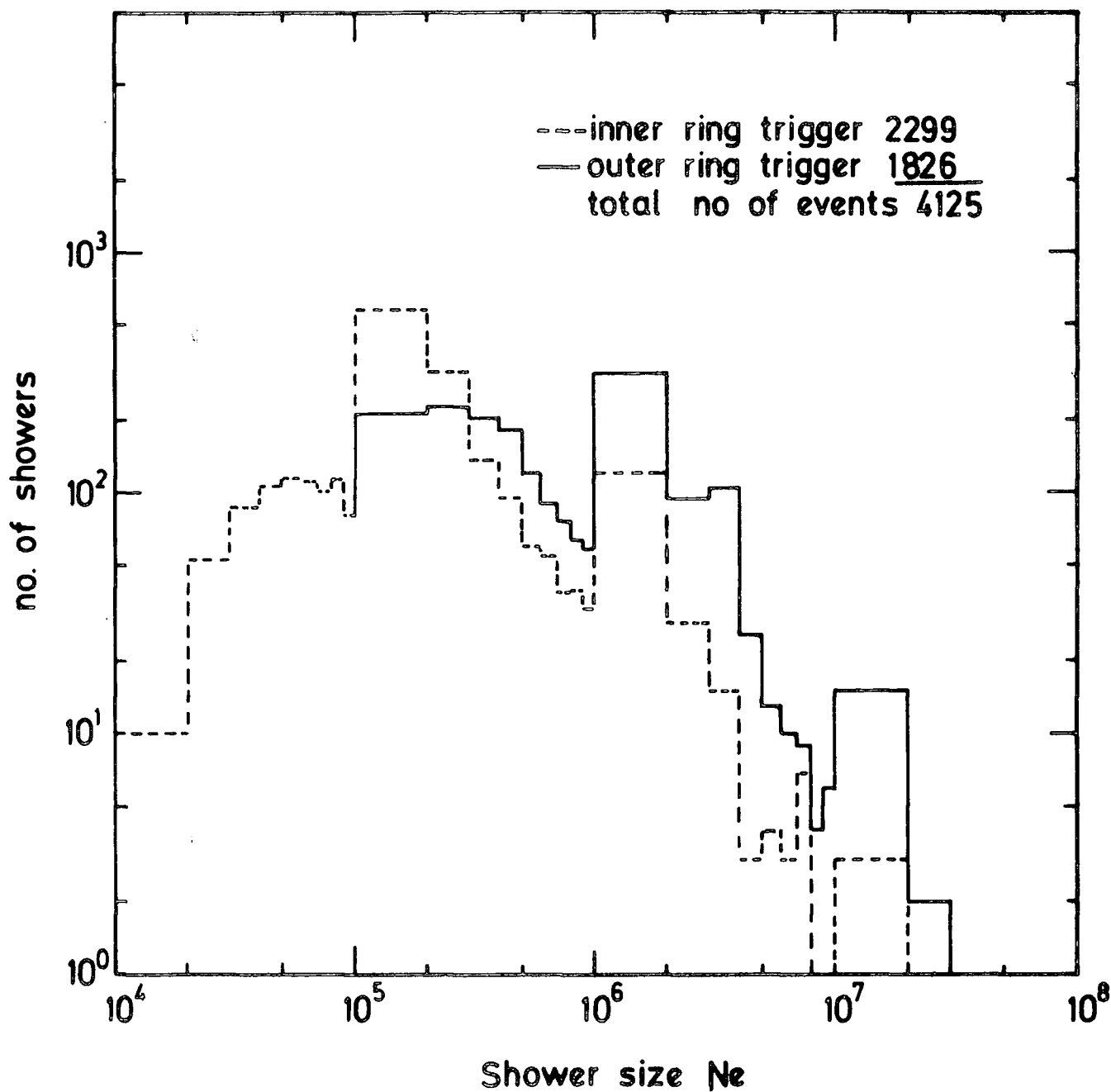
Figure 7.6a :   Shower size distribution for all measurable showers.
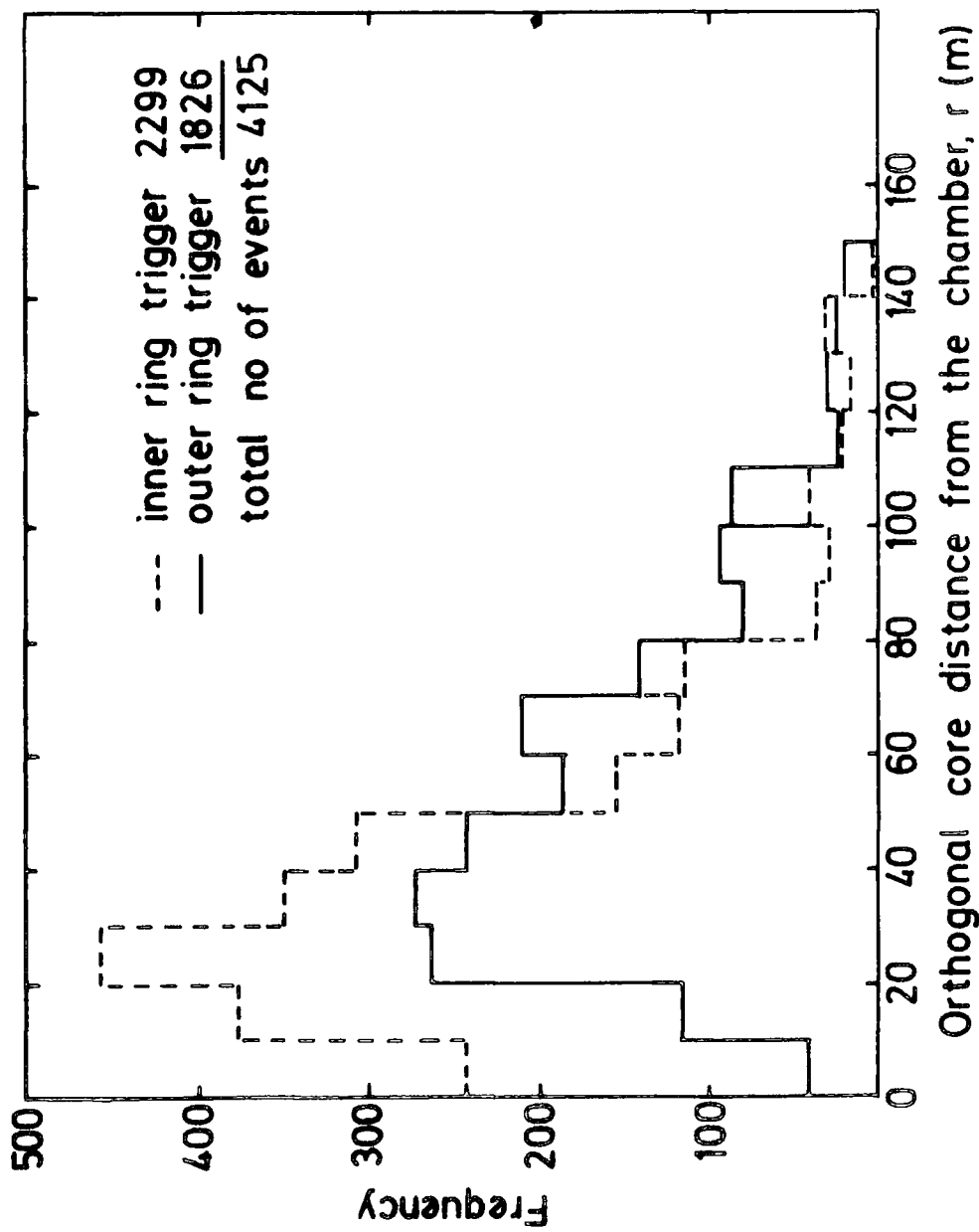
Figure 7.6b :   Core distance distribution for the 4125 analysable shower triggers.

than 75 meters as shown in Table 7.8 and Figure 7.7 to 7.8b.
From Figure 7.7 and Table 7.7, it is seen that the two quark
candidates are in the small core distance range and both
are observed in E.A.S. selected by the inner ring selection
system but only one has all shower information.

7.4.3 The Quark Candidates

To decide whether the two observed quark-like events
are genuine quarks, it is first necessary to consider the
expected number of background muons. Background muons may
simulate low efficiency tracks in the expected e/3 quark
region of (17-50) flashes in (F 2a & F 2b) if they traverse
the sensitive volume of the chamber in the time domain 100 to
161 μs before the chamber trigger (see Figure 7.2).   Knowing
the calculated flux of muons (31.5 sec^{-1}) through the chamber
acceptance volume, the expected number of background muons
simulating e/3 quarks in a sample of 4,547 triggers is
4547 x 61.10^{-6} x 31.5 = 8.7.   This is larger than the observed
number of 2 and the lack of background muon events can only
be accounted for as a statistical fluctuation.   Therefore,
there is a high possibility that the two observed events are
background muons that simulate e/3 quark-like tracks.
Examining the quark candidates individually shows that for
the first event, there is evidence of knock on electron
flashes on the quark-like track. Also, the measured projected
zenith angle of the quark-like track is -16.5° compared with
an expected value of + 1.0° assuming that a genuine quark
track would be close in direction with the E.A.S. arrival
direction.   This evidence strongly suggests that the first
event is a background muon.

No. of n measurable tracks in chamber	Frequency of n tracks in chamber $r_H <75$ m	Frequency X n	Frequency of n tracks in chamber $r_H \geqslant 75$ m	Frequency X n	Frequency of n tracks in chamber $r_H > 0$	Frequency X n
0	2863	0	481	0	3344	0
1	472	472	103	103	575	575
2	121	242	33	66	154	308
3	22	66	13	39	35	105
4	5	20	6	24	11	44
5	1	5	3	15	4	20
6	1	6	0	0	1	6
7	1	7	0	0	1	7
8	0	0	0	0	0	0
Totals	3486	818	639	247	4125	1065

TABLE 7.8 : Frequency of observing no. of measurable tracks in chamber for different ranges of core distance.
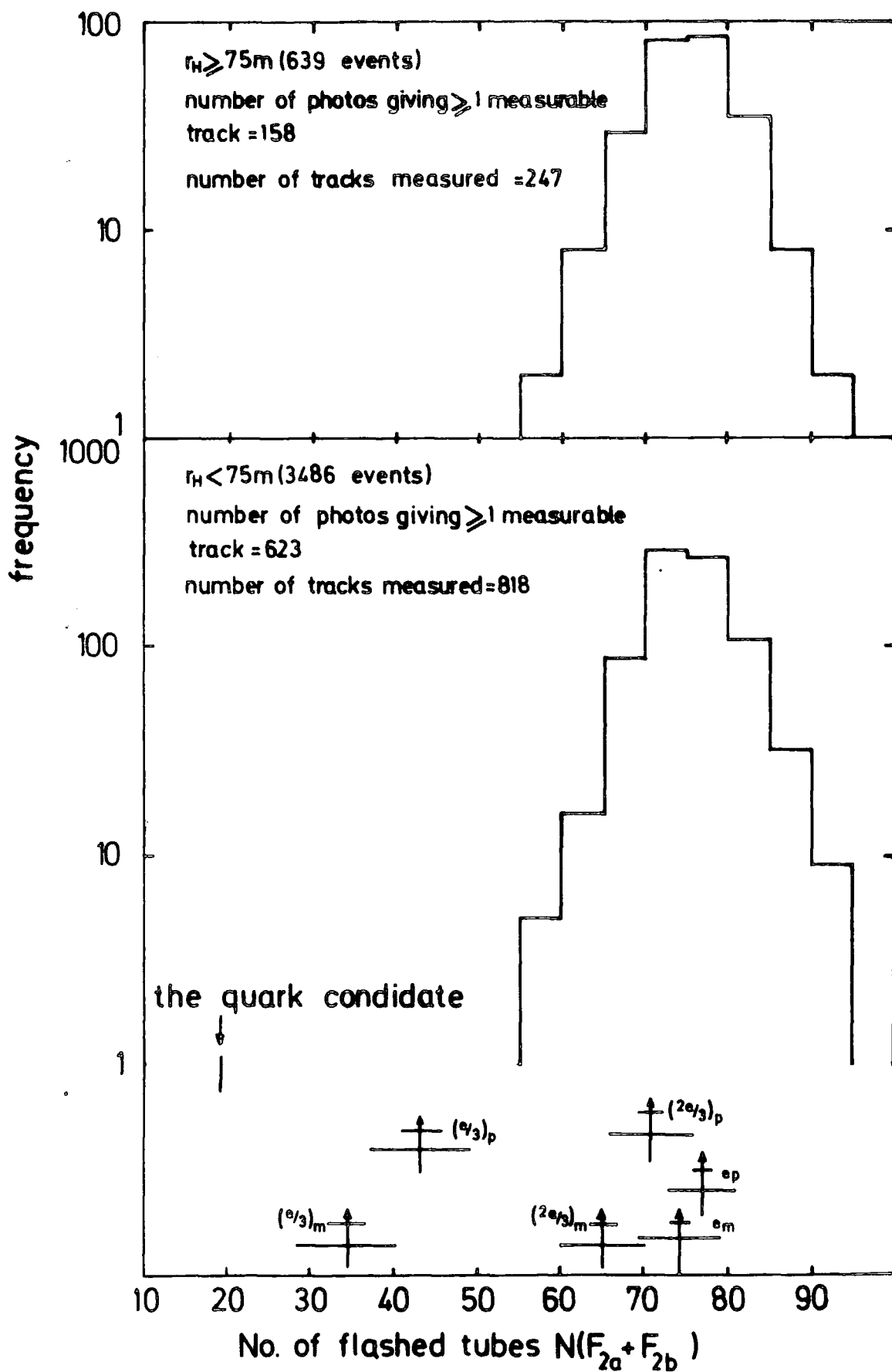
Figure 7.7 : Frequency distribution of the observed number of flashes
in $F2_a + F2_b$ for different ranges of core distance. The
events in the expected region of number of flashes in
$F2_a + F2_b$ for charged e/3 pts are also indicated.
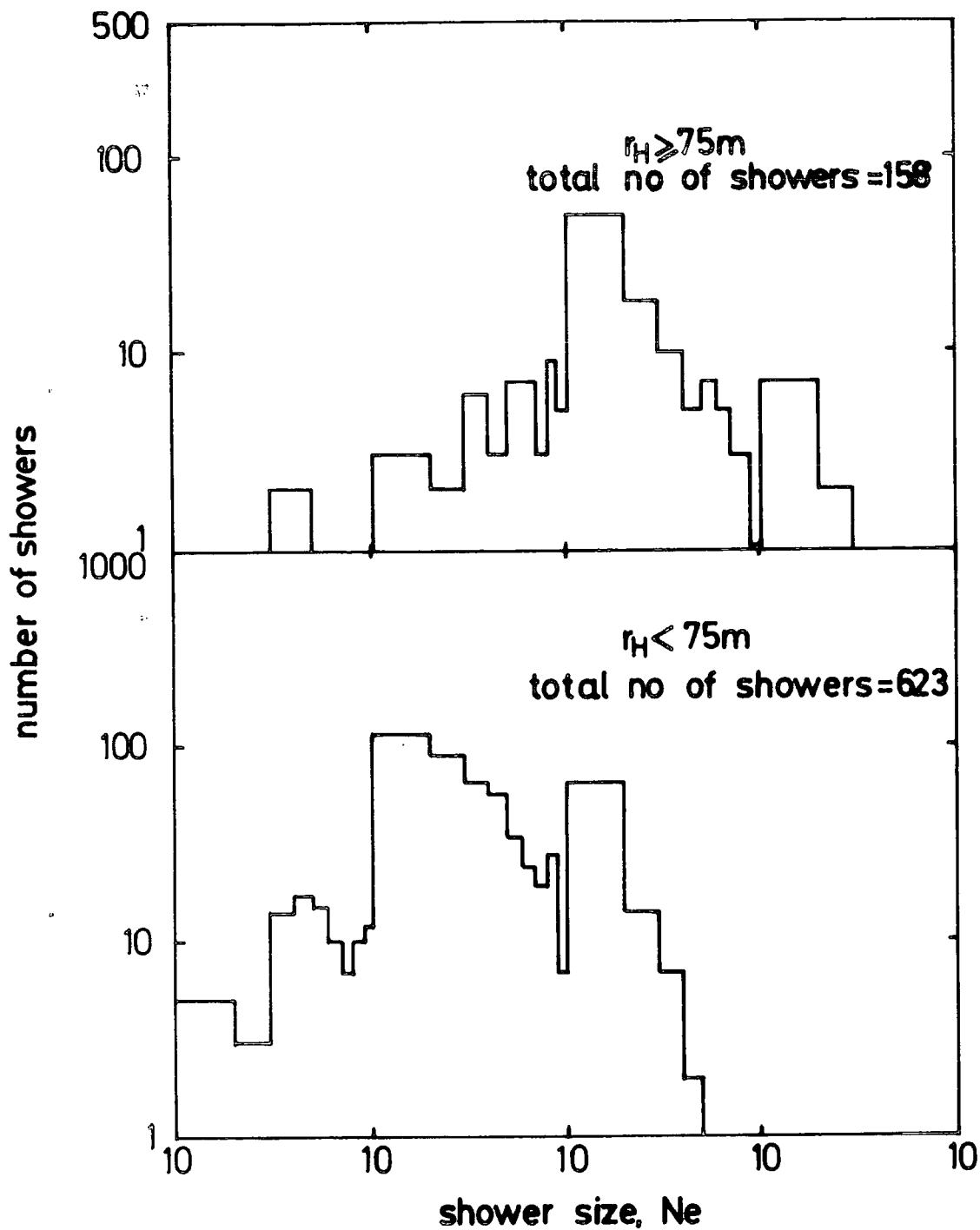
Figure 7.8a : Shower size distribution of events with ≥ 1
measurable track in chamber for different ranges
of core distance.

Total number of showers with $r_H < 75m = 623$
Total number of showers with $r_H > 75m = 158$

Frequency

Core distance r_H (m)

75m
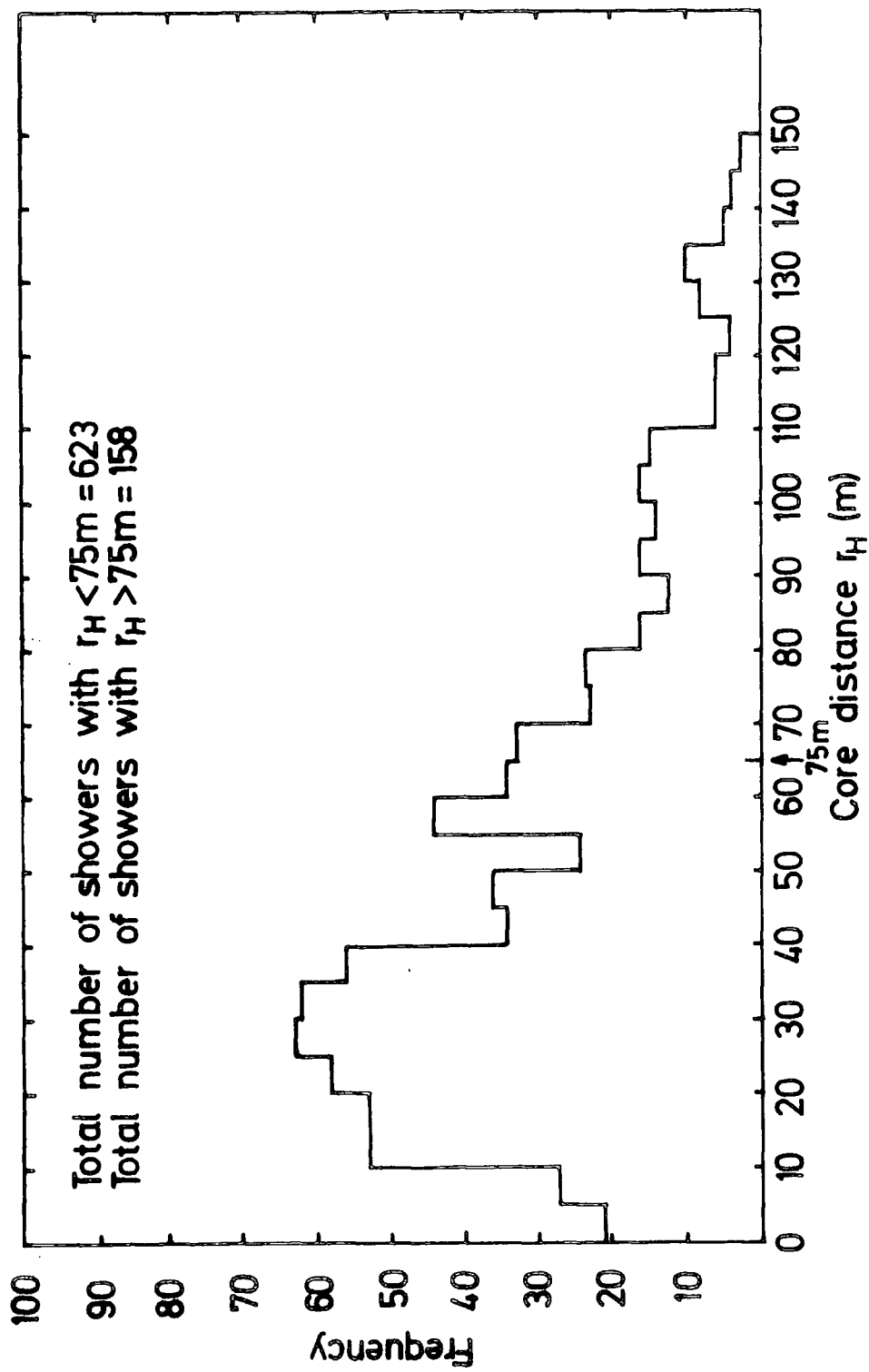
Figure 7.8b : Core distance distribution of showers with $\geqslant 1$ measurable track in chamber.

The second event also shows evidence for a low efficiency knock on electron track having a total of 4 flashed tubes occurring just below the middle of F2a . For a genuine quark track producing a knock on electron the number of flashed tubes on this track should be larger. Also, it is seen from Figure 7.4b that the quark-like track makes a large angle with the high efficiency track in the chamber which is almost certainly related to the E.A.S. producing the trigger. Unfortunately, no fast timing measurement was available from the E.A.S array to determine the shower arrival direction for this event but the evidence presented above is sufficient to rule out it being a genuine quark.

7.4.4 Conclusion

From a sample of 4547 E.A.S. triggers covering the size range 10^4 - 10^7 particles and the core distance range 0-100 m from the flash tube chamber, no evidence for a finite flux of charge e/3 quarks has been found. In all 1,136 tracks of penetrating charge e particles were measured. Thus the ratio of penetrating charge e/3 particles to penetrating charge e particles is $< \frac{1}{1,136}$ for E.A.S. in the size range and core distance range detailed in the text.

CHAPTER 8

THE ARRIVAL DIRECTIONS OF E.A.S

IN GALACTIC COORDINATES

8.1   INTRODUCTION

As the earth spins around its axis, different parts of the sky will be scanned by an instrument on the earth. Thus, if point sources of high energy cosmic rays exist or there is anisotropy in their arrival directions, then a variation in detection rate with sidereal time is expected. Time variations of E.A.S may also be produced by changes in atmospheric temperature and pressure but these effects should average themselves out over a long observation time.

8.2   PREVIOUS ANISOTROPY MEASUREMENTS IN THE E.A.S ENERGY RANGE

Since the discovery of cosmic rays in (1912), efforts have been made by many workers to find any significant aniso-tropy of the primary flux in sidereal time. No positive result has been obtained or if it has, it has not been confirmed by other similar experiments.   In recent years (after 1975) more precise experiments have been carried out. The first strong evidence of an anisotropy in the primary energy range of $(10^{13}-10^{14})$ eV, was given by Gombosi et al (1975) and Nagashina et al (1977).

In the higher energy range, between 10^{14} and 10^{17} eV, a review paper by Linsley and Watson (1977) also gave positive evidence for an anisotropy which was supported by the positive experimental result of Pollack et al (1978) where the shower primary energy range of $6.10^{16}-10^{20}$ eV, was investigated.

In these experiments the anisotropy was specified by
the amplitude of the first harmonic which was fitted to the
observed sidereal variation. Amplitudes of previous work
were examined and summarized by Wolfendale et al (1977,1978)
and Kiraly et al (1979) and are shown in Figure (8.1). Two
features of this analysis are of particular interest in under-
standing the nature and origin of cosmic rays. As is shown
in the figure, the first feature is the increase of aniso-
tropy with energy. Second, is the change of slope of aniso-
tropy versus energy at around 3.10^{15} eV where the primary
energy spectrum also has a change of slope.

8.3   PRESENT WORK

8.3.1 Experimental Arrangement

The Durham E.A.S. array was described in Chapter two
and has been used in the present experiment to detect E.A.S
using both the inner and outer ring triggering modes. The
outer ring trigger was also used independently, where the
record of the events with relatively greater shower size
range was desired.

The advantage of this array is its sensitivity to
the shower size range of (10^5-10^6) particles which covers
particle energies around 3.10^{15} ev which is of particular
significance in measurements of anisotropy as this is the
energy region in which the primary energy spectrum changes
slope.

Apart from the shower size, the required parameters
from the array were the occurrence time of the events and
also the arrival direction,(the zenith angle, θ, and azimuth
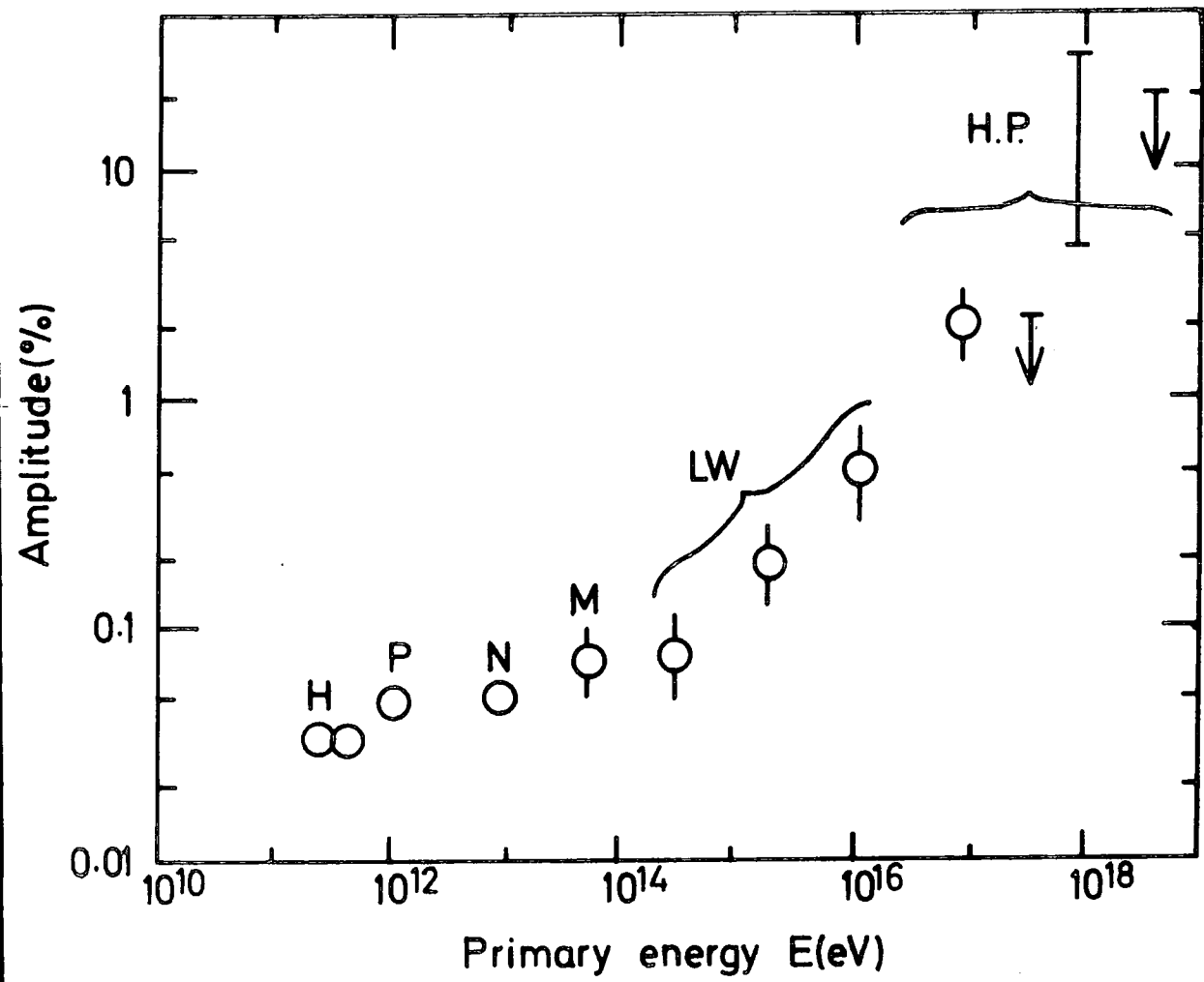
Figure 8.1 :   Amplitude of harmonic analysis versus
                    primary energy (after Wolfendale, et al 1977,1978)

angle, ϕ, of individual showers which is obtained from the timing information of the shower front). From knowing the arrival direction (θ, ϕ) of the primary particles, it is possible to calculate its corresponding arrival direction in celestial coordinates (right ascension, RA, and declination,δ), where the conversion was performed by the equations given by Prescott (1977) which are as follows :

(a) $\quad \sin \delta \quad = \quad \sin \delta_0 \cos\theta + \cos\delta_0 \sin\theta \cos\phi$

(b) $\quad \sin H \quad = \quad \dfrac{\sin\theta \; \sin\phi}{\cos \delta}$

$$(8.1)$$

(c) $\quad RA \quad = \quad \gamma + H$

(d) $\quad \cos H \quad = \quad \dfrac{\cos\theta - \sin \delta_0 \sin \delta}{\cos \delta \; \cos\delta_0}$

where $\qquad \delta_0 \; = \quad$ latitude of the array (54.75^0)

$\qquad\quad \gamma \; = \quad$ local sidereal time

$\qquad\quad H \; = \quad$ Hour angle

A more meaningful picture of these parameters and their relationship is given in Figure (8.2).

The measured right ascension and declination of individual showers have been converted into galactic coordinates (latitude and longitude) and the following
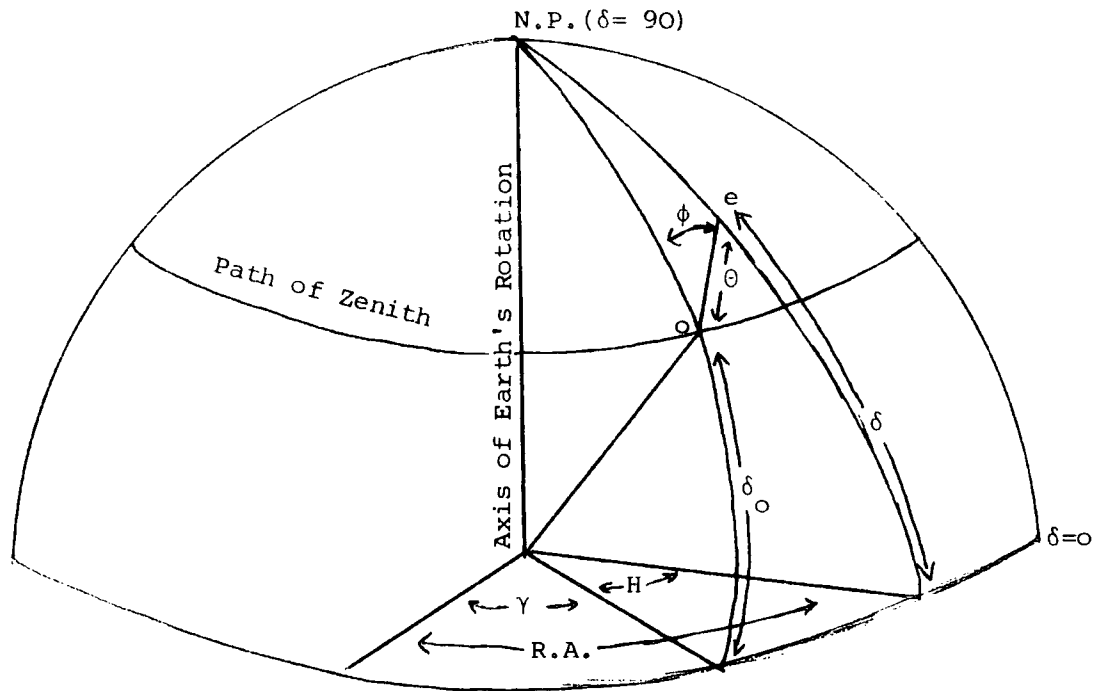
Figure 8.2 :   Presentation of the arrival direction
                of an event e in celestial coordinates
                where o is the projection of the array

formulae given by Lang (1974) were used :

(a) $\sin b'' = \sin\delta \cos 62.6^O - \cos\delta \sin(RA-282.25^O)\sin 62.6^O$

(b) $\sin(\ell'' -33) = \dfrac{\cos\delta \sin(\alpha -282.25^O)\cos 62.6^O + \sin\delta \sin 62.6^O}{\cos b''}$

$$(8.2)$$

(c) $\cos(\ell'' -33) = \dfrac{\cos\delta \cos(\alpha -282.25^O)}{\cos b''}$

where $\ell'' $ = galactic longitude

             $b'' $ = galactic latitude

To obtain the right ascension, it is seen from equation (8.1c) that a knowledge of the sidereal time of each individual shower is required. The sidereal time is obtained from the solar occurrence time of the event which is discussed in the next section.

8.3.2 Conversion of Local Solar Time to Local Sidereal Time

The E.A.S used in the present analysis were recorded during the period March to July 1977. For each event the local time of its occurrence was recorded. During the period March 21st to October 23rd 1977 local time was British summer time which is one hour ahead of Greenwich mean time. Having established the Greenwich mean time (which is also called Universal time) of each event the local sidereal time of its occurrence was found using the Astronomical Ephemeris for 1977. The procedure is best illustrated by an example.

Example   What is the local mean sidereal time of an EAS observed
on March 28th 1977 at 18 hr 26 min 43 sec local time.

   18hr 26min 43sec local time = 17 hr 26min 43sec Greenwich
                                         mean time (GMT)

Zero hours GMT on March 28th 1977 = 12hr 21min 10.889sec side-
real time at Greenwich (see p 13 of 1977 Astronomical Ephemeris)

Add 17hr. 26min 43sec

$$\underline{17\text{hr } 26\text{min } 43\text{sec}}$$
$$29\text{hr } 47\text{min } 53.889\text{sec}$$

Add 2min 51.946sec for gain of
sidereal time on GMT in
17hr 26min 43sec. See p 515
of 1977 Astronomical Ephemeris

$$\underline{2\text{min } 51.946\text{sec}}$$
$$29\text{hr } 50\text{min } 45.835\text{sec}$$

Subtract 24hr to give the local
mean sidereal time at Greenwich

$$\underline{24\text{hr}}$$
$$5\text{hr } 50\text{min } 45.835\text{sec}$$

Subtract 6min 17.2sec to give the
local mean sidereal time at Durham
which is at a longitude 1° 34.3
west of Greenwich

$$\underline{6\text{min } 17.200\text{sec}}$$

Local mean sidereal time of the
EAS

$$\underline{\underline{5\text{hr } 44\text{min } 28.635\text{sec}}}$$

8.3.3 The Sin-Ambiguity

To calculate the celestial and galactic coordinates, the first three equations of (8.1) and the first two equations of (8.2), seem to be sufficient to obtain these coordinates. This is true for obtaining declination (δ) and galactic latitude ($b^{''}$) as their range variation is from 0 to $\pm$ 90 degrees. Therefore if their sin-values from equations (8.1a) and (8.2a) is between 0 and $\pm$ 1 the angle derived would be 0 to $\pm$ 90 which satisfy the required values. But for obtaining the hour angle (H) and galactic longitude ($\ell^{''}$) their range variation is from 0 to 360° equations (8.1b) and (8.2b) are not sufficient, since from the following table ;

Angle Degree	0-90	90-180	180-270	270-360
sin	+	+	-	-
cos	+	-	-	+

Table 8.1

If the sin-value is between 0 to 1 or positive the angle could be in the range of (0-90) or (90-180) degree. Also if the sin-value is between 0 to -1 or negative then the angle could be in the range of (180-270) or (270-360) degree. To remove this sin-ambiguity another equation for 'cos' was independently used to find the relevant angle. The equations for obtaining hour angle (H) and galactic longitude ($\ell^{''}$) are equation (8.1d) and (8.2c) respectively. To show the sin-

ambiguity more clearly an example of obtaining galactic coordinates through the equations (8.1 and (8.2) is now given.

starting data

information

$$\begin{cases} \theta = 35^{\circ} \\ \phi = 162^{\circ} \\ \delta_{o} = 54.75^{\circ} \\ \gamma = 11.5 \text{ hr} \end{cases}$$

To obtain the celestial coordinates equations (8.1) are used :

$$\sin \delta = \sin \delta_{o} \cos\theta + \cos\delta_{o} \sin\theta \cos\phi \rightarrow \delta \text{ (declination)} = 20.8^{\circ}$$

$$\sin H = \frac{\sin\theta \sin\phi}{\cos\delta} \rightarrow \sin H = 0.19 > 0 \rightarrow H = \text{arc sin } (0.19)$$

According to lable 8.1 the hour angle (H) could have two values :

$$H : \begin{cases} H' = 10.93^{\circ} \\ \text{or} \\ H'' = \pi - H' = 169.07^{\circ} \end{cases} \quad (1)$$

To choose the relevant H value the following formulae is used :

$$\cos H = \frac{\cos\theta - \sin \delta_{o} \sin\delta}{\cos \delta_{o} \cos\delta} = 0.98 > 0$$

Since the sin and cosin values of H are both positive then from Table 8.1 the hour angle (H) is in the range of (0-90) degree. It is thus concluded from (1) that

$$H = H' = 10.93^{\circ}$$

To obtain the right ascension

$$RA = \gamma + H$$

and having
$$\begin{cases} H = 10.93^\circ = 0.73 \text{ hr} \\ \\ \gamma = 11.5 \text{ hr} \end{cases} \longrightarrow RA = 12.23 \text{ hr}$$

So the celestial coordinates are $\underline{RA= 12.23 \text{ hr}}$ and $\underline{\delta = 20.81^\circ}$

which are converted to corresponding galactic coordinates

(b'', ℓ'') by equations (8.2) as follows :

$$\sin b'' = \sin \delta \cos 62.6 - \cos \delta_0 \sin (RA-282.25) \sin 62.6$$

and having
$$\begin{cases} RA = 12.23 \text{ hr} \\ \delta = 20.81^\circ \end{cases} \longrightarrow b'' \text{ (galactic latitude)} = 79.57^\circ$$

Now to evaluate galactic longitude (ℓ''), where its equation

is

$$\sin (\ell'' - 33) = \frac{\cos \delta \sin (RA-282.25) \cos 62.6 + \sin \delta \sin 62.6}{\cos b''}$$

$$\begin{cases} \sin (\ell'' - 33) = -0.61 < 0 \\ \\ \text{apparent arc } \sin (\ell'' - 33) = -37.8^\circ = a \end{cases}$$

According to Table 8.1 the angle ($\ell'' - 33$) could have two values :

$$\begin{cases} \ell'' - 33 = 2\pi - |a| \longrightarrow \ell'' = 335.2 \\ \\ \text{or} \qquad\qquad\qquad\qquad\qquad\qquad\qquad (2) \\ \\ \ell'' - 33 = \pi + |a| \longrightarrow \ell'' = 250.8^\circ \end{cases}$$

To choose the relevant galactic longitude (ℓ'') the following formula is used

$$\cos(\ell'' - 33) = \frac{\cos\delta\cos(RA - 282.25^{\circ})}{\cos b''}$$

$$\cos(\ell'' - 33) = -0.79 < 0$$

Since the sin and cosin of the angle ($\ell'' - 33$) are both negative, then from Table 8.1, ($\ell'' - 33$) is in the range (180-270) degree. It is thus concluded from (2) that ;

$$\ell'' - 33 = \pi + |a| \rightarrow \ell'' = 250.8^{\circ}$$

Thus the galactic coordinates are $\underline{\ell'' = 250.8}$ and $\underline{b'' = 79.57^{\circ}}$

8.3.4 Method of Calculating the Expected Number of Showers in Galactic Coordinates Assuming they are Isotropically Distributed in Space

Having obtained the measured number of showers arriving from different cells of galactic coordinates, it is required to calculate the expected numbers assuming that the occurrence of an EAS is uniformly probable in sidereal time. To obtain such expected numbers the following procedures were performed ;
(a) The probability of a shower arriving with zenith angle θ and azimuthal angle ϕ
$p(\theta, \phi)$ was calculated as follows ;
Assume $I(\theta) = I(o)\cos^n\theta$ m^{-2} s^{-1} st^{-1} for a horizontal collecting area A in time t .
No. of events with $\theta \rightarrow \theta + d\theta$ = $I(\theta)A\cos\theta \cdot 2\pi\sin\theta d\theta \cdot t$

$$= I(0)\cos^n\theta \cdot A\cos\theta \cdot 2\pi\sin\theta \cdot d\theta \cdot t$$

$$= I(0) \cdot A \cdot 2\pi t \cos^{n+1}\theta \sin\theta d\theta$$

$$= const \cos^{n+1}\theta \sin\theta d\theta$$

The probability that a shower of given zenith angle has ϕ in range $\phi \rightarrow \phi + d\phi = \dfrac{d\phi}{2\pi}$. The probability that a shower has zenith angle in the range $\theta \rightarrow \theta + d\theta$ and ϕ in the range $\phi \longrightarrow \; + d\phi$ is thus

$$p(\theta, \phi) d\theta d\phi = \text{const.} \cos^{n+1}\theta \; \sin\theta \, d\theta \; \frac{d\phi}{2\pi}$$

$$= K\cos^{n+1}\theta \, \sin\theta \, d\theta \, d\phi$$

Requiring $\displaystyle\int_{0}^{\pi/2} \int_{0}^{2\pi} p(\theta, \phi) \, d\theta d\phi = 1$

$$K \int_{0}^{\pi/2} \int_{0}^{2\pi} \cos^{n+1}\theta \cdot \sin\theta \, d\theta d\phi = 1$$

$$K \int_{0}^{\pi/2} \cos^{n+1}\theta \, \sin\theta \, d\theta \int_{0}^{2\pi} d\phi = 1$$

$$K \int_{\cos\theta = 0}^{\cos\theta = 1} \cos^{n+1}\theta \; d(\cos\theta) . 2\pi = 1$$

$$K \left[\frac{\cos^{n+2}\theta}{n+2} \right]_{\cos\theta=0}^{\cos\theta=1} . 2\pi = 1$$

$$K \left[\frac{1}{n+2} \right] . 2\pi = 1 \longrightarrow K = \frac{n+2}{2\pi}$$

$$p(\theta, \phi) \, d\theta d\phi = \frac{n+2}{2\pi} . \cos^{n+1}\theta . \sin\theta d\theta \, d\phi$$

The probability of a shower being incident at θ, ϕ.

$$p(\theta, \phi) = \frac{n + 2}{2\pi} \cos^{n+1} \theta . \sin \theta \text{ radian}^{-2}$$

(b) For N showers randomly distributed in a total sensitive time T_s of sidereal time the number expected in an interval t to $t + dt$ of sensitive time t_s is $N. t_s/T_s$. For these showers the number $n(\theta, \phi) d\theta d\phi$ expected in the zenith angle range θ to $\theta + d\theta$ and ϕ to $\phi + d\phi$ is

$$n(\theta, \phi) d\theta d\phi = \frac{n + 2}{2\pi} \cos^{n+1} \theta . \sin \theta \, d\theta \, d\phi . N \, t_s/T_s$$

Converting from azimuthal angle, zenith angle, sidereal time to right ascension and declination and then to galactic coordinates the expected number of showers in given ranges of galactic coordinates can be calculated. Most of the calculation was carried out by computer and Figure 8.3 shows an example of the print-out obtained. For the 2,608 events producing both inner and outer ring triggers of the Durham EAS array, Figure 8.10 can be used to show that for an iso-tropic distribution of EAS in sidereal time the number of showers expected in the sidereal time range 16.00-17.00 hrs is 260.8. The computer print-out gives the expected number of these events that should have the galactic coordinates shown. With similar information for the whole 24 hour period of side-real time, the total expected number of events in given cells of galactic longitude and latitude can be calculated and this is how the expected number of EAS shown in brackets in figures 8.14, 8.15 and 8.16 have been calculated.

Figure 8.3 :   Illustrative print-out of the computer program used

to calculate the expected number of showers with the state

average galactic latitude and longitude for an expected

number of showers occurring in a given interval of

sidereal time. For the example shown, the time interval

is 16.00 - 17.00 hrs, mean = 16.50 hrs. The sum of the

probabilities in the fifth column is 1.00. The total

number of showers in the sixth column is 260.7998.

AVERAGE OF TWO SIDEREAL TIME RANGES (IN HOURS) = 16.50

NO. OF EXPECTED SHOWERS IN ONE HR. SIDEREAL TIME = 260.7998

PROB.. OF SHOWERS BEING INCIDENT AT THETA AND PHI ANGLES

	Theta Average	PHI Average	G.Latit	G.Longt	Probability of shower	Expected Number
	IN DEGREES		IN DEGREES			
2473	5.0	18.0	39.32	89.01	0.0150	3.9233
2474						
2475	5.0	54.0	37.34	85.99	0.0150	3.9233
2476						
2477	5.0	90.0	37.01	82.15	0.0150	3.9233
2478						
2479	5.0	126.0	38.43	78.69	0.0150	3.9233
2480						
2481	5.0	162.0	41.15	76.78	0.0150	3.9233
2482						
2483	5.0	198.0	44.25	77.31	0.0150	3.9233
2484						
2485	5.0	234.0	46.46	80.37	0.0150	3.9233
2486						
2487	5.0	270.0	46.84	84.83	0.0150	3.9233
2488						
2489	5.0	306.0	45.22	88.61	0.0150	3.9233
2490						
2491	5.0	342.0	42.33	90.11	0.0150	3.9233
2492						
2493						
2494	15.0	18.0	33.42	99.04	0.0336	8.7588
2495						
2496	15.0	54.0	28.05	90.39	0.0336	8.7588
2497						
2498	15.0	90.0	27.16	80.09	0.0336	8.7588
2499						
2500	15.0	126.0	30.99	70.55	0.0336	8.7588
2501						
2502	15.0	162.0	38.54	64.20	0.0336	8.7588
2503						
2504	15.0	198.0	47.76	63.81	0.0336	8.7588
2505						
2506	15.0	234.0	55.16	72.53	0.0336	8.7588
2507						
2508	15.0	270.0	56.55	88.71	0.0336	8.7588
2509						
2510	15.0	306.0	50.89	100.94	0.0336	8.7588
2511						
2512	15.0	342.0	41.90	103.58	0.0336	8.7588
2513						
2514						
2515	25.0	18.0	26.81	107.73	0.0304	7.9354
2516						
2517	25.0	54.0	18.64	94.07	0.0304	7.9354
2518						
2519	25.0	90.0	17.29	78.37	0.0304	7.9354
2520						
2521	25.0	126.0	23.12	63.63	0.0304	7.9354
2522						

2523	25.0	162.0	34.70	52.69	0.0304	7.9354
2524						
2525	25.0	198.0	49.49	48.89	0.0304	7.9354
2526						
2527	25.0	234.0	63.08	60.55	0.0304	7.9354
2528						
2529	25.0	270.0	66.05	95.23	0.0304	7.9354
2530						
2531	25.0	306.0	54.94	116.05	0.0304	7.9354
2532						
2533	25.0	342.0	39.94	116.52	0.0304	7.9354
2534						
2535						
2536	35.0	18.0	19.78	115.35	0.0162	4.2287
2537						
2538	35.0	54.0	9.17	97.36	0.0162	4.2287
2539						
2540	35.0	90.0	7.41	76.82	0.0162	4.2287
2541						
2542	35.0	126.0	14.98	57.48	0.0162	4.2287
2543						
2544	35.0	162.0	29.88	42.33	0.0162	4.2287
2545						
2546	35.0	198.0	49.22	33.53	0.0162	4.2287
2547						
2548	35.0	234.0	69.31	40.94	0.0162	4.2287
2549						
2550	35.0	270.0	74.95	109.00	0.0162	4.2287
2551						
2552	35.0	306.0	56.76	133.81	0.0162	4.2287
2553						
2554	35.0	342.0	36.68	128.59	0.0162	4.2287
2555						
2556						
2557	45.0	18.0	12.34	122.44	0.0051	1.3381
2558						
2559	45.0	54.0	-0.31	100.44	0.0051	1.3381
2560						
2561	45.0	90.0	-2.48	75.34	0.0051	1.3381
2562						
2563	45.0	126.0	6.68	51.80	0.0051	1.3381
2564						
2565	45.0	162.0	24.32	32.98	0.0051	1.3381
2566						
2567	45.0	198.0	46.99	18.91	0.0051	1.3381
2568						
2569	45.0	234.0	71.98	11.54	0.0051	1.3381
2570						
2571	45.0	270.0	81.18	149.43	0.0051	1.3381
2572						
2573	45.0	306.0	56.01	151.75	0.0051	1.3381
2574						
2575	45.0	342.0	32.20	139.55	0.0051	1.3381
2576						
2577						
2578	55.0	18.0	4.80	129.13	0.0009	0.2239
2579						
2580	55.0	54.0	-9.88	103.69	0.0009	0.2239
2581						

2582	55.0	90.0	-12.36	73.84	0.0009	0.2239
2583						
2584	55.0	126.0	-1.68	46.30	0.0009	0.2239
2585						
2586	55.0	162.0	18.25	24.45	0.0009	0.2239
2587						
2588	55.0	198.0	43.08	5.87	0.0009	0.2239
2589						
2590	55.0	234.0	69.64	341.65	0.0009	0.2239
2591						
2592	55.0	270.0	78.71	207.55	0.0009	0.2239
2593						
2594	55.0	306.0	52.66	168.14	0.0009	0.2239
2595						
2596	55.0	342.0	26.95	149.33	0.0009	0.2239
2597						
2598						
2599	65.0	18.0	-2.81	135.61	0.0001	0.0147
2600						
2601	65.0	54.0	-19.33	106.95	0.0001	0.0147
2602						
2603	65.0	90.0	-22.24	72.22	0.0001	0.0147
2604						
2605	65.0	126.0	-10.02	40.76	0.0001	0.0147
2606						
2607	65.0	162.0	11.82	16.52	0.0001	0.0147
2608						
2609	65.0	198.0	37.88	354.63	0.0001	0.0147
2610						
2611	65.0	234.0	63.59	321.38	0.0001	0.0147
2612						
2613	65.0	270.0	70.62	230.59	0.0001	0.0147
2614						
2615	65.0	306.0	47.61	181.56	0.0001	0.0147
2616						
2617	65.0	342.0	21.10	158.20	0.0001	0.0147
2618						
2619						

8.4   ANALYSIS OF THE DATA AND RESULTS

A total number of 3577 events were recorded in the time period March to July 1977.   Showers were selected initially using an outer ring trigger and later a combined inner or outer ring trigger of the Durham EAS array.

The size distribution and the measured Θ and ϕ distributions for all the data, the outer ring trigger data and the combined inner and outer ring trigger data, are given in Figure (8.4) to (8.8), where the measured zenith and azimuthal angle distributions are also shown in the figures. For the measured Θ distribution the function of the form $I(\Theta) = I(0) \cos^n \Theta$ where $I(0)$ is the vertical intensity and $I(\Theta)$ the intensity at zenith angle Θ was fitted to the data. The best values of n were calculated to be 8.2 for all the data, 8.5 for the outer ring trigger data and 8.0 for the combined inner and outer ring trigger data.

The next step in the analysis was to investigate any anisotropy in sidereal time. For the present data the operational time distributions and frequency-time variations of events in solar and sidereal time are given in Figures (8.9), (8.10), and (8.11).   The dotted lines are the expected distributions which were calculated assuming a uniform distribution in sidereal time. χ^2 probability tests between the measured and expected number of events in different intervals of sidereal time showed that they are not far from being randomly distributed.   An interesting point arises from the comparison of the combined inner and outer ring trigger data (events with $\bar{N} = 3.10^5$ pts) with the outer ring trigger data (events with $\bar{N} = 1.11.10^6$ particles).   The χ^2 test shows that the
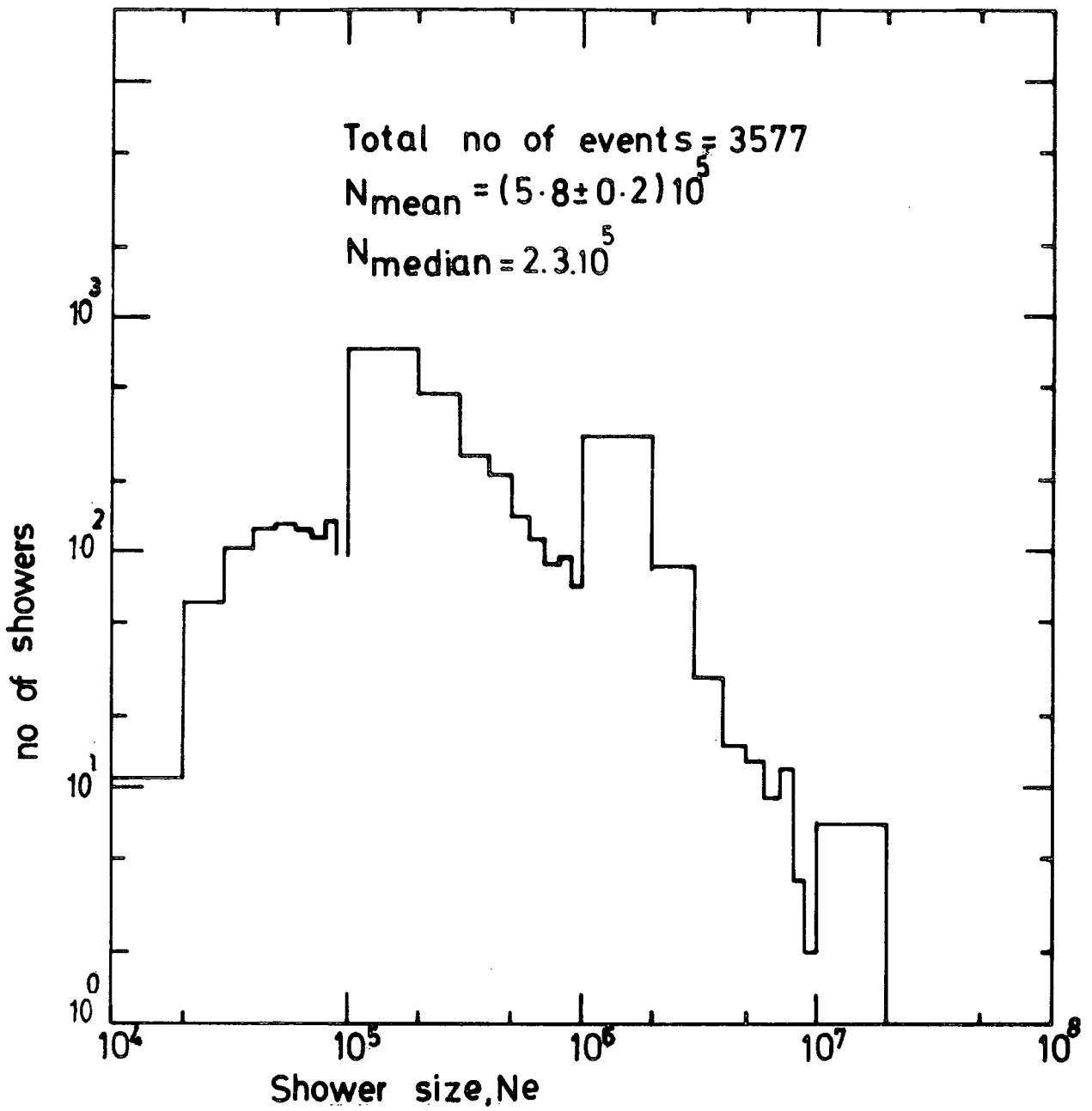
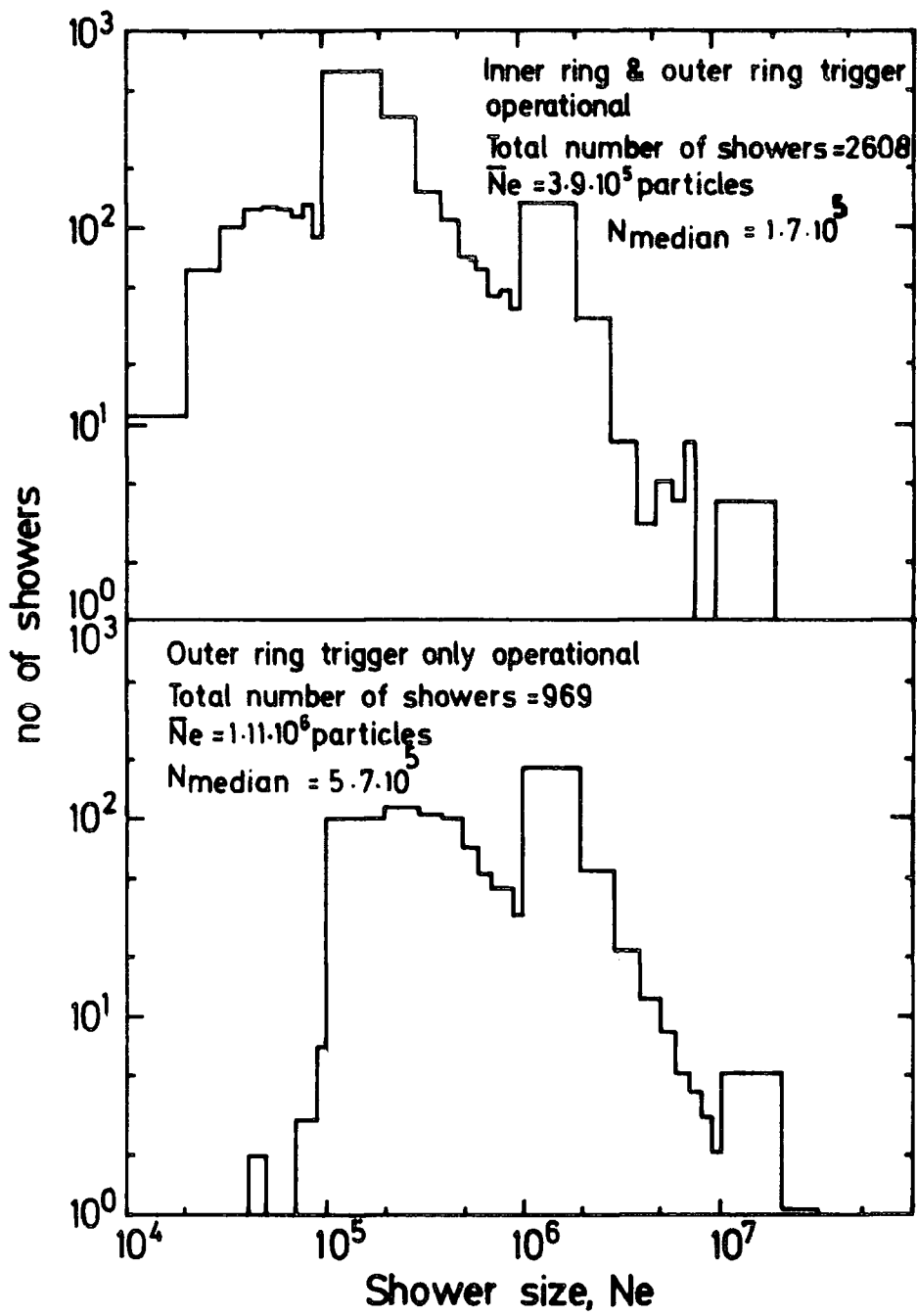Figure 8.4 :   Shower size distribution of all the data.

Figure 8.5 :   Shower size distributions for different triggering
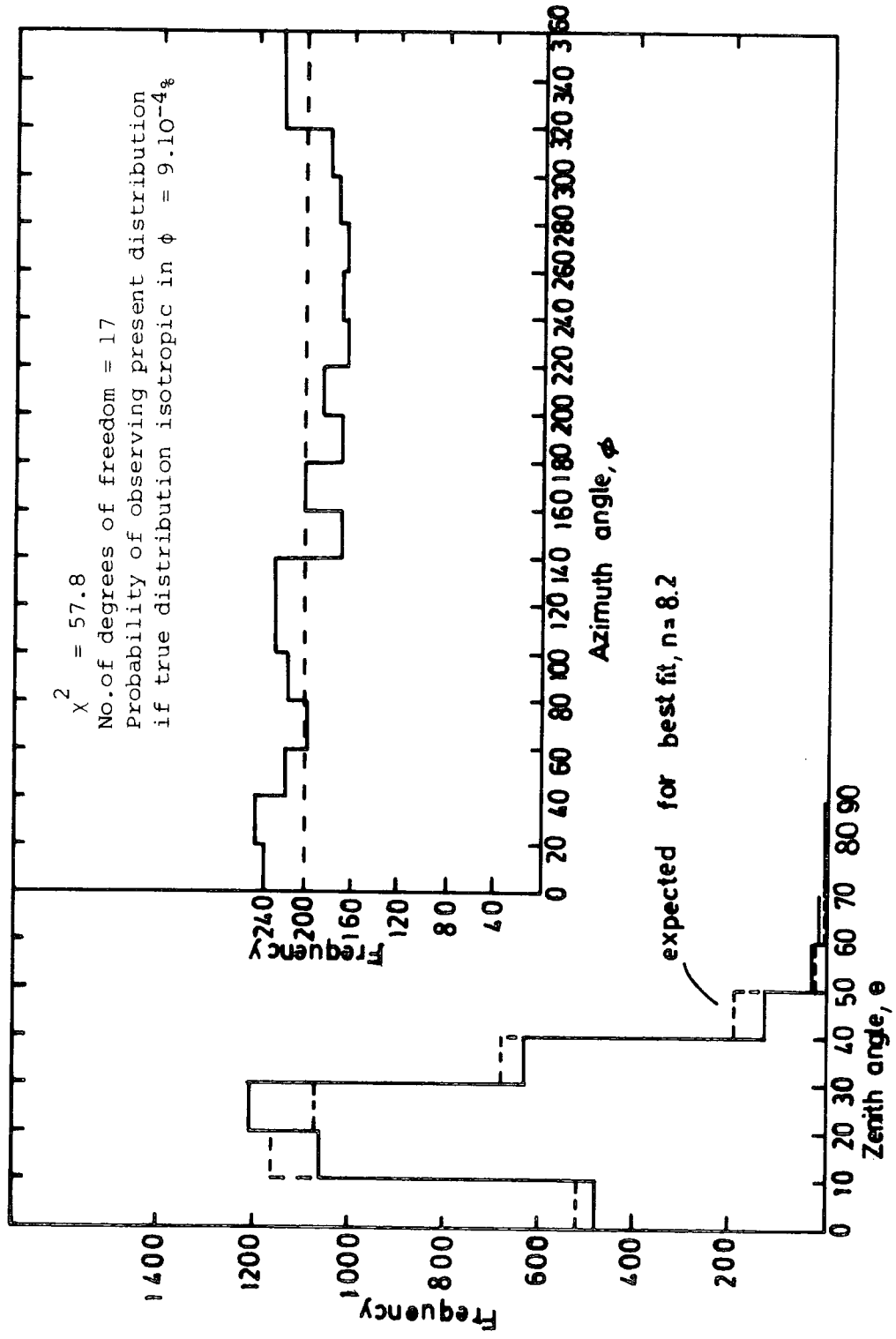systems

Total no. of events = 3577

χ^2 = 57.8

No.of degrees of freedom = 17

Probability of observing present distribution

if true distribution isotropic in ϕ = 9.10^{-4}%

expected for best fit, n = 8.2

Azimuth angle, ϕ

Zenith angle, θ

expected

Frequency

Figure 8.6 :   Zenith and azimuth angle distributions of all the data.

outer ring trigger only operational
total no of showers = 969

$x^2 = 61.1$
No of degrees of freedom = 17
Probability of observing present distribution if true
distribution isotropic in $\phi = 4 \cdot 1 \cdot 10^{-4}$ %

Azimuth angle ϕ

Frequency

expected for best fit, n = 8.5

Frequency
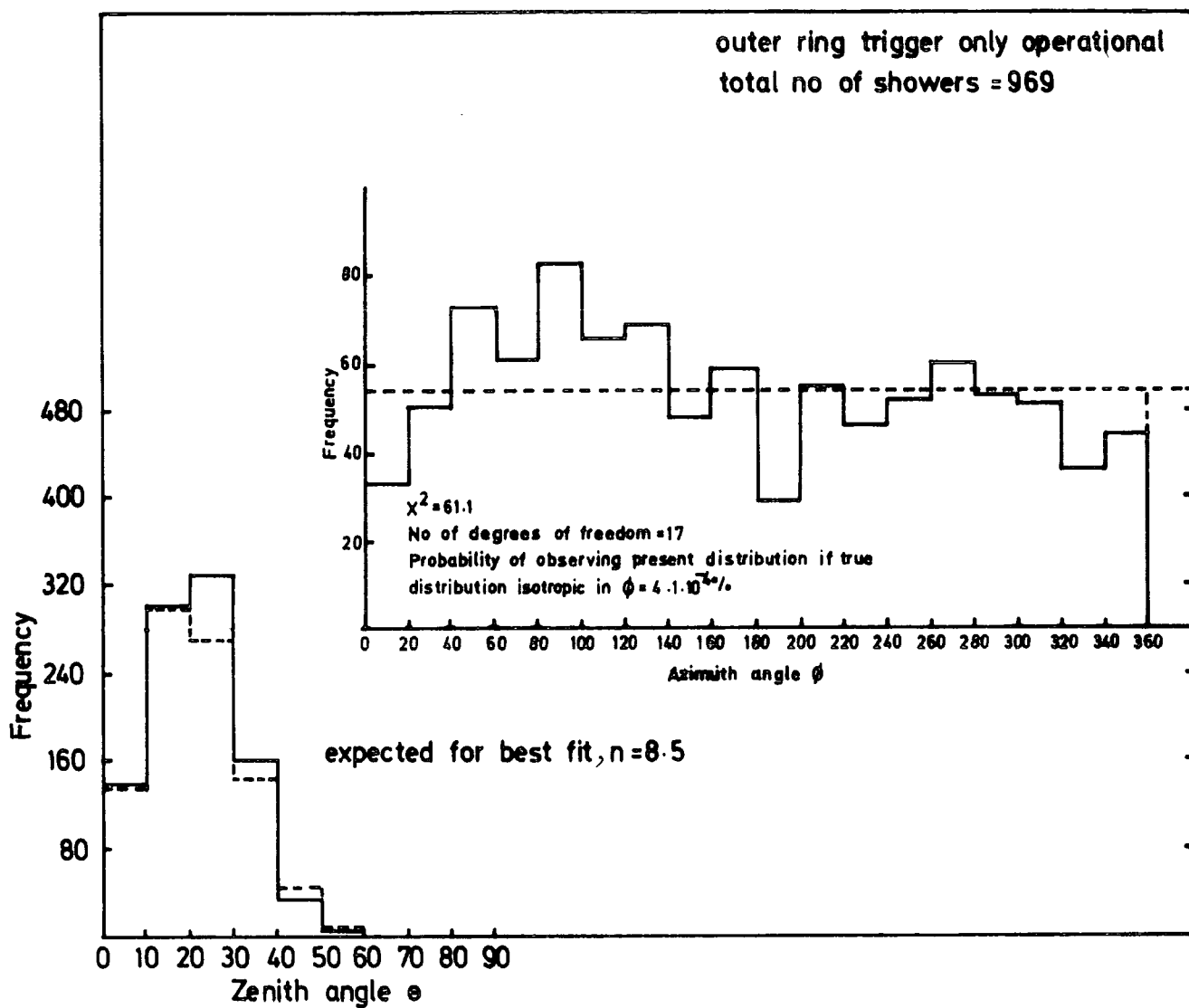
Zenith angle θ

Figure 8.7 :   Zenith and azimuth angle distribution of showers
                    selected by the outer ring trigger. Dotted lines
                    are the predicted distribution.
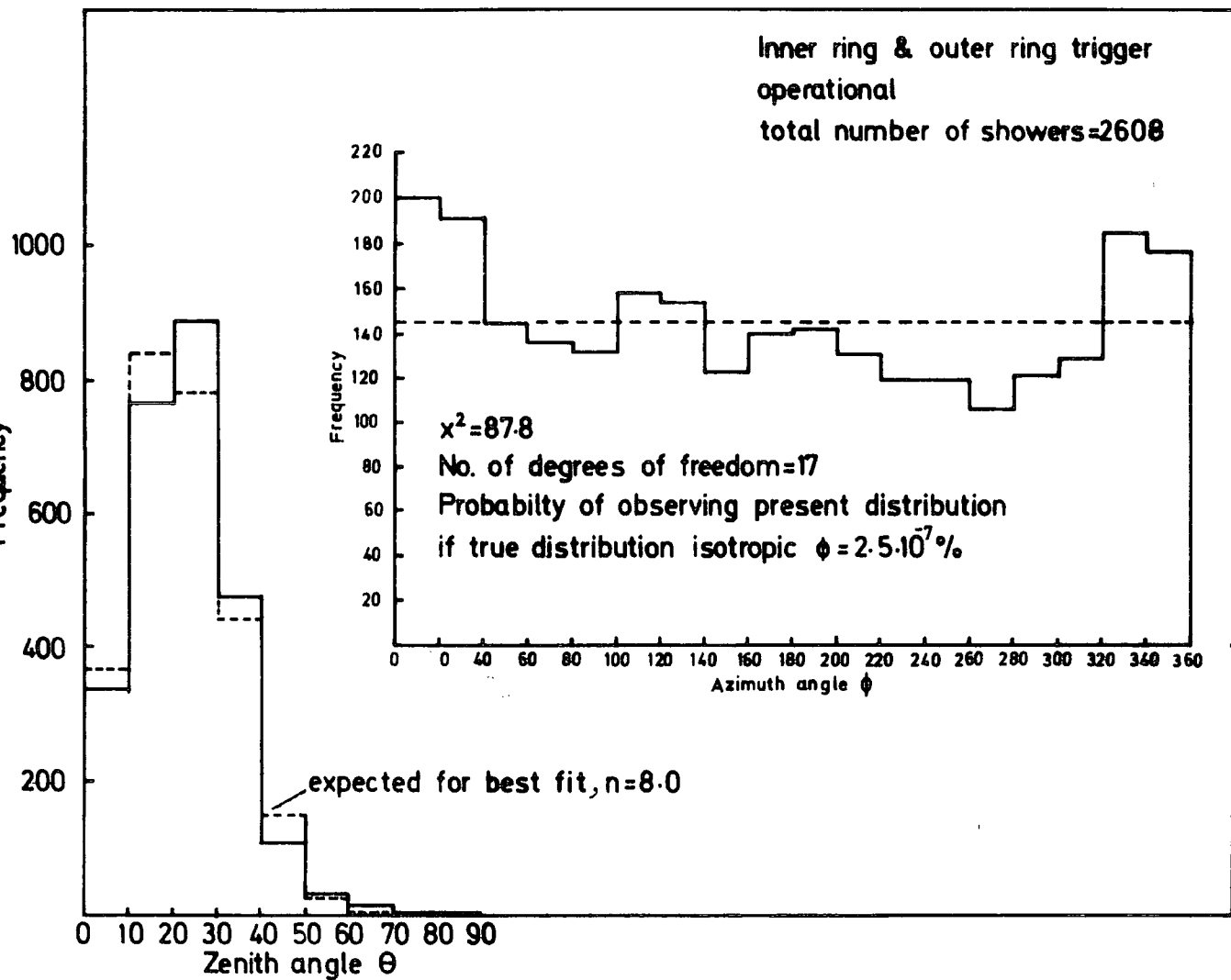
Figure 8.8 :   Zenith and azimuth angle distribution of showers
              selected by the combined inner and outer ring
              triggers. Dotted lines are the predicted distributions.
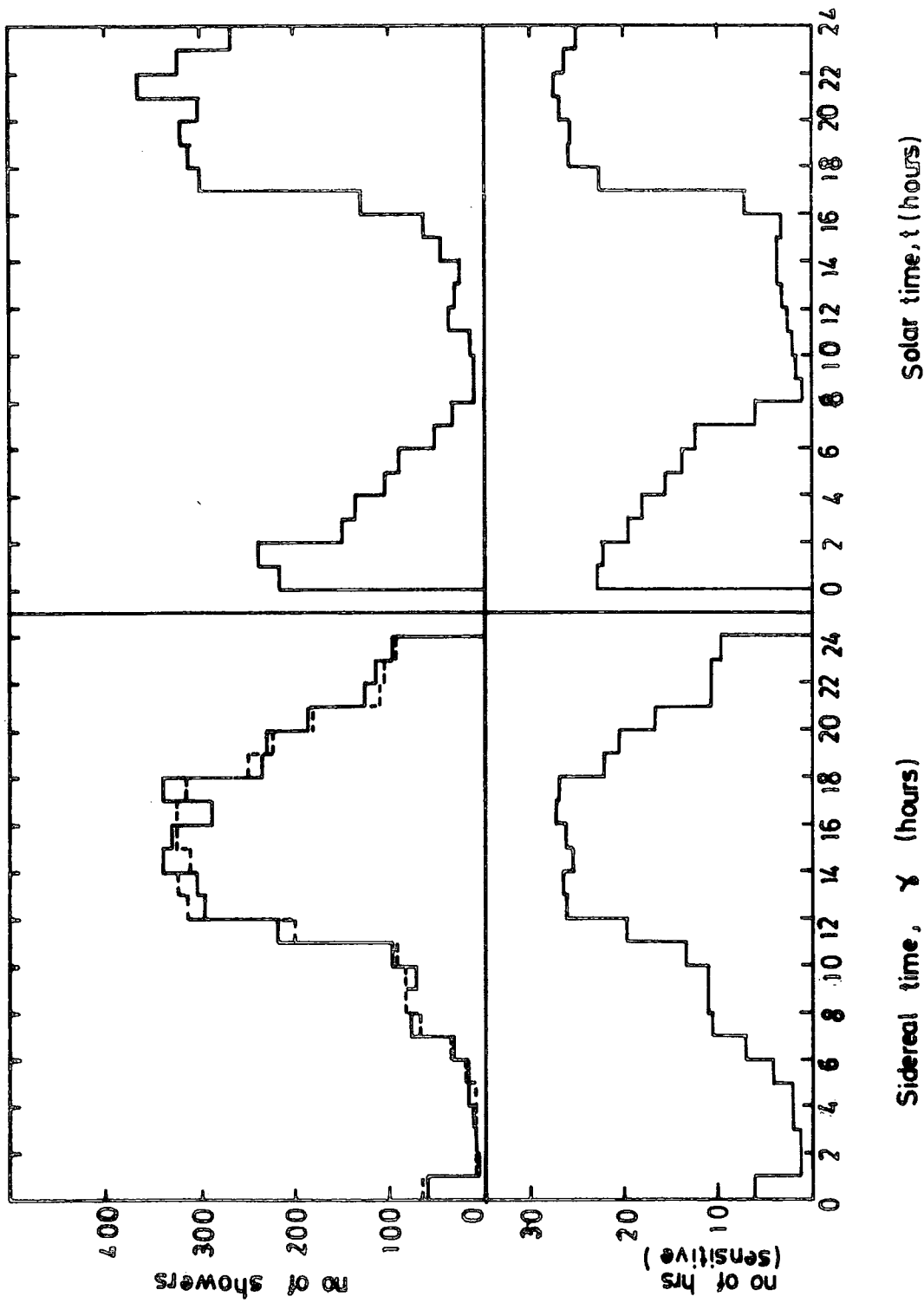
Figure 8.9 The operational time distributions and frequency time variations of E.A.S. in solar and sidereal time for all the data. Dotted line is predicted distribution if it is isotropic in sidereal time.
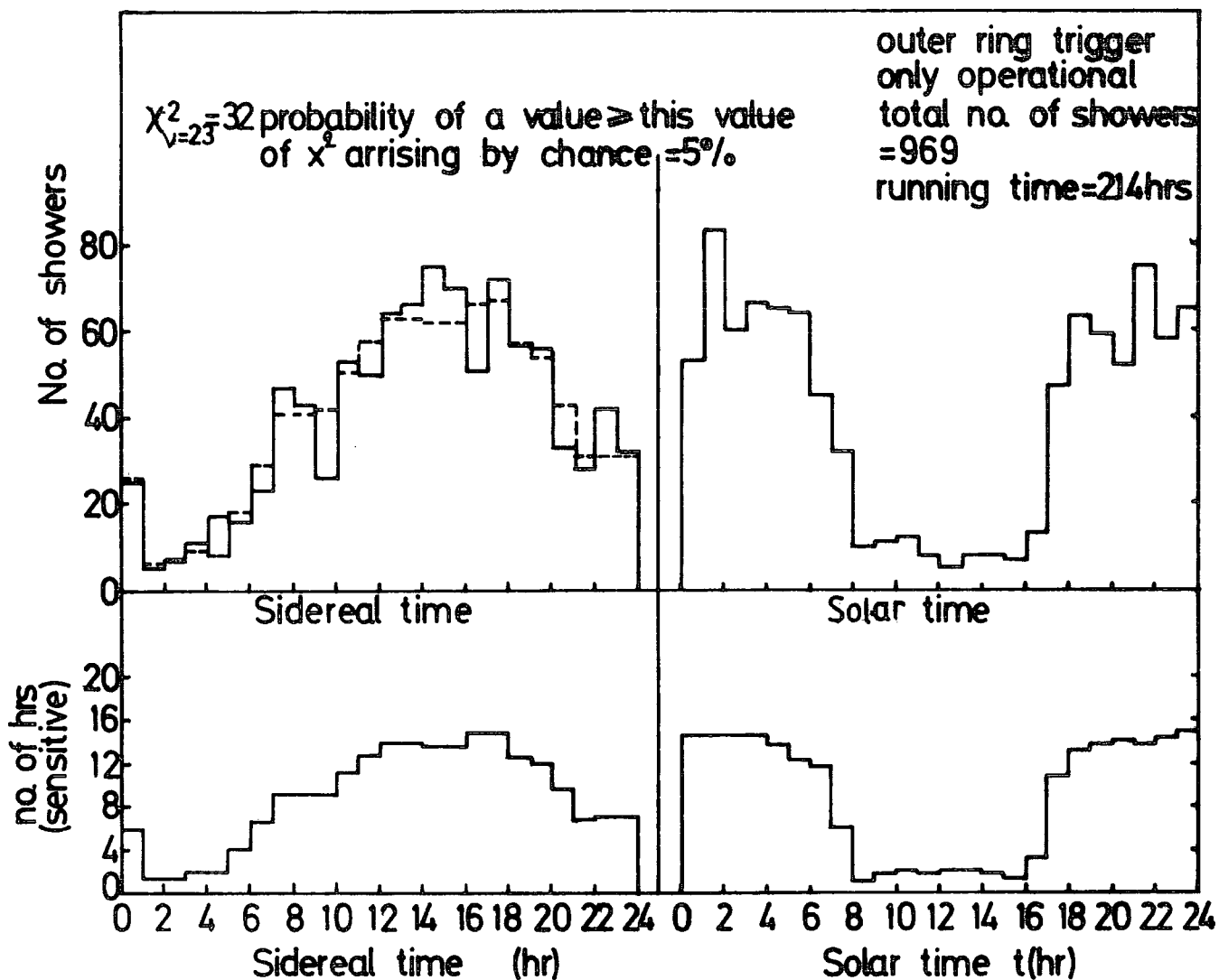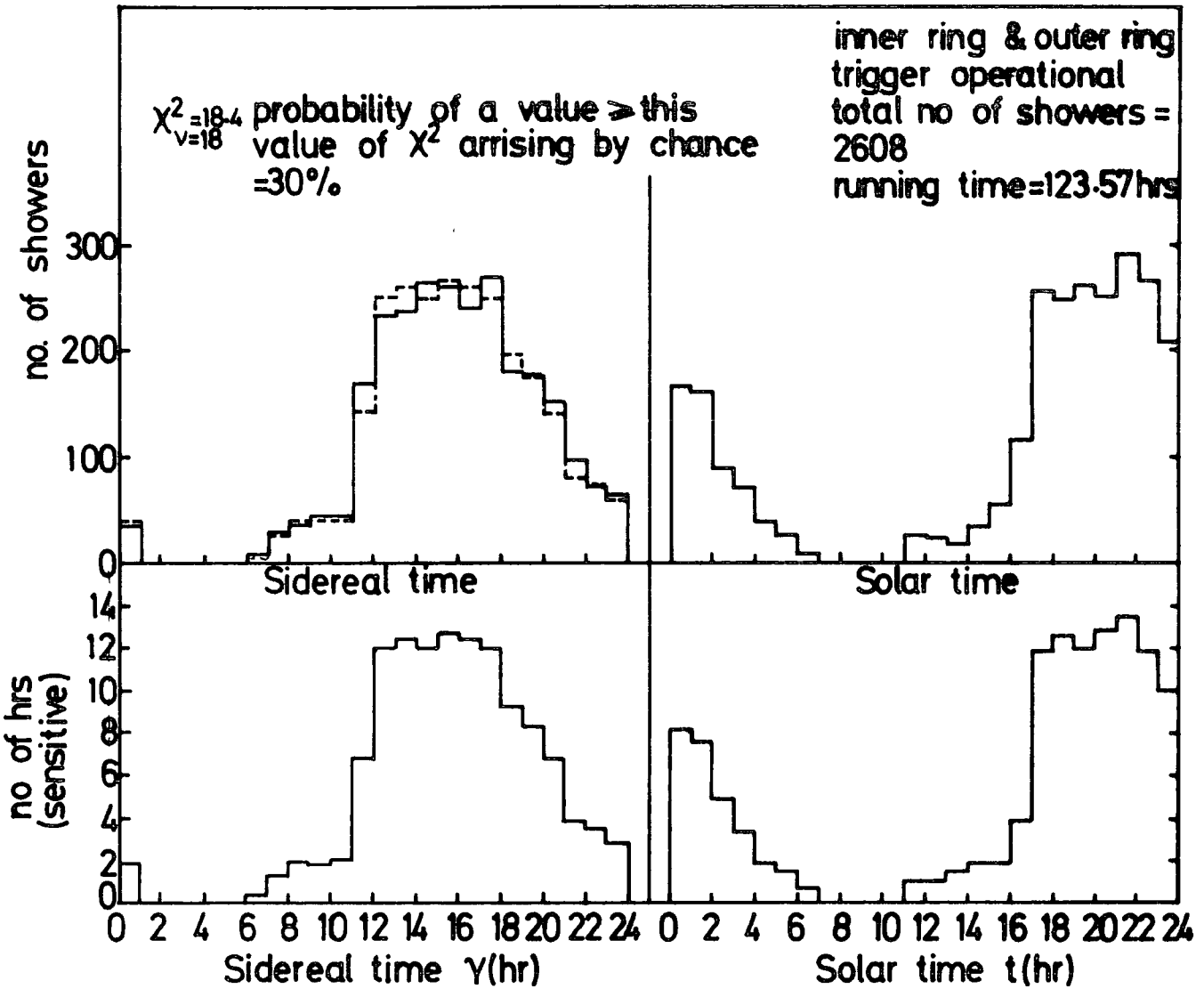
Figure 8.10 :   The operational time distributions and frequency-time
                 variations of E.A.S. in solar and sidereal time for
                 outer ring triggers.   Dotted line is predicted
                 distribution if it is isotropic in sidereal time.

Figure 8.11 : The operational time distributions and frequency-time variation of E.A.S. in solar and sidereal time for inner and outer ring triggers. Dotted line is predicted distribution if it is isotropic in sidereal time.

probability of the data in the two samples is consistent

with a uniform distribution in sidereal time decreases from

30% to 5% as $\bar{N}$ increases from 3.10^5 to $1.11.10^6$.   Thus the

measurements suggest an anisotropy of primary particles in

sidereal time which increases with their primary energy.

The next step was the analysis of the data in galactic

coordinates.   The right ascension and declination distributions

of the observed showers are shown in Figures (8.12) and (8.13).

The galactic latitude and longitude of the showers were obtained

from their declination and right ascension producing the galactic

frequency distributions of Figures (8.14), (8.15) and (8.16).

As shown in the figures, the number of observed showers in

30 by 20 degree longitude-latitude cells are summed and shown

in the corresponding squares.   The figures in the brackets

are the expected number of showers assuming they are iso-

tropically distributed in space (Section 8.3.3.).   The same

data is also presented graphically in Figures 8.17 to 8.22).

Inspection of Figure 8.14, which is based on all the 3577

observed showers, shows that overall there is good agreement

between observation and expectation assuming a uniform distri-

bution in sidereal time except for the cells marked * and **.

In the first case the observed number of events 43 exceeds

the expected number of events 19.67 by 3.6 standard deviations

and in the second case the observed number of events 229 exceeds

the expected number 158.65 by 4.6 standard deviations.   In

both cases the major contribution to the excess comes from the

combined inner and outer ring trigger data (Figure 8.15) rather

than the outer ring trigger data (Figure 8.16).   The combined

inner and outer ring trigger data has lower average energy
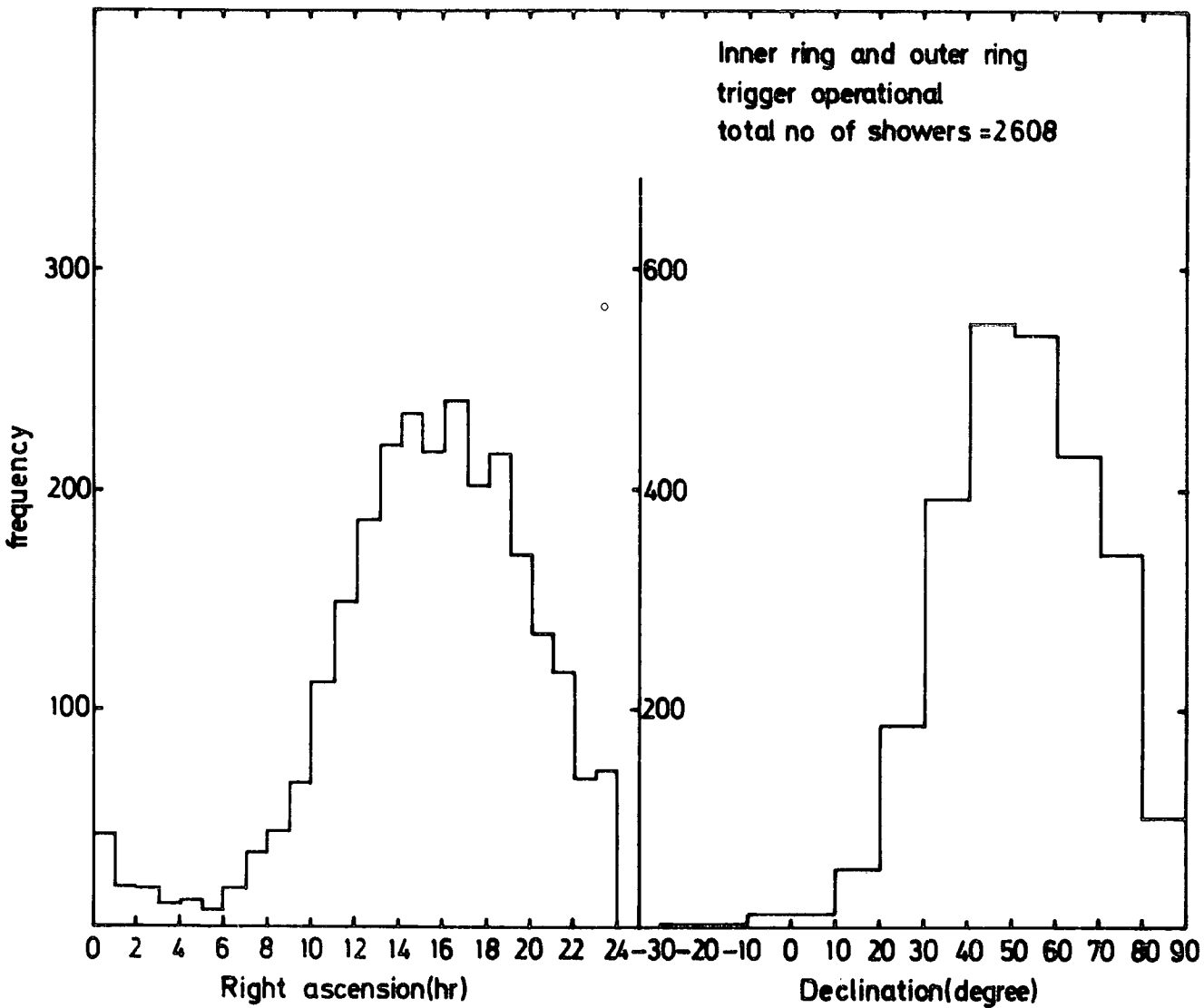
Figure 8.12 :   Distribution of E.A.S. in celestial coordinates for
                 inner ring and outer ring triggers.
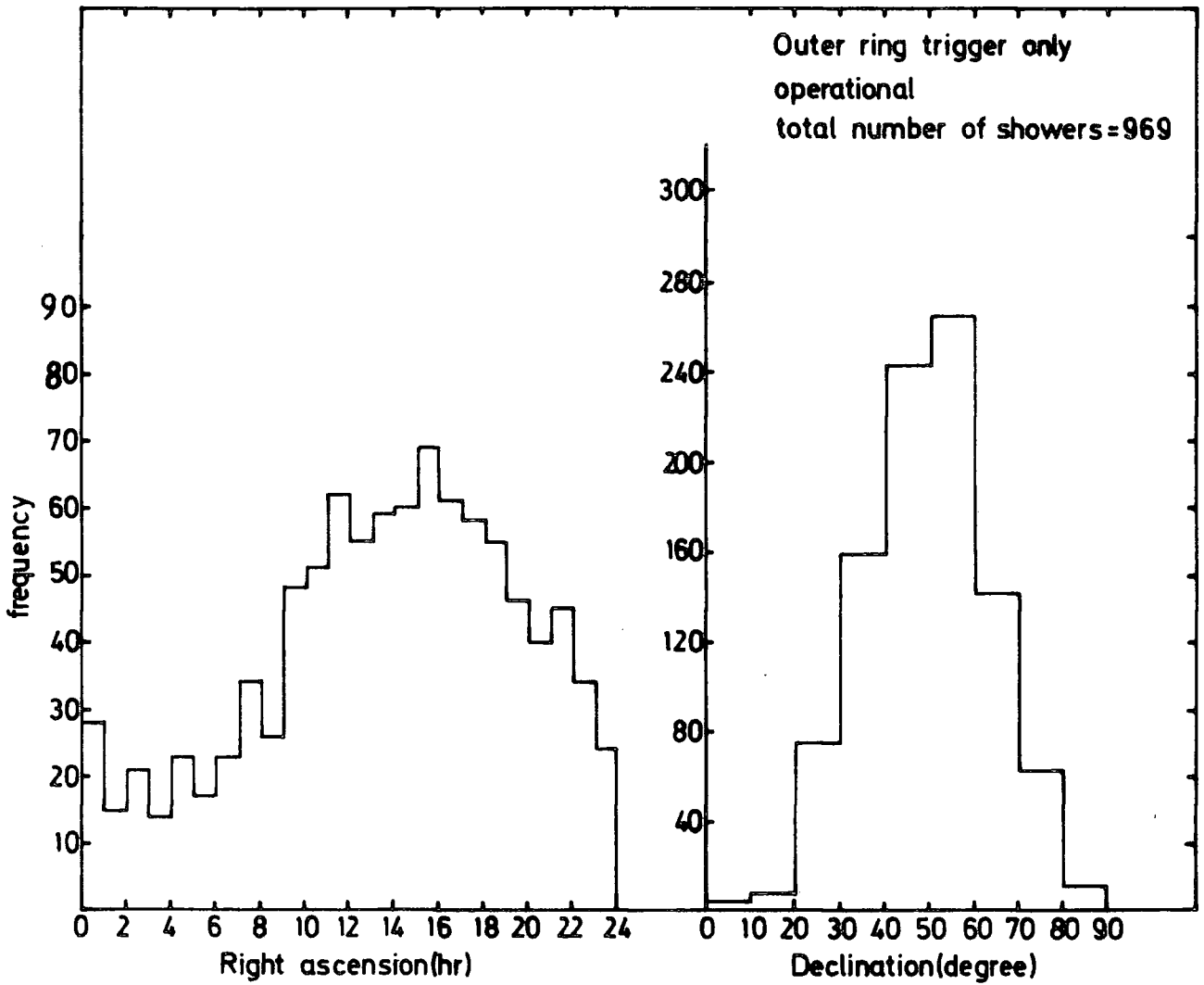
Figure 8.13 :   Distribution of E.A.S. in celestial coordinates
                 for outer ring triggers,

Figure 8.14 :   The observed and expected frequency distribution

of E.A.S. in galactic coordinates for all the data.

The expected distribution is calculated assuming it is

isotropic in the galaxy.

Total no. of events = 3577
observed (expected).

$\chi^2 = 33.83$
$\nu = 73$

Probability of a value $\geq$ this value of χ^2 if true distribution is isotropic in galactic coordinates = 99.5%

Galactic latitude, b' (°) \ Galactic longitude, ℓ' (°)	30	60	90	120	150	180	210	240	270	300	330	360	Total
90–70	12(7.7)	31(28.31)	41(43.15)	47(74.34)	43(19.67)*	28(36.43)	20(30.74)	14(5.56)	4(4.89)	9(8.21)	5(2.57)	4(6.39)	258(267.96)
70–50	9(17.23)	75(67.45)	159(167.08)	214(239.2)	180(175.63)	106(102.09)	40(49.67)	14(11.34)	4(2.77)	1(0.35)	1(0.54)	4(2.48)	807(835.87)
50–30	8(5.69)	95(96.69)	282(292.62)	337(345.37)	229(158.65)**	108(134.97)	34(31.66)	2(2.74)	2(0.38)	0(0.012)	1($<10^{-3}$)	3(0.05)	1100(1068.72)
30–10	4(0.47)	41(54.6)	276(295.03)	305(270.14)	64(80.87)	74(62.41)	17(21.01)	3(1.1)	0($5.4 \cdot 10^{-2}$)	0($<10^{-3}$)	0($<10^{-3}$)	1($<10^{-3}$)	784(785.63)
10–(−10)	0(0.0)	13(19.55)	136(139.2)	167(179.93)	65(57.42)	23(24.75)	4(6.12)	0(0.18)	0($<10^{-3}$)	0(0.0)	0(0.0)	0(0.0)	408(427.17)
(−10)–(−30)	2($2 \cdot 10^{-3}$)	2(2.12)	45(35.43)	89(85.15)	40(34.78)	9(5.73)	0(0.82)	0($2.4 \cdot 10^{-3}$)	0($<10^{-3}$)	0(0.0)	0(0.0)	0(0.0)	187(164.03)
(−30)–(−50)	0($<10^{-3}$)	2(0.17)	2(3.26)	22(15.62)	6(6.13)	1(1.01)	0(0.037)	0($<10^{-3}$)	0(0.0)	0(0.0)	0(0.0)	0(0.0)	32(26.23)
(−50)–(−70)	0($<10^{-3}$)	0($6.5 \cdot 10^{-3}$)	0(0.15)	0(0.61)	0(0.54)	0(0.018)	0($3 \cdot 10^{-4}$)	0($<10^{-3}$)	0(0.0)	0(0.0)	0(0.0)	0(0.0)	0(1.32)
Total													3577(3577)

Figure 8.14

Figure 8.15 :   The observed and expected frequency distribution

of E.A.S in galactic coordinates for inner and

outer ring triggers.

Total no. of events = 2608

Inner and Outer Ring Trigger

b^{II} (°) \ ℓ^{II} (°)	0	30	60	90	120	150	180	210	240	270	300	330	360
90	12(6.06)	26(22.43)	31(33.9)	38(59.55)	33(15.03)*	20(27.2)	13(22.9)	11(4.53)	3(3.7)	7(6.47)	5(1.53)	3(5.3)	202(207.6)
70	8(15.2)	58(54.35)	115(133.3)	161(193.3)	132(130.2)	72(70.43)	23(31.1)	10(7.25)	2(2.05)	1(0.33)	0(0.43)	3(1.95)	585(639.89)
50	8(5.1)	79(76.8)	205(229.2)	280(270.6)**	186(112.07)	57(77.9)	21(15.92)	21(1.27)	0($<10^{-3}$)	0(0.01)	1($<10^{-3}$)	3(0.04)	843(789.09)
30	4(0.36)	29(42.6)	212(230.9)	245(209.7)	41(46.87)	29(24.51)	7(8.98)	3(0.49)	0($2.4{\times}10^{-3}$)	0($<10^{-3}$)	0($<10^{-3}$)	0(0.0)	570(564.41)
10	0(0.02)	5(14.94)	105(104)	116(126.6)	35(30.06)	5(5.97)	0(1.6)	0(0.07)	0($<10^{-3}$)	0(0.0)	0(0.0)	0(0.0)	269(283.26)
-10	2($<10^{-3}$)	1(1.77)	32(25.78)	60(58.6)	16(19.33)	5(1.25)	0(0.15)	0($4{\times}10^{-4}$)	0($<10^{-3}$)	0(0.0)	0(0.0)	0(0.0)	116(106.88)
-30	0($<10^{-3}$)	2(0.13)	13(10.07)	6(3.51)	1(0.29)	0(0.01)	0($<10^{-3}$)	0(0.0)	0(0.0)	0(0.0)	0(0.0)	0(0.0)	23(16.07)
-50	0($<10^{-3}$)	0($4.5{\times}10^{-3}$)	0(0.09)	0(0.36)	0(0.35)	0($2.3{\times}10^{-3}$)	0($<10^{-3}$)	0($<10^{-3}$)	0(0.0)	0(0.0)	0(0.0)	0(0.0)	0(0.8)
-70													2608(2603)

Galactic longitude, ℓ^{II} (°) →

Galactic latitude, b^{II} (°) ←

Figure 8.15

Figure 8.16 :   The observed and expected frequency distribution

of E.A.S in galactic coordinates for outer ring

triggers.

Outer ring trigger

Total no. of events = 969

Galactic latitude b (°) \ Galactic longitude l (°)	0–30	30–60	60–90	90–120	120–150	150–180	180–210	210–240	240–270	270–300	300–330	330–360	Total
90	0(1.64)	5(5.88)	10(9.25)	9(15.79)	10(4.64)*	8(9.23)	7(7.84)	3(1.03)	1(1.19)	2(1.74)	0(1.04)	1(1.09)	56(60.36)
70	1(2.03)	17(13.1)	44(33.78)	53(45.9)	48(45.43)	34(31.66)	17(18.57)	4(4.09)	2(0.72)	0(0.02)	1(0.11)	1(0.53)	222(195.98)
50	0(0.59)	16(19.89)	77(63.42)	57(74.77)	43(46.58)**	51(57.07)	13(15.74)	0(1.47)	0(0.2)	0(2.9.10^{-3})	0(<10^{-3})	0(0.01)	257(279.7)
30	0(0.11)	22(12.0)	64(64.13)	60(60.44)	23(34)	45(37.9)	10(12.03)	0(0.61)	0(3.10^{-3})	0(<10^{-3})	0(<10^{-3})	0(<10^{-3})	214(221.22)
10	0(3.1.10^{-3})	5(4.61)	31(35.2)	51(53.33)	30(27.36)	18(18.78)	4(4.52)	0(0.11)	0(<10^{-3})	0(<10^{-3})	0(0.0)	0(0.0)	139(143.91)
−10	0(2.10^{-3})	1(0.35)	13(9.65)	29(26.55)	24(15.45)	4(4.48)	0(0.67)	0(2.10^{-3})	0(<10^{-3})	0(0.0)	0(0.0)	0(0.0)	71(57.15)
−30	0(<10^{-3})	0(0.04)	1(1.2)	9(5.55)	0(2.62)	0(0.72)	0(0.027)	0(<10^{-3})	0(0.0)	0(0.0)	0(0.0)	0(0.0)	10(10.16)
−50	0(<10^{-3})	0(2.10^{-3})	0(0.06)	0(0.25)	0(0.19)	0(0.016)	0(3.10^{-4})	0(<10^{-3})	0(0.0)	0(0.0)	0(0.0)	0(0.0)	0(0.52)
−70													969(969)

Galactic longitude, l'' (°)

Galactic latitude, b'' (°)
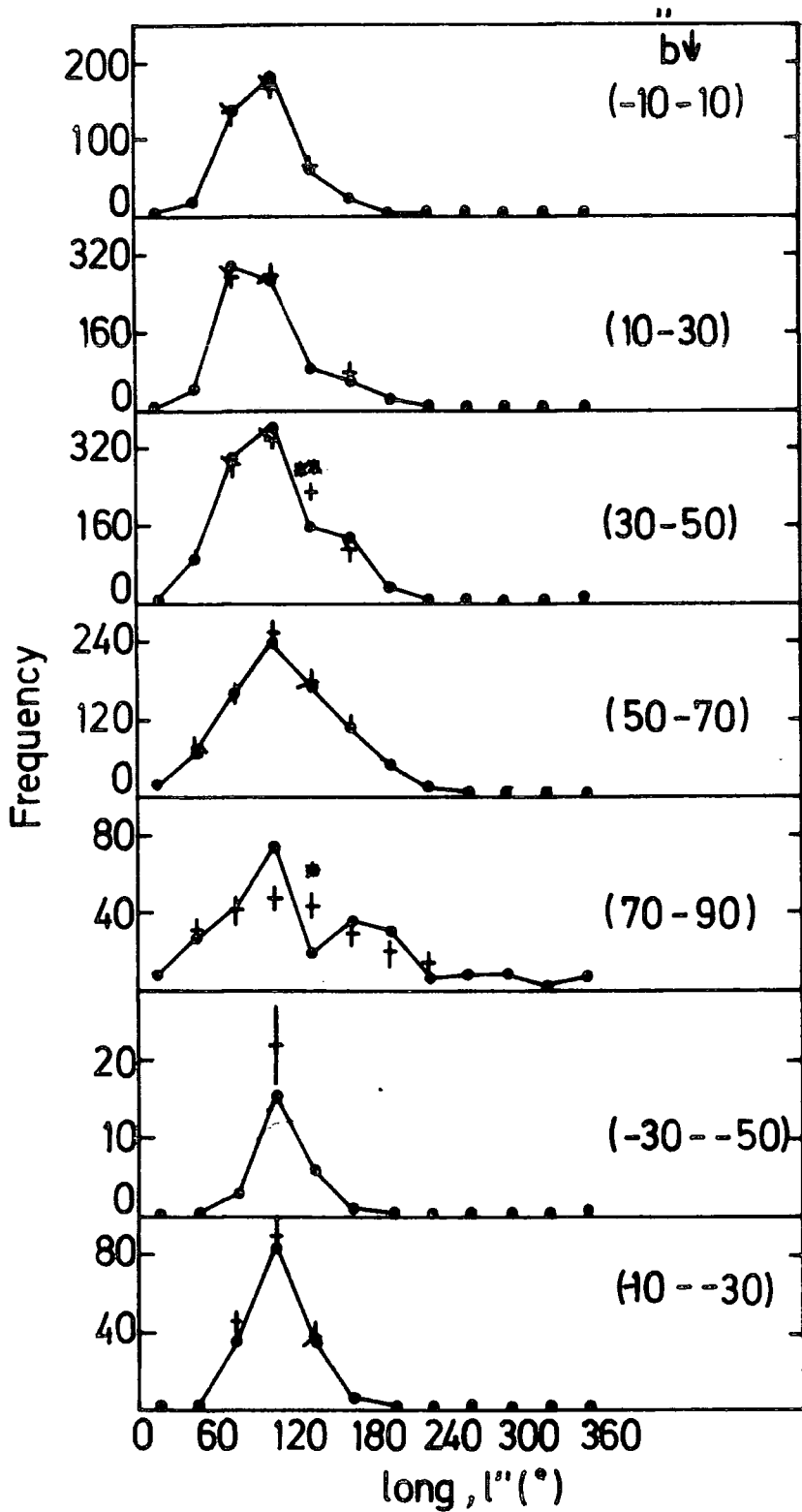
Figure 8.16

Figure 8.17 : Variation of the expected number of showers with galactic longitude for different ranges of galactic latitude. The observed number of events in cells containing ≥ 10 showers are plotted.
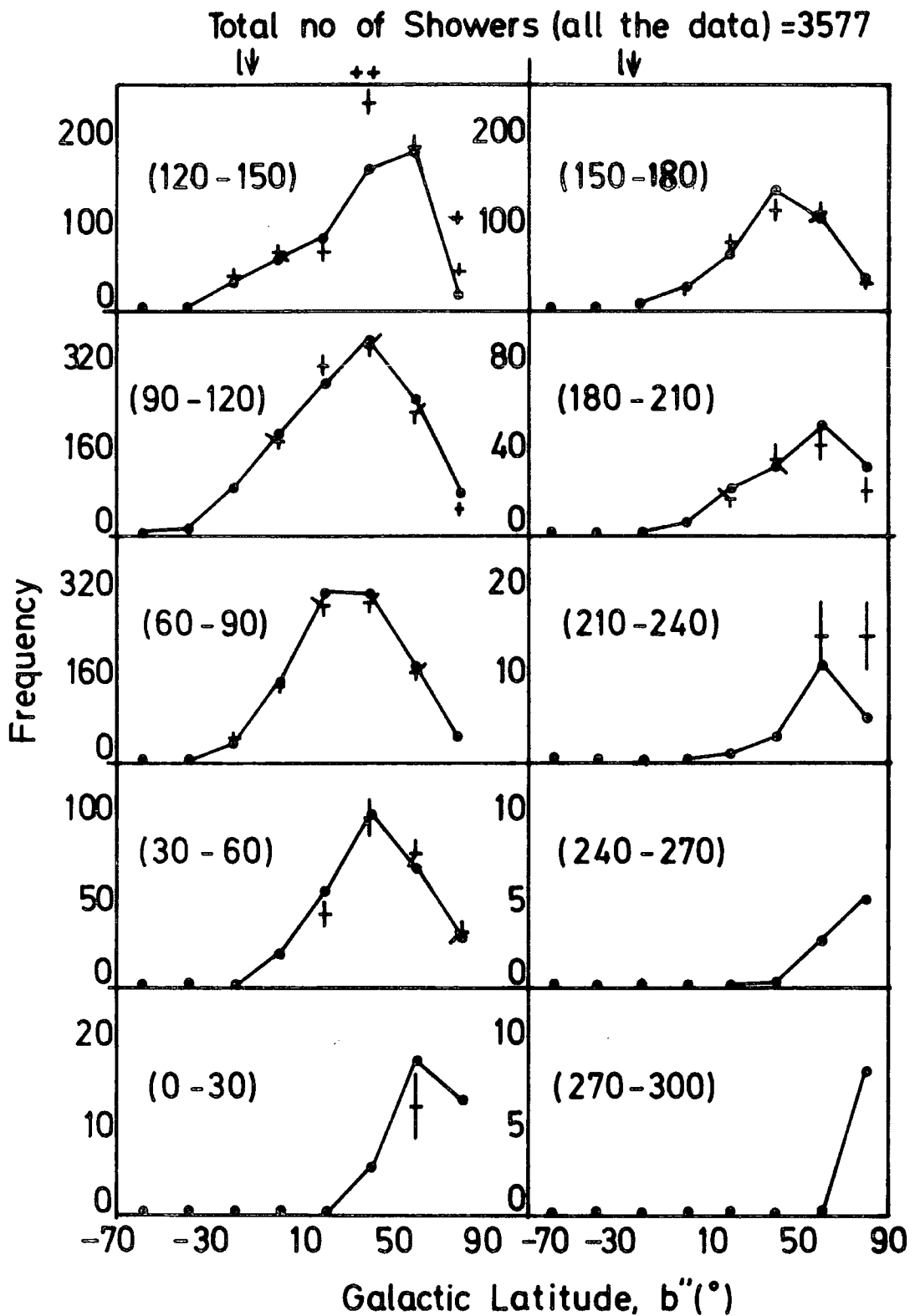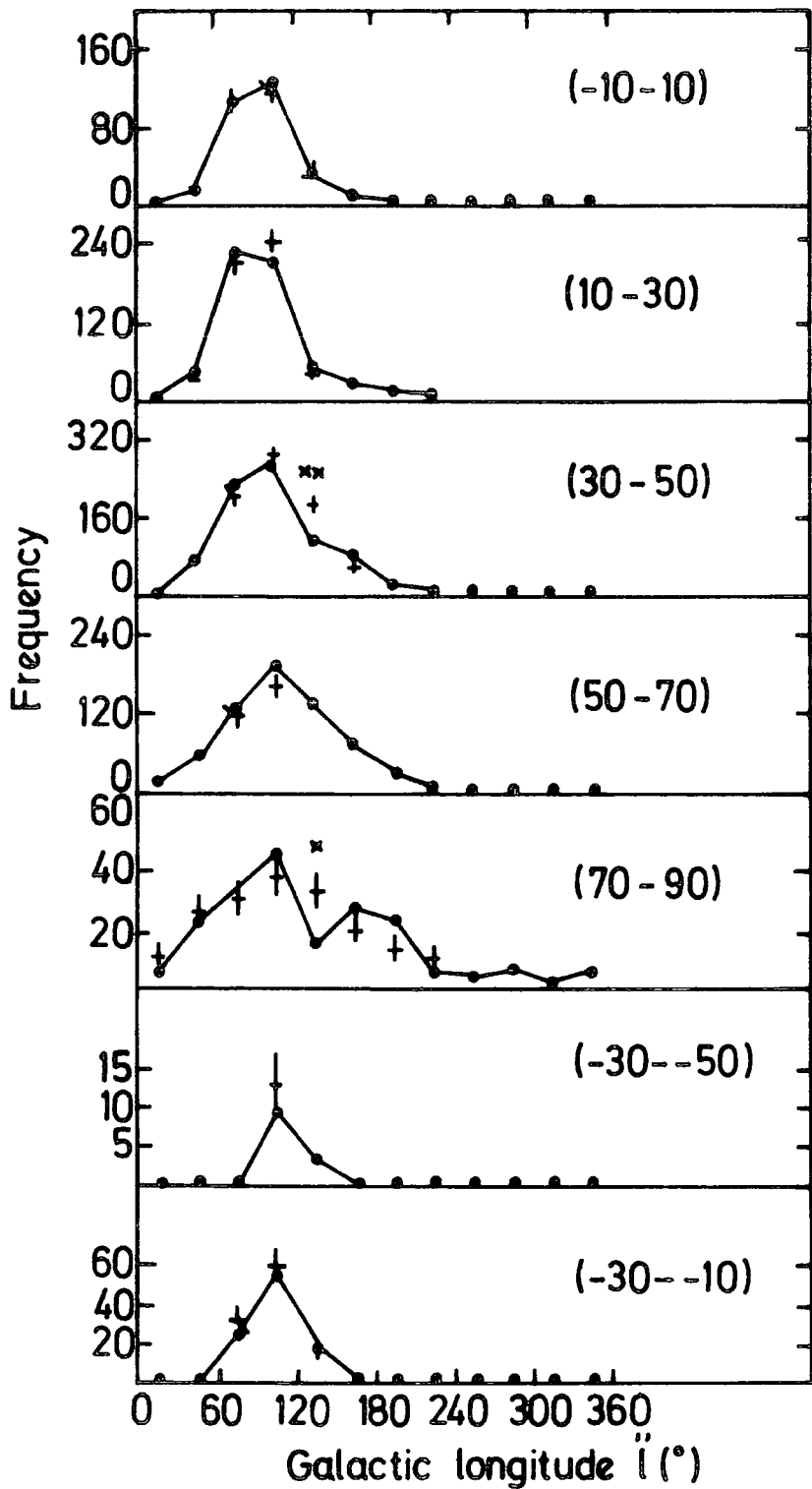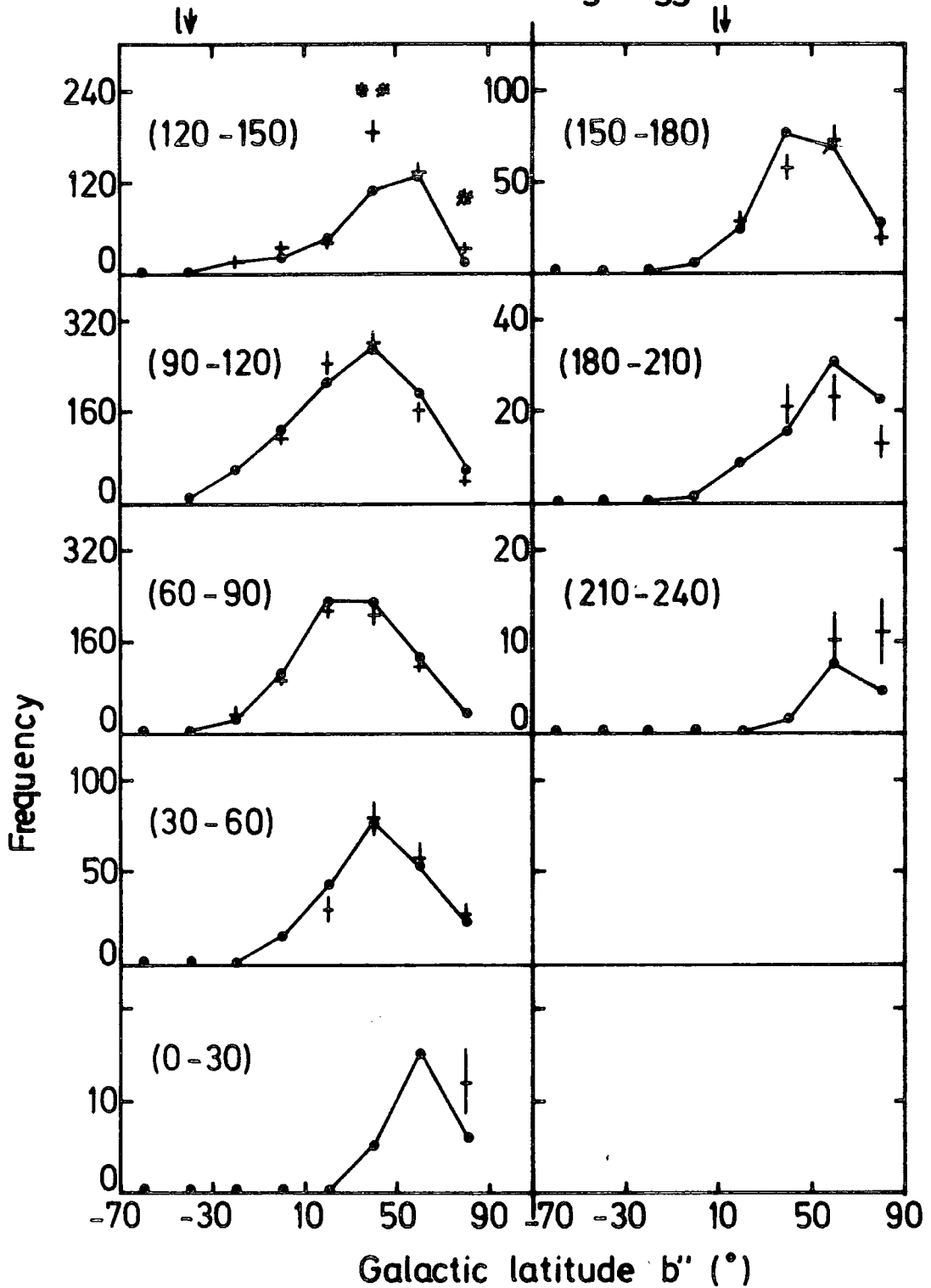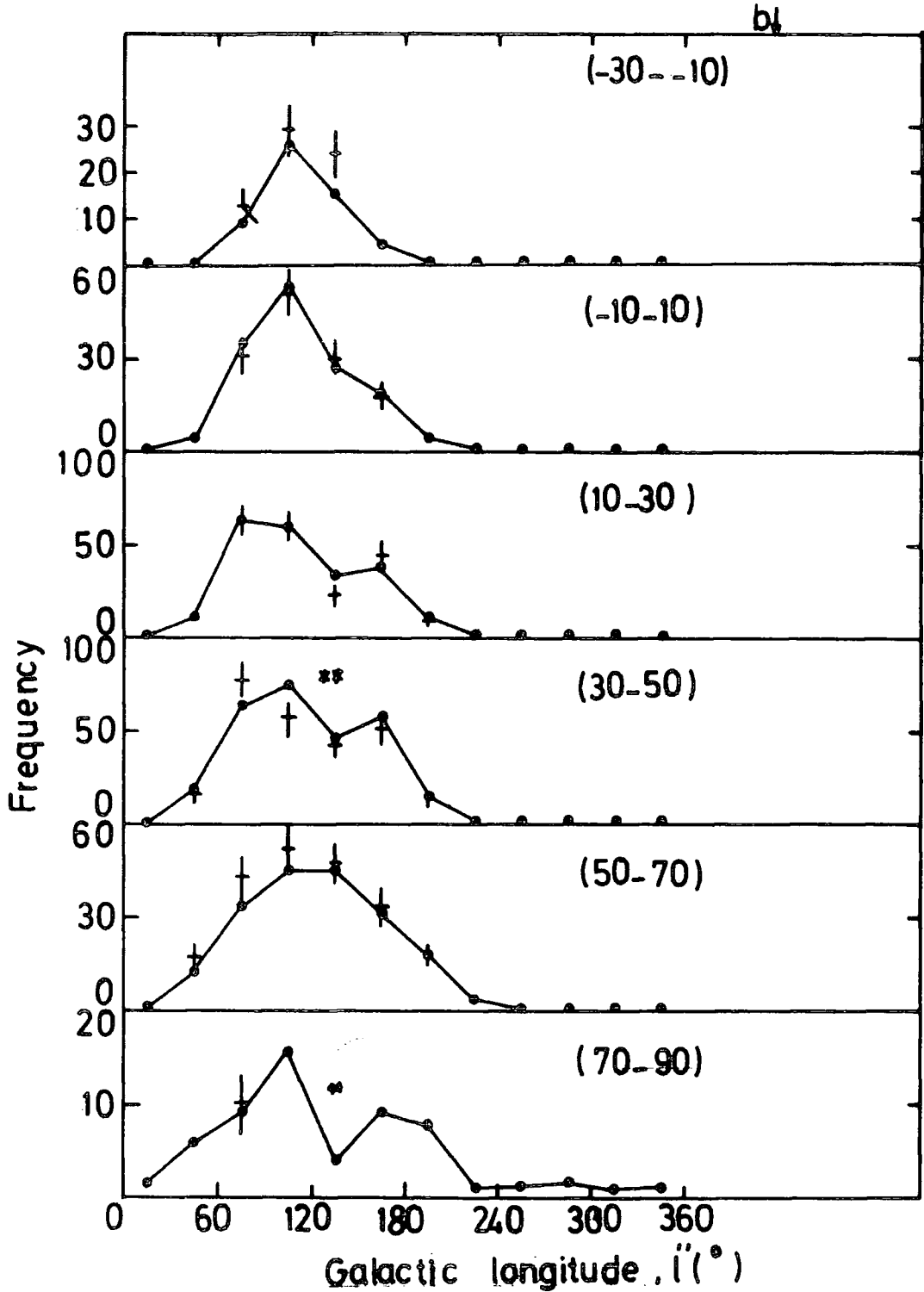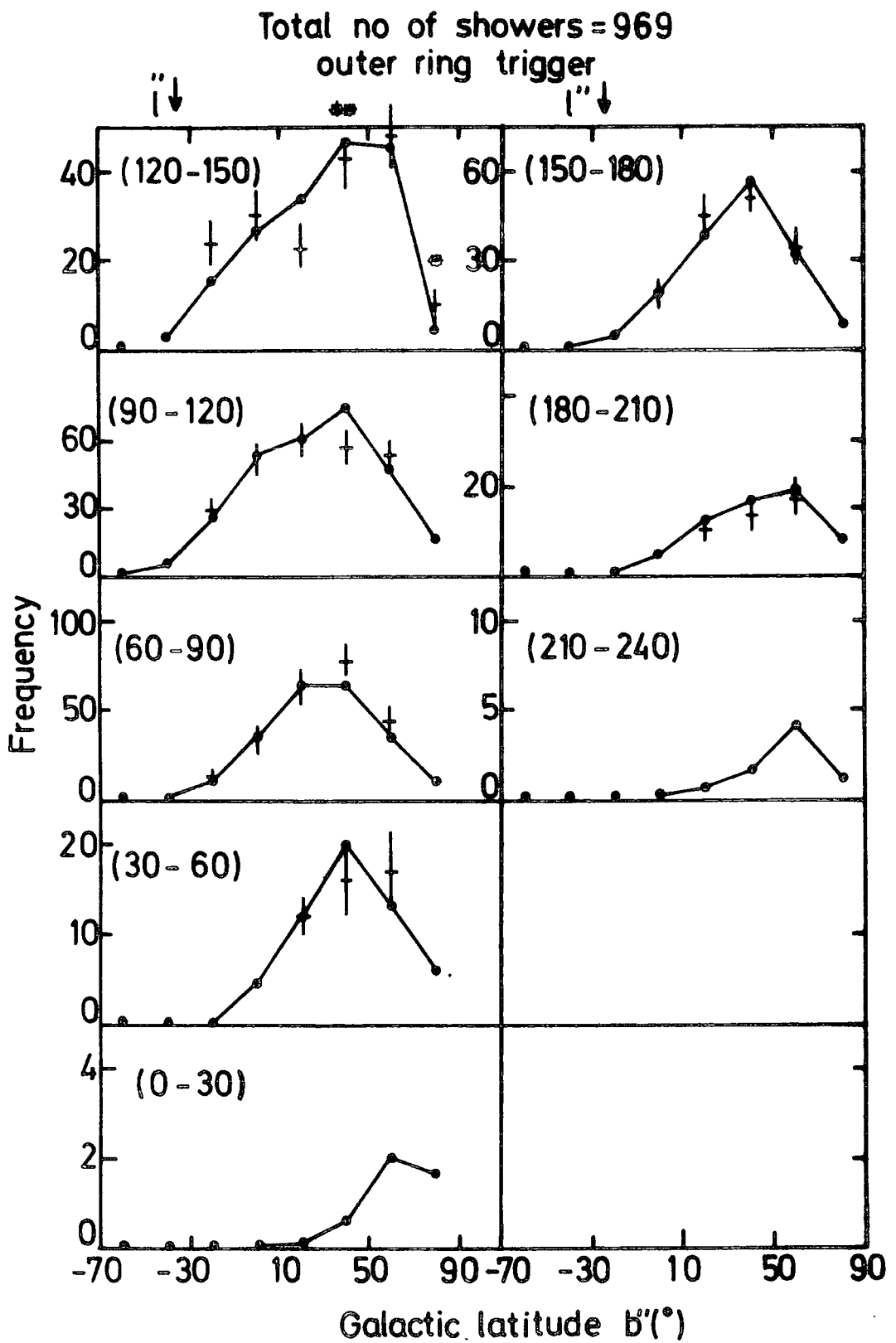
Figure 8.18 : Variation of the expected number of showers with galactic latitude for different ranges of galactic longitude. The observed number of events in cells containing ≥ 10 showers are plotted.

Figure 8.19 : Variation of the expected number of showers with galactic longitude for different ranges of galactic latitude. The observed number of events in cells containing ⩾ 10 showers are plotted.

Figure 8.20 : Variation of the expected number of showers with galactic latitude for different ranges of galactic longitude. The observed number of events in cells containing ≥ 10 showers are plotted.

Figure 8.21 : Variation of the expected number of showers with galactic longitude for different ranges of galactic latitude. The observed number of events in cells containing ≳ 10 showers are plotted.

Figure 8.22 : Variation of the expected number of showers with galactic
latitude for different ranges of galactic longitude.
The observed number of events in cells containing ≥ 10
showers are plotted.

($\bar{N} = 3.1u^5$) than the outer ring trigger data ($\bar{N} = 1.11.10^6$).

8.5   CONCLUSION

Overall the arrival directions of EAS seem to be isotropically distributed in space. Some evidence is found for a possible increase in intensity from two directions with galactic longitude and latitude ($135^O \pm 15^O$, $4u^O \pm 10^O$) and ($135^O \pm 15^O$, $8u^O \pm 10^O$).

The galactic coordinates of the two galactic cells shown in Figure 8.14 which contain a significantly larger number of events than expected have been compared with the galactic coordinates of supernova remnants, pulsars, quasars, X and Y-ray sources which are shown in Figures (8.23) to (8.27). It is seen from the figures that there are no observed X, Y or supernova remnants (they are mostly in the galactic plane) in our excess regions of events (represented by squares). However, there is some correlation with pulsar and quasar sources. The properties of these sources has been investigated in spite of not every pulsar or quasar having all the required information at the present time. The ones known are shown in Figures 8.28 and 8.29. The ones in the square regions for quasars show no sign of any anomalous property whereas the pulsar (PU8U9 + 74) shows the interesting property of having one of the longest ages and shortest distance from earth of known pulsars.
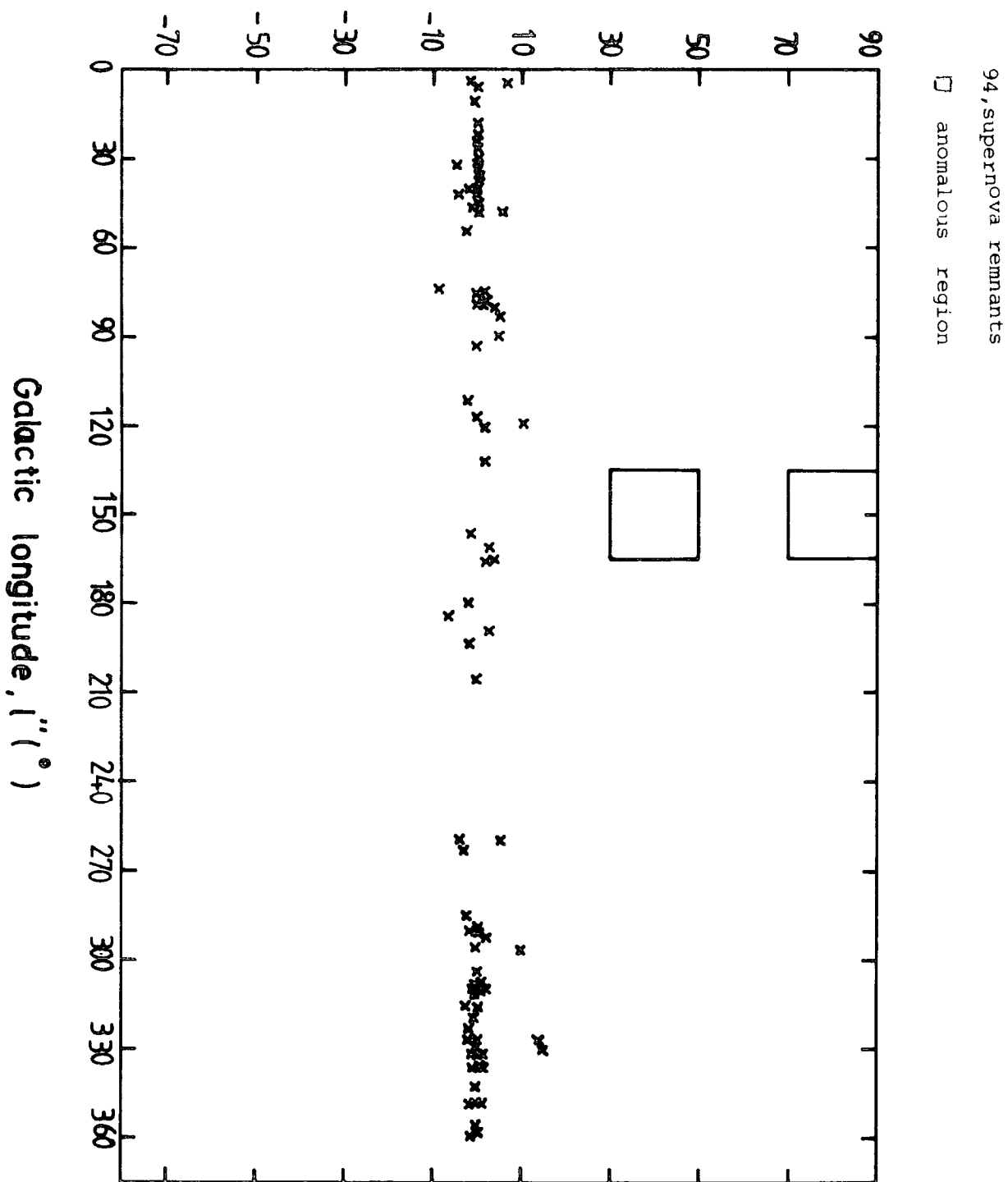
Figure 8.23 : Known supernova remnants in galactic coordinates,
(From "Astrophysical Formulae", Lang (1974)).
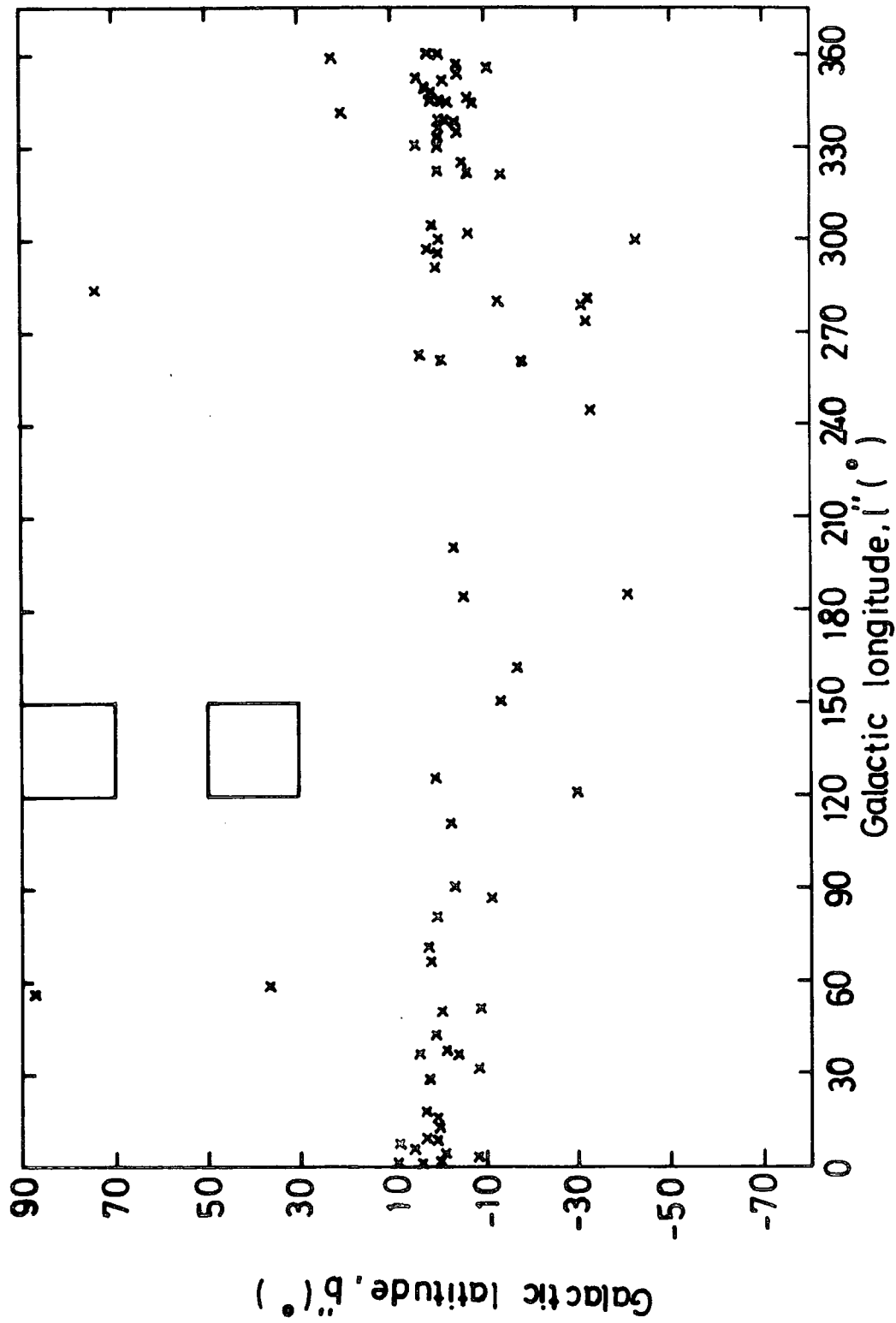
79 X-ray sources (UHURU Satellite)

(2-6) KeV intensities ⩾ .10 counts/sec/detector

Figure 8.24 : 79 X-ray sources in galactic coordinates, (From the Fourth URURU Catalogue of
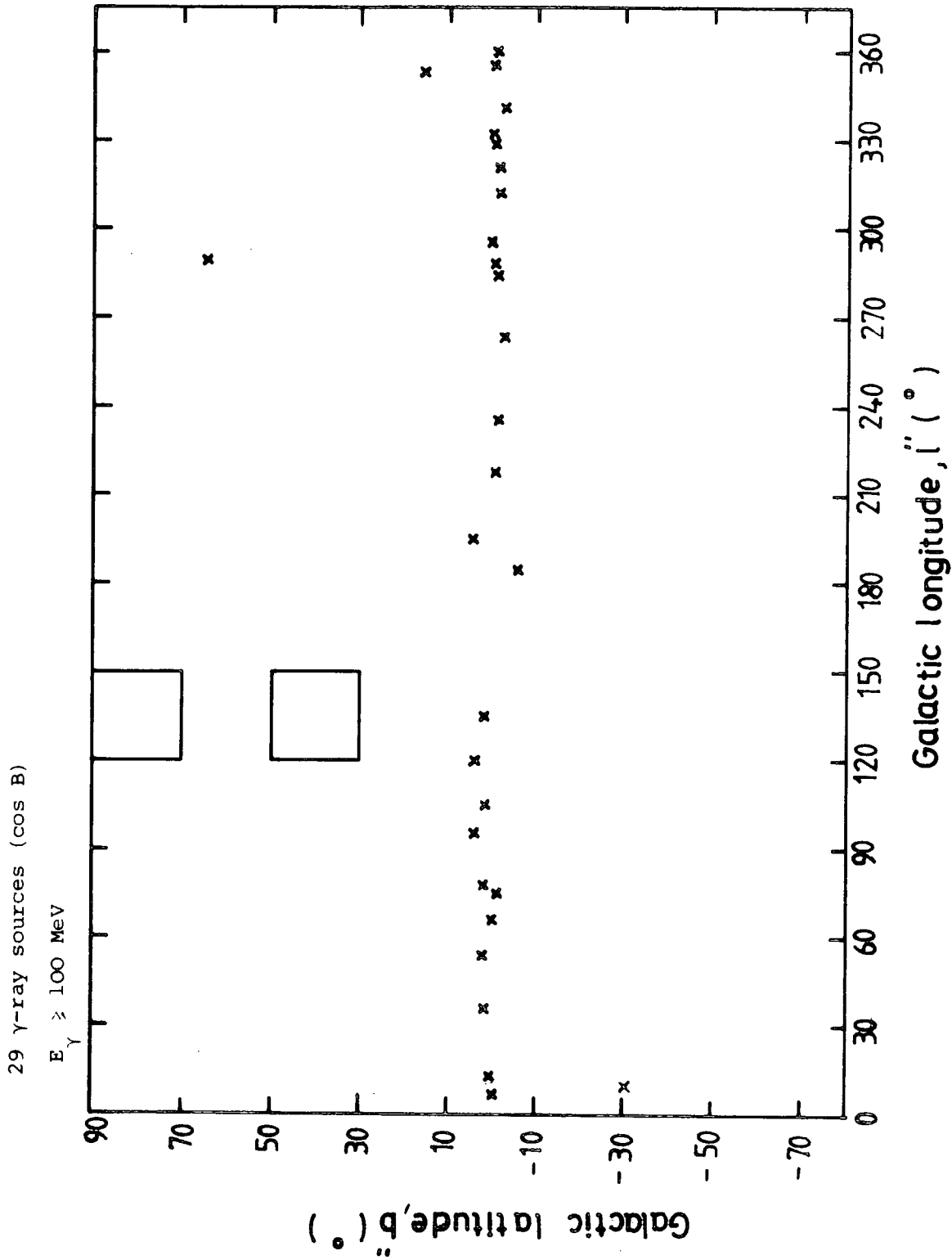X-Ray sources, Forman (1978)).

Figure 8.25 : Known γ ray sources in galactic coordinates, (Europhysics Study Conference, (1979), Gamma ray Astronomy after Cos-B).
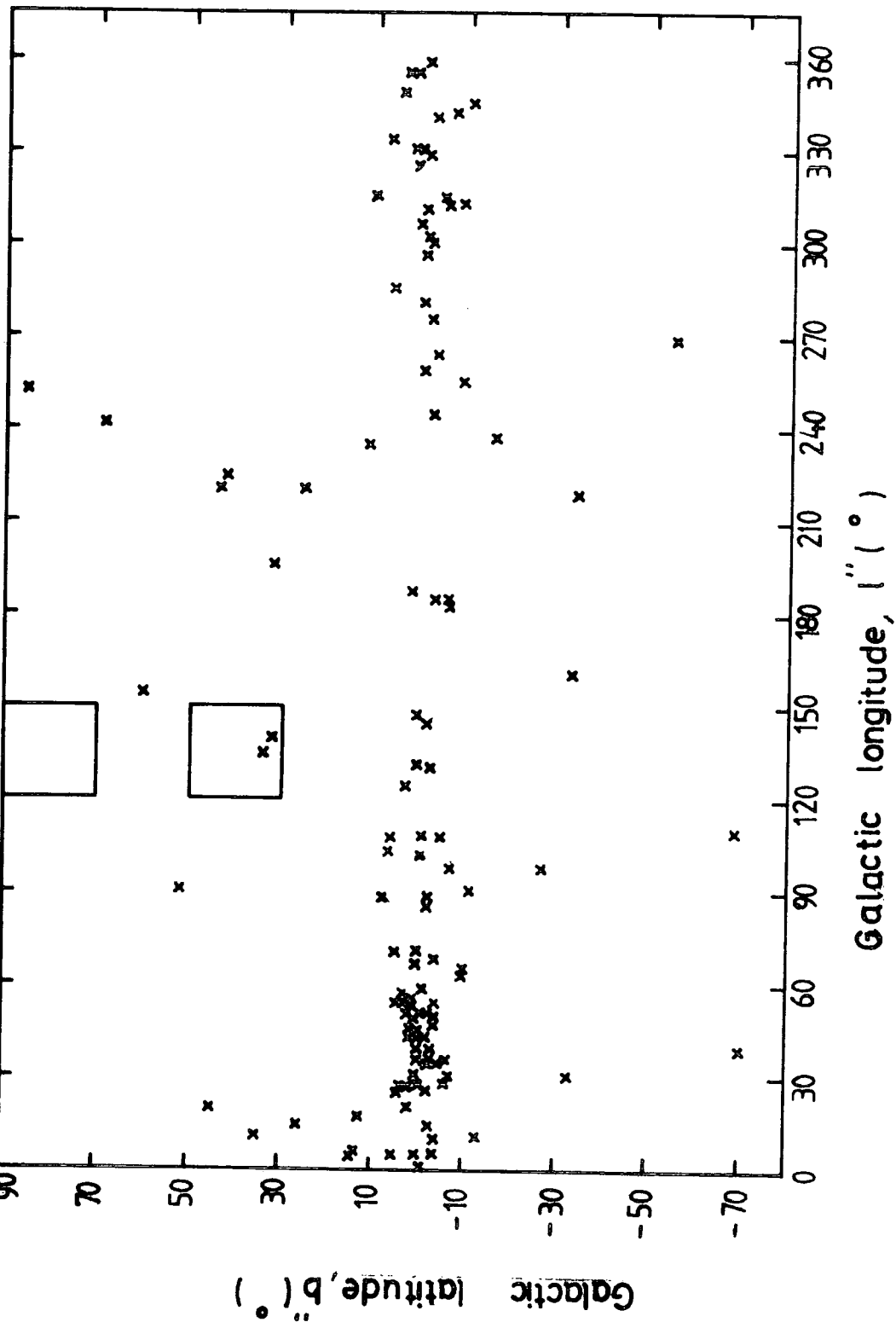
Figure 8.26 : Known pulsars in galactic coordinates (from "Pulsars", Manchester et al, (1977))

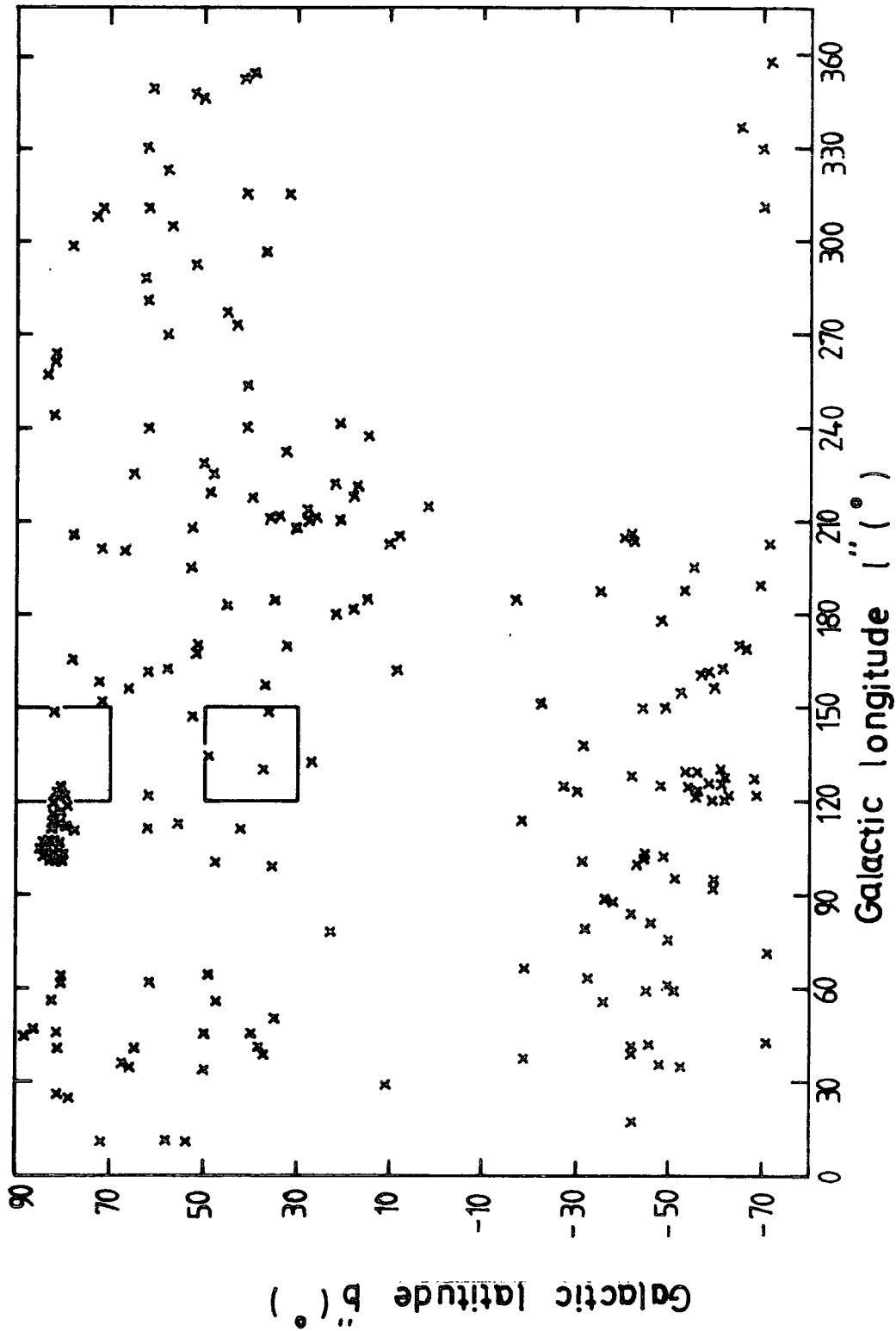Quasars (flux density at 1400 MHz)
□ anomalous region

Figure 8.27 : Known quasars in galactic coordinates, (from "Astrophysical Formulae", Lang (1974)).
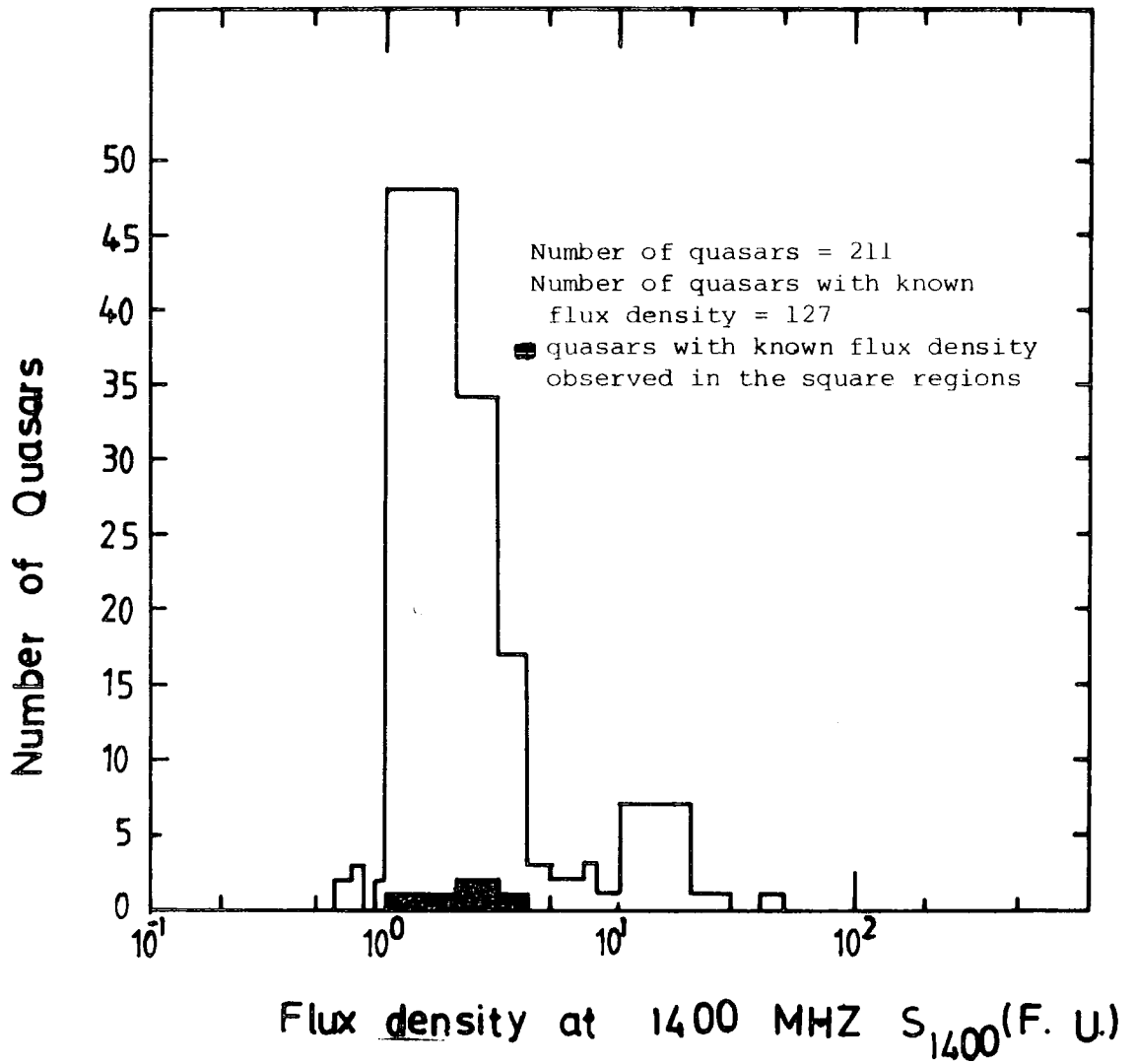
Figure 8.28 : Flux density distribution of known quasars
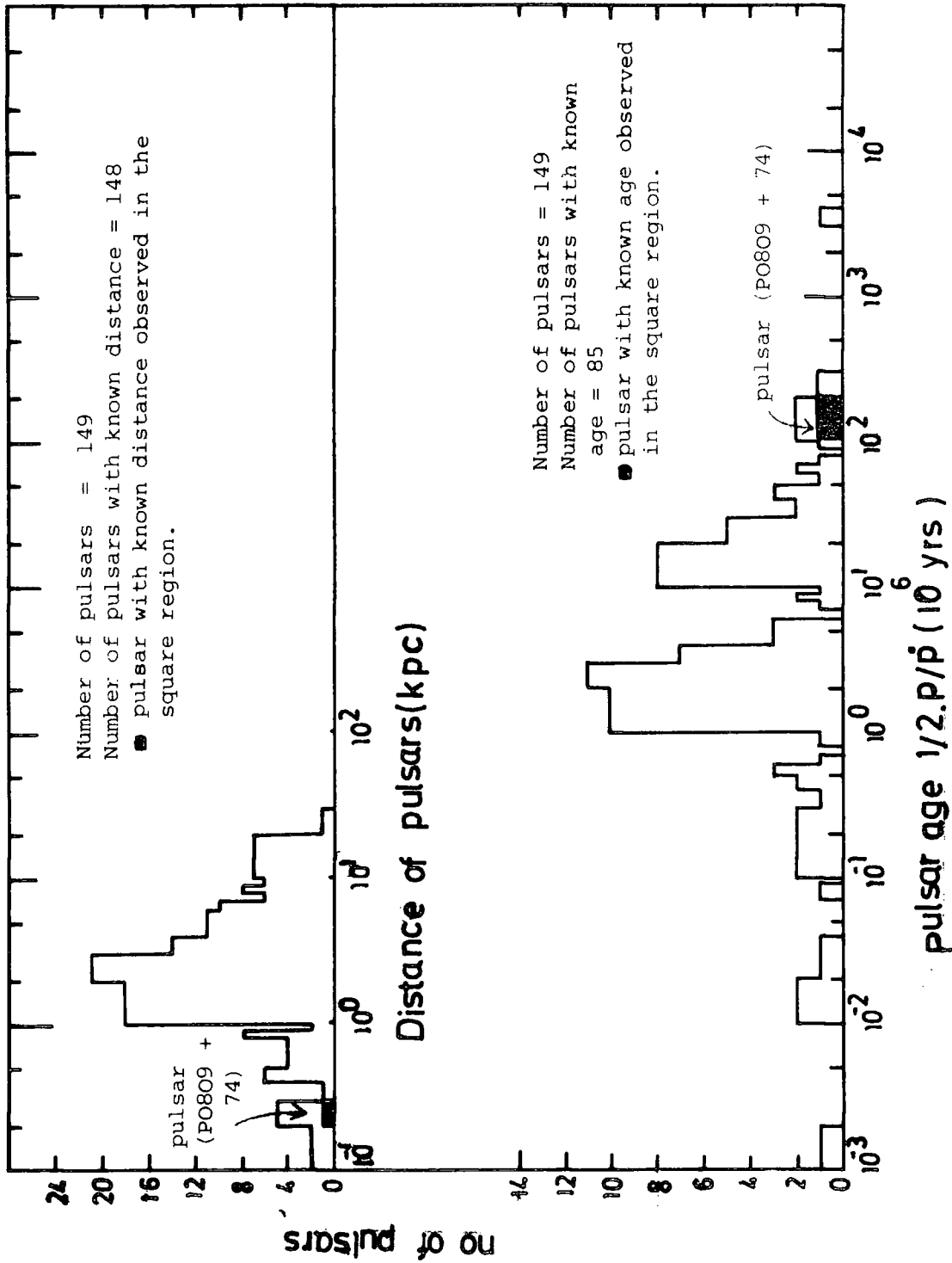(from "Astrophysical Formulae", Lang (1974)).

Figure 8.29 : Age and Distance Distributions of Known Pulsars (from "Astrophysical Formulae", Lang (1974)).

CHAPTER 9

CONCLUSION

The Durham E.A.S. array and a large flash tube chamber were used to study the details of E.A.S.phenomena, that give an understanding of elementary particles, nuclear interactions and also the nature and origin of E.A.S.

The study of the electron component and the age parameter, s, of individual E.A.S. in the size range of 10^4-10^7 particles showed that they do not all obey the same structure function. The mean and the standard deviation of the age parameter distribution of the showers showed that on average they are independent of zenith angle. The observed large fluctuation of the age parameter distribution indicates no significant fraction of heavy nuclei in primary cosmic rays since these would produce a negligible fluctuation.

A measurement of the size spectrum was obtained taking into account the age parameter of E.A.S. and the results showed that it is not quite consistent with previous work. The difference is at large sizes $>10^7$ pts and is due to an increase of age parameter with shower size which results in a larger average size.

A correlation between the electron and muon component was also found. The results showed on average that old showers have more muons and a flatter lateral distribution of muons than young showers (i.e. $\frac{\Delta_\mu (s > 1.2)}{\Delta_\mu (s \leq 1.2)} = 1.24 \pm 0.05$). In the search for quarks two candidates were found but these are believed to be due to background muons which simulate e/3 quark-like tracks. This gave the ratio of penetrating charge e/3

particles to penetrating e particles as $< \dfrac{1}{1,136}$ for the present experiment.

An analysis of the arrival directions of E.A.S. in galactic coordinates has been made. Evidence for an excess of events from galactic directions with latitude $b'' = (30-50)$ and $b''(70-90)$ and both having galactic longitude of $''(120^{\circ}-150^{\circ})$ were observed.

APPENDIX A

EVALUATION OF THE FRACTION OF PARTICLES WHICH FALL BEYOND A DISTANCE FROM THE SHOWER AXIS DIRECTION IN PURE ELECTRON PHOTON CASCADES

The fraction of electrons that fall at core distance $>r$ is given by $F(>r,s) = \int_{r}^{\infty} 2\pi r \, S(r,s)dr$ where $S(r,s) = c(s) \, r^{s-2} \, (1 + r)^{s-4.5}$ is the electron structure function for showers of age parameter s, r is the core distance in Moliere units (79 m at sea level) and $c(s)$ is a normalisation factor such that $\int_{0}^{\infty} 2\pi r \, S(r,s)dr = 1$. $F(>r,s)$ is evaluated in two parts for $0<r\leqslant k$ and $r> k$. k is the distance beyond which the structure function tends to a straight line on a log-log plot so it is well approximated by $\frac{A}{r^{\alpha}}$. The parameters A and α are simply obtained, so for any $r\geqslant k$, the integral

$$F(>r,s) = \int_{r}^{\infty} 2\pi r \, S(r,s)dr = \int_{r}^{\infty} 2\pi A \, \frac{r}{r^{\alpha}} = 2\pi A \int_{r}^{\infty} r^{1-\alpha}dr$$

is calculated. Because of the complexity of the function $S(r,s)$ the formula $S(r,s) = \frac{A}{r^{\alpha}}$ cannot be used for $0< r\leqslant k$ and is evaluated numerically. The results are shown in Figures A1 and A2.
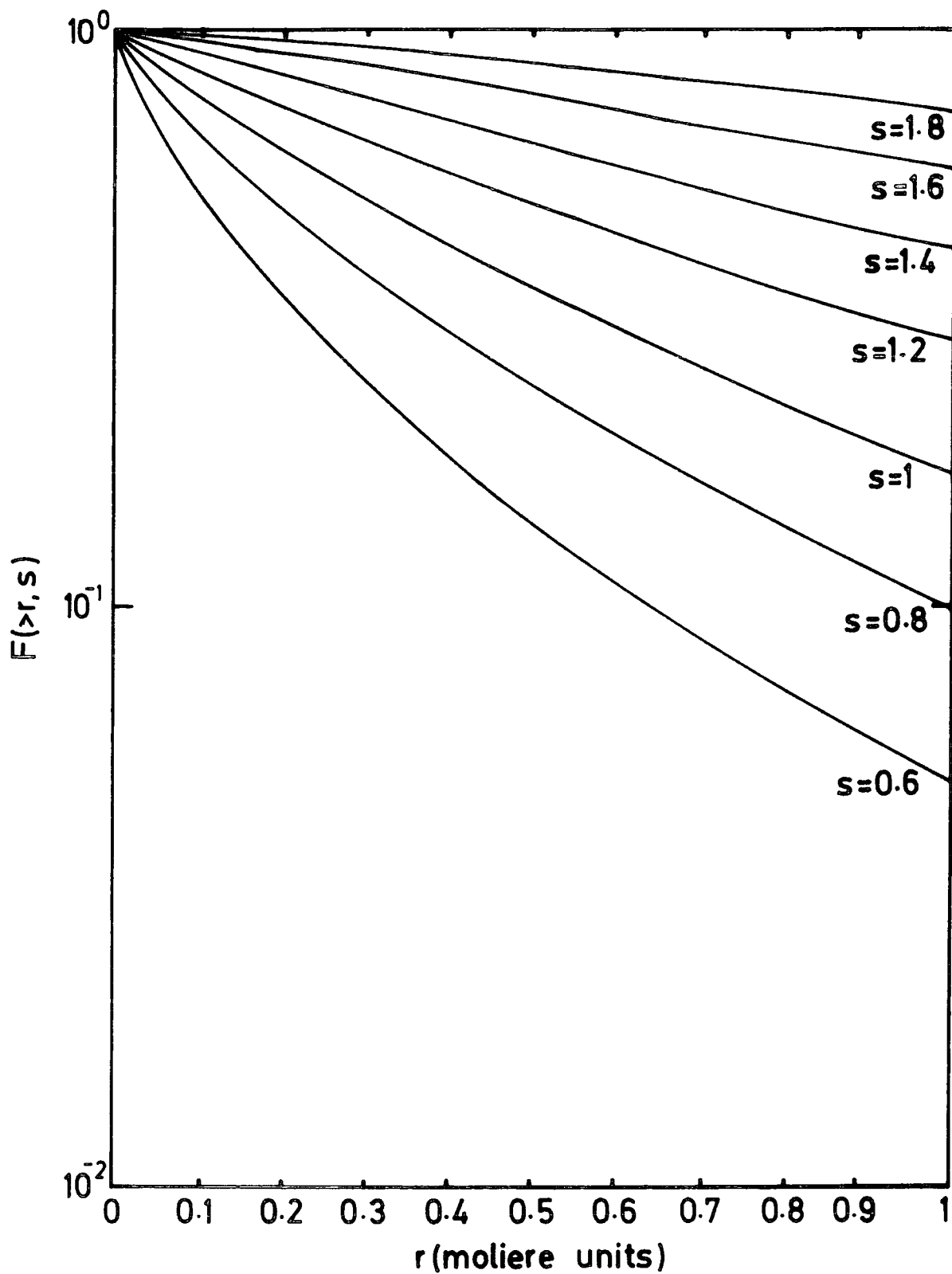
Figure A1 :   The fraction of electrons F(>r,s) that fall at core
distance >r in pure electron photon showers for r in
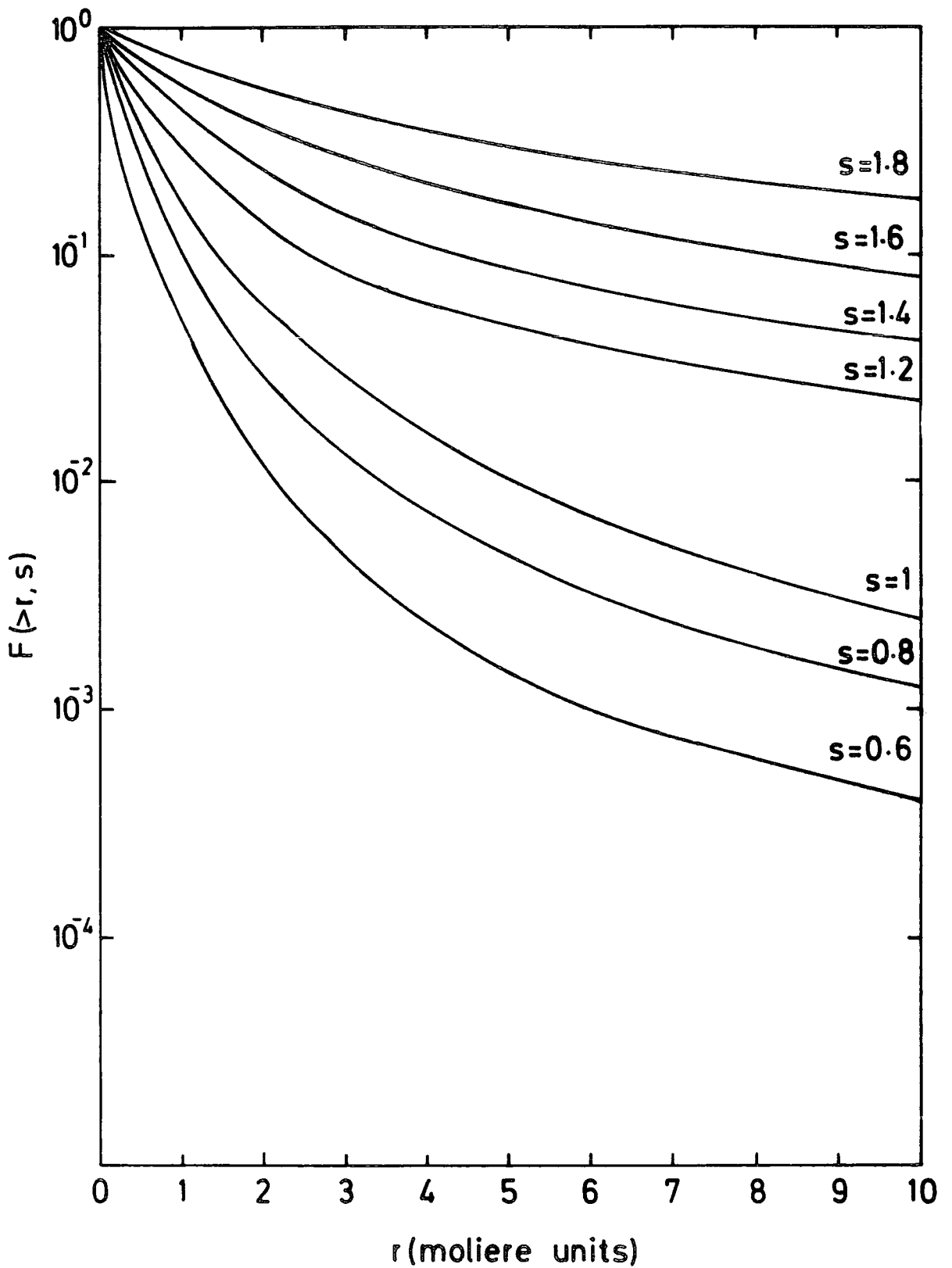the range 0-1 Moliere unit.   s is the age parameter
of the shower.

Figure A2 : The fraction of electrons F(>r,s) that fall at core distance >r
in pure electron photon cascades for r in the range
0-10 Moliere units.   s is the age parameter of the shower.

A COPY OF THE CERN MINUIT PROGRAM USED TO MINIMIZE THE N.K.G.

FUNCTION FOR THE AGE PARAMETER AND SHOWER SIZE

TERMINAL SYSTEM FORTRAN G (21.8)   FCN

```
0001              SUBROUTINE FCN(NPAR,G,F,X,IFLAG)
0002              DIMENSION G(150),X(150),R(15),DR(14),CHISQ(14),VR(14),
                 *E(14),AH(14),XD(15),YD(15),ZD(15),SY(15),Y(15)
0003              DIMENSION FC(14)
0004              COMMON/KEEP/K,DTIT,R
0005              GO TO(1,2,2,2),IFLAG
0006         1    CONTINUE
0007              DATA AH/0.75,2.0,2.0,2.0,2.0,2.0,2.0,0.8,0.8,1.0,
                 *1.0,1.2,1.0,1.6/
0008              DATA XD/0.0,-12.3,-45.0,14.0,45.0,0.3,-5.0,-24.0,
                 *-24.0,25.5,22.0,39.5,-0.5,-7.9,-9.5/
                  DATA YD/0.0,-5.64,29.5,3.5,14.0,-26.8,-58.5,7.5,
                 *7.5,8.5,-17.0,-36.5,-17.0,-5.11,-6.2/
0010              DATA ZD/0.0,-4.83,-13.46,0.16,0.21,0.18,-8.67,
                 *-12.75,-12.75,0.75,-11.4,-8.2,0.6,-4.7,0.0/
0011              READ(5,100)(K,(DR(I),I=1,10))
0012              READ(5,150)((DR(I),I=11,14),DTIT,FA,XE,YE)
0013       100    FORMAT(I8,10F6.1)
0014       150    FORMAT(8F 6.1)
0015              TIT=DTIT*3.14/180.
0016              FA=FA*3.14/180.
0017              DO 30 I=1,14
0018              VR(I)=ABS(DR(I)*AH(I))
0019              E(I)=SQRT(1.436*VR(I)+SQRT(VR(I))+0.25)
0020        30    CONTINUE
0021         2    CONTINUE
0022              HN=X(1)
0023              S=X(2)
0024              F=0.0
0025              DO 200 I=1,14
0026              IF(DR(I).LT.0.0)GOTO200
0027              Y(I)=ABS(((XD(I)-XE)**2+(YD(I)-YE)**2+(ZD(I)**2)-(SIN(TIT)*
                 *((XD(I)-XE)*COS(FA)+(YD(I)-YE)*SIN(FA))+(ZD(I)*COS(TIT)))**2))
0028              SY(I)=ABS(SQRT(Y(I)))
0029              IF(SY(I).LT.0.5)SY(I)=0.5
0030              FO(I)=(HN/79.**2)*AH(I)*0.366*(S**2)*((2.077-S)**1.25)*
                 *(((SY(I))/79.)**(S-2.))*((SY(I))/79.+1.)**(
                 *S-4.5)
0031              CHISQ(I)=((FC(I)-VR(I))/E(I))**2
0032              F=F+CHISQ(I)
0033       200    CONTINUE
0034              IF(IFLAG.NE.3)GO TO 24
0035              DO 40 I=1,15
0036              A=XD(I)-XE
0037              B=YD(I)-YE
0038              C=ZD(I)
0039              ABC=A**2+B**2+C**2
0040              SI=A*COS(FA)+B*SIN(FA)
0041              SI=SI*SIN(TIT)+C*COS(TIT)
0042              SI=SI**2
0043              SUBI=ABS(ABC-SI)
0044              R(I)=SQRT(SUBI)
0045        40    CONTINUE
0046              WRITE(6,77)K
0047        77    FORMAT(I8)
0048              DO 300 I=1,14
0049              IF(DR(I).LT.0.0)GOTO300
```

```
0050          WRITE(6,400)R(I),VR(I),DR(I),CHISQ(I),FC(I),E(I)
0051    400   FORMAT(2X,F8.2,3X,F6.2,5X,F10.3,6X,F12.4,4X,2F12.4)
0052    300   CONTINUE
0053          WRITE(6,101)R(15),R(1)
0054    101   FORMAT(4X,F8.4,4X,F8.4)
0055     24   CONTINUE
0056          RETURN
0057          END
```

TERMINAL SYSTEM FORTRAN G (21.8)   STAND

```
0001          SUBROUTINE STAND
0002          DIMENSION A(1000),B(1000),EA(1000),EB(1000),R(15)
0003          DIMENSION KA(300),DTITA(300),RA1(300),RA15(300)
0004          DIMENSION DR(14),XD(15),YD(15)
0005          COMMON/MINIMA/AMIN,UP,NEWMIN,ITAUR,SIGMA/CONVER/EPSI,APSI,VTEST,
             *NSTEPQ,NECN,NFCNMX
0006          COMMON/PAREXT/U(150),W(150),WERR(150),MAXEST,NU/PARINT/
             *X(55),XT(55),DIRIN(55),MAXINT,NPAR/LIMITS/ALIM(150),
             *BLIM(150),LCODE(150),
             *LOORSP(150),LIMSET/TITLE/TITLE(55),ISW(7),NBLOCK
0007          COMMON/KEEP/K,DTIT,R
0008          DIMENSION G(150)
0009          ITER=151
0010          DO 10 I=1,ITER
0011          ITAUR=0
0012          CALL FCN(NPAR,G,AMIN,U,4)
0013          CALL SEEK
0014          NFCNMX=4000
0015          EPSI=0.01
0016          VTEST=0.04
0017          APSI=EPSI
0018          NFCN=0
0019          CALL SIMPLX
0020          NFCN=0
0021          CALL MIGRAD
0022          IF(ISW(2).GT.2) GOTO11
0023          CALL HESSE
0024     11   CONTINUE
0025          CALL FCN(NPAR,G,AMIN,U,3)
0026          A(I)=U(1)
0027          B(I)=U(2)
0028          KA(I)=K
0029          DTITA(I)=DTIT
0030          RA1(I)=R(1)
0031          RA15(I)=R(15)
0032          IF(I.FQ.ITER)GOTO20
0033          CALL FCN(NPAR,G,AMIN,U,1)
0034     10   CONTINUE
0035     20   CONTINUE
0036          DO 1951 II=1,ITER
0037          PRINT 66
0038          PRINT 1952,II,KA(II),DTITA(II),RA1(II),RA15(II),B(II),A(II)
0039   1952   FORMAT(1X,'I',I5,' I ',I8,4(' I ',F8.2),' I ',E10.3,
             *' I ',8X,'I',8X,'I')
0040     66   FORMAT(1X,96('-'))
0041   1951   CONTINUE
0042          PRINT 66
0043          RETURN
0044          END
```

APPENDIX C

THE EFFECT OF SAMPLING DENSITY FLUCTUATIONS ON THE COLLECTING AREA FOR SHOWERS OF A GIVEN SIZE FOR A GIVEN E.A.S. SELECTION TRIGGER

Consider the collecting area for showers of size 3.10^5 selected by an outer ring trigger, $\Delta_c (\geqslant 4 \ m^{-2})$. $\Delta_{13} (\geqslant 2 \ m^{-2})$. $\Delta_{33} (\geqslant 2 \ m^{-2})$. $\Delta_{53} (\geqslant 2 \ m^{-2})$ where the area of detector C is 0.75 m^2 and the areas of detectors 13, 33 and 53 are 2 m^2. Suppose the showers are incident vertically and the electron lateral distribution is given by the Greisen average electron lateral distribution function (s = 1.25). This means that the collecting area is calculated for a minimum number of particles = 3 at C and 4 at the other three triggering detectors, which is the area of the spherical triangle shown in Figure C_1. To get a more exact estimate of the collecting area the effect of sampling density fluctuations at the detectors should be taken into account. Taking the fluctuations as Poissonian,

$$p(r) = \frac{e^{-z} z^r}{r!}$$

where $p(r)$ is the probability of observing r when the mean number expected is z. For any core position (x,y) in the array at which a shower of size 3.10^5 falls, the core distance from a triggering detector and therefore the average number of particles through it can be calculated.

Figure C.1 : Scale diagram showing the collecting area for a vertical shower of size 3.10^5 with $s = 1.25$ selected by an outer ring trigger Δ_c ($\geqslant 4m^{-2}$). Δ_{13} ($\geqslant 2m^{-2}$), Δ_{33} ($\geqslant 2m^{-2}$) and assuming no sampling density fluctuations. 6 radius vectors on which the effect of sampling density fluctuations on collecting area are also shown in the figure.

20m

vertical shower
Ne = 3.10^5
s = 1.25
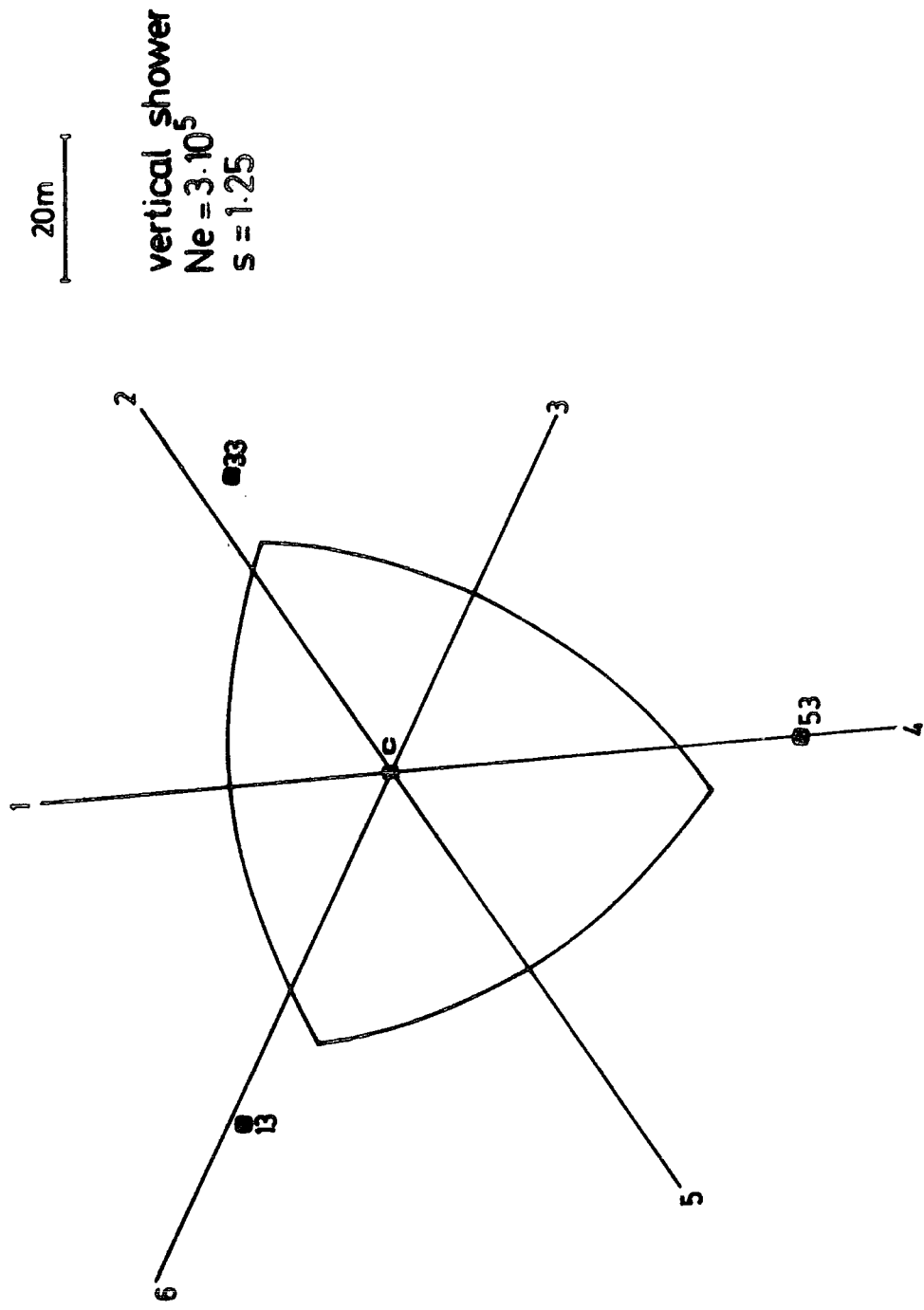
for the case of the outer ring detectors $p(r)$ is

$$p(r) = e^{-z} (1 + \frac{z^1}{1!} + \frac{z^2}{2!}) \quad \text{for detector C}$$

$$= e^{-z} (1 + \frac{z^1}{1!} + \frac{z^2}{2!} + \frac{z^3}{3!}) \quad \text{for detectors}$$
$$13, 33 \text{ and } 53$$

where z is the mean number of particles through the detector
and the first term is the probability of there being zero,
the second term being the probability of there being 1, etc.
The detection probability for a shower falling at the
position (x,y) is the sum of all the detector probabilities
or

$$P(r) = \sum_i p_i(r) : i = C, 13, 33 \text{ and } 53$$

In the present case $P(r)-r$ for each of 6 radius vectors (as
chosen in figure C.1) was evaluated and the results are given
for the case of fluctuations and no fluctuation in Figure C.2.
The collecting area A is given by

$$A = \int_{\theta=0}^{2\pi} \int_{r=0}^{\infty} r d\theta \, dr \, P(r)$$

A measure of the effect of fluctuation on the collecting area

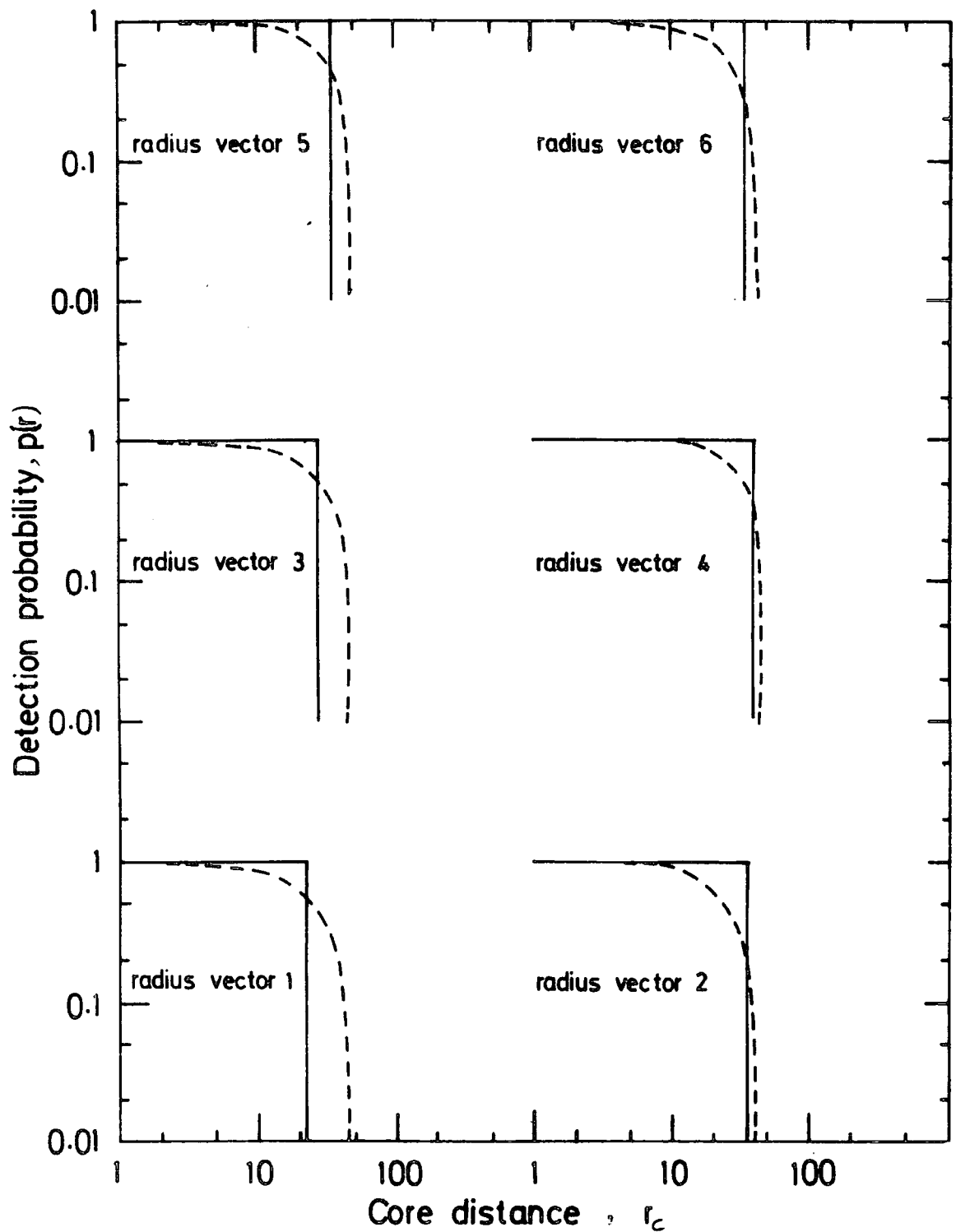Figure C.2 : The detection probability for a shower of size 3.10^5 pts with s = 1.25 selected by the outer ring trigger as a function of core distance from the central detector r_c for each of 6 radius vectors as shown in figure C.1. The detection probability assuming no sampling density fluctuations are shown by the solid line and the dashed line shows the effect of sampling density fluctuations.

for each radius vector is

$$\frac{\int_{0}^{\infty} r \, dr \, P(r)}{\int_{0}^{r_{max}} r \, dr} = \frac{\int_{0}^{\infty} r \, dr \, P(r)}{\frac{r_{max}^{2}}{2}} = \frac{\text{fluctuation collecting area}}{\text{no fluctuation collecting area}} = F$$

Table C.2 shows the values of F for the 6 radius vectors together with the mean value of $\bar{F}$ which shows the effect of sampling density fluctuations on collecting area for a shower of size 3.10^{5} particles. It is seen that $\bar{F} = 0.95 \pm 0.15$ which indicates the effect is small. The collecting area assuming no sampling density fluctuation for a vertical shower of size 3.10^{5} with s = 1.25 is $3.2.10^{3} \, m^{2}$ (see Figure C.3). A more exact estimate of the collecting area taking the sampling density fluctuations factor $\bar{F}$ into account is

$$3.2.10^{3} \, m^{2} \times 0.95 = 3.04.10^{3} \, m^{2}$$

The coordinates of the centres of the detectors used in the present work (see Table C1) were slightly different to those given by Abdullah et al (1979).

Detector	C	11	13	31	33	51	53	12	42	61	62	32	41	52
X Coordinate (m)	0	-12.3	-45	14	45	0.3	-5	-24	39.5	-7.9	-43.1	25.5	22	-0.5
Y Coordinate (m)	0	-5.64	29.5	3.5	14	-26.8	-58.5	7.5	-36.5	-5.11	-18.3	8.5	-17	-17
Z Coordinate (m)	0	-4.83	-13.46	0.16	0.21	0.18	-8.67	-12.75	-8.2	-4.7	-10.3	0.75	-11.4	0.6

TABLE C.1 : The detector's coordinates of the Durham E.A.S. Array.

Radius Vector	F
1	1.57
2	0.52
3	1.30
4	U.66
5	1.04
6	0.64
Average	$\bar{F} = 0.95 \pm 0.15$

Table C.2 :   The value of the ratio of fluctuation collecting area to the no fluctuation collecting area, F for a shower of size 3.10^5 with s = 1.25 selected by the outer ring selection trigger for the 6 radius vectors shown in Figure C.1. The average value $\bar{F}$ is also given.
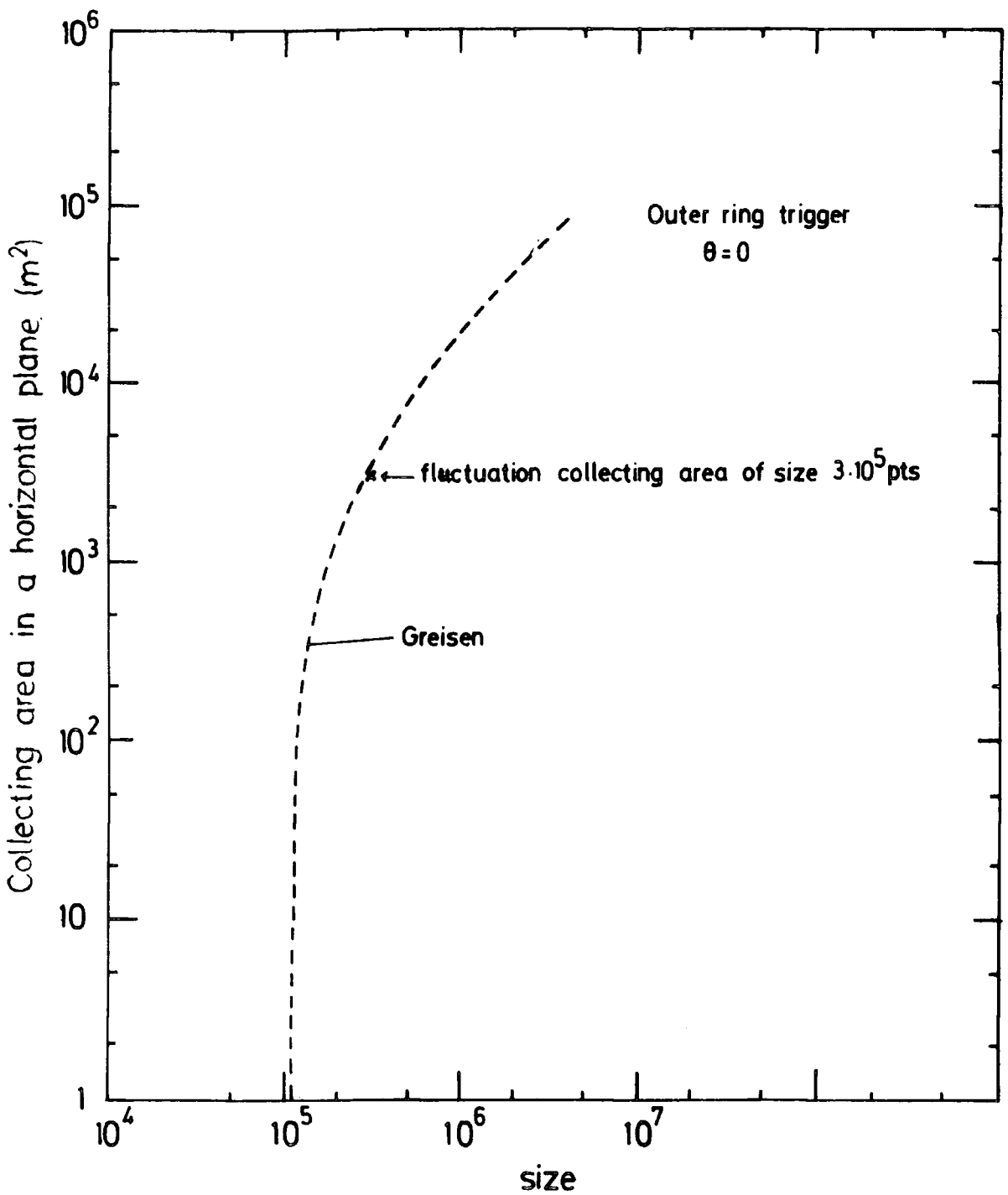
Figure C.3 : The collecting area as a function of shower
size for E.A.S. selected by an outer ring
trigger. For size 3.10^5 pts the no. fluctuation
collecting area is compared with the fluctuation
collecting area which is marked by a solid circle.

APPENDIX D

THE EFFICIENCY OF DETECTING SINGLE PENETRATING CHARGED PARTICLES TRAVERSING A SHIELDED FLASH TUBE CHAMBER AS A FUNCTION OF CORE DISTANCE IN EXTENSIVE AIR SHOWERS

In order to obtain the efficiency of the chamber the effect of burst production (i.e. hadron interactions in the shielding lead and iron) should be considered. The efficiency of the chamber depends on each individual event and decreases with increasing burst size which occurs in the chamber. The possibilities of burst production could be of four types as given in Figure D1. For each type the efficiency of detecting a single penetrating particle is measurable as formulated below each type shown in Figure D1a to Figure D1d. The efficiency of all events described in Chapter 7 have been individually measured accordingly and grouped into core distance ranges of 0-5, 5-10, 10-20 and 20-30 meters from the chamber where shower size ranges of less and bigger than the median size of the data ($Ne=3.10^5$ pts) were chosen for analysis. The shower size distributions of events for the above mentioned core distances are given in Figure D2 and their corresponding average efficiency -core distance results are given in Figure D3. It is noted that these measurements are for the basic data and should be corrected for the effect of core location errors. Assuming that the core location errors are Gaussian with a standard deviation of 6.0 m (see Chapter 3) and also that the detection efficiency, η has the form $\eta = 1 - e^{-r/r_o}$, a simulation work

was performed which showed that the best values of r_0 that
fit the measurements for $10^4 < N < 3.10^5$ and $N > 3.10^5$ pts are
$r_0 = (1.55 \pm 0.15)$m and $r_0 = (3.25 \pm 0.65)$m respectively
as given in Table D1. These functions are plotted in
Figure D3. It is seen that the efficiency η of detecting
single penetrating particles decreases as the core distance
decreases, due to high energy hadrons interacting in the
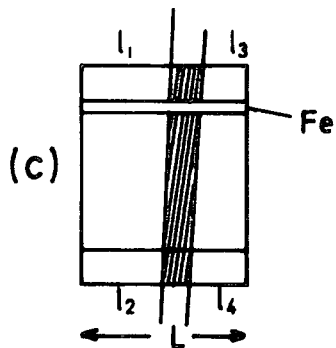shielding material.

(a)
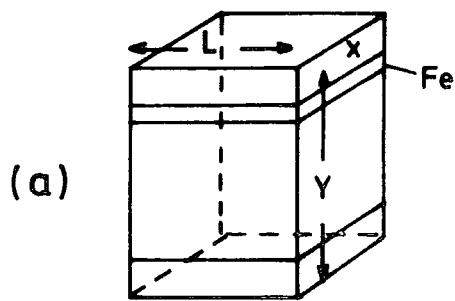
Aperture = solid angle x area

$$= \frac{Lx}{y^2} \cdot Lx$$

$$= \frac{L^2 x^2}{y^2}$$

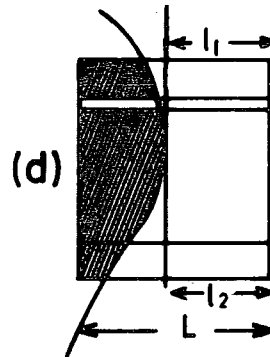probability of detecting a single particle = 1 in this case

(b)
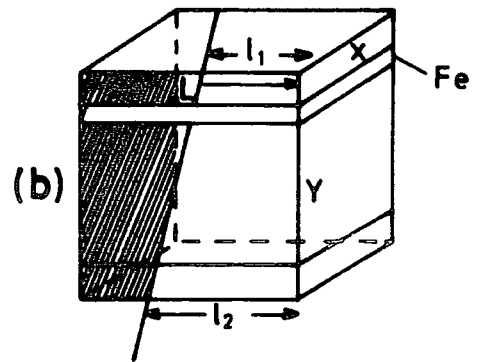
Aperture = solid angle x area

$$= \frac{l_1 x}{y^2} \cdot l_2 x$$

$$= \frac{l_1 l_2 x^2}{y_2}$$

probability of detecting a single particle = $l_1 l_2 \frac{x^2}{y^2} \Big/ \frac{L^2 x^2}{y^2} = \frac{l_1 l_2}{L^2}$

(c)

Probability of detecting a single particle = $\frac{l_1 l_2}{L^2} + \frac{l_3 l_4}{L^2}$

(d)

Probability of detecting a single particle $\simeq \frac{l_1 l_2}{L^2}$

Figure D1 : Typical burst production occurring in the chamber, affecting the efficiency for detecting a single penetrating charged particle.
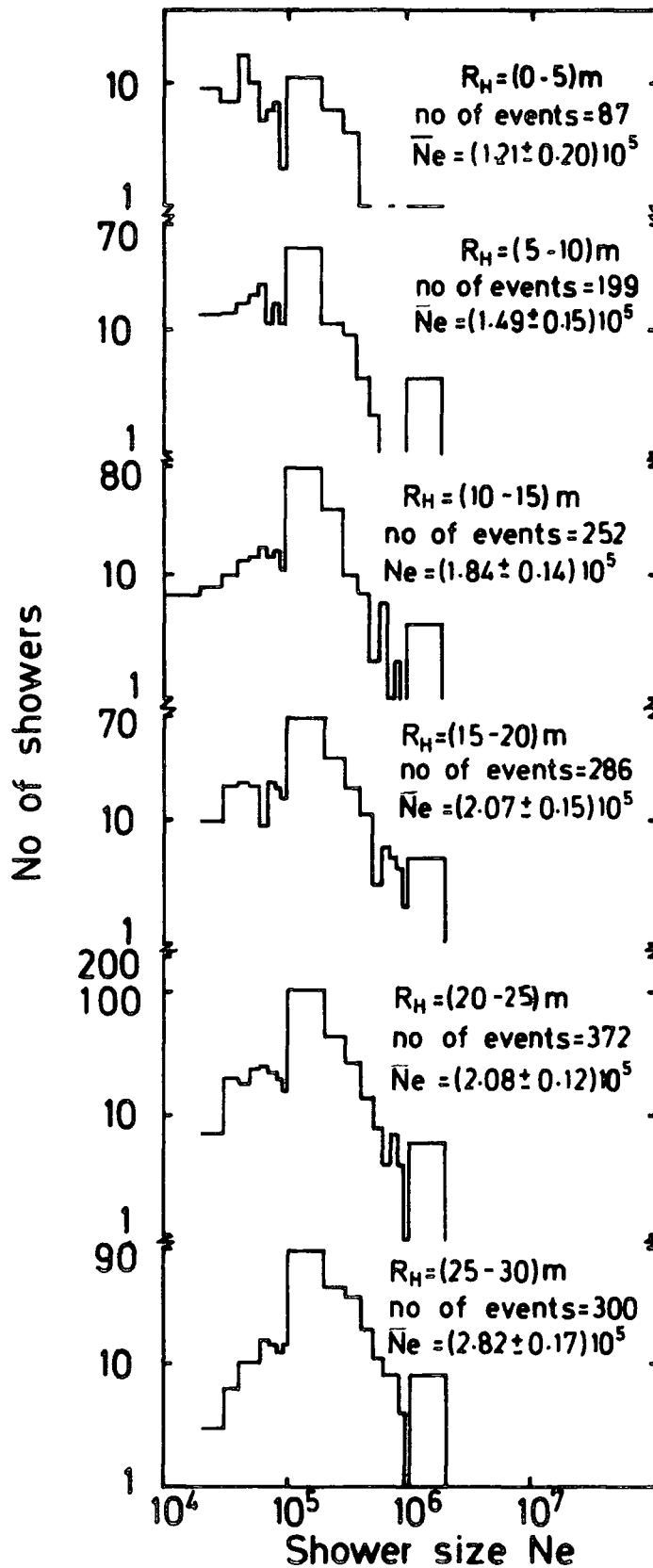
Figure D2 : Size distribution of showers falling in different ranges of orthogonal core distance R_H from the centre of the flash tube chamber used in the present analysis.

Shower size range	r_o in $\eta = 1-e^{-r/r_o}$
$10^4 < N < 3.10^5$	(1.55 ± 0.15) m
$N > 3.10^5$	(3.25 ± 0.65) m

TABLE D 1 :   Values of r_o in the efficiency-core distance function
for detecting a single penetrating charged particle,
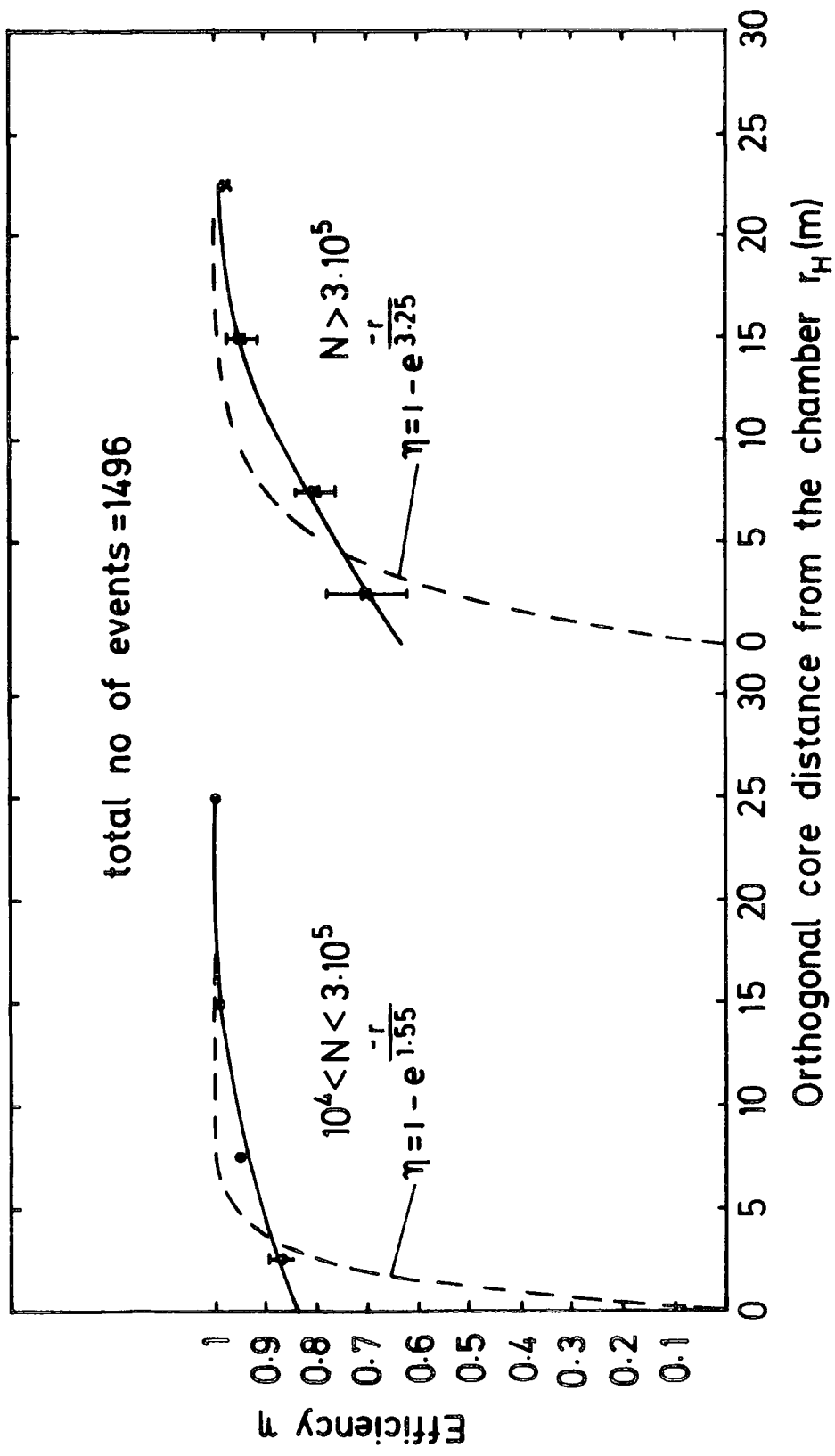for different ranges of shower size.

Figure D3 : The efficiency η of detecting a penetrating particle as a function of orthogonal core distance. — raw measurements uncorrected for core location error .

--- true variation for a core location error of 6.0 m.

APPENDIX E

CONSISTENCY OF THE PRESCOTT (1977) AND THE CLARK ET AL (1958)

FORMULAE FOR DETERMINING THE RIGHT ASCENSION AND DECLINATION

FROM THE MEASURED ARRIVAL DIRECTION OF AN E.A.S.

In Chapter Eight the formulae given by Prescott (1977) were used to determine the right ascension and declination of a shower with a measured zenith angle θ and azimuthal angle ϕ (measured in a clockwise direction from geographic north) occurring at a given local sidereal time. Alternative formulae have been given by Clark et al (1958) in terms of the direction cosines of the arrival direction and this appendix is to show that the two sets of formulae are consistent.

Consider a shower arriving at the point O in Figure E1 and suppose the shower makes direction cosines ℓ, m, n with the axes x, y, z. Ground level is the plane x, y and the y axis points in the direction of geographic north.

Prescott, I.C., "A study of the muon and electromagnetic components

of E.A.S", Ph.D. Thesis, Nottingham University,

May, 1977. (See Figure 3.4)

Clark, G., Earl, J., Kraushaar, W., Linsley, J., Rossi, B., and

Scherb, F., 1958, Supplements AP Volume VIII, Serie X del Nuovo Cimento,
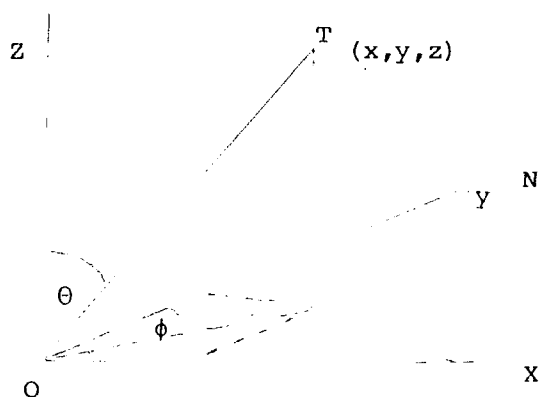
No.2, pp 622-652 (see page 644).

Figure E1.

$$\ell = \cos \hat{T_0 x} = \frac{x}{oT} = \frac{oT \sin\theta \sin\phi}{oT} = \sin\theta \ \sin\phi \tag{1}$$

$$m = \cos \hat{T_0 y} = \frac{y}{oT} = \frac{oT \sin\theta \cos\phi}{oT} = \sin\theta \ \cos\phi \tag{2}$$

$$n = \cos \hat{T_0 z} = \frac{z}{oT} = \cos\theta \tag{3}$$

From (1) and (2) ℓ^2 and $m^2 = \sin^2\theta\left(\sin^2\phi + \cos^2\phi\right) = \sin^2\theta$

$$\sin\theta = \sqrt{\ell^2 + m^2} \tag{4}$$

The equations given by Prescott (1977) are

$$\sin\delta = \sin\delta_o \cos\theta + \cos\delta_o \sin\theta \ \cos\phi \tag{5}$$

$$\sin H = \frac{\sin\theta \sin\phi}{\cos\delta} \tag{6}$$

$$RA = \gamma + \sin^{-1}\left(\frac{\sin\theta \sin\phi}{\cos\delta}\right) \tag{7}$$

Using equation (4) and equation (2), equation (5) becomes ,

$$\sin\delta = \sin \delta_o . \left[1 - \ell^2 - m^2\right]^{\frac{1}{2}} + \cos \delta_o . m \tag{8}$$

Substituting from (1) in (7) gives

$$RA = \gamma + \sin^{-1} \frac{\ell}{\cos\delta} \tag{9}$$

Equations (4),(8) and (9) are the equations given by Clark et al (1958), for determining the right ascension and declination of a shower with arrival direction given by direction cosines(ℓ,m,n) at local sidereal time γ at a station situated at a latitude δ_o.

REFERENCES

PICCR - Proceeding Int.Conf. Cosmic Rays.

Acharya, B.S., et al (1979), PICCR, Kyoto, 9, 109.

Acharya, B.S., et al (1979), PICCR, Kyoto, 13, 287.

Aguirre, C., et al (1973), PICCR, Denver, 4, 2592.

Allan, H.R., et al (1968), Cana,J.Phys., 46, 598.

Allison, W.W.M., et al (1970), Phys.Rev.Lett.,25, 550.

Anderson, C.D., et al (1938), Phys.Rev., 54, 88.

Antreasyan, D., et al (1977),Phys.Rev.Lett.,39, 513.

Ashton, F., et al (1968), Cana, J.Phys., 46, 1125.

Ashton, F., et al (1971), J.Phys.A. 4, 895.

Ashton, F., et al (1973), PICCR, Denver, 4, 2610.

Ashton, F., (1973a), Cosmic Rays at Ground Level,
        Ed.Wolfendale, A.W., (Inst. of Phys).

Ashton, F., et al (1975), PICCR, (Munich), 8, 2719.

Ashton, F., et al (1977), PICCR, (Plovdiv), 8, 2, 11, 400.

Ashton, F., et al (1979), PICCR, (Kyoto), 13, 243.

Balasubrahmanyan, V.K., et al (1973), Ap.J., 185, 109.

Bell, M.C., (1974), Ph.D.Thesis, Durham University.

Bennett, S., et al (1961), Phys.Rev., 124, 1982.

Boyd, R.N., et al (1977), Phys.Rev.Lett., 40, 216.

Bray, A.D., et al (1964), Nuovo Cim., 32, 827.

Brennan, M.H., et al (1958), Nuovo Cim., Supp., 8, 653.

Briatore, L., et al (1968), Nuovo Cim., A57, 850.

Catz, P., et al (1975), PICCR, (Munich), 12, 4329.

Chin, S., et al (1971), Nuovo Cim., 219, 419.

Chu, W.T., et al (1970), Phys.Rev.Lett., 24, 917.

Chudako, A.E., et al (1979), PICCR, (Kyoto), 8, 217.

Clark, G.W., et al (1958), Nuovo Cim, Supp., $\underline{8}$, 623.

Clark, G.W., et al (1961), Phys.Rev., $\underline{122}$, 637.

Cocconi, G., (1961), Handbuch der Physik, Vol.XLVI/I, 215-271.

Crouch, P.C., et al (1980), Preprint, University of Adelaide, August, 1980.

De Beer, J.E., et al (1966), Proc.Phys.Soc., $\underline{89}$, 567.

De Beer, J.E., et al (1968), J.Phys., A, Ser.2, $\underline{1}$, 72.

Evans, A., (1971), Ph.D.Thesis, Leeds University.

Galbraith, W., (1958), Extensive Air Showers (Butterworths Scientific Publication).

Geitel, H., (1900), Physik., Z, $\underline{2}$, 116.

Gell-Mann, M., (1964), Phys.Lett., $\underline{8}$, 214.

Gockel, A., (1911), Physik, Z, $\underline{12}$, 295.

Gombosi, T., et al (1975) : Nature, $\underline{255}$, 687 ; PICCR,(Munich, $\underline{2}$, 587.

Greisen, K., (1956), Progress in Cosmic Ray Physics, Vol.3, Chapter $\underline{1}$, (Amsterdam, North Holland).

Greisen, K., (1960), Ann.Rev.Nuc.Sci., $\underline{10}$, 63.

Hara, T., et al (1979), PICCR, (Kyoto), 13, 148.

Hasegawa, H., et al (1962), J.Phys.Soc., Japan, A-III, Supp. $\underline{17}$, 189.

Hayakawa, S.,et al (1969), Cosmic Rays (Wiley Interscience).

Hayman, P.J., et al (1962), Proc.Phys.Soc., $\underline{80}$, 710.

Hess, V.F., (1912), Physik., Z, $\underline{13}$, 1084.

Hillas, A.M., (1970), Acta, Phys. Hung., $\underline{29}$, Supp., $\underline{3}$, 539.

Hillas, A.M., (1972), Cosmic Rays, Pergamon Press.

Hillas, A.M., (1975), Phys. Reports., 20C, 74.

Jones, L.W., (1977), Rev. Mod. Phys., $\underline{49}$, 717.

Jullivsson, E., (1975), PICCR, (Munich), $\underline{8}$, 2689.

Kabonov, N.V., et al (1973), PICCR, (Denver), 4, 2534.

Karakula, S., et al (1974), J.Phys., A, 1, 437.

Kempa, J., et al (1974), J.Phys., A, 7, 1213.

Khristiansen, G.B., et al (1971), The American Translation
        of the (Izuestia Academy NAUK USSR Physics Series
        "Bulletin"), 35, 1909.

Khristiansen, G.B., et al (1972), Preprint,Moscow University,

Khristiansen, G.B., et al (1975), PICCR, (Munich), 8, 2801.

Kiraly, P., et al (1979), Nuovo Cim., 2, N.7, 1.

Kitajima, T., et al (1979), PICCR, (Kyoto), 11, 158.

Kolhorster, W., (1914), Deutsch,Phys. Gesell.Verh., 16, 719.

Krider, G.P., et al (1970), Phys.Rev., D1, 835.

Lang, K.R., (1974), Astrophysical Formula, 504.
Linsley, J, et al (1977) PICCR, Plovdiv, 12, 203.
Lloyd, J.L., (1960), Proc., Phys., Soc., 75, 387.

Manchester, R.N., et al (1977), Pulsars, 237.

McCusker, C.B.A., et al (1968), Cana.J.Phys., 46, 33.

McCusker, C.B.A., et al (1969), Phys. Rev. 177, 1902.

Millikan, R.A., (1910), Phil.Mag., 19, 209.

Millikan, R.A., (1926), Phys. Rev., 28, 851.

Miyake, S., et al (1973), PICCR, Denver, 5, 3220.

Nagashima, K., et al (1977), PICCR, Plovdiv, 2, 154.

Nishimura, J., and Kamata, K., (1952), Prog.Theor.Phys.,1,185.

Nishimura, J., and Kamata, K., (1958),Prog.Theor.Phys.,Supp.,
        6, 93.

Olejniczak, J., and Wolfendale, A.W.(1977), J.Phys., G:
        Nucl.Phys, 3, 847.

Parvaresh, A., (1975), Ph.D.Thesis, Durham University.

Peters, B., (1961), Nuovo Cim., 22, 800.

Pollock, A.T.M., et al (1978), J.Phys., G, 4, 113.

Prescott, I.C., (1977), Ph.D.Thesis, Nottingham University.

Raham, D.S., et al (1970), Phy.Rev.Lett., 24, 279.

Regener, V.H., (1951), Phys.Rev., 84, 161.

Sakata, S., (1956), Prog.Theor.Phys., 16, 686.

Samorski, M., (1971), PICCR, Hobart, 3, 959.

Samorski, M., (1979), PICCR, Kyoto, 13, 260.

Sinclair, D., (1970), (unpublished).

Smart, W.M., (1931), Text book on Spherical Astronomy,
        University of Cambridge.

Smith, A.C., (1976), Ph.D.Thesis, Durham University.

Snyder, H.S., (1949), Phys.Rev. 76, 1563.

The Astronomical Ephemeris, 1977, H.M.S.O, London, 526.

The Europhysics Study Conference, (1979), Gamma-ray astronomy
        after Cos-B, by B.N.Swanenburg.

The Fourth URURU Catalog of X-Ray Sources, by W.Forman,(1978),
        Center for Astrophysics, No. 763, Harvard College
        Observatory.

Thielheim, K.O., et al (1970), J.Phys., A, 3, 79.

Trümper, J., (1969), PICCR, Budapest, Invited Papers, 497.

Vernov, S.N., et al (1968), Cana, J.Phys., 46, S197.

Vernov, S.N., et al (1970), Acta.Phys.Hung., 29, Supp., 3,429.

Udowczyk, J., et al (1973), PICCR,Denver, 4, 2605.

Udowczyk, J., (1973), Cosmic Rays at Ground Level,
        Ed. Wolfendale, A.W., (Inst. of Physics).

Williams, R.W., (1948), Phys.Rev., 74, 1689.

Wilson, C.T.R., (1900), Proc.Cambs.Phil.Soc., 11, 32.

Wolfendale, A.W., et al (1970), Phys.Lett., B31, 410.

Wolfendale, A.W., (1978), Cosmic Ray Astrophysics,
        University of Hong Kong.

Zweig, G., (1964), Cern, Preprints, TH401, TH412.